



# FREE-BOUNDARY SIMULATIONS OF MHD PLASMA INSTABILITIES IN TOKAMAKS

Francisco Javier Artola Such

## ► To cite this version:

Francisco Javier Artola Such. FREE-BOUNDARY SIMULATIONS OF MHD PLASMA INSTABILITIES IN TOKAMAKS. Plasma Physics [physics.plasm-ph]. Université Aix Marseille, 2018. English.  
NNT : . tel-02012234

HAL Id: tel-02012234

<https://theses.hal.science/tel-02012234>

Submitted on 8 Feb 2019

**HAL** is a multi-disciplinary open access archive for the deposit and dissemination of scientific research documents, whether they are published or not. The documents may come from teaching and research institutions in France or abroad, or from public or private research centers.

L'archive ouverte pluridisciplinaire **HAL**, est destinée au dépôt et à la diffusion de documents scientifiques de niveau recherche, publiés ou non, émanant des établissements d'enseignement et de recherche français ou étrangers, des laboratoires publics ou privés.



THÈSE DE DOCTORAT  
Université Aix-Marseille

École doctorale 352: *Physique et Sciences de la Matière*  
Specialité: **Energie, Rayonnement et Plasma**

---

FREE-BOUNDARY SIMULATIONS OF MHD PLASMA  
INSTABILITIES IN TOKAMAKS

---

Presentée par:  
**Francisco Javier ARTOLA SUCH**

Physique des Intéractions Ioniques et Moléculaires (DSC)—AMU—CNRS, UMR7345  
ITER Organization, Route de Vinon-sur-Verdon, 13067 St Paul Lez Durance, France

Soutenue publiquement le 27/11/2018 devant le jury composé de:

Hinrich	LÜTJENS	CPHT, Ecole Polytechnique	Rapporteur
Fabio	VILLONE	Universita' di Napoli Federico II	Rapporteur
Matthias	HOELZL	IPP-Garching	Examinateur
Marina	BECOULET	CEA, IRFM	Examinateur
Peter	BEYER	PIIM, AMU	Directeur de thèse
Alberto	LOARTE	ITER Organization	Co-directeur de thèse
Guido	HUIJSMANS	CEA, IRFM	Supervisor CEA - invité

Nov 2015 - Nov 2018

*A mi familia y amigos*

The present work has been financed by the doctoral school "École doctorale 352: *Physique et Sciences de la Matière*" at Aix-Marseille University (France). Two thirds of this thesis were carried out at the PIIM laboratory (*Physique des Intéractions Ioniques et Moléculaires*) and the remaining third was conducted at ITER Organization under the memorandum of understanding (LGA-2016-A-6). Disclaimer: ITER is the nuclear facility INB no. 174. The views and opinions expressed herein do not necessarily reflect those of the ITER Organization.

# Acknowledgements

I would like to thank all the people that have been by my side during these three challenging years of my PhD. It is not uncommon for PhD students to have difficulties immersing themselves into the world of research and dealing with their supervisors. In this respect, I consider myself one of the most fortunate PhD students of the fusion community.

Apart from being academically and professionally exceptional, my supervisors have always supported me unconditionally over the past three years. In this respect, I want to specially thank Guido Huijsmans who has always welcomed me into his office with patience and has granted me with his time and wisdom every time I have needed it. Similarly Alberto Loarte and Peter Beyer have always found the time to assist and advise me even in their busiest and most stressful times. I want to stress that I'm deeply grateful to all of them for their advice and motivating scientific conversations.

There are probably too many people from which I have received technical help and encouragement to mention all of them, however, I want to specially thank Matthias Hoelzl for his constant and useful support and for his encouragement to pursue higher scientific achievements. As well I want to thank the people from the PIIM laboratory, the IRFM, IPP, JET, the JOREK group and the ITER science division for their useful advice and conversations. Finally I'm deeply grateful to my PhD and postdoctoral colleagues Sabine Nasr, Toon Weyes, Daan van Vugt, Pierluigi Migliano, Ryan Sweeney and many others that have accompanied me in this adventure.

Of course this work would not have been possible without the administrative help that I got from different institutions. Specially I would like to thank the doctoral school ED352 for their financial help, the PIIM, IPP and the ITER secretaries and EUROfusion for the access to the High Performance Computer (Marconi-Fusion).

## A mi gente

Pese a lo afortunado que he sido durante mi tesis, a veces el doctorado puede poner a prueba la fuerza mental de uno, y durante estos tres años, he pasado sin duda momentos difíciles de estrés y de desánimo. El apoyo incondicional de mi madre y de mi padre ha sido esencial para salir adelante, pues siempre me han sabido escuchar con paciencia y me han sabido reconfontar. Así mismo quiero agradecer a todos mis amigos y allegados que me han motivado a seguir adelante, especialmente a Aisling, que ha estado conmigo en los momentos más complicados y también en los más felices. También quiero agradecer a Carlos, entre muchas otras cosas, las horas que pasó ayudándome con mis estudios desde mi infancia y su insistencia en continuar mi carrera académica. Finalmente no puedo sino recordar a mi abuelo Pepe, quien despertó y potenció mi interés por la naturaleza con cientos de revistas y documentales cuando era niño y que de seguro, se habría llevado una buena alegría al oír estas páginas.

# Résumé en français

## Introduction générale

L'un des principaux défis pour la lutte contre le changement climatique est l'obtention d'une source d'énergie propre, abondante et durable. À cet égard, la production d'énergie avec des réactions de fusion thermonucléaire est une candidate potentielle pour la solution à long terme. Actuellement, deux types principaux de machines sont considérés comme possibles futurs réacteurs à fusion: le tokamak et le stellarator. Dans ces réacteurs, un plasma chaud ionisé est confiné à l'aide d'un champ magnétique intense. Puisqu'un tel plasma est généralement hors équilibre thermodynamique, il est le siège d'instabilités qui détériorent son confinement et peuvent également endommager les composants qui l'entourent. Même si l'étude des plasmas magnétiquement confinés a commencé à la fin de la deuxième guerre mondiale, des nombreuses questions concernant les origines et la dynamique de ces instabilités, en raison de leur nature non-linéaire et complexe, ont besoin de clarification. Cette thèse doit être considérée comme une contribution à l'étude de ces instabilités au sein des tokamaks, qui doivent être comprises, prédictes et contrôlées car actuellement, elles constituent l'un des obstacles les plus complexes pour l'obtention de l'énergie de fusion.

Le sujet de cette thèse est l'étude d'un type particulier d'instabilités de tokamak avec des simulations numériques MagnetoHydroDynamiques (MHD). La recherche de ce type d'instabilités nécessite un traitement spécial des conditions au bord du plasma pour le champ magnétique, où l'interaction du plasma avec le vide et les structures conductrices environnantes doit être prise en compte. Le code JOREK-STARWALL est adapté et appliqué afin d'étudier la physique de deux instabilités de frontière libre particulières: les modes localisés au bord ("Edge Localized Modes", ELMs) déclenchés par des oscillations de la position verticale du plasma et les événements de déplacement vertical ("Vertical Displacement Events", VDEs). La motivation pour étudier ces instabilités vient du fait qu'elles peuvent produire des

grandes charges thermiques et électromagnétiques sur les composants entourant plasma, ce qui est une préoccupation pour les futurs tokamaks à grande échelle tels que ITER et DEMO, où grandes quantités d'énergie thermique et magnétique peuvent être libérées.

### **Sujet de recherche 1: déclenchement des ELMs par des oscillations de la position verticale**

Lorsque les tokamaks fonctionnent dans le régime de haut confinement ("high-confinement mode", H-mode), des grands gradients de pression et des densités de courant électrique apparaissent en raison d'une réduction du transport turbulent au bord du plasma. Cette région où les gradients de pression sont forts est appelée le piédestal. Les gradients et les hautes densités de courant au piédestal sont limités par une instabilité localisée au bord du plasma, laquelle induit des charges thermiques significatives et pulsées qui réduisent périodiquement les gradients de densité et de température. Ces instabilités appelées ("Edge Localized Modes", ELMs) peuvent expulser jusqu'à un 10% de l'énergie thermique du plasma par l'éjection de filaments chauds et par conduction thermique dans la direction parallèle au champ magnétique, qui devient stochastique. Les ELMs sont généralement associées à l'apparition de modes *peeling-balloonning*, un type d'instabilité MHD.

Pour les futurs tokamaks tels que ITER et DEMO, les ELMs naturels ne peuvent pas avoir lieu en raison des limites d'érosion des composants en contact avec le plasma et en raison du contrôle du contenu en impuretés. Pour faire face à ces problèmes, le contrôle de la fréquence des ELMs ( $f_{\text{ELM}}$ ) pourrait jouer un rôle très important. À cet égard, il a été observé que l'énergie libérée par ELM ( $\Delta W_{\text{ELM}}$ ) décroît avec la fréquence des ELMs ( $\Delta W_{\text{ELM}} \propto f_{\text{ELM}}^{-1}$ ) et aussi que l'augmentation de  $f_{\text{ELM}}$  peut aider à expulser les impuretés situées à l'intérieur du plasma. Une des techniques possibles pour contrôler  $f_{\text{ELM}}$  consiste à déclencher les ELMs avec des oscillations de la position verticale du plasma, souvent appelées "vertical kicks" ou "vertical jogs". Cette technique a été utilisée pour le contrôle de la fréquence des ELMs dans le régime de type I relevant pour ITER au tokamak ASDEX-Upgrade et au tokamak JET. Cette méthode consiste à appliquer perturbations axisymétriques sur le champ magnétique radial qui conduisent aux oscillations de la position verticale du plasma. Lorsque la fréquence des oscillations verticales dépasse la fréquence naturelle des ELMs,  $f_{\text{ELM}}$  s'adapte à la fréquence de l'oscillation verticale. Pour

ITER, les oscillations verticales sont considérées comme une technique de soutien pour les opérations initiales avec plasmas à demi-courant et demi-champ magnétique (7.5 MA, 2.65 T) afin de compléter le schéma de contrôle des ELMs de base (perturbations magnétiques résonantes) au fur et à mesure du développement de l'application de cette technique.

Afin de clarifier les bases physiques de cette approche de contrôle des ELMs et son application à ITER, la combinaison des codes JOREK et STARWALL est utilisée. De même, ces études numériques visent à comprendre les observations expérimentales rapportées dans le tokamak JET sur le mécanisme de déclenchement des ELM, qui sont les suivantes:

- Le déclenchement des ELMs se produit lorsque le plasma est déplacé une distance vertical minimale ( $\Delta Z$ ) vers le point X. La vitesse ( $v_z$ ) du mouvement vertical ne joue qu'un rôle mineur.
- Le mécanisme de déclenchement n'est pas efficace lorsque le plasma s'éloigne du point X.
- Cette technique est plus efficace (en termes d'un  $\Delta Z$  inférieur requis) quand la collisionnalité du plasma est plus faible.

## Sujet de recherche 2: VDEs and courants de halo

La géométrie et l'elongation du plasma sont des ingrédients clés pour augmenter la performance de fusion. Cependant, le principal inconvénient des plasmas allongés est qu'ils sont toujours instables aux déplacements verticaux axisymétriques ( $n = 0$ ). Cette instabilité appelée événement de déplacement vertical ("Vertical Displacement Event", VDE) est stabilisée par la présence de structures conductrices environnantes, qui ralentissent l'échelle de temps du mouvement vertical au temps donné par la résistance des conducteurs ( $\tau_w$ ). Pour l'opération de ces plasmas, un système de contrôle de rétroaction est nécessaire afin de contrôler la position verticale. Dans le cas d'un VDE non contrôlé, le plasma se met en contact avec la paroi, moment auquel une partie du courant de plasma est transféré au mur, générant ce que l'on appelle des courants de halo.

Les courants de halo entraînent des forces de Laplace importantes sur la chambre à vide et sur les structures conductrices. En raison de la réduction du volume du plasma pendant le mouvement vertical, la valeur du facteur de sécurité ( $q$ ) peut décroître considérablement et

le plasma peut devenir instable face aux modes MHD du type *kink*. Cela provoque une déformation 3D du plasma, la localisation toroïdale des courants de halo et la rotation des courants de halo. Une préoccupation concernant cette rotation pour ITER est la possibilité d'une résonance de la rotation des courants de halo et les forces électromagnétiques associées sur la chambre à vide avec les modes propres mécaniques de la machine. La physique des VDE en trois dimensions et en particulier les causes de la rotation du plasma au cours des VDE ne sont pas bien établies.

Dans cette thèse, l'instabilité VDE est analysée avec des simulations MHD. Premièrement, différents comparaisons complexes avec d'autres codes MHD existants avec des conditions de bord à frontière libre sont effectués dans le but de valider JOREK-STARWALL. L'influence du rapport entre le temps résistif du plasma et le temps résistif des structures conductrices ( $\tau_{CQ}/\tau_w$ ) sur la fraction de courant de halo (HF) est analysée avec un plasma d'ITER axisymétrique. Finalement, des simulations VDE préliminaires à trois dimensions sont effectuées dans le but d'étudier la rotation de l'asymétrie du courant de halo et sa dépendance avec  $\tau_{CQ}$  pour des VDE d'ITER à basse température et avec une paroi axisymétrique.

## Théorie et méthodes à frontière libre développées pour JOREK-STARWALL

Les simulations des ELMs déclenchées avec des oscillations de position verticale et les simulations des VDE sont très similaires en termes du cadre numérique requis. En plus de la description MHD à trois dimensions, les deux phénomènes nécessitent des conditions à frontière libre pour le mode axisymétrique ( $n = 0$ ) afin de permettre des mouvements verticaux du plasma. Les conditions au bord à frontière libre consistent en une relation des composantes tangentielles du champ magnétique  $\mathbf{B}_{tan}$  avec la composante normale  $B_n$  et avec les courants dans les structures conductrices ( $\mathbf{Y}$ ). Cette relation donnée par STARWALL est implémentée dans la méthode numérique des éléments finis en tant qu'une condition au bord naturelle. Dans cette thèse, une dérivation originale des équations du code STARWALL a été développée avec une extension pour les courants de halo. La dérivation est basée sur l'application du méthode des éléments finis aux équations de Maxwell et à la loi d'Ohm en utilisant une approximation à paroi fine. Finalement, la condition au bord trouvée, y compris

le terme courant de halo ( $\mathbf{J}_\perp$ ), est

$$\mathbf{B}_{\tan} = \mathbf{M}_{ey} \mathbf{Y} + \sum_l^3 \mathbf{M}_{\parallel e,l} \mathbf{A}_{p,l}^e + \mathbf{M}_{yJ} \mathbf{J}_\perp \quad (1)$$

où  $\mathbf{A}_{p,l}$  est le potentiel vecteur magnétique au bord du plasma et  $\mathbf{M}$  indique des différentes matrices géométriques. De même, la contribution des courants de halo est maintenant incluse dans l'équation de l'évolution temporelle des courants des structures conductrices

$$\dot{\mathbf{Y}} = -M_{yy} \mathbf{Y} - \sum_l^3 M_{ye,l} \dot{\mathbf{A}}_{p,l}^e - M_{yJ} \dot{\mathbf{J}}_\perp \quad (2)$$

où le symbol point dénote dérivation par rapport au temps.

L'une des réalisations importantes de cette thèse a été l'implémentation correcte des bobines poloïdales dans JOREK-STARWALL avec des courants pouvant varier dans le temps. Grâce à cette dernière mise en œuvre, une comparaison axisymétrique avec le code DINA a été réalisée avec succès pour une oscillation de la position verticale avec un plasma d'ITER réaliste. Cette comparaison a montré l'intérêt de mettre en œuvre toutes les inductances mutuelles du système, en particulier l'inductance mutuelle entre les composants passifs et les bobines, autrement le déplacement final du plasma obtenu pour un ensemble de courants donné pourrait être surestimé d'un facteur 2.

Finalement, une attention particulière a été accordée aux conditions initiales qui nécessitent le calcul d'un équilibre à frontière libre. La difficulté réside dans le fait que le problème de l'équilibre à frontière libre comprenant un ensemble de bobines poloïdales est en général un problème mal posé, conduisant à une mauvaise convergence de la solution de l'équation d'équilibre Grad-Shafranov. Dans cette thèse, la méthode des itérations de Picard est utilisée avec des systèmes de contrôle à rétroaction sur la position du plasma et sur le courant total qui contraignent la solution de ces équilibres. Cette technique est vérifiée avec le calcul d'un équilibre à frontière libre d'un plasma expérimental du tokamak ASDEX-Upgrade qui est comparé avec succès à la solution fournie par le code d'équilibre CLISTE.

## Résultats sur le sujet de recherche 1: Mécanisme de déclenchement des ELMs avec des oscillations de la position verticale

Pendant le mouvement vertical, des courants électriques sont induits au bord du plasma. Un modèle analytique simplifié a été dérivé afin

d'illustrer l'origine du changement du courant toroïdal de bord ( $\delta I_\phi^{w_r}$ ), en montrant qu'il est indépendant de la vitesse du mouvement vertical pour les plasmas fortement conducteurs (faible résistivité du plasma  $\eta$ ) et résultant d'un changement du flux externe au bord ( $\delta\psi_{ext}$ ) et du petit rayon ( $\delta w_r$ )

$$\delta I_\phi^{w_r} = \frac{4\pi}{\mu_0 R_0} [\delta\psi_{ext}(a) - B_\theta(r_0)R_0\delta w_r - \eta J_\phi \delta t] \quad (3)$$

L'induction de courant de bord a été étudiée numériquement avec JOREK-STARWALL pour un plasma allongé simplifié et pour un plasma d'ITER réaliste à demi-courant et demi-champ magnétique (7.5 MA, 2.65 T) en mode H. Pour le cas simplifié, l'analyse a montré que le courant induit peut être compris comme une réaction d'écrantage du plasma contre le changement de flux magnétique externe, qui peut être produit par une forte asymétrie dans les bobines avec des courants variant dans le temps ou par le mouvement du plasma à travers d'un champ magnétique inhomogène. Le cas ITER a révélé que le courant de bord induit peut également être lié à la compression du plasma en raison de son mouvement dans le champ magnétique verticalement asymétrique. De plus, les résultats indiquent que la compression et le courant induit peuvent être augmentés en choisissant différentes géométries et formes d'onde pour le courant dans les bobines utilisées pour déplacer le plasma.

Pour la première fois, la phénoménologie du déclenchement des ELMs par des oscillations de la position verticale a été simulée dans un schéma MHD dynamique et auto-cohérent. Le mode  $n = 6$  initialement stable, est déstabilisé par un mouvement descendant et reste stable lors de l'application d'un déplacement ascendant pour le plasma d'ITER. Le mode déstabilisé a la structure d'un mode *peeling-balloonning* avec une forte composante *peeling*. Des simulations supplémentaires avec un plasma initialement instable ont révélé que le mode est stabilisé par le mouvement ascendant et encore déstabilisé par un mouvement descendant. Les simulations réalisées avec JOREK-STARWALL ont révélé que le profil du courant de bord initial détermine le déplacement vertical minimal requis pour déstabiliser les ELMs. Des déplacements plus grands étant nécessaires pour des courants de bord initiales inférieurs. En accord avec les observations expérimentales, le déclenchement des ELMs dépend du déplacement vertical du plasma ( $\Delta Z$ ) plutôt que de la vitesse verticale. Pour les applications pratiques à ITER, le déplacement vertical minimum requis pour le déclenchement des ELMs dépendra fortement du courant

initial, qui devrait être important à ITER en raison de la faible collisionnalité des plasmas en mode H.

Ces simulations confirment l'hypothèse du courant de bord induit en tant que le mécanisme de la déstabilisation des ELM chez ITER. La nécessité de déplacements plus grandes pour les courants initiaux plus faibles et le fait que le courant de bord augmente pour les mouvements descendants renforcent l'idée du courant de bord comme principal facteur de la déstabilisation. Le mode déstabilisé présente également une forte structure d'un mode du type *peeling*. Ce mécanisme peut également expliquer la faible dépendance du déclenchement des ELMs de la vitesse verticale comme l'équation (4.6) indique. Le rôle des modifications du profil de la pression au cours de l'oscillation verticale ne semble pas être le facteur principal du déclenchement des ELMs. Cependant, une évaluation précise des effets des changements du gradient de pression sur le déclenchement des ELMs par des oscillations de la position verticale nécessite des investigations supplémentaires.

## Résultats sur le sujet de recherche 2: VDEs et courants de halo à ITER

Au cours de cette thèse, JOREK-STARWALL a été appliqué pour simuler des VDEs. Premièrement, des différents tests de performance et comparaisons ont été réalisés. Ces tests ont montré que le mur idéal de STARWALL est capable de conserver correctement le flux magnétique poloïdal, que les taux de croissance linéaires calculés pour les VDEs concordent bien avec des autres codes MHD en frontière libre existants et que l'évolution du plasma en 2D est bien reproduite pour un plasma d'ITER qui rentre en contact avec la première paroi.

De plus, des simulations VDE ont été effectuées pour un plasma d'ITER (15MA/5.3T), révélant l'universalité des courbes  $Z_{\text{axis}}(I_p)$  à faibles rapports  $\tau_{\text{CQ}}/\tau_w$ . Ces courbes sont indépendantes des échelles de temps tel que prédit par [KB17]. L'influence du ratio  $\tau_{\text{CQ}}/\tau_w$  sur la fraction de courant de halo (HF) a été évaluée, indiquant qu'une fraction de halo minimale existera (d'environ  $\sim 8\%$ ) quels que soient les schémas de contrôle du temps résistif du plasma utilisés dans ITER. Dans les cas où les ratios  $\tau_{\text{CQ}}/\tau_w$  sont élevés, les VDE purs sont déstabilisés et le plasma arrive à la première paroi avec tout son courant initial. Ces cas montrent une fraction de halo maximale de (36%) qui est un facteur 5 plus grand que le HF minimum attendu et est similaire aux valeurs trouvées par le code DINA [Leh+15]. Dans le cas

d'une disruption contrôlée à ITER, ces simulations prédisent une fraction de courant de halo comprise entre 10 et 15 %, ce qui correspond à des événements avec des charges électromagnétiques acceptables.

Finalement, des simulations préliminaires des VDEs asymétriques à basse température ont été effectuées. Dans ces simulations, un mode du type *kink* résistif  $m = 2/n = 1$  est déstabilisé au bord du plasma où la surface rationnelle  $q = 2$  existe. La structure du mode provoque une asymétrie toroïdale des courants de halo caractérisée par un faible facteur d'asymétrie toroïdal ("Toroidal Peaking Factor", TPF) de l'ordre de 1.15 qui est indépendant du temps de résistif du plasma. La structure asymétrique des courants de halo complète environ 0.5 rotations autour du tore. La fréquence moyenne de cette rotation est de l'ordre de 0.5 kHz pour un temps résistif du plasma de 11 ms et dépend de  $\tau_{\text{CQ}}$  suivant la loi  $\langle f_h \rangle \sim \tau_{\text{CQ}}^{-0.5}$  en bon accord avec les observations expérimentales présetées en [Mye+17]. Lorsque le mode asymétrique est ajouté à la simulation, une augmentation soudaine de la fraction de halo est observée. Par conséquent, l'interaction du mode 2/1 avec le mode  $n = 0$  est capable d'induire une quantité supplémentaire du HF qui ne peut pas être observée avec des codes 2D. Ce résultat révèle l'importance de simulations 3D afin de prédire les courants de halo.

# Contents

<b>1</b>	<b>Introduction</b>	<b>1</b>
1.1	General introduction . . . . .	1
1.1.1	A brief history of fusion and tokamaks . . . . .	2
1.1.2	Tokamaks and magnetic confinement . . . . .	4
1.2	MHD instabilities in tokamaks . . . . .	5
1.2.1	MHD theory . . . . .	5
1.2.2	Edge Localized Modes (ELMs) . . . . .	11
1.2.3	ELM control . . . . .	15
1.2.4	Vertical Displacement Events (VDEs) and disruptions . . . . .	21
1.3	Scope of this thesis . . . . .	26
<b>2</b>	<b>Tokamak modelling</b>	<b>29</b>
2.1	Plasma domain: the JOREK code . . . . .	30
2.1.1	Plasma equations: the reduced and full MHD models . . . . .	31
2.1.2	Spatial discretization and finite element method . . . . .	35
2.1.3	Time discretization and solvers . . . . .	37
2.1.4	Simulation phases . . . . .	38
2.2	Vacuum, coils and wall domain: the STARWALL code . . . . .	39
2.3	The JOREK-STARWALL coupling . . . . .	42
<b>3</b>	<b>Free-boundary theory and methods for JOREK-STARWALL</b>	<b>45</b>
3.1	STARWALL's general derivation . . . . .	45
3.1.1	Formulation of the STARWALL's equations . . . . .	45
3.1.2	The weak form . . . . .	48
3.1.3	Matrix form . . . . .	49
3.1.4	$\mathbf{B} \times \mathbf{n}$ at the JOREK boundary . . . . .	52
3.2	Computation of free-boundary equilibria . . . . .	53
3.2.1	Picard iterations and FEM . . . . .	53
3.2.2	Fixed-boundary equilibria . . . . .	54
3.2.3	Free-boundary equilibria . . . . .	55
3.2.4	Reconstruction of experimental equilibria . . . . .	57
3.2.5	Identification of plasma boundary and special points . . . . .	58
3.3	Optimization of coil currents for arbitrary equilibria . . . . .	60
3.4	Implicit imposition of coil currents over time . . . . .	63
<b>4</b>	<b>Simulation of Edge Localised Mode triggering via vertical oscillations</b>	<b>67</b>
4.1	Introduction . . . . .	67
4.2	Understanding the axisymmetric induction of edge currents during vertical oscillations . . . . .	68
4.2.1	Simple elongated plasma . . . . .	69

4.2.2	ITER case . . . . .	72
4.3	ELM triggering for an ITER plasma . . . . .	76
4.4	Conclusions . . . . .	80
<b>5</b>	<b>Vertical Displacements Events</b>	<b>83</b>
5.1	Tests and benchmarks for JOREK-STARWALL . . . . .	83
5.1.1	Test for the toroidal net-current potential . . . . .	83
5.1.2	Benchmark for the source/sink current potentials . . . . .	84
5.1.3	Benchmark with M3D-C1 . . . . .	86
5.1.4	Axisymmetric comparison with the DINA code . . . . .	89
5.2	Studies for ITER VDEs . . . . .	92
5.2.1	Universality of the $Z_{\text{axis}}(I_p)$ curve at low $\tau_{\text{CQ}}/\tau_w$ for ITER . . . . .	92
5.2.2	Influence of the $\tau_{\text{CQ}}/\tau_w$ ratio in the halo current fraction . . . . .	93
5.2.3	Simulations of cold AVDEs in ITER . . . . .	95
<b>6</b>	<b>Conclusions and future work</b>	<b>101</b>
<b>Appendices</b>		<b>104</b>
A.1	Plasma shape and geometry . . . . .	105
B.2	JOREK variables and normalization . . . . .	106
C.3	Geometrical matrices in STARWALL . . . . .	107
D.4	Poloidal current evolution equation in reduced MHD . . . . .	109
D.4.1	Consistency of the toroidal Faraday's equation with the equilibrium condition . . . . .	109
<b>Bibliography</b>		<b>111</b>



# Chapter 1

## Introduction

*We are the victims, but we are also the crime. And the only one who can judge us, is the Earth in time.*

---

**Born of Osiris, Follow the signs**

### 1.1 General introduction

Over the last centuries, the overwhelming developments in technology and scientific knowledge have considerably increased the life expectancy of the human race. The machine era has simplified laborious work, increased human's production efficiency and reduced the world's distances with faster communications and transportation. As a consequence, the human population has been growing exponentially during the last two centuries in addition to the material and energy needs.

However, the resulting massive consumption of energy and resources could be very harmful not just for the environment, but also for mankind. Empirical evidence shows that there's a clear correlation between the increase of the world's average temperature and the increase of the concentration of Greenhouse gasses due to human activity [Mei+09]. In addition to the loss of diversity in the world's fauna and flora caused by deforestation, sea acidification and the increase of world's average temperature, the accelerated melting of ice in the Earth's poles [Mil08] will increase the sea level causing massive problems of migration. Among many other consequences, climate change may also modify the distribution of water resources, increase the risks for human health, intensify extreme weather events and impose heavy costs on different sectors of the economy.

Even if the international community is taking measures to fight climate change [COP15], larger efforts may be required. The solution to climate change may come from the development of more sustainable and more efficient technologies, a radical change in human mentality and lifestyle or a combination of both. In this respect, fusion as a clean, vast, dense and safe source of energy could play a decisive role in the long term solution.

The most feasible thermonuclear reaction envisioned on Earth (in terms of the lowest temperature required) is the fusion of ionized deuterium ( $D^+$ ) and tritium ( $T^+$ ), the two heavier isotopes of hydrogen, into Helium ( $He^{+2}$ )



where a neutron ( $n$ ) and a total kinetic energy of 17.6 MeV, shared between both  $He^{+2}$  and  $n$ , are released. In order to fuse the deuterium and tritium ions, very high temperatures are

required to overcome the Coulomb barrier between the two positively charged nuclei. At such temperatures (of the order of tens of millions of degrees Celsius) matter is fully ionized - this state of matter is known as plasma. This plasma state exhibits a rich variety of physical phenomena involving electromagnetic fluid and kinetic effects.

Nowadays two main type of devices are considered as possible future fusion reactors, the tokamak and the stellarator. As these systems are out of thermodynamic equilibrium, they are prone to instabilities that deteriorate the plasma confinement. This work has to be regarded as a contribution to the study of these instabilities in tokamaks, which need to be understood, predicted and controlled as they are currently one of the most complicated impediments to the goal of fusion energy.

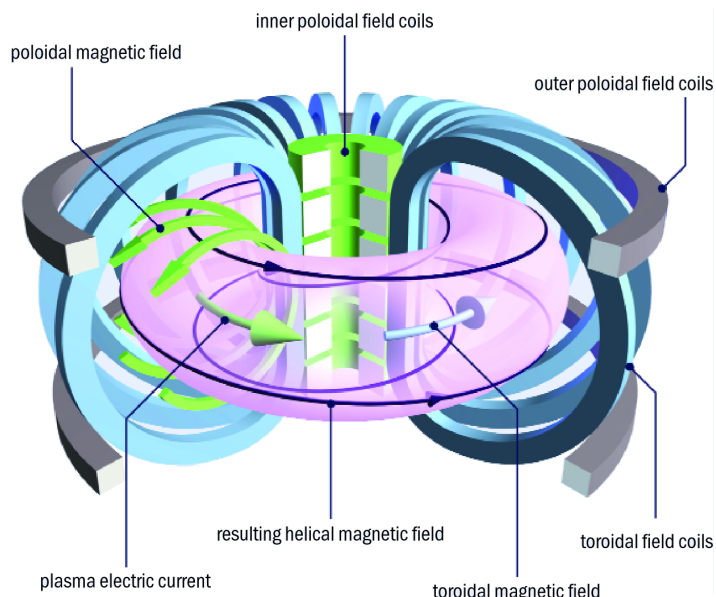


FIGURE 1.1: Schematic picture showing the basics of a tokamak's design. Figure obtained from [PBP06].

### 1.1.1 A brief history of fusion and tokamaks

When the hydrogenic fusion reactions fuelling the sun were discovered during the first half of the 20th century, the thought arose that this "latent power" could be controlled "for the well-being of the human race - or for its suicide" [BS02]. Driven by the aim of controlling thermonuclear reactions, physicists started attempting to confine a hot plasma with magnetic fields and to heat it with radio-frequency waves in 1938 in the USA [BS02]. The research field of magnetically confined plasmas started after World War II. During the 50s, several magnetic confinement devices were conceived and tested in the fusion research centres of USA, UK and the Soviet Union. Inspired by a letter written in 1950 by a Red Army sergeant called Oleg Lavrentiev, the physicists Andrei Sakharov and Igor Tamm conceived a very promising magnetic confinement device in the Kurchatov Institute in Moscow. Their idea was to confine the plasma in a toroidal chamber with a strong guiding toroidal field and to induce a toroidal current within the plasma in order to have a resulting helical magnetic field (see figure 1.1). These toroidally symmetric devices, thereafter named tokamaks, were able to considerably improve the particle confinement by cancelling the particle vertical drifts thanks to the helicity of the magnetic field. The tokamak concept led the fusion field since UK scientists visited their Soviets counterparts in Moscow to verify their incredible announcement that they had reached temperatures of 1 keV (more than 10 million degrees Celsius) in 1969.

In the following decades, several tokamaks were constructed with different geometries, magnetic properties and heating and diagnostic systems. During this time significant progress was made in controlling the main plasma instabilities and in increasing the heating efficiency. The current world record of fusion power was achieved in 1997 in the JET tokamak (Joint European Torus) in Oxfordshire UK. The obtained fusion gain factor<sup>1</sup> was  $Q = 0.63$  with a 50%-50% mix of deuterium and tritium and a heating power of 25 MW [K+99].

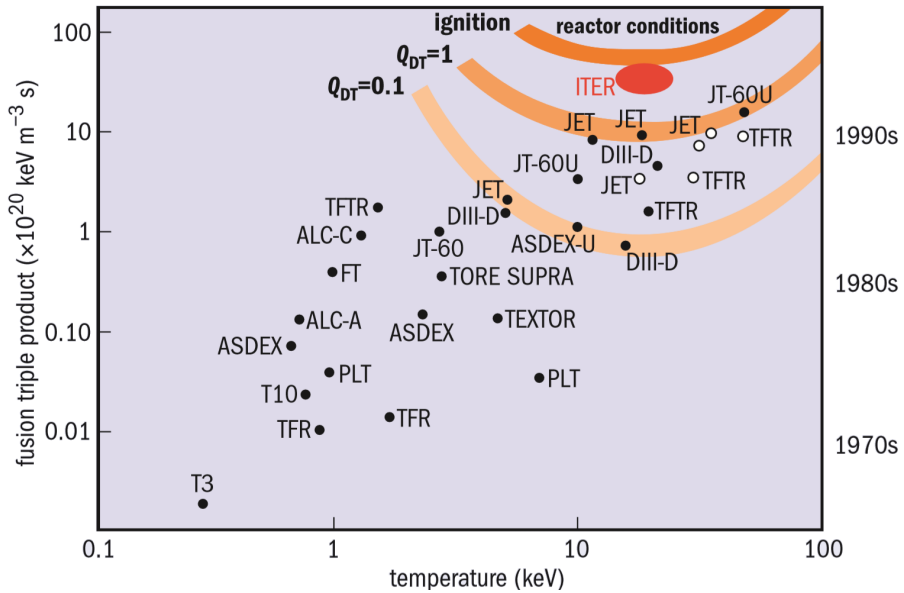


FIGURE 1.2: Fusion triple product as a function of the core ion temperature for different tokamaks [PBP06].

An important figure of merit to characterize the probability of attaining fusion is the so-called triple product. The triple product is the result of multiplying the ion plasma density ( $n_i$ ) with the ion temperature ( $T_i$ ) and with the confinement time ( $\tau_E$ ), a quantity describing the time-scale in which the plasma loses its thermal energy. The Lawson criterion [Fre14] gives the minimum value for the triple product to achieve ignition, a state in which the produced fusion power is such that the fusion reaction can be self-sustained without the need of external heating power. The Lawson criterion for a 50%-50% mix of deuterium and tritium is

$$n_i k_B T_i \tau_E > 8 \text{ atm} \cdot \text{s} \quad (1.2)$$

The confinement time ( $\tau_E$ ) is the most intricate parameter in the calculation of the triple product as current modelling capabilities are still not sufficient for its prediction. The calculation of  $\tau_E$  for future tokamaks is made with an extrapolation based on scaling laws constructed with current experiments

$$\tau_E^{\text{IPB98(y)}} \propto I_p^{0.93} R^{1.97} B_\phi^{0.15} P_{\text{heat}}^{-0.69} n^{0.41} \varepsilon^{0.58} \kappa_a^{0.78} M^{0.20} \quad (1.3)$$

where  $I_p$  is the plasma current,  $R$  is the major radius,  $B_\phi$  is the toroidal magnetic field,  $n$  is the particle density,  $\varepsilon$  is the inverse aspect ratio,  $\kappa_a$  is the plasma elongation and  $M$  is the average ion mass [CCE99]. The progress made in the achievement of higher triple products and fusion gains during the last decades is shown in figure 1.2. The advances of fusion experiments as measured with the triple product, followed a similar trend to the Moore's law for transistors in CPUs until the 2000s. The strong dependence of the confinement time with the machine size

---

<sup>1</sup>The fusion gain factor ( $Q \equiv P_{\text{fus}}/P_{\text{heat}}$ ) is defined as the produced fusion power divided by the required heating power to maintain the plasma in steady state

$(R)$  led to the design of larger scale tokamaks whose complexity decelerated the growth of the fusion performance in the last two decades.

In November 1985, an agreement between Ronald Reagan and Mikhail Gorbachev led to an international effort to construct a large-scale tokamak capable of producing net fusion power. This project known as ITER, was approved in 2006 and it is currently being built in the south of France. Among other goals to demonstrate the feasibility of fusion, ITER is designed to achieve a fusion gain of  $Q = 10$ . Even if the design of the ITER tokamak is already defined, there are still open questions regarding underlying physics, the control and the scaling with machine size of several plasma instabilities. The development and application of numerical tools in order to understand and predict such instabilities in ITER is one of the main motivations of this work.

### 1.1.2 Tokamaks and magnetic confinement

In a tokamak, the magnetic field-lines wrap into the so-called magnetic flux surfaces (see figure 1.3). The important property of these surfaces is that particles cannot drift across them provided that the magnetic field is sufficiently strong. This is a consequence of the conservation of the toroidal momentum ( $P_\phi$ ) of a charged particle due to the toroidal symmetry of the system

$$P_\phi = mv_\phi R + e\psi = \text{constant} \approx e\psi \quad (1.4)$$

where  $m$  is the particle's mass,  $v_\phi$  is the toroidal velocity,  $R$  is the major radius of the tokamak,  $e$  is the particle's charge and  $\psi \equiv A_\phi/R$  is the toroidal magnetic vector potential divided by the major radius. The surfaces of constant magnetic flux  $\psi$  describe the nested magnetic flux surfaces shown in figure 1.3. The concept of the magnetic flux surfaces is very relevant as they provide the radial confinement that allows the achievement of very high temperatures. Nevertheless, collisions and collective interactions between particles lead to a radial transport that degrades the confinement.

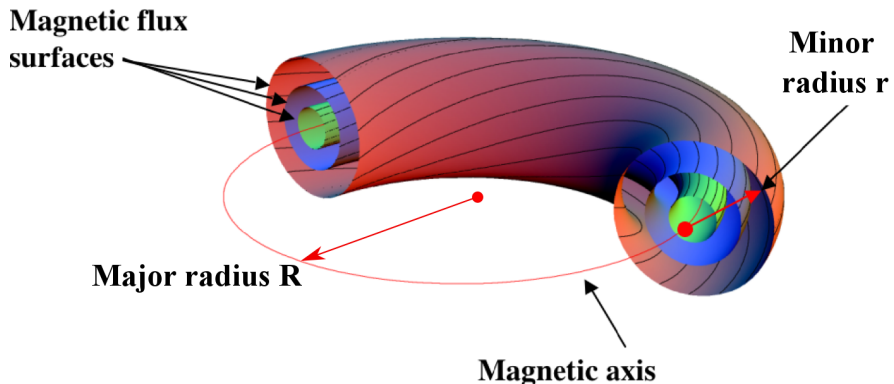


FIGURE 1.3: Schematic picture showing the wrapping of the magnetic field lines (black curves) forming magnetic flux surfaces. Adapted from [AW].

In every magnetic surface, the pitch angle of the magnetic field lines is described with the safety factor  $q$ . The safety factor is equal to the number of turns made in the toroidal direction ( $\phi$ ) for each turn in the poloidal direction ( $\theta$ )

$$q(\psi) = \frac{d\phi}{d\theta} \quad (1.5)$$

When the value of  $q$  is rational, the field lines are closed and they return to the initial poloidal position after  $n$  toroidal turns. These are the so-called rational magnetic surfaces which are very relevant for the study of plasma instabilities (see section 1.2.1).

Another important figure of merit is the  $\beta$  factor. This factor describes the performance of a tokamak with the ratio of the thermal pressure and the magnetic pressure

$$\beta = \frac{\langle p \rangle}{B_0^2/2\mu_0} \quad (1.6)$$

where  $\langle p \rangle$  is the average plasma pressure and  $B_0$  is the magnetic field strength at the plasma geometric center.

## 1.2 MHD instabilities in tokamaks

In this section the theory of magnetohydrodynamics in which this work is based is reviewed. The first subsection presents the MHD model and its main properties, where the energy principle is exposed as a tool to study the MHD stability and to classify different types of instabilities. In subsections 1.2.2, 1.2.3 and 1.2.4 the MHD instabilities that are the subject of this work are examined.

### 1.2.1 MHD theory

Magnetohydrodynamics (MHD) is a theory based on a fluid model that describes the macroscopic equilibrium and stability properties of electrically conducting fluids. The equations characterizing MHD are a combination of Maxwell's equations of electromagnetism and of Navier-Stokes equations for fluids. The applicability of this model is very broad as it can describe different physical systems, such as astrophysical and laboratory plasmas as well as liquid metals. In the case of fusion devices, MHD theory has been able to predict several operational limits associated with the onset of violent instabilities. In fact, it could be stated that the main goal of MHD in the fusion field, is to provide plasma configurations with sufficiently high thermal pressure and stability to satisfy the requirements for a commercial fusion reactor.

The MHD model is formally derived from a more fundamental and inclusive kinetic description of the plasma, which describes the behaviour of the ion and electron distribution functions. Specifically, the MHD equations are obtained by evaluating the mass, momentum and energy moments of the Boltzmann's equation, which describes the evolution of the distribution functions [GGP04]. Depending on the chosen ordering approximations that are required to close the system of equations, different MHD versions can be derived. The following system of equations form the so-called resistive MHD

$$\text{Mass:} \quad \frac{\partial \rho}{\partial t} + \nabla \cdot (\rho \mathbf{v}) = 0 \quad (1.7a)$$

$$\text{Momentum:} \quad \rho \frac{d\mathbf{v}}{dt} = \mathbf{J} \times \mathbf{B} - \nabla p \quad (1.7b)$$

$$\text{Energy:} \quad \frac{d}{dt} \left( \frac{p}{\rho^\gamma} \right) = 0 \quad (1.7c)$$

$$\text{Generalized Ohm's law:} \quad \mathbf{E} + \mathbf{v} \times \mathbf{B} = \eta \mathbf{J} \quad (1.7d)$$

$$\text{Maxwell-Gauss:} \quad \nabla \cdot \mathbf{B} = 0 \quad (1.7e)$$

$$\text{Maxwell-Faraday:} \quad \frac{\partial \mathbf{B}}{\partial t} = -\nabla \times \mathbf{E} \quad (1.7f)$$

$$\text{Maxwell-Ampère:} \quad \mu_0 \mathbf{J} = \nabla \times \mathbf{B} \quad (1.7g)$$

where the electromagnetic variables are the magnetic field  $\mathbf{B}$ , the electric field  $\mathbf{E}$  and the current density  $\mathbf{J}$ . The fluid variables are the mass density  $\rho$ , the fluid velocity  $\mathbf{v}$ , the pressure  $p$  and the resistivity  $\eta$ . Also,  $\gamma$  is the ratio of specific heats and  $d/dt \equiv \partial/\partial t + \mathbf{v} \cdot \nabla$  is the convective time derivative. The latter system can be written in its conservative form [GGP04] revealing that the MHD equations are conservation laws for the mass, the momentum, the energy and the magnetic flux.

More complex models including two-fluid, viscous and kinetic effects (i.e. trapped particles, finite ion gyro-radius, energetic particles) can be derived. The simplest model is obtained by neglecting the resistive effects (by dropping the  $\eta\mathbf{J}$  term in equation (1.7d)) which is the so-called ideal MHD. The main property of ideal MHD arises from the *frozen theorem*, which states that the fluid velocity  $\mathbf{v}$  is attached to the magnetic field lines. In words of Hannes Alfvén<sup>2</sup>: "In view of the infinite conductivity, every motion (perpendicular to the field) of the liquid in relation to the lines of force is forbidden because it would give infinite eddy currents. Thus the matter of the liquid is "fastened" to the lines of force". This leads to important topological constraints on the allowable dynamical motions of the plasma. In fact the property of "froze-in" field line topology can be taken as the basic definition of ideal MHD.

The characteristic time-scales of ideal MHD instabilities are given by the Alfvén time

$$\tau_A = a/v_A \quad (1.8)$$

where  $a$  is the spatial size of the considered physical system and  $v_A = |\mathbf{B}|/\sqrt{\mu_0\rho}$  is the Alfvén velocity. The Alfvén velocity is the group velocity of the Alfvén waves which are the basic solutions of the MHD equations. For a Deuterium plasma with an ionic particle density of  $n_i = 10^{20}\text{m}^{-3}$ , a magnetic field strength of  $B = 1\text{ T}$  and a minor radius of  $a = 1\text{ m}$ , the Alfvén time is  $\tau_A = 0.65\mu\text{s}$ .

Although the resistive term ( $\eta\mathbf{J}$ ) is typically very small for plasmas of fusion interest [Fre14], it can play a very important role. As this term does not arise from an electrostatic potential, it contributes to Faraday's law allowing a new class of motions that are forbidden in ideal MHD. In addition, MHD modes can develop a singular behaviour around the rational surfaces of the plasma causing large and narrow current densities, making the  $\eta\mathbf{J}$  term to become very relevant. These motions are related with the change of topology of the magnetic field, allowing the reconnection and tearing of the field-lines. These phenomena arise on a hybrid time-scale mixing the fast time-scales of ideal MHD with long resistive diffusion scales  $\tau_R = \mu_0 a^2/\eta$ . Typical values for the hybrid scale are of the order of 1 ms.

## The extended energy principle

A basic problem of most physical systems is to determine whether a given equilibrium is stable or unstable when it is subjected to a small perturbation. When dealing with a complicated system of equations such as (1.7), a basic analysis is to linearise the equations over a time-independent equilibrium with first order time-dependent fluctuations. Then every plasma quantity  $h$  is written in the form

$$h(\mathbf{r}, t) = h_0(\mathbf{r}) + h_1(\mathbf{r})e^{\omega t} \quad (1.9)$$

where  $\omega$  is the complex growth rate and  $h_1 \ll h_0$ . This form allows to classify the stability of the equilibrium by solving for  $\omega$ . If  $\text{Re}(\omega) < 0$  the perturbation will be quickly damped and the equilibrium will be stable. In the other hand if  $\text{Re}(\omega) > 0$  the perturbation will grow

---

<sup>2</sup>Hannes Alfvén was a Swedish plasma physicist and winner of the 1970 Nobel Prize for his work on MHD.

exponentially and then it will be unstable. The real (imaginary) part of  $\omega$  will be the growth rate (frequency) of the perturbation that will be noted as  $\gamma$  ( $\omega_R$ ).

The conservation properties of ideal MHD allow to determine whether an MHD equilibrium is unstable or not with a powerful formulation known as the energy principle [Fre14]. In this formulation all the perturbed variables can be written in terms of the perturbed plasma displacement  $\boldsymbol{\xi}(\mathbf{r})$ , which is defined by  $\mathbf{v}_1 = \partial_t \boldsymbol{\xi}$ . By multiplying the momentum equation (1.7b) with the complex conjugate  $\boldsymbol{\xi}^*$  and integrating over the plasma and vacuum volume, the total potential energy  $\delta W$  is defined

$$\delta W = \delta W_F + \delta W_S + \delta W_V \quad (1.10)$$

$$\delta W_F = \frac{1}{2\mu_0} \int_P \left[ |\mathbf{B}_{1,\perp}|^2 + B_0^2 |\nabla \cdot \boldsymbol{\xi}_\perp + 2\boldsymbol{\xi}_\perp \cdot \boldsymbol{\kappa}|^2 + \mu_0 \gamma p_0 |\nabla \cdot \boldsymbol{\xi}|^2 - 2\mu_0 (\boldsymbol{\xi}_\perp \cdot \nabla p_0) (\boldsymbol{\xi}_\perp^* \cdot \boldsymbol{\kappa}) - \mu_0 J_0 \llbracket \boldsymbol{\xi}_\perp^* \times \mathbf{b} \cdot \mathbf{B}_{1,\perp} \rrbracket \right] dV \quad (1.11)$$

$$\delta W_S = \frac{1}{2\mu_0} \int_{S_p} |\mathbf{n} \cdot \boldsymbol{\xi}_\perp| \mathbf{n} \cdot \llbracket \nabla (B_0^2/2 + \mu_0 p_0) \rrbracket dS \quad (1.12)$$

$$\delta W_V = \frac{1}{2\mu_0} \int_V |\hat{\mathbf{B}}_1|^2 dV \quad (1.13)$$

where the  $\delta W_F$  is the plasma potential energy,  $\delta W_S$  is the potential energy contained at the plasma surface and  $\delta W_V$  is the potential energy in the vacuum surrounding the plasma. The equilibrium magnetic field is expressed as  $\mathbf{B}_0 = B_0 \mathbf{b}$  and the curvature of the magnetic field is  $\boldsymbol{\kappa} \equiv \mathbf{b} \cdot \nabla \mathbf{b}$ . Finally the symbols  $\perp$  and  $\parallel$  represent the perpendicular and parallel directions to the magnetic field,  $\mathbf{n}$  is a vector normal to the plasma boundary,  $\hat{\mathbf{B}}_1$  is the perturbed vacuum magnetic field and  $\llbracket f \rrbracket$  represents the jump of  $f$  across the plasma boundary.

The energy principle states that an MHD equilibrium is unstable if the total potential energy  $\delta W$  is negative

$$\delta W(\boldsymbol{\xi}) < 0 \quad (1.14)$$

for all displacements  $\boldsymbol{\xi}(\mathbf{r})$  that are bound in norm and satisfy the boundary conditions. Therefore the destabilizing terms are those that can make the potential energy become negative. The expressions (1.10)-(1.13) are very suitable to identify the equilibrium quantities that may destabilize instabilities. The first three terms of equation (1.11) represent the energy that is absorbed by waves and they are stabilizing as they are positive by construction. The  $|\mathbf{B}_{1,\perp}|^2$  represents the energy required to bend the magnetic field lines and excite the Alfvén wave, the second term corresponds to the excitation of the fast wave and the third one to the slow wave.

The plasma displacements that are unstable will tend to minimize the stabilizing terms. A usual method to find the unstable modes is to find the eigenfunctions that minimize the potential energy by solving a type of Euler-Lagrange equation. The parallel component of the plasma displacement  $\boldsymbol{\xi}_\parallel$  only appears in the term representing the compression of the plasma  $\nabla \cdot \boldsymbol{\xi}$ . This component will generally be such that the energy spent compressing the plasma is minimum and thus making most of the MHD instabilities incompressible. A common feature describing tokamak instabilities is the poloidal and toroidal structure of the perturbation. In closed field line systems, the poloidal and toroidal periodicity can be used to choose a Fourier decomposition for the perturbed variables

$$\boldsymbol{\xi}(\mathbf{r}) = \sum_{m,n} \boldsymbol{\xi}_{mn}(r) e^{i(m\theta - n\phi)} \quad (1.15)$$

where  $m$  and  $n$  are the poloidal and toroidal mode numbers,  $\theta$  and  $\phi$  are the poloidal and toroidal angles and  $\boldsymbol{\xi}_{mn}(r)$  are radial functions. In order to minimize the stabilizing effects

caused by the bending of the magnetic field lines, the displacement vector is constant along the equilibrium field lines requiring

$$\mathbf{k}_{mn} \cdot \mathbf{B}_0 \propto (m - nq) = 0 \quad (1.16)$$

where  $\mathbf{k}_{mn}$  is the wave vector of the mode  $\xi_{mn}(r)e^{i\mathbf{k}_{mn}\cdot\mathbf{r}}$  and  $q$  is the equilibrium safety factor. Therefore a mode characterized by a set of  $(m, n)$  numbers will be more unstable in the rational surfaces of the plasma where  $q = m/n$ . This feature has been extensively observed in tokamak experiments as well as numerical simulations.

In ideal MHD, unstable modes can only be driven either by the pressure gradient ( $\nabla p_0$ ) term of equation (1.11), or by the parallel current ( $J_{0\parallel}$ ) term. Therefore the MHD instabilities can be first classified into pressure and current driven modes. A second distinction can be made by using the location of the mode. Modes that can be unstable when the plasma boundary is fixed ( $\xi(\mathbf{r}_{\text{bnd}}) = 0$ ) are called internal modes. On the other hand the modes that require a deformation of the plasma boundary are called external or free-boundary modes. For the free-boundary modes it is essential to take into account the plasma boundary and vacuum contributions where natural boundary conditions must be applied. These are the type of modes that are the subject of this thesis.

For the pressure driven modes, the curvature of the magnetic field  $\kappa$  plays a very important role. In tokamaks the curvature is mainly given by the toroidal magnetic field and its vector points to the center of the torus. On the other hand, the pressure gradient points to the core of the plasma, causing the pressure gradient to point towards the center of the torus at the low field side and to the opposite direction at the high field side (see appendix 1). The so-called *ballooning* modes are pressure driven modes that appear in the low field side where the curvature is unfavourable (see figure 1.4). Ballooning modes are very localized and thus they present large toroidal mode numbers  $n$ . The toroidicity of tokamaks allow the different poloidal mode numbers to couple so the amplitude of the ballooning mode is localized in the region of unfavourable curvature. Ballooning modes can be classified as internal modes as they can exist with fixed boundary conditions. These modes are of high relevance for tokamaks as they can lead to violent and repetitive crashes and loss of pressure. Such instabilities are also called Edge-Localised Modes and will be presented in the next section.

It has been observed that pressure driven modes limit severely the tokamak performance. In fact, it could be stated that the biggest success of the ballooning theory was to give a reasonable estimate for the maximum achievable  $\beta$  value

$$\beta_N \equiv \frac{aB_\phi}{I_p[\text{MA}]} \beta [\%] < g \quad (1.17)$$

where  $a$  is the plasma minor radius,  $B_\phi$  is the toroidal field and  $I_p$  is the plasma current in MA units. The factor  $g$  depends on the plasma shape and the form of the plasma profiles. A rough estimate for this value is given by the so-called Troyon limit [Wes78] where  $g = 2.8$ . Experimentally, the criterion<sup>3</sup>  $\beta_N < 4l_i$  is found to be a good estimate.

The modes that are driven by the parallel current density ( $J_{0\parallel}$ ) are often referred to as kink modes. Depending on the safety factor at the plasma boundary, these modes can appear at the edge of the plasma and then they are called external kink modes. In contrast with ballooning modes, the most unstable external kink modes have a low toroidal mode number and are not localized. Moreover these modes require free-boundary conditions to be destabilized. The large radial extent of these modes (see figure 1.4) has an important impact on the global stability of the plasma. In practice the external kink modes limit the minimum edge safety factor to

---

<sup>3</sup>Here  $l_i$  is the internal inductance characterizing the plasma current profile.

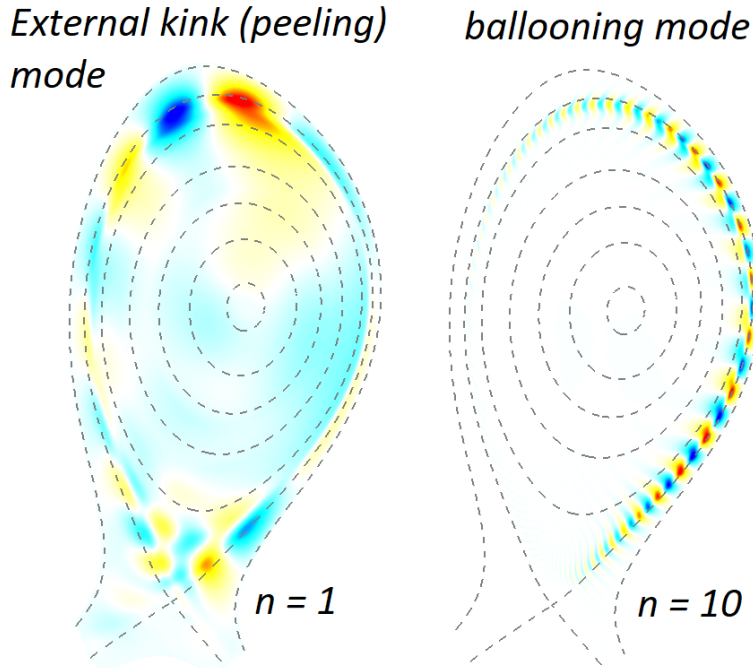


FIGURE 1.4: Mode structure in the poloidal plane of a  $n = 1$  external kink (peeling) mode and a  $n = 10$  ballooning mode. Adapted from [Höl+18].

$q_a \geq 2.5 - 3$  and thus the plasma current for a given toroidal field<sup>4</sup>. External kink modes should be avoided as they can lead to violent disruptions causing a sudden loss of the thermal and magnetic energy. Internal kink modes also exist and are relevant for tokamak operation. Experimentally, the most frequent internal kink mode is the so-called *sawteeth* instability, which arises when  $q < 1$ . The *sawteeth* limits the core current density of the plasma with rapid crashes that expel pressure and current from the plasma core keeping  $q_{\text{core}} \approx 1$ .

## Region of validity of MHD

As a fluid model, MHD is a simplified theory that neglects the kinetic effects of the plasma and therefore it is important to assess the question of its applicability. In the following, we list and comment the spatial and time scales regimes in which MHD is valid.

The first assumption of most of the different MHD models is that the MHD phenomena should involve velocities ( $V_{\text{MHD}}$ ) which are much smaller than the speed of light ( $c$ )

$$(V_{\text{MHD}}/c)^2 \ll 1 \quad (1.18)$$

which is very well satisfied for typical Alfvén velocities ( $\sim 10^6$  m/s) and allows to neglect the displacement current in the Maxwell-Ampère's law. Another basic consideration is the assumption of quasi-neutrality, which implies that the ion and electron densities are locally equal ( $n_i \approx n_e$ ). This requirement restricts the MHD spatial scales ( $L_{\text{MHD}}$ ) to be bigger than the Debye length ( $\lambda_{\text{Debye}}$ )

$$\lambda_{\text{Debye}}/L_{\text{MHD}} \ll 1 \quad (1.19)$$

which allows to neglect the electric field in the momentum equation (1.7b) causing the magnetic forces to be dominant. For a typical tokamak plasma with  $T_e = 3$  keV and  $n = 10^{20} \text{ m}^{-3}$  the Debye length is  $\lambda_{\text{Debye}} = 6 \times 10^{-5}$  m, which justifies the use of MHD for its typical spatial scales that range from centimetres to meters.

---

<sup>4</sup>The edge safety factor ( $q_a$ ) depends on the plasma current and toroidal field as ( $q_a \propto B_\phi/I_p$ )

A third asymptotic assumption is to neglect the electron inertia in the momentum equation for the electrons. This implies that the MHD frequencies ( $\omega_{\text{MHD}}$ ) are small compared to those of the electron plasma frequency ( $\omega_{pe}$ ) and the electron cyclotron frequencies ( $\omega_{ce}$ )

$$\omega_{\text{MHD}} \ll \omega_{pe} \quad \text{and} \quad \omega_{\text{MHD}} \ll \omega_{ce} \quad (1.20)$$

which for the plasma parameters given above and a magnetic field of  $B = 5$  T have per value  $\omega_{pe} \approx 6 \times 10^{11}$  Hz and  $\omega_{ce} \approx 9 \times 10^{11}$  Hz. This assumption is similarly very well satisfied as  $\omega_{\text{MHD}} = 2\pi/\tau_A \approx 5 \times 10^7$  Hz. In addition a strongly magnetized plasma is assumed for ideal MHD, which allows to neglect additional terms in Ohm's law

$$(r_{Li}/L_{\text{MHD}}) \ll 1 \quad (1.21)$$

where  $r_{Li}$  is the ion Larmor radius. The latter condition is most often justified as the  $r_{Li}$  is of the order of millimetres.

The last assumption involves the plasma collisionality. In ideal MHD, all the dissipative terms (except for the resistivity) are neglected by considering that the plasma is highly collisional in the time scales of interest. Similarly, the collisionality assumption allows to consider a single fluid as the equilibration of ion and electron temperatures  $T_i = T_e$  can take place. The collisionality condition requires

$$\tau_{ei} \ll \tau_{\text{MHD}} \quad (1.22)$$

where  $\tau_{ei}$  is the electron-ion collision time. Unfortunately this condition is never satisfied for the fusion plasmas of interest, for instance, in the previous example  $\tau_{ei} \approx 3 \times 10^{-5}$  s and  $\tau_{\text{MHD}} \approx 10^{-7}$  s. This disconcerting result contradicts the empirical evidence which demonstrates that ideal MHD provides a good description of most macroscopic plasma behavior. A more detailed examination of ideal MHD, shows that in many cases the model is still reliable even though the collision dominated assumption is not justified. An argument is that the mass conservation law is always valid and that the perpendicular momentum conservation law is shown to be valid in the collisionless regime [Fre14] provided a strong magnetization. However the parallel momentum equation and the energy equation are still not valid in the collisionless limit. Nevertheless, these equations don't play an important role if the plasma is incompressible ( $\nabla \cdot \mathbf{v} = 0$ ) [Fre14]. As shown in previous subsection, the MHD instabilities tend to be incompressible in order to minimize the stabilizing terms of the potential energy, this property explains the fact that ideal MHD can be applied outside of its formal region of validity.

Finally it is important to remind the physics that are typically not covered for most of the MHD models

- Turbulent transport with kinetic effects
- Radiation
- Resonant particle effects
- Larmor radius effects
- Fast particles
- Plasma-wall interaction
- Radio-frequency heating and current drive
- Tokamak collisional (or neoclassical) transport

However some of these effects (such as the radiation or transport) may be included in the MHD models by adding the appropriate terms to the MHD equations.

### 1.2.2 Edge Localized Modes (ELMs)

One of the biggest breakthroughs in the tokamak community was the discovery of the so-called H-mode<sup>5</sup>, a high confinement operation regime of the plasma. In the early 80's, this new regime of confinement was found in the ASDEX tokamak [Wag+82] by increasing the heating power above a certain threshold, after which, the confinement considerably improved. In the H-mode regime, the improvement of plasma confinement originates from a sharp reduction of the turbulent transport at the plasma edge. The plasma edge region where the transport of heat and particles is significantly reduced is referred to as the transport barrier. Thanks to the transport barrier, the pressure profile increases considerably for the same amount of heating power, thus leading to a large improvement in the fusion performance. Nevertheless, the transport barrier exists in a very narrow region of the plasma (of the order of a few centimetres for current experiments) where the temperature and density profiles show very steep gradients that can lead to violent instabilities.

This region where the steep gradients arise is referred to as the plasma pedestal (see the zoomed edge region in figure 1.6 (b)). The gradients of the pedestal are limited by an MHD instability that is very localized at the plasma edge, which induces large and pulsed heat loads that reduce periodically the density and temperature gradients. These instabilities were named Edge Localized Modes (ELMs) by Keilhacker et al [Kei+84].

In experiments, ELMs are characterized by repetitive spikes in the  $D_\alpha$  emission signals indicating a loss of particles from the main plasma arriving at the divertor, which is a key particle and impurity control component of a tokamak (see appendix 1). The loss of particles is accompanied by a loss of energy at each ELM, of the order of 1-10% of the thermal energy of the plasma. An ELM flattens the large density and temperature pedestal gradients typically in a period of time of the order of  $200\mu\text{s}$ . The losses are not limited to the edge pedestal but can extend up to as much as 20% of the plasma radius from the edge inwards. After the ELM crash, the plasma recovers and the density and temperature gradients build up until the next ELM is triggered. The length of this recovery phase determines the frequency of the ELMs. This depends on how much energy/particles was lost and the heating power/particle source into the transport barrier.

Based on the ELM frequency and the energy released per ELM, these instabilities are historically classified into three types. The type-I ELMs are those which are the most violent and can expel up to 10% of the plasma thermal energy. The frequency of this type of ELMs increases with the heating power [Zoh96] and it lies in a wide range (1 – 100 Hz). On the other hand, the type-III ELMs expel less energy, their frequency is much higher (of the order of several hundred of Hz) and it decreases with the heating power. During the L-H transition the type-III ELMs appear in the first place and they are suppressed when the heating power is further increased. After that an ELM-free period takes place, and when the heating power is further increased the type-I ELMs appear. Finally the type-II ELMs are very small pedestal instabilities (even smaller than the type-III ELMs) and their physics is poorly understood.

## The theory behind ELMs

The fast time scales (tens of  $\mu\text{s}$ ) and the macroscopic behaviour of ELMs indicate that ELMs are most likely ideal MHD instabilities. In the last decades a significant effort has been made in order to characterize the stability limits of ELMs. The first comparison of experimental data with ideal MHD limits was performed in [Goh+88] in the DIII-D tokamak (San Diego). In this work, the measured pre-ELM pressure gradient at the pedestal agreed within error bars with the stability limit of infinite- $n$  ballooning modes. The question of whether it was possible to

---

<sup>5</sup>In opposition, the previous regime with poor confinement is named as the L-mode or low confinement mode.

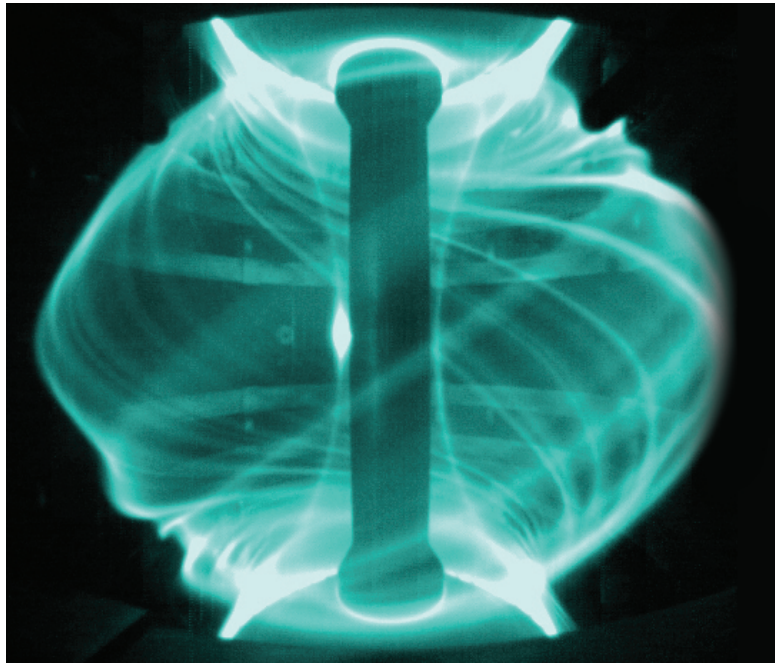


FIGURE 1.5: An Edge Localized Mode in the MAST spherical tokamak showing a filamentary helical structure [A K].

access the so-called second stability region of ballooning modes was raised. In this theoretical stability region [CHT79], the pressure gradient could be indefinitely increased provided a low shear of the safety factor ( $s \equiv d(\log q)/d(\log r)$ )<sup>6</sup>, which would be of great interest as it would allow to increase the plasma performance.

Unfortunately, later studies revealed that other type of instabilities limit the increase of pressure gradient in the second stability region. These instabilities were found when taking into account finite- $n$  modes and the large current densities that also appear in the pedestal (see blue curve of figure 1.6) (b)). The large current densities of the pedestal are due to the *bootstrap* current, a current contribution arising from the neoclassical theory that is proportional to the pressure gradient and inversely proportional to the collisionality [SAL99]. These large edge currents can destabilize *peeling* modes, which are a type of edge localized external kink modes characterized by low- $n$  numbers and a dominant poloidal mode number. In the MHD edge theory developed by Connor et al [Con+98], it was demonstrated that the coupling of peeling and ballooning modes led to a reduction of the stable region.

Nowadays, the pedestal stability of a given plasma is assessed with a peeling-ballooning stability diagram. These type of diagrams (see figure 1.6 (a)) are constructed by calculating the ideal MHD stability of a family of equilibria with different pedestal pressure gradients and current densities. Typically the total current ( $I_p$ ), the ratio between total kinetic pressure and the poloidal magnetic pressure ( $\beta_p$ ) and the plasma shape are the same for the different equilibria. In figure 1.6, an example of a peeling-ballooning stability diagram for an expected ITER  $Q = 10$  plasma is shown. For low pedestal currents, high- $n$  ballooning modes are encountered when increasing the pedestal pressure (the *ballooning limit*). On the other hand, another stability limit is found for high pedestal currents and low pedestal pressures, a limit that arises from the destabilization of low- $n$  peeling modes. For high edge currents and pressure gradients, a region named the *peeling-balloonning nose* is accessed where both pressure and edge current destabilize medium- $n$  peeling-balloonning modes. The trajectory that an experimental plasma follows in the stability diagram depends on the plasma collisionality, which determines

---

<sup>6</sup>Here  $r$  is a cylindrical radial coordinate describing circular magnetic flux surfaces

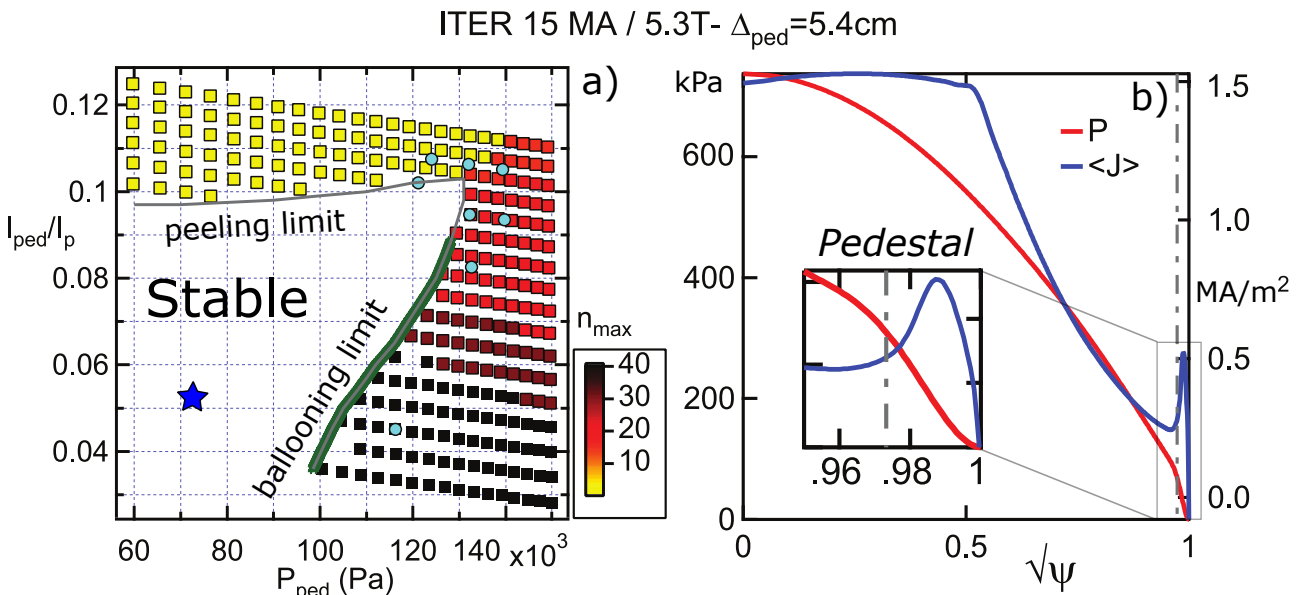


FIGURE 1.6: (a) Edge stability diagram for an ITER  $Q = 10$  plasma. The axis of abscissas shows the pressure at the top of the pedestal and the axis of ordinates shows the fraction of toroidal current within the pedestal with respect to the total plasma current. The coloured squares represent the most unstable  $n$  modes. The equilibrium shown in figure (b) is placed in the diagram with a blue star. (b) Pressure and averaged current profile as a function of the radial coordinate  $\sqrt{\psi_N}$  for the ITER case. These figures were obtained from [Mag+13].

the amount of bootstrap current for a given pressure gradient.

In experiments, higher pressures and edge currents are obtained at higher plasma triangularities (see definition in appendix 1). This is in agreement with numerical calculations of peeling-balloonning stability limits, where the stable *nose* region is significantly expanded for higher plasma triangularities. Additionally, it has been recently observed that the achievable pedestal height can be increased at higher core pressures [Cha+14], which may be explained from the stabilizing effect of the Shafranov shift<sup>7</sup> ( $\Delta_{sh} \sim \beta_p$ ) on peeling-balloonning modes [CHH16; Oos+18].

More complex models have been recently developed in order to predict the pressure at the top of the pedestal (pedestal height) and the pedestal width. The EPED model [Sny+11] has been able to achieve a good agreement with experiments (see figure 1.7) by including kinetic effects in the peeling-balloonning description. Experimentally, it has been observed that during the pressure profile recovery after an ELM crash, the local pressure gradients are saturated before the next ELM onset. During the saturation of the local gradients, the pedestal keeps growing from the edge towards the core of the plasma. In the EPED model, the gradients are locally saturated due to the destabilization of kinetic ballooning modes (or KBMs). When the pedestal width has grown sufficiently from the edge towards the plasma core, the peeling-balloonning modes become unstable leading to ELMs.

The non-linear dynamics of ELMs has been studied extensively as well. In particular the code JOREK [HC07], which is used in this work, has been able to reproduce several ELM features observed in experiments and has provided important physical understanding for these phenomena. In experiments, hot filamentary structures are ejected from the main plasma during ELMs (see figure 1.5). These filaments have been observed in JOREK as well, and it

<sup>7</sup>The Shafranov shift is defined as the distance of the magnetic axis from the plasma geometric center (see appendix 1)

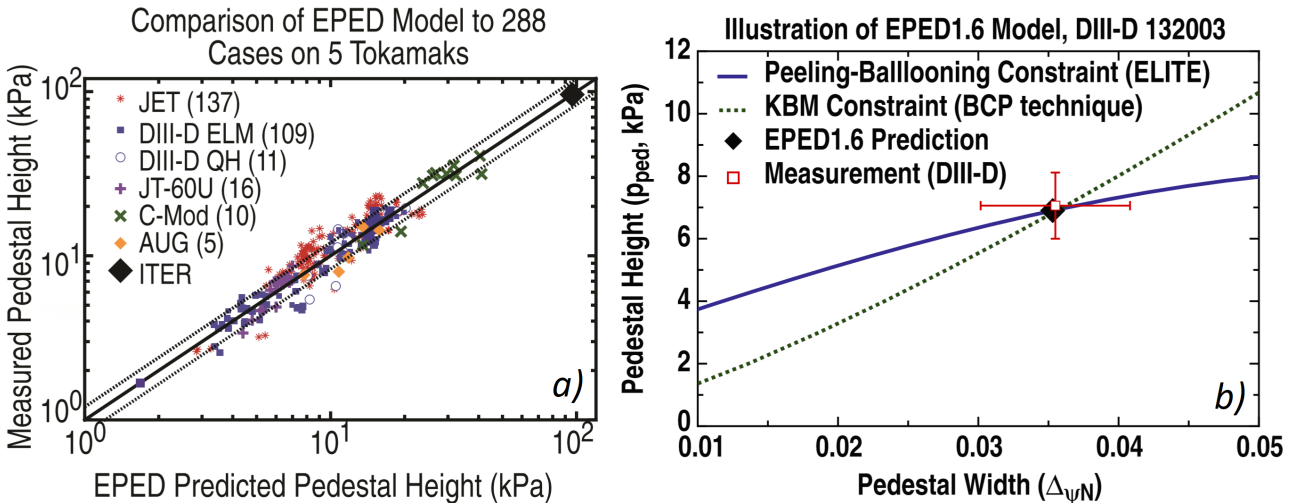


FIGURE 1.7: (a) Predicted pedestal height by the EPED model versus measured pedestal height in several tokamaks [Sny+15]. (b) Predicted pedestal width and height limits by the peeling-balloonning constraint, the KBM constraint and the EPED mode together with the DIII-D experimental value [Sny+11].

has been discovered that they originate from the  $\mathbf{E} \times \mathbf{B}$  flow<sup>8</sup> created by the ballooning modes. The typical radial speed of the filaments measured in experiments is of the order of  $\sim 1$  km/s, which is recovered in the numerical simulations [Höl+18]. When these filaments are ejected, the fast transport along the field-lines releases the contained energy and particles as they move out. In [Min+17], JOREK ELM simulations have been compared directly with experiments in the ASDEX Upgrade tokamak (AUG), where the range of dominant  $n$  numbers during an ELM, the drop of the radial electric field and the ELM duration have been successfully validated. In chapter 2 an overview of the JOREK code is given with its main contributions to the ELM theory.

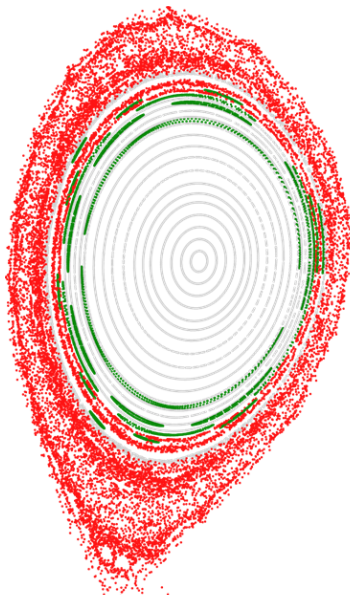


FIGURE 1.8: Poincaré plot showing the edge ergodization of the magnetic field during an AUG ELM simulated with JOREK. Adapted from [Höl+18].

The strong magnetic perturbation created by ELMs is able to produce the stochastization

<sup>8</sup>This flow is found when applying the cross product with  $\mathbf{B}$  to equation (1.7d) giving  $\mathbf{v}_{\perp} \approx \mathbf{E} \times \mathbf{B}/B^2$ .

of the plasma edge (see figure 1.8). The produced stochastic magnetic field allows a direct connection of the main plasma with the divertor targets along the reconnected field-lines. In addition to the convective losses caused by the radial motion of the ELM filaments, the connexion of the main plasma and divertor target generates large parallel conductive losses. The parallel conductive losses affect mainly the electron temperature as their parallel conductivity is much larger than the ions conductivity ( $\kappa_{\parallel,e} \sim 40\kappa_{\parallel,i}$ ).

### 1.2.3 ELM control

One of the critical issues on the tokamak path to nuclear fusion as a source of electricity is realizing a high confinement mode of plasma operation without the large, pulsed heat loads that usually result from type-I ELMs. While ELMs might provide sufficient edge particle loss to prevent helium ash and impurity accumulation in a burning plasma core, they also may severely limit the lifetime of the divertor. Therefore ELM control techniques or ELM-free modes will play a very important role for future tokamaks.

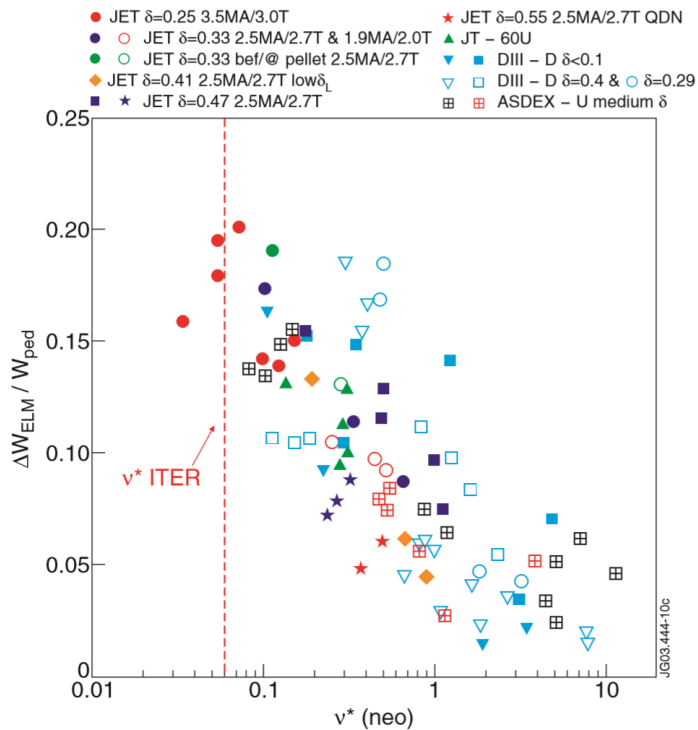


FIGURE 1.9: Normalised ELM energy loss versus pedestal collisionality for different tokamaks with Type I ELMy H-mode plasmas [Loa+03].

The combination of large amplitude ELMs and their short time-scale leads to transiently very large energy flows into the divertor and large heat loads on the plasma facing components. Depending on the dominant type of ELM losses ('convective' or 'conductive'), natural type-I ELMs may be acceptable or not for future large scale tokamaks such as ITER [Loa+04]. The expected ELM energy loss in ITER is extrapolated from the conductive losses, which are inversely proportional to the collisionality (see figure 1.9). Following this scaling, natural type-I ELMs may produce losses of the order of 20 MJ for ITER Q=10 plasmas. The material limits related with the melting point of plasma facing components require that the ELM energy losses should be smaller than 0.7 MJ [Loa+14] for ITER Q=10 plasmas. Consequently, natural type-I ELMs are not allowed in ITER and ELM control techniques are required to control the ELM power fluxes. A possibility to reduce the ELM heat loads is to take advantage of the empirical

inverse dependence of the ELM energy losses on the ELM frequency [Loa+02]

$$\Delta W_{\text{ELM}} = (0.2 - 0.4) P_{\text{SOL}} / f_{\text{ELM}} \quad (1.23)$$

where  $P_{\text{SOL}}$  is the power flowing out from the main plasma into the escape-off layer. Thus by increasing the ELM frequency, the ELM energy losses can be reduced. The use of the empirical law (1.23) implies that for ITER Q=10 plasmas the ELM frequency should be increased by a factor 30, leading to an estimated frequency of  $f_{\text{ELM}} = 45$  Hz. For the previous calculation, empirical assumptions are also required for the scaling of the surface area in which the ELM heat loads are spread with the ELM size and frequency. It is important to note that these are extrapolations based on current experiments and that well validated ELM physics models are still essential to complement these calculations.

For the ITER tokamak, the material chosen for the divertor is tungsten (W) as it has many advantages in terms of lifetime and lower fuel retention. Its main drawback is the low allowable concentration of tungsten ( $\sim 10^{-5}$ ) within the plasma. Higher concentrations may lead to fuel dilution and the increased radiative losses may lead to a thermal collapse and to a consequent disruption. In this respect, ELMs may help to avoid tungsten accumulation by flushing the W ions out from the plasma. In [Fed+15] the dependence of the tungsten concentration on the ELM frequency was studied in the JET ITER-like wall discharges, revealing that the confinement time for the tungsten particles ( $\tau_W$ ) is inversely proportional of the ELM frequency as  $\tau_W \sim f_{\text{ELM}}^{-0.45}$ . Therefore the increase of the ELM frequency may be as well a useful technique to control the amount of impurities and to keep the plasma clean. For ITER H-mode plasmas this gives a lower limit on the ELM frequency ( $f_{\text{ELM}} > 15$  Hz).

There are currently three ELM-control methods that have been successfully tested in tokamaks. The three techniques are listed below.

- **ELM control by resonant magnetic perturbations (RMPs):** The RMP technique consists in applying small non-axisymmetric magnetic perturbations (of the order of  $10^3 - 10^4$  smaller than the total magnetic field) using dedicated coils called "RMP coils". In addition to ELM mitigation, this technique can also lead to total ELM suppression. The aim of this method is to generate a stochastic region at the plasma edge in order to enhance the radial transport so the pressure gradient stays below the ELM-triggering threshold. The magnetic perturbation produced by the RMP coils can induce chains of magnetic islands at the resonant (or rational) surfaces. After a given amplitude of the RMP coil currents, the chains of islands can overlap, creating the chaotic or stochastic region. However, the physics mechanism leading to ELM mitigation or suppression by RMPs still requires detailed investigations. While ELM suppression by RMPs was first obtained in the DIII-D tokamak [Eva+05] and later on AUG, only ELM mitigation was obtained in JET. Moreover ELMs were triggered when the RMP technique was applied in the MAST tokamak. In particular the 3D plasma response and the screening of the perturbation by plasma flows seem to play a very important role to explain these different results. For ITER, RMPs is one of the main ELM control schemes foreseen. For this purpose, a set of 27 in-vessel coils will be installed in ITER with a maximum coil carrying current capability of 90 kAt and an applied toroidal symmetry of  $n = 3 - 4$ .
- **ELM triggering by pellet injection:** This method consists in injecting D-D or D-T ice pellets in order to increase the pressure gradient where the pellet ablation occurs. If a sufficiently large pellet ablates in the pedestal region, the local increase of the pedestal pressure leads to an edge localized mode [Lan+08]. The main idea of this method is to trigger more frequent ELMs by increasing the frequency at which the pellets are injected. In DIII-D [Bay+13], this technique has demonstrated very high capabilities

by reducing the ELM energy deposited at the divertor by a factor  $\sim 12$ . In addition to ELM frequency control, this method can also be used for particle fuelling, provided that the fuel can penetrate into the plasma core. Although efforts have been made to simulate this ELM control scheme [Fut+14; Loa+14], uncertainties still remain for the practical application of this technique to ITER and, in particular, for the optimization of the pellet characteristics (mass, velocity, injection location) for efficient ELM triggering while minimizing the fuel throughput required.

- **ELM control by vertical position oscillations (*vertical kicks*):** As for the pellet injection scheme, this method is based on the increase of the ELM frequency to decrease the ELM energy losses. The method consists in applying axisymmetric perturbations on the radial magnetic field that lead to oscillations in the vertical position of the plasma column. When the frequency of the vertical oscillations exceeds the natural ELM frequency, experimental observations indicate that the ELM frequency can lock to the vertical oscillation frequency. Consequently the ELM frequency can be tuned by changing the frequency of the applied perturbation. This technique is explained in more detail in the next section as it is one of the main topics of research of this thesis (see chapter 4).

### ELM control via vertical position oscillations

Triggering of Edge Localized Modes (ELMs) with vertical position oscillations was first reported in the TCV tokamak [Deg+03]. The experiments showed that imposing a vertical plasma oscillation using poloidal field coils (PF coils), leads to a reliable locking of the ELM frequency to the vertical oscillation frequency. These vertical oscillations often called "vertical kicks" or "vertical jogs" were also used for ELM frequency control in the ITER-relevant type-I ELM regime in ASDEX Upgrade [Lan+04] and JET [Lun+15] tokamaks.

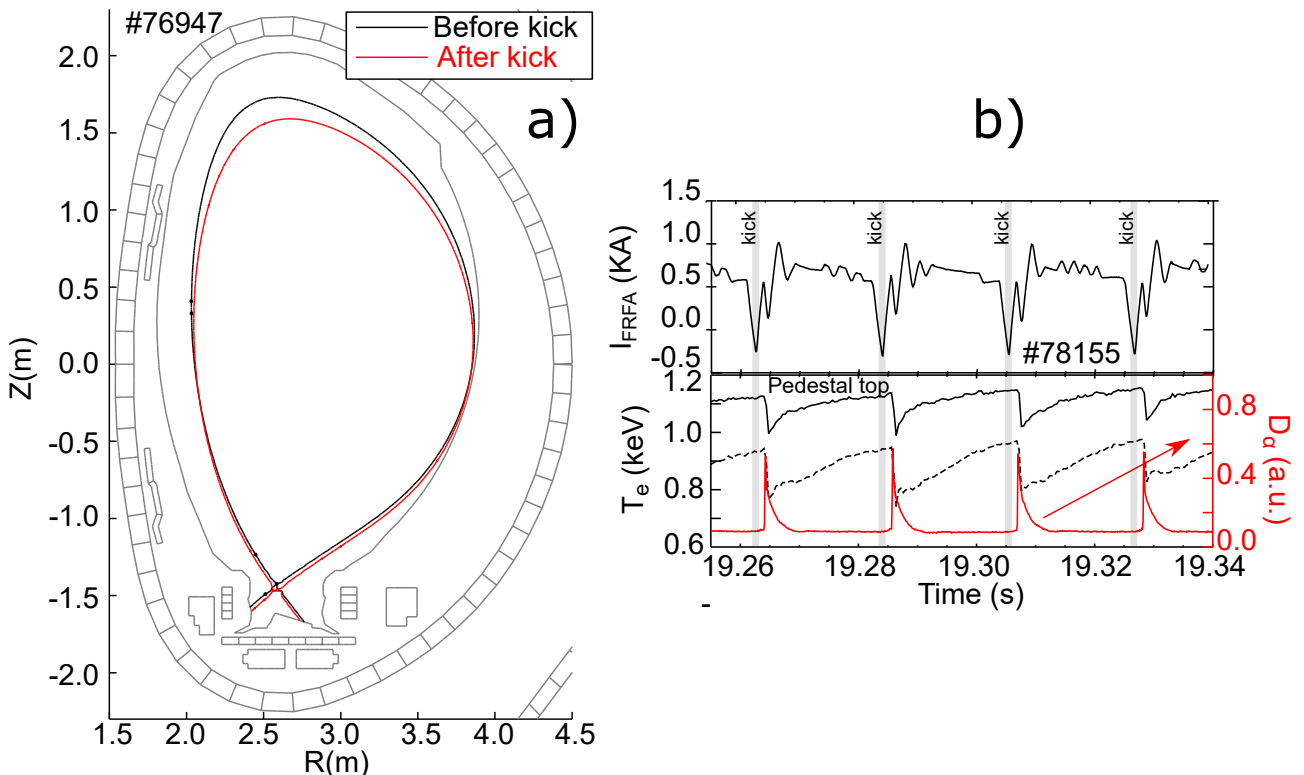


FIGURE 1.10: (a) Plasma separatrix before and after a vertical kick in JET. (b) Current applied in the control system for the vertical position (FRFA) and the ELM signatures (the  $D_\alpha$  emission) over time. Figures were obtained from [Lun+15].

One of the main advantages of this technique with respect to the RMP ELM control scheme is that the increase of the ELM frequency can play an important role in controlling the impurity content of the plasma. In this respect, tungsten accumulation may occur for low current operation in ITER with low frequency ELMs regardless of the energy losses [Loa+14]. In addition, the application of this method is far less challenging than the pellet injection scheme. The vertical control system that all tokamaks with high plasma elongation require, can usually be adapted to obtain the periodic vertical oscillations without major changes in the tokamak design. For ITER, vertical oscillations are considered as a back-up technique [Loa+14] for the initial non-active operation up to half current and half magnetic field (7.5MA, 2.65T) to supplement the baseline ELM control scheme (RMPs) as its application is developed. For the high current operation, the expected required vertical displacements to achieve ELM control ( $\sim 5$  cm) would need coil currents beyond the engineering design limits (due to the associated ohmic heating that needs to be removed by circulating water inside the conductors).

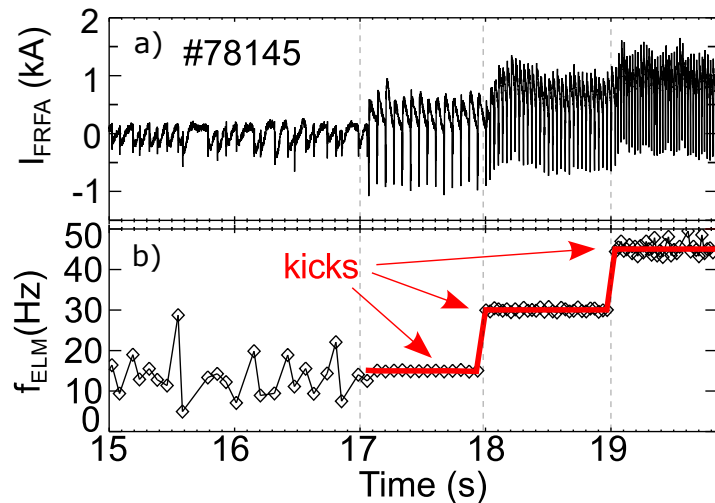


FIGURE 1.11: Control of the ELM frequency via vertical kicks in JET. (a) Current in the JET's vertical control system (FRFA) and (b) ELM frequency. Figures obtained from [Lun+15].

In several tokamak experiments, ELMs have been triggered at similar peak-to-peak normalized vertical displacements of  $\delta Z/R_0 \sim 1.0 - 1.6\%$ . An example of a experimental vertical kick performed in the JET tokamak is shown in figure 1.10. In JET, ELMs are preferentially triggered when the plasma moves towards the main X-point (as it occurs in AUG). During the vertical motion, the plasma separatrix experiences a deformation as the top part of the plasma moves faster than the lower part (see figure 1.10 (a)). The implications of this deformation on the plasma equilibrium are explored in chapter 4. In figure 1.10 (b) it can be observed that the ELMs ( $D_\alpha$  spikes) are synchronized with the application of the current perturbations in the JET's fast vertical control system (FRFA). The effectiveness of this method is presented in figure 1.11, where the ELM frequency increases accordingly with the kick frequency.

It is important to note that a minimum kick size is required to achieve robust ELM frequency control. The minimum required kick size was studied in JET (see figure 1.12), which it is varied in terms of  $A_{\text{kick}}(\text{Wb}) = \Delta V \times \Delta t_{\text{kick}}$ , where  $\Delta V$  is the applied voltage difference in the vertical position control and  $\Delta t_{\text{kick}}$  is duration of a single kick. As it can be observed in figure 1.12 (a), the enhanced confinement factor<sup>9</sup> ( $H_{98}$ ) is not significantly affected by the use of this technique, which is a very relevant feature for future applications of this method. In order to reveal the physical mechanism triggering ELMs through this technique, it is important to determine which is the key parameter destabilizing the ELMs, the vertical velocity or the

<sup>9</sup>The confinement factor ( $H_{98}$ ) is defined as  $\tau_E/\tau_E^{\text{IPB98}}$

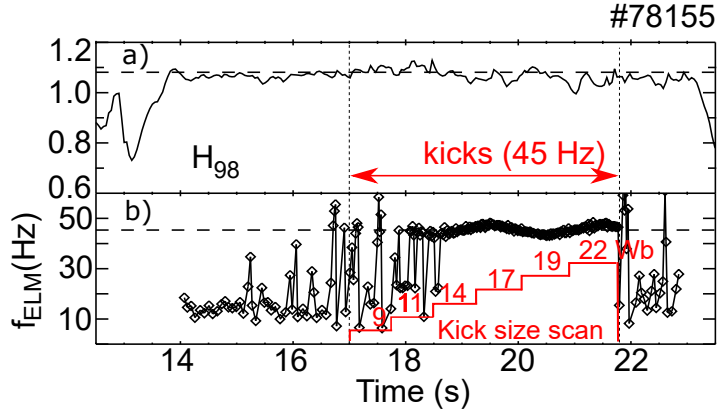


FIGURE 1.12: Study of the required kick size in JET experiments to achieve robust control of the ELM frequency. (a) Enhanced confinement factor ( $H_{98}$ ) and (b) ELM frequency. The kick size is calculated as  $A_{kick}(\text{Wb}) = \Delta V \times \Delta t_{kick}$ , where  $\Delta V$  is the applied voltage difference in the FRFA system and  $\Delta t_{kick}$  is duration of a single kick. Figures were obtained from [Lun+15].

amplitude of the vertical displacement. For that purpose, experiments were conducted in JET where these two parameters were varied for constant  $A_{kick}$  (see figure 1.13). These experiments revealed that ELMs were triggered at similar vertical displacements ( $\Delta Z_p \sim 1 \text{ cm}$ ) but at different plasma velocities. This fact indicates that the vertical displacement is the key parameter to achieve ELM frequency control.

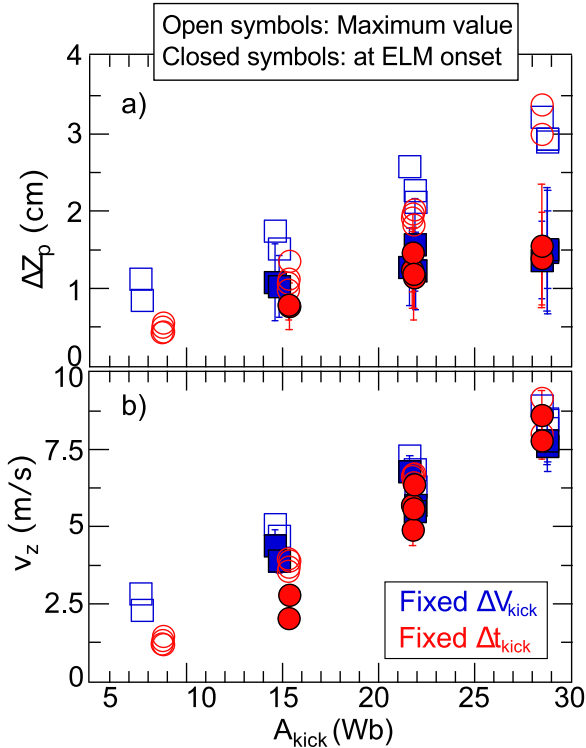


FIGURE 1.13: (a) Amplitude of the vertical plasma displacement ( $\Delta Z_p$ ) and plasma vertical velocity ( $v_z$ ) during kicks vs. kick size ( $A_{kick}(\text{Wb}) = \Delta V \times \Delta t_{kick}$ ). Two different types of kicks are presented: with fixed  $\Delta t_{kick}$  (in red) and with fixed  $\Delta V$  (in blue). Figures were obtained from [Lun+15].

JET experiments have also revealed that for the same kick size, it is more likely to achieve ELM control at higher pedestal temperatures and lower pedestal densities (see figure 1.14). This fact directly points to the collisionality as a key factor for the efficiency of the vertical kicks. The collisionality is known to play an important role in the peeling-balloonning stability of

the pedestal. At lower collisionalities, larger bootstrap currents are formed for similar pressure gradients, thus the plasma moves vertically in the peeling-balloonning stability diagram (see figure 1.6 (a)) as the collisionality is decreased.

The collisionality dependence of the ELM triggering through vertical kicks points to the bootstrap current as a potential candidate for the triggering mechanism. In fact, the vertical motion of the plasma through an up-down asymmetric magnetic field, leads to the induction of electric currents at the plasma edge, which can directly influence the ELM stability. If the edge current is the main destabilizing factor, a lower edge collisionality would lead to a higher bootstrap current and consequently, a lower perturbation would be required to reach the ELM stability threshold for the edge current. This is the physical mechanism that was proposed to explain the ELM triggering through vertical kicks in [Deg+03]. However the authors of [Kim+09] argued that for the AUG case, ELMs were destabilized when the edge current was decreasing and therefore, ELMs could be triggered by other more subtle factors such as the change in plasma shape or in pressure gradient.

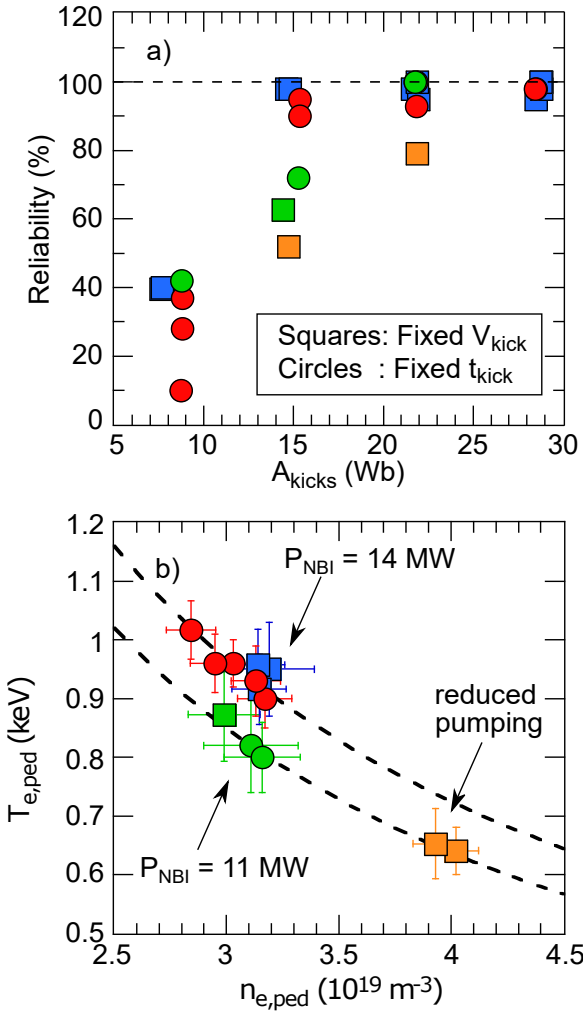


FIGURE 1.14: (a) Percentage of kick triggered ELMs versus kick size for different plasma conditions. (b) Pedestal temperature and density range covered in the kick scan. Different colors are used to identify discharges with different pedestal parameters. The dashed lines represent curves with constant pressure. Figures were obtained from [Lun+15].

One of the main goals of this work is to clarify which is the determining factor for the ELM destabilization through MHD simulations and as well, to provide an understanding of the current induction during the plasma motion in ITER plasmas. In chapter 4, the analysis of the current induction and its influence in the ELM stability during kicks is presented.

### 1.2.4 Vertical Displacement Events (VDEs) and disruptions

Plasma shaping and elongation has proven to be a very important ingredient to increase the fusion performance. As it can be observed in the scaling law for the confinement time (1.3),  $\tau_E$  improves significantly when increasing plasma elongation ( $\kappa_a$ ). The increment of  $\kappa_a$  has an important stabilizing effect as it allows to increase the edge safety factor for the same amount of total current ( $q_a \propto (1 + \kappa_a^2)/I_p$  [Fre14]). The stable peeling-balloonning region can also be extended with higher plasma elongation and triangularity, allowing a higher pedestal pressure. These features justify that nowadays tokamaks are operated with highly elongated plasmas.

However, the main drawback of elongated plasmas is that they are typically unstable to axisymmetric ( $n = 0$ ) vertical displacements. The vertical instability comes from the fact that two opposite and balanced forces ( $\mathbf{F}_{1p}$  and  $\mathbf{F}_{2p}$ ) are required to stretch the plasma in the vertical direction (see figure 1.15). These are Laplace forces produced by radial magnetic fields ( $\mathbf{B}_1$  and  $\mathbf{B}_2$ ) created with PF coil currents ( $\mathbf{I}_1$  and  $\mathbf{I}_2$ ). As the magnetic field strength is inversely proportional to the plasma-coil distance, if a small vertical displacement ( $\delta Z$ ) is applied, the force balance is lost as the plasma approaches one coil and moves away from the other. As the plasma approaches the closest coil, the vertical motion is further enhanced as the coil pulls it even stronger. This leads to an exponential growth of the vertical position ( $Z = Z_0 + \delta Z e^{\gamma t}$ ). The loss of vertical control that can happen in tokamaks due to this instability is known as a Vertical Displacement Event (VDE).

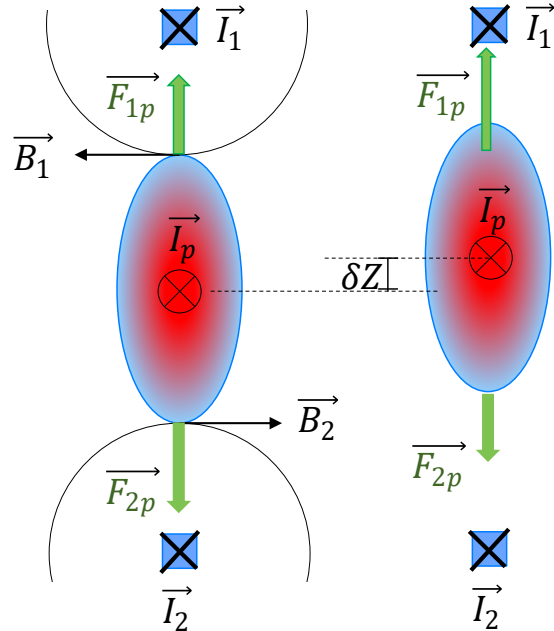


FIGURE 1.15: Schematic explanation of the vertical axisymmetric instability.

If the VDE is not stabilized, the loss of balance of such large electromagnetic forces leads to a very fast motion in the time scales of the Alfvén time [Wes78]. When passive conductors are located near the plasma, the vertical motion induces mirror currents in the conductors that stabilize the VDE in time-scales given by the conductors resistive time.

The analysis of the VDE growth rate for general cases requires numerical solutions. For a cylindrical elliptical plasma with minor and major semi-axes  $a$  and  $b$  (see figure 1.16), an analytical solution can be found. In this case the plasma is surrounded by an elliptical conducting shell (wall) described with minor and major semi-axes  $a'$  and  $b'$ . If the surrounding shell is ideally conducting, the VDE is totally stable provided that the following geometrical criterion

is satisfied [WC11]

$$\frac{b-a}{b+a} < \left( \frac{b+a}{b'+a'} \right)^2 \quad (1.24)$$

If the previous criterion is violated the instability occurs on the inertial time scale. For finite wall conductivities ( $\sigma_w$ ), the VDE is unstable even if the previous criterion is satisfied. In that case the growth rate is given by

$$\gamma = (\tau_R D)^{-1} \quad (1.25)$$

where  $\tau_R = \mu_0 \sigma_w d \bar{b}$  is the resistive penetration time of the shell defined by the wall thickness ( $d$ ) and the average wall radius ( $\bar{b}$ ) and

$$D \equiv \frac{b+a}{b-a} \left( \frac{b+a}{b'+a'} \right)^2 - 1 \quad (1.26)$$

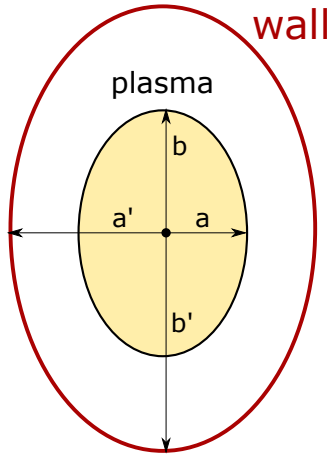


FIGURE 1.16: Elongated plasma with uniform current density and conducting shell.

The effect of the plasma elongation plays a role through the coefficient  $D$ . In figure 1.17, the contribution of the plasma elongation to the growth rate is given for different plasma-wall minor radius ratios ( $a/a'$ ) and assuming  $\kappa_w \equiv b'/a' = \kappa_a$ . The function  $D^{-1}$  reveals that the effect of  $\kappa_a$  is stronger as the wall is moved away from the plasma.

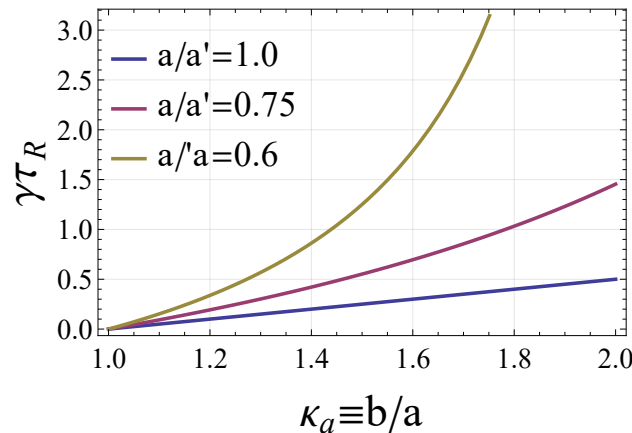


FIGURE 1.17: Effect of plasma elongation in the VDE growth rate for different plasma-wall minor radius ratios.

Toroidal effects are stabilizing for rigid plasma displacements as they are found to be more stable for larger inverse aspect ratios ( $\varepsilon \equiv a/R_0$ ) [Wes78]. The current density profile has a small effect on the stability criterion for the ideally conducting wall position but it can dramatically influence the growth rate for the resistive instability [HF89]. In this respect  $\gamma$  increases with the internal inductance of the plasma ( $l_i$ ). For tokamak operation, passive conductors are typically placed near the plasma so the vertical instability occurs in the resistive time-scale ( $\tau_R$ ) and the VDE can be effectively controlled with a vertical position control system.

## Disruptions and cold VDEs

In tokamaks, a disruption is a violent loss of plasma confinement and control due to the development of a large scale plasma instability. Disruptions result in the plasma being extinguished in fast time scales producing large thermal and electromagnetic loads in the structures surrounding the plasma. In future reactors like ITER, these loads have the potential to produce significant damage to the tokamak components and therefore disruptions should be predicted and controlled.

A disruption consists of two consecutive phases: the thermal quench (TQ) where the thermal energy of the plasma is rapidly lost and the current quench (CQ) when the plasma current is lost due to the drop of plasma conductivity after the TQ. The expected TQ and CQ phases for an ITER plasma are shown in figure 1.18.

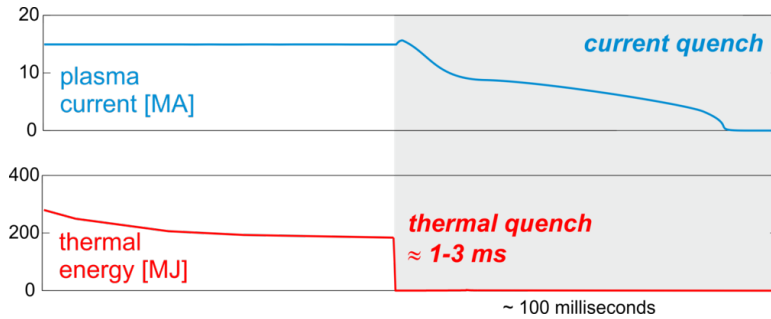


FIGURE 1.18: Scheme showing the expected phases for an ITER disruption. Plot adapted from [Leh18].

The thermal quench phase is characterized by a violent MHD activity which causes the stochasticization and the reconnection of the magnetic field lines. During this phase, the thermal energy is lost through the open field lines connecting the plasma core and the plasma edge in the order of a few milliseconds. The origin of the thermal quench typically arises from the onset of a growing resistive instability [Boo12] that causes the reconnection. The destabilization of the resistive instabilities can be caused by a drop of the edge temperature due to radiative processes and changes in the density and current profiles. After the TQ, a sudden increase of 5-20% of the plasma current is observed. This increase of  $I_p$  known as the *current spike*, is thought to be a consequence of the magnetic flux conservation inside the tokamak vessel after the flattening of the current profile produced by the TQ.

At the end of the thermal quench, the plasma temperature is typically of the order of  $\sim 10$  eV. As the plasma resistivity ( $\eta$ ) has a temperature dependence given by the Spitzer formula ( $\eta \propto T^{-3/2}$ ), the plasma becomes highly resistive and the current is lost in the  $L/\mathcal{R}$  time of the plasma<sup>10</sup>. Depending on the final temperature and on the concentration of impurities in the

<sup>10</sup>Here we refer to the  $L/\mathcal{R}$  time as the characteristic time of a resistor-inductor circuit, where  $\mathcal{R}$  is the total plasma resistance and  $L$  is the total plasma inductance.

plasma, the current quench time ( $\tau_{\text{CQ}}$ ) varies between a few milliseconds and a few hundreds of milliseconds.

The perturbation in the radial force balance caused by the loss of thermal energy and the drop in the plasma internal inductance at the TQ, leads the plasma to a new radial position where it can be highly unstable to VDEs. Therefore after the TQ, the vertical position control of the plasma is typically lost and VDEs develop in the wall time ( $\tau_w$ ). If the current quench time ( $\tau_{\text{CQ}}$ ) is much faster than wall time ( $\tau_w$ ), the wall behaves as an ideal conductor and the mirror currents provide the vertical equilibrium. In that case the plasma moves in a series of equilibrium states where the vertical position is a monotonic function of the plasma current [KB17]

$$Z_{\text{axis}}(t) = f(I_p(t)) \quad (1.27)$$

where  $Z_{\text{axis}}$  is the vertical position of the magnetic axis and  $f$  is the monotonic function depending on the wall geometry and in the plasma current profile. For ITER mitigated disruptions the expected value of for  $\tau_{\text{CQ}}$  is 50-150 ms and the wall resistive time is around 500 ms. Therefore for mitigated disruptions, the post-TQ vertical displacements in ITER are expected to be in the regime described with expression (1.27). It is important to note that in this regime the plasma will enter in contact with the wall at the same  $I_p$  regardless of how fast are the time-scales of the decay of the plasma current.

### Asymmetric VDEs (AVDEs)

In the case of a non-controlled VDE, the plasma moves onto the wall at which time part of the plasma current flows into the first wall, generating the so-called halo currents (see figure 1.19). The halo currents lead to large Laplace forces on the vacuum vessel and on the in-vessel components. Due to the reduction of the plasma cross section during the fast vertical movement, the value of the safety factor can drop considerably and the plasma can become unstable to additional MHD instabilities, i.e. external kink modes [Zak08]. This causes a 3D deformation of the plasma, the toroidal localisation of the halo currents and the rotation of the toroidally asymmetric halo currents. A particular concern of this rotation is the possibility of a resonance of the rotation of the halo currents and the associated electromagnetic forces to the vessel with the mechanical eigenmodes of the machine [Sch+11]. The physics of the 3D VDEs and particularly the causes for the rotation of the plasma during the VDEs are not well established.

The halo current is characterized with the amount of current entering the wall per toroidal radian

$$I_{\text{halo}}(\phi) \equiv \frac{1}{2} \int |J_n| dl \quad (1.28)$$

with  $J_n$  being the normal current density to the wall and the line integral is performed over the poloidal length of the wall. In order to characterize the amount of halo current, the halo current fraction is defined as

$$\text{HF} \equiv \frac{\int I_{\text{halo}} d\phi}{I_{p0}} \quad (1.29)$$

where  $I_{p0}$  is the initial total toroidal current.

Another important figure of merit to characterize the amplitude of the toroidal asymmetry of the VDE is the toroidal peaking factor (TFP)

$$\text{TPF} \equiv \frac{\max(I_{\text{halo}})}{\int I_{\text{halo}} d\phi / 2\pi} \quad (1.30)$$

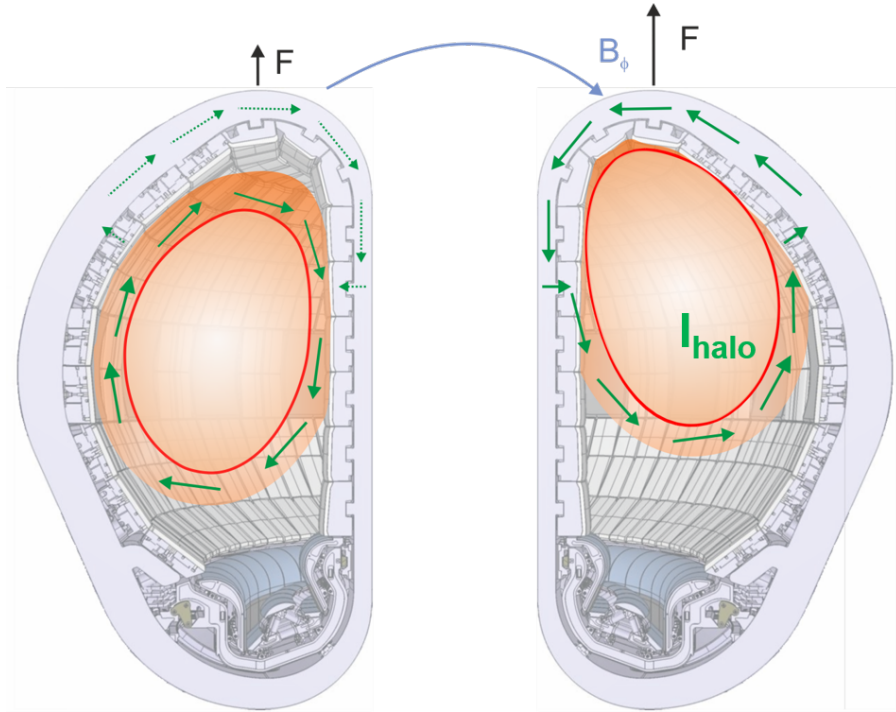


FIGURE 1.19: Schema of an asymmetric VDE showing halo currents flowing into the ITER’s first wall and vacuum vessel. Figure adapted from [Leh+15].

where  $\max(I_{\text{halo}})$  is the maximum angular current density  $I_{\text{halo}}$ .

The product  $\text{HF}_{\text{max}} \times \text{TPF}$  indicates the maximum local poloidal halo current density as a function of the initial current ( $I_{p0}$ ). The calculation of this product has important engineering implications for ITER as it is critical for the calculation of the maximum expected Laplace forces in the in-vessel components that determine the operational limits. The toroidal peaking factors and maximum halo fractions are shown in figure 1.20, where the maximum  $\text{HF}_{\text{max}} \times \text{TPF}$  product is  $\sim 0.75$ . Experimental observations show that the  $\text{HF}_{\text{max}} \times \text{TPF}$  is found to decrease with the edge safety factor [Eid+15].

The structure of the toroidal asymmetry plays an important role as well. Experiments show that the dominant toroidal mode number is typically  $n = 1$  with smaller contributions of other low mode numbers [Gra+96]. The toroidal velocity of the halo current asymmetry does not vary much over the different tokamak experiments and it lies in the range of 1-10 km/s [Mye+17]. The experimental scaling law for this velocity [Mye+17] has been found to be

$$\langle v_h \rangle \propto (\tau_{\text{CQ}}/R)^{-0.5} \quad (1.31)$$

The mechanism that drives this rotation does not depend strongly on the total plasma current ( $I_p$ ) or the toroidal magnetic field ( $B_\phi$ ) [Mye+17]. For ITER mitigated disruptions, the empirical scaling laws indicate that the halo rotation frequency is expected to be larger than  $\langle f_h \rangle = 20$  Hz, which is above the critical ITER resonance range of 3-20 Hz [Sch+11]. However frequencies of the order of 6-20 Hz could be expected for unmitigated disruptions with large  $\tau_{\text{CQ}}$ . As the origin of this rotation is not yet well understood, special care should be taken when using these empirical extrapolations and numerical tools are still needed to understand and reliably predict the asymmetric properties of the VDEs.

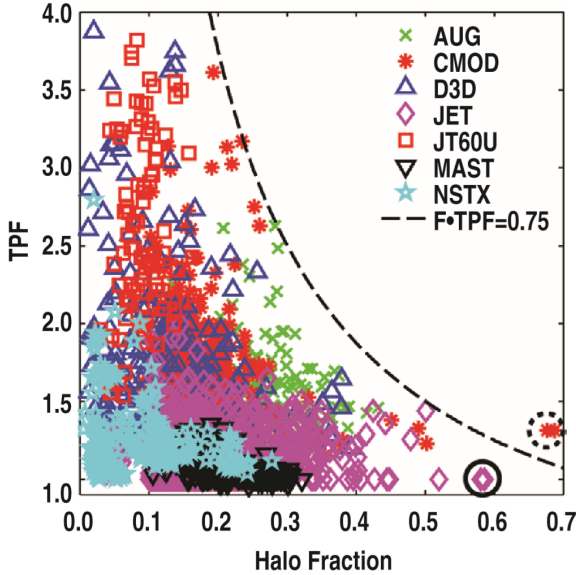


FIGURE 1.20: Toroidal peaking factor versus the maximum halo fraction during AVDEs in different tokamak experiments [Eid+15].

### 1.3 Scope of this thesis

The aim of this thesis is to study the ELM triggering via vertical oscillations as well as the VDE instability with self-consistent numerical simulations. Even if these two types of instabilities are not directly related, they require the same numerical framework. In particular, the simulation of vertical displacements that is common to both phenomena, requires the implementation of the so-called free-boundary conditions for the magnetic field, which should include resistive walls, passive conductors and poloidal field coils. If the effect of the external components on the plasma is not correctly modelled, these instabilities cannot be studied and compared with experiments.

For the simulation of these instabilities, the JOREK-STARWALL code suit is used. JOREK is a code that solves the 3D MHD equations for the plasma in toroidal geometry and STARWALL calculates the contribution to the magnetic field of the resistive walls, passive conductors and coils. The JOREK-STARWALL code suit is described in detail in chapter 2, where the physics models and the used approximations are presented.

A significant part of this thesis entails the adaptation of JOREK-STARWALL for the simulation of ELM triggering via vertical kicks and VDEs. In chapter 3, a newly developed derivation of the STARWALL's system of equations is performed based on a finite element method approach. The STARWALL's derivation is generalized by allowing an extension of the present version to full MHD models including halo currents, arbitrary coils and passive conductors. In addition, different methods related with free-boundary boundary conditions, such as the calculation of experimental and arbitrary free-boundary equilibria and the imposition of time-varying coil currents are described and tested in chapter 3.

In chapter 4, the axisymmetric features of the vertical position oscillations together with their effect on the ELM stability are assessed. In order to clarify the physics basis behind this ELM control approach and its potential for application in ITER, the JOREK-STARWALL code suit is applied. The origin of the induced edge currents during the vertical motion is studied with an analytical model and simulations. The influence of the vertical position oscillations in the pedestal stability is analysed for different vertical position displacements, vertical velocities and initial pedestal bootstrap currents for an ITER plasma. These numerical studies aim to

understand and reproduce the experimental observations summarized in section 1.2.3, where a minimum kick size is required to trigger an ELM regardless of the plasma vertical velocity and the triggering efficiency increases at smaller collisionalities (or at higher bootstrap currents).

The VDE instability is analysed as well with MHD simulations in chapter 5. First, complex benchmarks with existing free-boundary MHD codes are performed with the aim to validate JOREK-STARWALL. The influence of the ratio of the current quench time and the wall time ( $\tau_{\text{CQ}}/\tau_w$ ) on the halo current fraction (HF) is analysed with an ITER plasma. Finally preliminary AVDE simulations are performed with the aim to study the rotation of the halo current asymmetry and its dependence on  $\tau_{\text{CQ}}$  for ITER cold VDEs with axisymmetric walls.



# Chapter 2

## Tokamak modelling

As previously mentioned in chapter 1, several concerns for the future fusion reactors are related to MHD instabilities and their control. The experimental conditions for “big size” tokamaks such as ITER cannot be completely reproduced in current experiments and therefore special care should be taken when extrapolating from existing devices. The prediction of ELMs and disruptions requires the use of well validated MHD models. The complexity of the MHD equations (2nd order non-linear PDEs in three dimensions) leads unavoidably to the development of powerful numerical codes. While analytical models give a basic understanding of the plasma dynamics, their predictive capabilities are not sufficient for complex tokamak geometries.

The important progress in High-Performance Computing (HPC) during the last decades is allowing the use of richer MHD codes. The validation of such numerical tools with experimental data is a key issue for the following reasons: validated codes can be used to better understand the plasma phenomena and to optimize the future fusion reactors performance and to increase their safety.

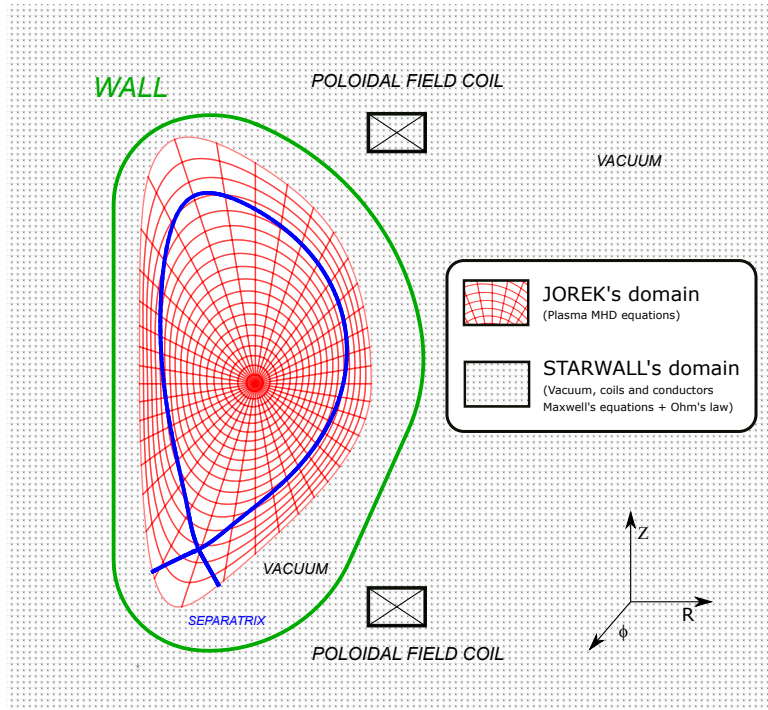


FIGURE 2.1: Scheme showing the domains belonging to JOREK and STARWALL.

In this chapter the physics models and the numerical approach used during this thesis are described. In section 2.1. the code JOREK is presented, which is used for the simulation of

the plasma region. In section 2.2 the STARWALL code is described, which takes into account the conducting structures and vacuum surrounding the plasma (see figure 2.1). Finally the coupling between JOREK and STARWALL will be explained in section 2.3.

## 2.1 Plasma domain: the JOREK code

The non-linear code JOREK solves the extended MHD equations in toroidal geometry. JOREK was conceived by G.T.A. Huijsmans at the CEA (Centre d’Energie Atomique) in France and its development began in 2002 [Huy+02].

The main motivation for its development was to study the non-linear dynamics of ELMs in full toroidal geometry including the plasma separatrix and open field-lines. Previously, the peeling-balloonning stability was mainly studied with linear MHD codes such as CASTOR [Ker+98] and MISHKA [Mik+97]. These codes use a straight field-line coordinate system and therefore the separatrix has to be truncated due to the singularities appearing in the jacobian at the X-point. The first studies with JOREK revealed the influence of the separatrix on the resistive edge peeling modes [HC07].

After the first observations of ELM dynamics in JOREK [Huy+09], several ELM studies followed as the code grew in complexity and efficiency. ELM control techniques such as pellet injection [Fut+14], RMPs [Ora+13] and vertical oscillations [Art+18] have also been numerically demonstrated. Finally, quantitative validation of JOREK simulations of ELMs in several tokamaks [Pam+16; Pam+17] were carried out showing reasonable agreement with experiments.

Presently the JOREK community is constantly growing and expanding over several international institutions: CEA (Commissariat à l’Enérgie Atomique), IPP (Max Planck Institute for Plasma Physics), CCFE (Culham Centre for Fusion Energy), ITER, TUE (Technische Universiteit Eindhoven), etc. The topics of research are no longer limited to ELMs and the code is applied to study different aspects of disruptions as well as other subjects. The different JOREK applications are listed below

- ELMs
  - ELM crashes including ExB and diamagnetic flows, stochastic layer formation, filament formation, divertor heat loads, non-linear mode spectrum.
  - ELM cycles, inter-ELM activity, and explosive ELMs
  - ELM control by pellets, RMPs, and vertical oscillations as well as the ELM free QH-mode regime.
  - Impurity transport during ELMs
- Disruptions
  - Thermal and current quench, massive gas injection and shattered pellet injection
  - Runaway electrons and its interaction with MHD
  - Vertical displacement events and halo currents
  - Tearing mode control
- Fast particle modes
- ITG turbulence

Other nonlinear MHD codes, such as BOUT++ [Dud+09], M3D [Par+99], M3D-C1 [Jar+08], XTOR [LL08], MEGA [TS98] and NIMROD [Gla+99] can also obtain advanced MHD simulations in tokamak geometry. While the MHD equations used in these codes and JOREK are similar, the distinguishing characteristics of JOREK lie on the spatial and temporal discretization. In the next sections the main features of JOREK will be described.

### 2.1.1 Plasma equations: the reduced and full MHD models

The modular structure of JOREK allows to implement different physics models without affecting other parts of the code. The current version of the code contains a set of models including different physics (parallel flows, diamagnetic flows, bi-fluid, neutrals, radiation...) which the user can choose at the compilation stage.

TABLE 2.1: Useful definitions

Symbol	Description
$\mu_0$	Vacuum permeability
$\rho_0$	Mass density at the plasma center
$\phi$	Toroidal angle
$\mathbf{e}_\phi$	Normalized toroidal basis vector
$\gamma$	Adiabatic constant expressing the ratio of specific heats
$pol$	"Poloidal", lying on the poloidal plane
$bnd$	"Boundary", plasma boundary or last closed flux surface
$axis$	The magnetic axis
$\perp$	Perpendicular to the magnetic field
$\parallel$	Parallel to the magnetic field
$\Delta^*$	$\equiv R^2 \nabla \cdot \left( \frac{1}{R^2} \nabla \right)$
$\Delta_{pol}$	$\equiv \frac{1}{R} \frac{\partial}{\partial R} \left( R \frac{\partial}{\partial R} \right) + \frac{\partial^2}{\partial Z^2}$
$\nabla_\parallel$	$\equiv \frac{\mathbf{B}}{ B ^2} \mathbf{B} \cdot \nabla$
$\nabla_\perp$	$\equiv \nabla - \nabla_\parallel$
$[A, B]$	$\equiv \mathbf{e}_\phi \cdot \nabla A \times \nabla B$ , Poisson bracket

In this section we present the equations of the model "303" which is the most used reduced MHD model and the recent full MHD model "710". First we define the variables, normalization and operators in the tables 2.1 and B.2 (1). The toroidal coordinate system  $(R, Z, \phi)$  shown in figure 2.1 is used in JOREK. In this system, the toroidal angle  $\phi$  increases in the clockwise direction when looking at the torus from above.

#### The reduced MHD model "303"

The most used JOREK model in the literature is the so called model "303". This model can be derived from the full visco-resistive MHD equations when the following ansatz for the magnetic field and for the velocity is chosen

$$\mathbf{B} = F_0 \nabla \phi + \nabla \psi \times \nabla \phi \quad (2.1)$$

$$\mathbf{v} = v_\parallel \mathbf{B} + R^2 \nabla \phi \times \nabla u \quad (2.2)$$

where the constant  $F_0$  corresponds to the vacuum magnetic field multiplied by the major radius. For the toroidal field, the ansatz is justified when the vacuum toroidal field is large compared to the toroidal field produced by the plasma ( $F \approx F_0$ ), which typically the case for

most of the tokamaks. The velocity ansatz can be understood as an  $\mathbf{E} \times \mathbf{B}$  velocity that lies in the poloidal plane

$$\mathbf{v}_\perp \approx \frac{\mathbf{E} \times \mathbf{B}_\phi}{B^2} \approx -R^2 \frac{\nabla \Phi}{F_0} \times \nabla \phi \quad (2.3)$$

where the velocity stream function can be identified with the electric potential  $u = \Phi/F_0$ . Note that the approximation  $\mathbf{B}_{pol} \ll \mathbf{B}_\phi$  has been used to give a physical understanding of the velocity ansatz, however once the ansatz is chosen no further approximations are required. In addition, the velocity ansatz is mathematically consistent with the assumption  $F \approx F_0$  as it can be demonstrated by applying the dot product of Faraday's law (1.7f) with  $R^2 \nabla \phi$

$$\frac{\partial F}{\partial t} = R^2 \nabla \phi \cdot \nabla \times (\mathbf{v} \times \mathbf{B}) = R^2 \nabla \cdot (F_0 \nabla u \times \nabla \phi) = 0 \quad (2.4)$$

This formulation has important numerical benefits as the toroidal field becomes incompressible and the high frequencies related to the fast magneto-sonic waves no longer exist [Gui15]. The reduced MHD model was first presented in 1976 by H.R. Strauss, with many subsequent modifications [Str76]. The complete system of equations based on this model that are used in JOREK are

$$\frac{\partial \rho}{\partial t} = -\nabla \cdot (\rho \mathbf{v}) + \nabla \cdot (D_\perp \nabla_\perp \rho) + S_\rho \quad (2.5)$$

$$\mathbf{e}_\phi \cdot \nabla \times R^2 \left( \rho \frac{\partial \mathbf{v}}{\partial t} = -\rho \mathbf{v} \cdot \nabla \mathbf{v} - \nabla(\rho T) + \mathbf{J} \times \mathbf{B} + \mu \Delta \mathbf{v} - \mathbf{v} S_\rho \right) \quad (2.6)$$

$$\mathbf{B} \cdot \left( \rho \frac{\partial \mathbf{v}}{\partial t} = -\rho \mathbf{v} \cdot \nabla \mathbf{v} - \nabla(\rho T) + \mathbf{J} \times \mathbf{B} + \mu \Delta \mathbf{v} - \mathbf{v} S_\rho \right) \quad (2.7)$$

$$\rho \frac{\partial T}{\partial t} = -\rho \mathbf{v} \cdot \nabla T - (\gamma - 1) \rho T \nabla \cdot \mathbf{v} + \nabla \cdot (\kappa_\perp \nabla_\perp T + \kappa_\parallel \nabla_\parallel T) + S_T \quad (2.8)$$

$$\frac{\partial \psi}{\partial t} = -R^2 \mathbf{B} \cdot \nabla u + \eta(j - j_0) \quad (2.9)$$

$$j = \Delta^* \psi \quad (2.10)$$

$$w = \Delta_{pol} u \quad (2.11)$$

where  $j_0$  is an artificial current source used to keep the current profile constant over time and avoid the current decay. The resistivity, parallel conductivity and viscosity can be either chosen to be spatially constant or to have the following temperature dependence

$$\eta(T) = \eta_0 \left( \frac{T_0}{T} \right)^{\frac{3}{2}}, \quad \kappa_\parallel(T) = \kappa_{\parallel,0} \left( \frac{T}{T_0} \right)^{\frac{5}{2}}, \quad \mu(T) = \mu_{c0} \left( \frac{T_0}{T} \right)^{\frac{3}{2}} \quad (2.12)$$

where  $T_0$  is the temperature at a reference point (usually the plasma core) and a reference value for  $\eta_0$ ,  $\kappa_{\parallel,0}$  or  $\mu_{c0}$  is given. These values can be estimated with the Spitzer expression for the resistivity and the Braginskii expressions for the other coefficients [Hub04]. The perpendicular diffusion coefficients  $D_\perp(\psi)$  and  $\kappa_\perp(\psi)$  are set by the user as flux dependent profiles. These profiles are typically used to maintain the large density and temperature gradients appearing at the pedestal by locally reducing the diffusion coefficients. Note that JOREK does not include a transport model that could calculate accurately these coefficients coming from the neoclassical transport theory and turbulence.

The full form of the reduced MHD equations in terms of the JOREK variables  $[\psi, u, j, w, T, \rho]$  is

$$\begin{aligned}\frac{\partial \rho}{\partial t} = & -\rho \left( -2 \frac{\partial u}{\partial Z} + \frac{1}{R} [v_{\parallel}, \psi] + \frac{F_0}{R^2} \frac{\partial v_{\parallel}}{\partial \phi} \right) + R[\rho, u] \\ & - v_{\parallel} \left( \frac{1}{R} [\rho, \psi] + \frac{F_0}{R^2} \frac{\partial \rho}{\partial \phi} \right) + \nabla \cdot (D_{\perp} \nabla_{\perp} \rho) + S_{\rho}\end{aligned}\quad (2.13)$$

$$\begin{aligned}R \nabla \cdot \left( R^2 \rho \frac{\partial \nabla_{pol} u}{\partial t} \right) = & [\rho R^4 w, u] - \frac{1}{2} [R^2 \rho, R^2 |\nabla_{pol} u|^2] \\ & - [R^2, \rho T] + [\psi, j] - \frac{F_0}{R} \frac{\partial j}{\partial \phi} + \mu R^2 \Delta w\end{aligned}\quad (2.14)$$

$$\begin{aligned}\rho B^2 \frac{\partial v_{\parallel}}{\partial t} + \frac{1}{R^2} \rho v_{\parallel} \nabla_{pol} \psi \cdot \nabla_{pol} \left( \frac{\partial \psi}{\partial t} \right) = & \frac{\rho}{2R} [\psi, v_{\parallel}^2 B^2] - \frac{\rho F_0}{2R^2} \frac{\partial (v_{\parallel}^2 B^2)}{\partial \phi} \\ & + \frac{1}{R} [\psi, p] - \frac{F_0}{R^2} \frac{\partial p}{\partial \phi} + \mu_{\parallel} B^2 \Delta v_{\parallel}\end{aligned}\quad (2.15)$$

$$\begin{aligned}\rho \frac{\partial T}{\partial t} = & -\rho T(\gamma - 1) \left( -2 \frac{\partial u}{\partial Z} + \frac{1}{R} [v_{\parallel}, \psi] + \frac{F_0}{R^2} \frac{\partial v_{\parallel}}{\partial \phi} \right) + \rho R[T, u] \\ & - \rho v_{\parallel} \left( \frac{1}{R} [T, \psi] + \frac{F_0}{R^2} \frac{\partial T}{\partial \phi} \right) + \nabla \cdot (\kappa_{\perp} \nabla_{\perp} T + \kappa_{\parallel} \nabla_{\parallel} T) + S_T\end{aligned}\quad (2.16)$$

$$\frac{\partial \psi}{\partial t} = R[\psi, u] - F_0 \frac{\partial u}{\partial \phi} + \eta(j - j_0)\quad (2.17)$$

$$j = \Delta^* \psi\quad (2.18)$$

$$w = \Delta_{pol} u\quad (2.19)$$

which are solved in the weak form with a finite element method. The following assumptions have been used for the derivation of the previous system

- The flows  $v_{\parallel}$  and  $R^2 \nabla \phi \times \nabla u$  have been decoupled in the parallel momentum equation 2.15 and in the vorticity equation 2.14.
- The viscosity terms are not derived but they are rather included as an ad-hoc viscosity.

This model is the base JOREK version of equations for which various extensions exist including diamagnetic and neoclassical flows and consistent bootstrap current evolution.

## The full MHD model "710"

The full MHD model used in JOREK [Hav+16] solves directly the following full MHD equations

$$\frac{\partial \rho}{\partial t} = -\nabla \cdot (\rho \mathbf{v}) + \nabla \cdot (D_{\perp} \nabla_{\perp} \rho) + S_{\rho}\quad (2.20)$$

$$\rho \frac{\partial \mathbf{v}}{\partial t} = -\rho \mathbf{v} \cdot \nabla \mathbf{v} - \nabla(\rho T) + \mathbf{J} \times \mathbf{B} + \Delta(\mu \mathbf{v})\quad (2.21)$$

$$\rho \frac{\partial T}{\partial t} = -\rho \mathbf{v} \cdot \nabla T - (\gamma - 1) \rho T \nabla \cdot \mathbf{v} + \nabla \cdot (\kappa_{\perp} \nabla_{\perp} T + \kappa_{\parallel} \nabla_{\parallel} T) + S_T\quad (2.22)$$

$$\frac{\partial \mathbf{A}}{\partial t} = \mathbf{v} \times \mathbf{B} - \eta \mathbf{J}\quad (2.23)$$

$$\mathbf{J} = \nabla \times \mathbf{B} = \nabla \times \nabla \times \mathbf{A}\quad (2.24)$$

The main difference with respect to the reduced model is that this model includes the full representation of the magnetic field and the velocity with three independent variables each. Another distinction with the reduced model is the chosen gauge for the magnetic vector potential  $\mathbf{A}$ . Note that while in the reduced model the electric field is expressed as  $\mathbf{E} = -\partial_t \mathbf{A} - \nabla \Phi$ , in the full model it is simply expressed as  $\mathbf{E} = -\partial_t \mathbf{A}$ . The gauge freedom is used to set  $\Phi = 0$  with obvious advantages. This gauge is called the Weyl gauge, also known as the Hamiltonian or temporal gauge.

## Boundary conditions (BCs)

A trivial set of possible BCs for the previous models are the Dirichlet boundary conditions where the variable values are constant over time. The Dirichlet boundary condition for the magnetic field  $\mathbf{B} = cte$  implies that the boundary behaves like an ideally conducting wall where the magnetic field is frozen. The resistive wall boundary conditions for the magnetic field are implemented as natural BCs and are presented in detail in section 2.3.

For the perpendicular velocity, a BC can be found by using the generalized Ohm's law

$$\mathbf{v}_\perp = \frac{1}{B^2} (\mathbf{E} \times \mathbf{B} + \eta \mathbf{J} \times \mathbf{B}) \approx \frac{1}{B^2} \mathbf{E} \times \mathbf{B} \quad (2.25)$$

Therefore the Dirichlet BC for the perpendicular velocity  $\mathbf{v}_\perp = 0$  implies that  $\mathbf{E}_\perp \approx 0$  and that the boundary also behaves like an ideally conducting wall for the perpendicular electric field. For the reduced model the typical BCs are simply  $u = 0$  and  $w = 0$ , which imply that the normal velocity to the wall is zero ( $\mathbf{n} \cdot \mathbf{v}_\perp = 0$ ) and that the vorticity vanishes. If the plasma is interfacing a resistive wall, the tangential components of the electric field can be linked to the wall currents by using the usual Ohm's law

$$\mathbf{n} \times \mathbf{E} = \mathbf{n} \times \mathbf{E}_{wall} = \eta_{wall} \mathbf{n} \times \mathbf{J}_{wall} \quad (2.26)$$

where the continuity of the tangential electric field [Jac99] has been used and  $\mathbf{n}$  is a unit vector perpendicular to the wall.

In JOREK, two types of boundaries can be defined, a boundary that is aligned with the field lines and a boundary that is perpendicular to the field-lines (open field-line boundary). For the parallel velocity, Bohm's boundary conditions [Rie91] can be used at the open field-line boundary. These BCs imply that the parallel velocity is equal to or bigger than the ion sound speed  $c_s$  at the entrance of the sheath that forms between the plasma and the targets. In JOREK, the equality condition is implemented

$$\mathbf{v}_\parallel \cdot \mathbf{n} = \frac{\mathbf{B} \cdot \mathbf{n}}{|\mathbf{B}|} c_s \quad (2.27)$$

where the sound speed is defined as  $c_s \equiv \sqrt{\gamma T}$ . Together with this BC, free outflow boundary conditions for the density and the temperature at the open field-line boundary can be implemented with the following sheath condition for the heat flux

$$nT\mathbf{v}_\parallel + \kappa_\parallel \nabla_\parallel T = \gamma_{sh} nT\mathbf{v}_\parallel \quad (2.28)$$

where  $\gamma_{sh}$  is an adimensional parameter called the sheath transmission coefficient with values of the order  $\sim 8$  for  $T_i/T_e \sim 1$  (see [Sta+00]).

### 2.1.2 Spatial discretization and finite element method

One of the key characteristics of JOREK is the spatial discretization which is based on a hybrid technique between a spectral and a finite element method. The toroidal periodicity of the tokamak is exploited by using Fourier harmonics in the toroidal direction. In addition to reducing the computational time, the Fourier harmonics allow to isolate the different types of instabilities that are characterized by the toroidal mode number "n" and to study their non-linear interactions.

In the poloidal plane the periodicity is lost when treating open field-lines. For this reason a finite element method is used for the  $(R, Z)$  plane. The JOREK variables and also the  $(R, Z)$  coordinates are expressed with the aid of a 2D finite element basis constructed with Bézier surfaces [CH08]. The Bézier surfaces were first used by the french engineer Pierre Bézier in the 1960s when he was working for the car manufacturer Renault [Béz82]. Bézier developed an original method to represent smooth curves in terms of a set of control points that was understandable by the computers controlling the machines. The main advantage of using these surfaces and curves in MHD codes is that they can be easily shaped and aligned to the magnetic field topology with a high degree of accuracy. The accurate alignment of the finite elements with the equilibrium flux surfaces significantly improves the representation of the radial and angular anisotropy of the MHD modes. As an example, one of the main difficulties of computational MHD is to treat correctly the large anisotropies in the heat conduction ( $\kappa_{\parallel}/\kappa_{\perp} \sim 10^9$ ) because small errors in the computation of the parallel and perpendicular gradients can cause numerical instabilities. In figure 2.2 we show an example of a grid construction with elements aligned to the magnetic topology. Another benefit of the grid alignment is that mesh accumulation can be easily used in the key flux surfaces where the modes develop.

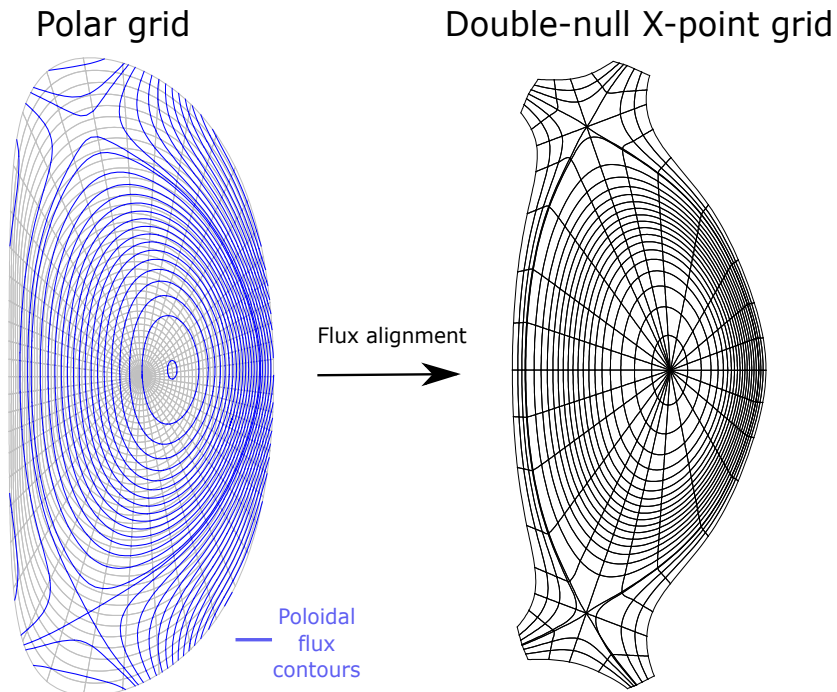


FIGURE 2.2: Grid construction in JOREK. A flux aligned grid is constructed from the previously calculated equilibrium computed in a simple polar grid. Note that these grids have far lower resolution than used in practice for visual purposes.

The poloidal plane is decomposed in quadrilateral cells that will be referred to as Bézier elements. In each of these Bézier elements the JOREK variables and the  $(R, Z)$  coordinates are interpolated with third order Bernstein polynomials with local coordinates  $(s, t)$ . One of the

benefits of the Bézier elements is that mesh refinement can be used, however this feature is not included in the current JOREK version. The chosen Bézier formalism satisfies C1 continuity across the elements so that the variables and their derivatives are continuous in the  $(R, Z)$  global coordinates but not on the local  $(s, t)$  ones. Within a Bézier element the coordinates  $\mathbf{R} \equiv (R, Z)$  and the variable  $\psi$  (as an example) have the following representation in the poloidal plane

$$\mathbf{R}(s, t) = \sum_{i=1}^4 \sum_{j=1}^4 \mathbf{R}_{i,j} B_{ij}(s, t) \quad (2.29)$$

$$\psi(s, t) = \sum_{i=1}^4 \sum_{j=1}^4 \psi_{i,j} B_{ij}(s, t) \quad (2.30)$$

where  $B_{ij}(s, t)$  are polynomial basis functions including the geometrical properties of the element, the index  $i$  loops over the four vertices of the quadrilateral element and the  $j$  index loops over the four degrees of freedom related to the third order polynomials. The complete decomposition including the toroidal dependence is given by a real Fourier series

$$\psi(s, t, \phi) = \psi_0(s, t) + \sum_{n=1}^{N-1} (\psi_n^c(s, t) \cos(n\phi) + \psi_n^s(s, t) \sin(n\phi)) \quad (2.31)$$

where  $N$  is the total number of toroidal harmonics including the axisymmetric mode ( $n = 0$ ).

## The Galerkin finite element method

The unknowns of the system become a finite set of coefficients  $(\psi_{ijn})$  thanks to the Bézier discretization, nevertheless the solution remains continuous due to the interpolating polynomials. A set of linear equations is constructed in the matrix form  $\mathbf{A} \cdot \mathbf{x} = \mathbf{b}$  in order to solve for these coefficients. A finite element method (FEM) is chosen in order to obtain the required matrices  $\mathbf{A}$  and  $\mathbf{b}$ . In the FEM the equations are projected with a test function  $v^*$  and integrated over the computational volume  $V$ . This method is illustrated below with the example of the heat diffusion equation  $\partial_t T = \nabla \cdot (\kappa \nabla T)$

$$\int_V v^* \frac{\partial T}{\partial t} dV = \int_V v^* \nabla \cdot (\kappa \nabla T) dV \quad (2.32)$$

where  $v^*$  is a known regular function. The latter expression is known as the weak form of the former equation. One of the main utilities of this method is that the order of the spatial derivatives can be reduced by integration by parts

$$\int_V v^* \frac{\partial T}{\partial t} dV = - \int_V \kappa \nabla v^* \cdot \nabla T dV + \int_S \kappa v^* \nabla T \cdot \mathbf{n} dS \quad (2.33)$$

where  $S$  denotes the surface enclosing the computational domain and  $\mathbf{n}$  is a unit vector normal to that surface. An additional advantage is that Neumann or Robin boundary conditions can be naturally implemented in the boundary terms without the need of any special treatment. For example in the heat diffusion equation, the boundary condition  $\nabla T \cdot \mathbf{n} = c(T)$  is simply implemented by replacing  $\nabla T \cdot \mathbf{n}$  by  $c(T)$  in the boundary term of (2.33). In this case the boundary conditions are not directly imposed and they are automatically satisfied after the solution of the problem. The Bubnow-Galerkin approach [Hir07] consists in taking the basis functions as the test functions (i.e.  $v^* = B_{ij}(s, t) \cos(n\phi)$ ). The method is a straightforward way to get a closed system of equations as there are as many unknowns as basis functions.

### 2.1.3 Time discretization and solvers

Another particular feature of JOREK is that the time-stepping scheme is fully implicit. While the solution of the implicit linear equations is far more computationally demanding than for the explicit methods, the implicit methods present several advantages. As opposed to the explicit schemes, the ratio between time step " $\delta t$ " and grid size " $\delta x$ " is not constrained by numerical instabilities, therefore the time-step can be chosen independently of the grid size. Particularly the convection and diffusion equations that are relevant for MHD are unconditionally stable with these schemes. Implicit schemes like the Crank-Nicholson or Gears scheme present this feature as well as the independence of the time-step on the frequencies of the system. This allows to adapt the time-step to the characteristic time of the instability of interest, ranging from 0.5-5 Alfvén times for ELMs to 10000 Alfvén time for slowly growing resistive modes.

For the time discretization, the MHD equations are written in the following form

$$\frac{\partial \mathbf{F}(\mathbf{u})}{\partial t} = \mathbf{G}(\mathbf{u}) \quad (2.34)$$

where  $\mathbf{u}$  is a vector containing the list of unknown variables and  $\mathbf{F}$  and  $\mathbf{G}$  are operators acting on  $\mathbf{u}$ . A general time-evolution scheme that linearises the previous system is given by [Hir07]

$$\left[ (1 + \xi) \left( \frac{\partial \mathbf{F}}{\partial \mathbf{u}} \right)^n - \delta t \theta \left( \frac{\partial \mathbf{G}}{\partial \mathbf{u}} \right)^n \right] \delta \mathbf{u}^n = \delta t \mathbf{G}^n + \xi \left( \frac{\partial \mathbf{F}}{\partial \mathbf{u}} \right)^{n-1} \delta \mathbf{u}^{n-1} \quad (2.35)$$

where  $\delta \mathbf{u}^n = \mathbf{u}^{n+1} - \mathbf{u}^n$  and  $\theta$  and  $\xi$  are numerical parameters. Parameter values satisfying  $\theta - \xi = 0.5$  are required to guarantee second-order accuracy of the time-evolution scheme. For instance, ( $\theta = 0.5$ ,  $\xi = 0$ ) corresponds to a linearized Crank-Nicholson scheme and ( $\theta = 1$ ,  $\xi = 0.5$ ) to the linearized Gears scheme. The scheme of equation 2.35 is the one implemented in JOREK where the user can choose between the Gears and the Crank-Nicholson schemes.

### Solving the system of equations

Once the system is discretized and the Galerkin FEM is applied, a solution for the formed system of equations  $\mathbf{A} \cdot \mathbf{x} = \mathbf{b}$  has to be found. The number of unknowns of the system is

$$\# \text{unknowns} = 4 \times N_{\text{nodes}} \times N_{\text{var}} \times (2N_{\text{harm}} - 1) \quad (2.36)$$

where  $N_{\text{nodes}}$  is the total number of grid nodes,  $N_{\text{var}}$  is the number of variables and  $N_{\text{harm}}$  is the number of different harmonics used. The factor 4 takes into account the degrees of freedom of the 3rd order Bernstein polynomials at each node. A small to medium size simulation will have  $N_{\text{nodes}} = N_{\text{rad}} \times N_{\text{pol}} \sim 2 \times 10^4$ ,  $N_{\text{var}} = 7$  and  $N_{\text{harm}} = 5$  so the number of unknowns is  $\sim 5 \times 10^6$ . This means that the number of elements of the  $\mathbf{A}$  matrix is  $2.5 \times 10^{13}$  (the square of the number of variables). Note that storing and handling such a matrix in a conventional format wouldn't be feasible as the memory required would be  $8 \text{ bytes} \times 2.5 \times 10^{13} = 200 \text{ TB}$ . However, the matrix is sparse and most of the entries are zeros. This is due to the fact that normally the variables at one node are only directly coupled with the neighbouring nodes. Therefore the most efficient way to store the matrix is in a sparse format where only the non-zero elements are stored. In this way the memory required is typically of the order of a few GBs.

In order to solve the system of equations, the *Pastix* [HRR02] library is used. This library developed in the INRIA institute (Bordeaux, France) solves systems of linear equations with sparse matrices using parallel computing. The solution is based on a **LU** factorisation method for the matrix  $\mathbf{A}$ . However the direct application of this method to large matrices is still

numerically too expensive. When the system contains non-linearities and significant coupling between the different Fourier harmonics, an iterative solution is applied. The chosen technique is the so-called GMRES method [SS86]. For the convergence of the iterative method a good pre-conditioning of the matrix is crucial. JOREK uses a physics based pre-conditioner that solves the submatrix of each Fourier harmonic independently using the **LU** factorisation by ignoring the non-linear coupling with other Fourier modes. In tokamaks, linear eigenmodes only involve one toroidal harmonic, which explains why this type of pre-conditioner can be used. The convergence during the GMREs iterations becomes challenging when reaching the non-linear phase and the coupling between the modes becomes relevant. If convergence is not attained after a chosen number of iterations the pre-conditioner is re-calculated, otherwise the pre-conditioner will be kept and used for the next time-step.

## 2.1.4 Simulation phases

In this section the main different steps and procedures during a typical JOREK run are listed by order of execution

- 1. Meshing:** The first step is the generation of a grid and the definition of the computational domain. Here the indices and the coefficients  $\mathbf{R}_{ij}$  (see equation (2.29)) at each node are computed. Typically the initial grid has a polar structure where the user specifies the number of subdivisions in the radial and polar directions, an example of a polar grid grid is shown in figure 2.2. During this step a file containing the geometrical information of the JOREK boundary is created. This file is imported by the code STARWALL in order to create the corresponding response file required to include free-boundary conditions in JOREK. The interfacing with STARWALL will be explained in section 2.3.
- 2. Static equilibrium generation:** Once the grid is defined, an equilibrium must be found and used as a starting point for the time evolution. The computation of the equilibrium involves the solution of the Grad-Shafranov equation [GKP10], which is the MHD momentum equation for a static axisymmetric equilibrium ( $\mathbf{v} = 0$  and  $\partial_t = \partial_\phi = 0$ ). The equation represents the balance between the pressure gradient and the Laplace forces ( $\mathbf{J} \times \mathbf{B} = \nabla p$ ). By exploiting axisymmetry, the Grad-Shafranov equation reads

$$\Delta^* \psi = -R^2 p'(\psi_N) - FF'(\psi_N) \quad (2.37)$$

where the pressure  $p$  and the poloidal current streaming function  $F$  are functions of the poloidal flux  $\psi$  (see table 2.1). The prime denotes a derivative with respect to the poloidal flux (i.e.  $p' \equiv dp/d\psi$ ). The  $p'$  and  $FF'$  profiles are given by the user together with the poloidal flux on the boundary of the domain. The equation is solved with the same Galerkin-FEM method as for the time evolution and by using the so called Picard iterations [Jar10].

For the reconstruction of experimental equilibrium, JOREK can import directly the required data from *eqdsk* files coming from existing tokamaks. After the construction of the equilibrium, a flux-aligned grid can be produced with the geometry of the found flux surfaces. For free-boundary simulations, a free-boundary equilibrium is required as a starting point. In section 3.2 the computation of free-boundary equilibria with Picard iterations is explained.

- 3. Axisymmetric time evolution:** An initial axisymmetric run is performed (only  $n = 0$ ) in order to establish the plasma flows and to obtain a steady state. If the chosen model contains parallel flows ( $v_{||} \neq 0$ ), it's particularly important to choose small time-steps at

the beginning of the simulation ( $\sim 10^{-3}$  Alfvén times) due to the initially large velocity gradients at the divertor targets created by the Bohm's boundary condition ( $v_{\parallel} = c_s$ ). The time-steps can be progressively increased as the gradients are smoothed, finally the parallel flows will be established in a time scale depending on the chosen parallel viscosity. During this phase is also important to adapt the diffusion coefficients ( $D_{\perp}$ ,  $\kappa_{\perp}$  and  $\kappa_{\parallel}$ ) and the particle and temperature sources ( $S_{\rho}$  and  $S_T$ ) in order to keep the temperature and density profiles unchanged over time. This is particularly important for ELM simulation studies where steady state profiles are suitable to study the stability of modes during the linear phase.

4. **Mode launching and linear phase:** When a steady state is found and the equilibrium flows are established, the different chosen Fourier harmonics are launched as small perturbations. Depending on the stability of the chosen mode, its energy will grow exponentially with a given growth rate  $\gamma$  or it will stay oscillating at the noise level. In this thesis cases will be shown where the evolution of the equilibrium itself is comparable to the growth of the instabilities and therefore the growth rates of the modes will vary over the linear phase (see section 4.3). The time-step values during this phase should be set depending on the time-scale of the growth of the instability of interest.
5. **Non-linear phase:** When the modes have grown enough the non-linear phase takes place and the non-linear coupling between the different modes becomes important. The non-linear coupling can destabilize modes that were linearly stable [Kre+13]. The time-steps have to be typically reduced to the order of  $\sim 1$  Alfvén time or smaller for the convergence of the GMRES iterative method as the pre-conditioner becomes less accurate with the non-linearities.

## 2.2 Vacuum, coils and wall domain: the STARWALL code

The implementation of free-boundary conditions is essential when simulating instabilities such as vertical displacements events (VDEs). The main reason is that the basic principle stabilizing the VDEs are the mirror (eddy) currents that arise inside the conducting structures outside the plasma domain. In the case of ideally conducting walls close enough to the plasma, the mirror currents completely stabilize the vertical instability. As previously explained in section 2.1.1, when Dirichlet BCs are applied the JOREK boundary acts like an ideally conducting wall, thus VDEs are always stable when applying these boundary conditions. Therefore more complex boundary conditions including resistive walls are needed.

JOREK has been coupled to the code STARWALL in order to apply natural boundary conditions for the magnetic field including resistive walls. STARWALL [MS15] is a code that was initially developed by P. Merkel at the Max-Planck Institute for Plasma Physics (Germany) in order to simulate resistive wall modes (RWMs) [McA14]. The vacuum, the 3D conducting structures (walls, coils) and all their mutual and self inductances are taken into account in this framework. In addition to the effect of current induction in resistive structures, it is also possible to include feedback control for the free-boundary instabilities by imposing currents in the STARWALL coils. The JOREK-STARWALL code has been previously used for VDE studies [Hoe+14] and also QH-modes [Liu+15]. For simplicity, all the conducting structures around the plasma will be denoted as *wall* in the following sections (see table 2.2 for other conventions).

**Model** The magnetic field solution in the STARWALL's domain (see figure 2.1) is obtained with a Green's function method thanks to the choice of the Coulomb gauge for the magnetic

TABLE 2.2: STARWALL's conventions and definitions.

Symbol	Description
<i>wall</i>	All considered conductors around the plasma
$d_w$	<i>wall</i> thickness
$\eta_w, \sigma_w$	<i>wall</i> resistivity, conductivity
$\mathbf{n}$	normal vector to the <i>wall</i>
$\tan$	Tangential to the conducting surface
$\mathbf{j}$	$\equiv \mathbf{J}_{\tan} d_w$ Surface currents flowing in the thin <i>wall</i>
$I$	Divergence-free current potential
$\phi^s$	Source/sink current potential
$Y$	Divergence-free current potential after similarity transform $\mathbf{Y} = S\mathbf{I}$
$\mathbf{B}_{\tan}$	$\equiv \mathbf{B} \times \mathbf{n}$

vector potential ( $\nabla \cdot \mathbf{A} = 0$ ). In practice the code gives the tangential field ( $\mathbf{B} \times \mathbf{n}$ ) on the JOREK boundary provided the normal field component ( $\mathbf{B} \cdot \mathbf{n}$ ) and the normal current density ( $\mathbf{J} \cdot \mathbf{n}$ ). As it is shown in section 3.1, the normal components of the magnetic field and the current density are sufficient to solve for the magnetic field in the STARWALL's domain. The equations being solved are the Maxwell's equations in the low frequency limit (2.38)-(2.40) together with Ohm's law in the conductive structures (2.41)

$$\mathbf{E} = -\frac{\partial \mathbf{A}}{\partial t} - \nabla \Phi \quad (2.38)$$

$$\Delta \mathbf{A} = -\mu_0 \mathbf{J} \quad (2.39)$$

$$\nabla \cdot \mathbf{J} = 0 \quad (2.40)$$

$$\mathbf{E} = \eta \mathbf{J} \quad (\text{only inside conducting structures}) \quad (2.41)$$

The exact form of the STARWALL's equations and discrete matrices was derived by with a variational principle [MS15]. When dealing with dissipative systems the formulation of equations with variational principles becomes normally very problematic. In the derivation performed in [MS15], these problems were avoided by formulating the problem linearly and thus assuming the exponential time dependence  $e^{\gamma t}$ . As JOREK is inherently non-linear, a more intuitive and general derivation has been developed during this thesis. The original derivation is based on the weak form the system (2.38)-(2.41) and it will be presented in section 3.1.

**The thin wall approximation** The STARWALL code uses the thin wall approximation which simplifies the numerical calculations by representing the conducting structures with infinitely thin surfaces. This approximation relies on the following assumptions

- The *wall* thickness is much smaller than its characteristic length ( $d_w \ll r_{wall}$ )
- Electric currents are homogeneous in the direction perpendicular to the *wall*

This allows to reduce the number of dimensions of the *wall* to 2D, which is numerically very convenient when inversion of matrices is involved. In order to satisfy the thin wall approximation, the diffusion of currents across the *wall* should be faster than the time-scale of the instability of interest. A magnetic field varying on a time-scale  $\tau$  penetrates into a conductor limited by the skin depth  $\delta_{skin} = \sqrt{\eta\tau/(\pi\mu_0)}$ , therefore the approximation is valid whenever the thickness of the thin wall is smaller than the skin depth so the current can be homogeneous across the conductor. This implies the following restriction for the studied time-scales depending on the wall thickness  $d_w$  and wall resistivity  $\eta_w$

$$\tau \gg \frac{\pi\mu_0 d_w^2}{\eta_w} \quad (2.42)$$

For ITER, the wall thickness is  $d_w = 6$  cm and the vacuum vessel is made of stainless steel which has a resistivity of  $\eta_w \approx 10^{-6}\Omega \text{ m}$ , hence the thin wall approximation is justified whenever the characteristic time-scales  $\tau$  are  $\tau \gg 14$  ms. This is well justified for natural ITER VDEs ( $\tau \sim 1$  s) and also reasonable for ITER mitigated disruptions ( $\tau > 50$  ms). In the cases where  $\tau \ll 14$  ms the wall becomes an ideal conductor as the field cannot penetrate inside it. In the latter case the resistivity can be set to 0 to represent the ideal wall effect. In the intermediate case where  $\tau \sim 14$  ms and the field has partially penetrated the wall, a decreased effective resistivity  $\eta_{\text{eff}} \approx \eta_w \delta_{\text{skin}} / d_w$  needs to be considered.

**Spatial discretization** The walls, coils and passive conductors are represented as 2D surfaces discretised in linear triangular elements. The simplicity of these elements allows to construct complex meshes for the walls including holes and sharp edges like (see figure 2.3 a). The nodes of the elementary triangles are ordered anti-clockwise (see figure 2.3 b). Within

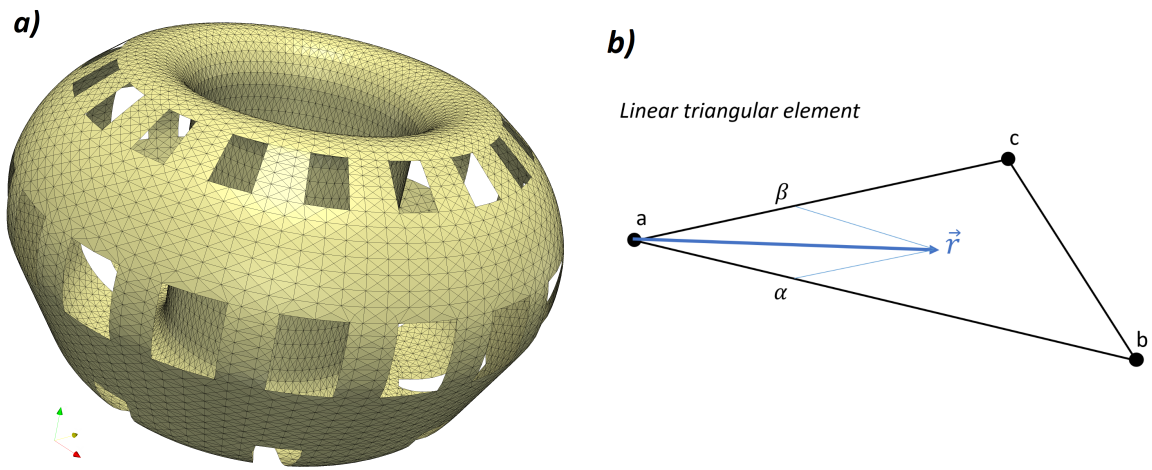


FIGURE 2.3: (a) ITER-like wall discretized in triangular elements. (b) Linear triangular element with local coordinates  $(\alpha, \beta)$ .

an element, the spatial coordinates ( $\mathbf{r}$ ) and variables ( $I$ ) are expressed in terms of the local coordinates ( $\alpha$  and  $\beta$ )

$$\mathbf{r} = \mathbf{r}_a + \alpha \mathbf{r}_{ba} + \beta \mathbf{r}_{ca} \quad (2.43)$$

$$I = I_a + \alpha I_{ba} + \beta I_{ca} \quad (2.44)$$

$$\alpha \geq 0, \beta \geq 0, \alpha + \beta \leq 1 \quad (2.45)$$

where  $I_{fg} = I_f - I_g$  and the subscripts denote the values at the nodes ( $a, b, c$ ).

**The Helmholtz decomposition of currents** As it will be shown in 3.1, when  $\mathbf{B} \cdot \mathbf{n}$  and  $\mathbf{J} \cdot \mathbf{n}$  are provided at the JOREK boundary, all the unknowns of the STARWALL's domain can be reduced to the surface currents  $\mathbf{j}$  flowing in the *wall*. Note that  $\mathbf{j} \equiv \mathbf{J}_{\tan} d_w$  has the dimensions of a linear current density [A/m]. The surface currents are represented in terms of the potentials  $I$  and  $\phi^S$  using the following Helmholtz decomposition

$$\mathbf{j} = \nabla I \times \mathbf{n} - d_w \sigma \nabla \phi^S \quad (2.46)$$

where  $\mathbf{n}$  is a vector perpendicular to the conducting surface and  $\sigma$  is the conductivity. The potential  $I$  is the stream function of the divergence-free eddy currents that are induced by long-range interaction. The second potential  $\phi^S$  is referred to as the source-sink current potential

[Zak+15] and represents the currents originated from the direct sharing of currents between plasma and wall. The second term can have a finite divergence. Note that while  $\nabla \cdot \mathbf{J} = 0$  is always verified, this is no longer true when considering only the tangential components if a normal current penetrates perpendicularly into the conducting surface  $\nabla \cdot \mathbf{j} = -\nabla \cdot (j_n \mathbf{n})$ .

## 2.3 The JOREK-STARWALL coupling

The JOREK-STARWALL coupling was first implemented and used by M. Hoelzl in 2012 [Höl+12]. The implementation was performed for the reduced MHD models and without taking into account halo currents. The coupling presented in this section has been generalized for full MHD models but is still restricted to eddy currents. The general extension with halo currents will be presented in section 3.1 as part of the original work performed during this thesis. In the following sections the boundary conditions at the JOREK-STARWALL interface, the coupling terms and the implicit implementation of the coupling in JOREK are shown.

### Boundary conditions at the JOREK-STARWALL interface

When integrating  $\nabla \cdot \mathbf{B} = 0$  over a small volume over the JOREK-STARWALL interface the continuity of the normal component of the magnetic field is found

$$\mathbf{n} \cdot \mathbf{B}_{\text{JOR}} = \mathbf{n} \cdot \mathbf{B}_{\text{STW}} \quad (2.47)$$

which forms the first boundary condition between JOREK and STARWALL. The second boundary condition is the continuity of the tangential magnetic field

$$\mathbf{n} \times \mathbf{B}_{\text{JOR}} = \mathbf{n} \times \mathbf{B}_{\text{STW}} \quad (2.48)$$

This boundary condition implies that there is no skin current at the interface between the two codes. This assumption is valid when the local thermal energy is small compared to the magnetic energy at the JOREK-STARWALL interface. This is due to the following pressure balance

$$\frac{B_{\text{JOR}}^2}{2\mu_0} + p \approx \frac{B_{\text{JOR}}^2}{2\mu_0} = \frac{B_{\text{STW}}^2}{2\mu_0} \quad (2.49)$$

Similarly to the normal component of the magnetic field, the absence of surface charges ( $\nabla \cdot \mathbf{J} = 0$ ) given by Ampère's law in the low frequency limit implies

$$\mathbf{n} \cdot \mathbf{J}_{\text{JOR}} = \mathbf{n} \cdot \mathbf{J}_{\text{STW}} \quad (2.50)$$

The continuity of the tangential electric field [Jac99] can be also used as a boundary condition for the JOREK plasma velocity

$$\mathbf{n} \times \mathbf{E}_{\text{JOR}} = \mathbf{n} \times \mathbf{E}_{\text{STW}} \quad (2.51)$$

### Coupling term in JOREK

In JOREK, the boundary condition for the magnetic field is implemented as a natural BC in one of the boundary integrals appearing with the finite element method. The BC is a relation between the normal and tangential components of the magnetic field ( $\mathbf{B} \times \mathbf{n} = f(\mathbf{B} \cdot \mathbf{n})$ ) that closes the system of equations. The JOREK coupling term arises from the Faraday-Ohm's law when integrating it by parts. In the full MHD model, equation (2.23) is projected with

the vectorial test function  $\mathbf{A}^*$  and integrated over the volume. The boundary integral appears when integrating the resistive term

$$\int_V \eta \mathbf{A}^* \cdot \mathbf{J} dV = \int_V \eta \mathbf{A}^* \cdot \nabla \times \mathbf{B} dV = \int_V \eta \mathbf{B} \cdot \nabla \times \mathbf{A}^* dV + \int_S \eta (\mathbf{B} \times \mathbf{A}^*) \cdot d\mathbf{S} \quad (2.52)$$

where the vectorial relation  $\mathbf{a} \cdot \nabla \times \mathbf{b} = \nabla \cdot (\mathbf{b} \times \mathbf{a}) + \mathbf{b} \cdot \nabla \times \mathbf{a}$  and the divergence theorem have been used. The boundary term is the term where the JOREK-STARWALL coupling is implemented as a natural boundary condition

$$\int_S \eta (\mathbf{B} \times \mathbf{A}^*) \cdot d\mathbf{S} = - \int_S \eta (\mathbf{B} \times \mathbf{n}) \cdot \mathbf{A}^* dS \quad (2.53)$$

A relation between the tangential component of the magnetic field  $\mathbf{B} \times \mathbf{n}$  and the normal component  $\mathbf{B} \cdot \mathbf{n}$  is provided by STARWALL and once  $\mathbf{B} \times \mathbf{n}$  is replaced by  $f(\mathbf{B} \cdot \mathbf{n})$  the system of equations is closed. For the reduced MHD model, the analogous boundary term appears in the current definition equation (2.10) when multiplying it by the test function  $j^*$  and integrating by parts

$$\int_V \frac{j^*}{R^2} \Delta^* \psi dV = - \int_V \frac{1}{R^2} \nabla j^* \cdot \nabla \psi dV + \int_S \frac{j^*}{R^2} (\nabla \psi \cdot \mathbf{n}) dS \quad (2.54)$$

Here the boundary term is similarly

$$\int_S \frac{j^*}{R^2} (\nabla \psi \cdot \mathbf{n}) = \int_S j^* (\mathbf{B} \times \mathbf{n}) \cdot \nabla \phi dS \quad (2.55)$$

where in this case the normal derivative of the flux has to be replaced by the relation given by STARWALL ( $\nabla \psi \cdot \mathbf{n} = f(\psi)$ ), which is a Robin's like boundary condition.

## Coupling term in STARWALL

In STARWALL, the equations for the currents flowing in the conductors are solved, which need to include the effect of the time-varying magnetic field produced by the plasma. The contribution of the JOREK magnetic field in the STARWALL's equations is included in the integral form of equation (2.39), where the Laplacian operator is inverted by using a Green's function method (see [Jac99]) in order to express the magnetic vector potential in terms of the currents

$$\mathbf{A}(\mathbf{r}) = \frac{\mu_0}{4\pi} \int_{V'} \frac{\mathbf{J}(\mathbf{r}')}{|\mathbf{r}' - \mathbf{r}|} dV' \quad (2.56)$$

where  $\mathbf{r}$  is the position vector. The term in which the JOREK contribution is implemented arises when applying STARWALL's finite element method to equation (2.56). The coupling term appears when multiplying the LHS of (2.56) the vectorial test function  $\mathbf{j}^* \equiv \mathbf{n} \times \nabla I^*$  and integrating it over the JOREK boundary surface

$$\int_S \mathbf{j}^* \cdot \mathbf{A} dS = \int_S (\nabla I^* \times \mathbf{A}) \cdot d\mathbf{S} = - \int_S I^* \mathbf{B} \cdot \mathbf{n} dS \quad (2.57)$$

where the vectorial identity  $\nabla I^* \times \mathbf{A} = \nabla \times (I^* \mathbf{A}) - I^* \nabla \times \mathbf{A}$  and the fact that  $\int_S \nabla \times (I^* \mathbf{A}) \cdot d\mathbf{S} = 0$  in closed surfaces have been used. The JOREK contribution is included into this term by using the continuity of the normal component of the magnetic field  $\mathbf{B} \cdot \mathbf{n} = \mathbf{B}_{\text{JOR}} \cdot \mathbf{n}$ . It should be noted that while equation (2.56) depends on the chosen gauge for the vector potential, the coupling term (2.57) is independent of this choice. Hence the vector potential can be directly plugged into the coupling term regardless of the chosen gauge in JOREK

$$\int_S \mathbf{j}^* \cdot \mathbf{A} dS = \int_S \mathbf{j}^* \cdot \mathbf{A}_{\text{JOR}} dS \quad (2.58)$$

## Implementation of the coupling in JOREK

The coupling must be implemented in JOREK respecting the implicit time scheme. The *wall* currents shouldn't be considered explicitly as they are instantaneously given by the changes of the magnetic field which in turn is affected by the *wall* currents. In the discretized form, the tangential field  $\mathbf{B}_{\tan} \equiv \mathbf{B} \times \mathbf{n}$  is provided by STARWALL as a function of the *wall* current potentials  $Y$  and the magnetic vector potential  $\mathbf{A}$  at the JOREK boundary

$$\mathbf{B}_{\tan,i} = \sum_k \mathbf{M}_{ik}^{ey} Y_k + \sum_l \sum_j \mathbf{M}_{ij,l}^{\parallel e} A_{l,j} \quad (2.59)$$

where the indices  $i$  and  $j$  label the degrees of freedom along the JOREK boundary, the index  $l$  runs over the 3 components of  $\mathbf{A}^{bnd}$  and the index  $k$  runs over all the degrees of freedom of the *wall* current potentials in the STARWALL's domain. The response matrices " $\mathbf{M}$ " are the geometrical coefficients that include the integrals of the Green's functions, the computational task of STARWALL is to calculate these matrices which are imported by JOREK at the beginning of the simulation. The evolution of the *wall* current potentials is derived from the Faraday-Ohm's law (see section 3.1)

$$\dot{Y}_k = -M_{kk}^{yy} Y_k + \sum_l \sum_j M_{kj,l}^{ye} \dot{A}_{l,j} \quad (2.60)$$

where the dot denotes the time derivative. By using the time stepping scheme presented in (2.35) for equation (2.60), the change of the current potentials  $\delta Y_k$  can be directly expressed in terms of the variables at previous time "n"

$$\delta Y_k^n = \sum_l \sum_j \hat{A}_{kj,l} \delta A_{l,j}^n + \hat{B}_{kk} Y_k^n + \hat{C}_{kk} Y_k^{n-1} + \sum_l \sum_j \hat{D}_{kj,l} \delta A_{l,j}^{n-1} \quad (2.61)$$

where the matrices with the symbol " $\hat{\cdot}$ " are combinations of the response matrices  $M$  (see appendix C.3). When discretizing the tangential field in time as  $\mathbf{B}_{\tan}^{n+1} = \mathbf{B}_{\tan}^n + \delta \mathbf{B}_{\tan}^n$  and equations (2.59) and (2.60) are used we obtain

$$\mathbf{B}_{\tan,i}^{n+1} = \sum_l \sum_j \hat{\mathbf{E}}_{ij,l} \delta A_{l,j}^n + \hat{\mathbf{F}}_{ik} Y_k^n + \hat{\mathbf{G}}_{ik} Y_k^{n-1} + \sum_l \sum_j \hat{\mathbf{H}}_{ij,l} \delta A_{l,j}^{n-1} \quad (2.62)$$

where the matrices with the symbol " $\hat{\cdot}$ " are similarly derived from the response matrices. Finally the expression (2.62) is plugged into the boundary integral (2.53), which is now expressed only in terms of the JOREK variables  $\delta \mathbf{u}^n$  and the wall currents of the previous time-step  $Y^n$ . Once the system of equations for  $\delta \mathbf{u}$  is solved, the change in the *wall* current potentials  $\delta Y_k$  is calculated with the solution of  $\delta \mathbf{A}$  by using the equation (2.61). Afterwards the value of the wall currents is updated with  $Y^{n+1} = Y^n + \delta Y^n$ . This completes the implementation of the implicit natural boundary conditions for the magnetic field including thin resistive walls in JOREK.

# Chapter 3

## Free-boundary theory and methods for JOREK-STARWALL

The present chapter exposes the main developments that have been implemented in JOREK-STARWALL during this PhD. In the first section a derivation of the STARWALL's equations and matrices is developed in detail. The derivation is a generalization of the eddy current formulation presented in [MS15] which now includes source/sink (*halo*) currents. The computation of free-boundary equilibria has been an important part of the present work and it is discussed in section 3.2. In particular the used methods to compute the equilibria are shown together with an example of the reconstruction of an experimental plasma. Finally a technique to find the optimal coil currents for an arbitrary axisymmetric equilibrium is presented in section 3.3 and a method to impose coil currents over time implicitly is explained in section 3.4.

### 3.1 STARWALL's general derivation

The exact form of the STARWALL's equations and discrete matrices was derived in the literature with a variational principle. When dealing with dissipative systems the formulation of equations with variational principles becomes normally very problematic. In the derivation performed in [MS15], these problems were avoided by formulating the problem linearly and thus assuming the exponential time dependence  $e^{\gamma t}$ . As JOREK is inherently non-linear, a more intuitive and general derivation has been developed during this thesis. The more general derivation that is presented in the following sections includes *halo* currents and is valid for full MHD models. The exposed derivation is done in SI units and the final form of the equations is converted into JOREK units.

#### 3.1.1 Formulation of the STARWALL's equations

As mentioned in the previous chapter, STARWALL is a code that provides the tangential field ( $\mathbf{B}_{tan}$ ) in the JOREK boundary given the normal field component ( $\mathbf{B} \cdot \mathbf{n}$ ) and the normal current ( $\mathbf{J} \cdot \mathbf{n}$ ). The relation between these components is found by solving the system of equations (2.38)-(2.41). As it will be shown below, the system of equations is reduced to a system of equations for currents flowing on different structures, where ( $\mathbf{B} \cdot \mathbf{n}$ ) and ( $\mathbf{J} \cdot \mathbf{n}$ ) at the JOREK boundary act as sources for these currents. Once the currents in all the domain are known in terms of ( $\mathbf{B} \cdot \mathbf{n}$ ) and ( $\mathbf{J} \cdot \mathbf{n}$ ), the ( $\mathbf{B}_{tan}$ ) relation can be found by using Biot-Savart's law.

The first step in the derivation is to express the magnetic vector potential in terms of the

electric currents. In order to do that, Ampère's law is inverted by using a Green's function method

$$\nabla^2 \mathbf{A} = -\mu_0 \mathbf{J} \quad \rightarrow \quad \mathbf{A}(\mathbf{r}) = \frac{\mu_0}{4\pi} \int_V \frac{\mathbf{J}(\mathbf{r}')}{|\mathbf{r} - \mathbf{r}'|} d^3 \mathbf{r}' \quad (3.1)$$

where  $\mathbf{J}(\mathbf{r}')$  is the current density flowing at the  $\mathbf{r}'$  position. The inversion of this equation is possible thanks to the choice of the **Coulomb gauge** ( $\nabla \cdot \mathbf{A} = 0$ ).

In principle, the integral appearing on equation (3.1) should be performed over all the volume of the JOREK's domain together with the STARWALL's domain. However, **the JOREK's domain volume integral is replaced by a surface integral on the JOREK's boundary, in which a virtual surface current ( $\mathbf{j}_c$ ) flows**. This property can be used without any approximation thanks to the the virtual-casing principle [SZ72], which shows that if there is a closed volume ( $V_c$ ) containing electric currents, the magnetic field outside  $V_c$  produced by those currents can be computed with a surface integral over the boundary of the enclosing the volume

$$\mathbf{A}_c(\mathbf{r}^{ext}) = \frac{\mu_0}{4\pi} \int_{V_c} \frac{\mathbf{J}_c(\mathbf{r}')}{|\mathbf{r}^{ext} - \mathbf{r}'|} d^3 \mathbf{r}' = \frac{\mu_0}{4\pi} \int_{S_c} \frac{\mathbf{j}_c(\mathbf{r}')}{|\mathbf{r}^{ext} - \mathbf{r}'|} dS' \quad (3.2)$$

where the  $\mathbf{A}_c$  is the contribution of the volume  $V_c$  to the magnetic vector potential at the position  $\mathbf{r}^{ext}$  lying outside  $V_c$ . Note here that the virtual currents  $\mathbf{j}_c$  have the dimensions of a linear current density [A/m]. As it will be shown, the virtual currents don't need to be explicitly calculated because they disappear naturally from the formulation as they can be written in terms of  $\mathbf{B} \cdot \mathbf{n}$  at the boundary. The virtual-casing principle can be easily demonstrated with the following physical example

*Let's assume that a magnet capable of producing an arbitrary field ( $\mathbf{B}_{magnet}$ ) is enclosed by a perfectly conducting and infinitely thin wall. If the magnet is switched on at a specific moment in time, the conducting wall will create mirror currents so the magnetic field outside the wall remains unchanged. If the initial field outside the wall was zero, it will remain zero, so  $\mathbf{B}_{ext} = \mathbf{B}_{magnet} + \mathbf{B}_{wall} = 0$  and therefore  $\mathbf{B}_{magnet} = -\mathbf{B}_{wall}$ . This means that the currents flowing on the thin wall are able to produce the same magnetic field as the magnet ( $\mathbf{B}_{magnet}$ ) outside the wall, as the magnet produces an arbitrary magnetic field, this demonstrates the virtual-casing principle.*

Apart from the JOREK boundary, all the conducting structures in the STARWALL's domain are represented as well with infinitely thin surfaces due to the thin wall approximation (see section 2.2). The problem is finally defined in terms of infinitely thin surfaces that are separated by vacuum regions and that interact through changes on the magnetic field.

## Evolution equations for the eddy currents

The so-called eddy currents are currents flowing in closed loops within conductors which are induced due to changes on the magnetic field. The evolution equation of these currents is given by Faraday's law, which can be written in terms of the electromagnetic potentials ( $\Phi, \mathbf{A}$ )

$$\nabla \times \mathbf{E} = -\partial_t \mathbf{B} \quad \rightarrow \quad \mathbf{E} = -\partial_t \mathbf{A} - \nabla \Phi \quad (3.3)$$

By plugging the expression for the vector potential (3.1) into equation (3.3), we obtain the following equation for the eddy currents

$$\partial_t \mathbf{A} = -(\mathbf{E} + \nabla \Phi) = \frac{\mu_0}{4\pi} \int_V \frac{\partial_t \mathbf{J}(\mathbf{r}')}{|\mathbf{r} - \mathbf{r}'|} d^3 \mathbf{r}' \quad (3.4)$$

In order to complete the system of equations, Ohm's law is used in the *wall*'s domain for the electric field and at the JOREK-STARWALL interface the magnetic vector potential  $\mathbf{A}_p$  is given

$$\text{At JOREK-STARWALL boundary } S_p : \quad \mathbf{A} = \mathbf{A}_p \quad (3.5)$$

$$\text{At } wall \text{ surface } S_w : \quad \mathbf{E}_w = \eta_w \mathbf{J}_w = \frac{1}{\sigma_w d_w} \mathbf{j}_w, \quad \nabla \Phi = \nabla \Phi_w \quad (3.6)$$

In the following, the subscripts *p* (plasma) and *w* (*wall*) respectively indicate that the quantity is evaluated at the JOREK-STARWALL boundary and at the *wall* surface. We remind that the notation *wall* represents all the conducting structures of the system including the coils as they are described with the same formalism. In the case of a coil, the electric potential  $\Phi_w$  is typically an externally applied voltage. We remind as well that  $\sigma$  stands for the electrical conductivity and that  $d$  stands for the thickness of the thin structure. In expression (3.6) the thin wall approximation has been used allowing to write  $\mathbf{J} = \mathbf{j}/d$  where  $[\mathbf{j}] = A/m$ .

By using the thin wall approximation and the virtual-casing principle, the volume integral appearing in equation (3.4) can be written as

$$\int_V \frac{\partial_t \mathbf{J}(\mathbf{r}')}{|\mathbf{r} - \mathbf{r}'|} d^3 \mathbf{r}' = \sum_{i=1}^{N_{\text{surf}}} \int \frac{\partial_t \mathbf{j}_i(\mathbf{r}')}{d_i |\mathbf{r} - \mathbf{r}'|} dS'_i dl'_{\perp,i} \approx \sum_{i=1}^{N_{\text{surf}}} \int \frac{\partial_t \mathbf{j}_i(\mathbf{r}')}{|\mathbf{r} - \mathbf{r}'|} dS'_i \quad (3.7)$$

where the volume integral is decomposed as a sum of  $N_{\text{surf}}$  surface integrals after integrating over the direction perpendicular to the surfaces ( $dl_{\perp}$ ). When the expression (3.7) is used in equations (3.4)-(3.6), the equations describing the eddy currents finally are

$$\mathbf{A}_p = \frac{\mu_0}{4\pi} \sum_{i=1}^{N_{\text{surf}}} \int \frac{\mathbf{j}_i(\mathbf{r}')}{|\mathbf{r} - \mathbf{r}'|} dS'_i \quad (3.8)$$

$$-\frac{\mathbf{j}_w}{\sigma_w d_w} - \nabla \Phi_w = \frac{\mu_0}{4\pi} \sum_{i=1}^{N_{\text{surf}}} \int \frac{\partial_t \mathbf{j}_i(\mathbf{r}')}{|\mathbf{r} - \mathbf{r}'|} dS'_i \quad (3.9)$$

### Evolution equation for the *halo* currents

The plasma can share current with the conducting structures by direct contact, we will refer to these currents as *halo* currents. The *halo* currents are modelled with the source/sink potentials presented in 2.2. The equation governing the *halo* currents is simply the absence of charge accumulation implying the free-divergence condition

$$\nabla \cdot \mathbf{J} = 0 \quad (3.10)$$

When separating the current density into a tangential and a normal component to the wall, the latter equation is

$$\nabla \cdot \mathbf{J}_{\tan} = -\nabla \cdot \mathbf{J}_n \approx \frac{\mathbf{n} \cdot \mathbf{J}|_{\text{inner},w} - \mathbf{n} \cdot \mathbf{J}|_{\text{outer},w}}{d_w} = \frac{\mathbf{n} \cdot \mathbf{J}|_{\text{inner},w}}{d_w} \quad (3.11)$$

where the thin wall approximation has been used in order to approximate the normal derivative of the normal current as well as the condition that no current is escaping the wall at its outer boundary ( $\mathbf{n} \cdot \mathbf{J}|_{\text{outer},w} = 0$ ). Note that the normal vector ( $\mathbf{n}$ ) points from the plasma side towards the wall exterior. By using the Helmholtz decomposition for the tangential currents (see section 2.2), equation (3.11) is simply a 2D Poisson equation for the currents

$$\nabla \cdot (\sigma_w d_w \nabla \phi^s) = -\mathbf{n} \cdot \mathbf{J}|_{\text{inner},w} = -\mathbf{n} \cdot \mathbf{J}|_{\text{plasma}} \quad (3.12)$$

where the continuity of normal current between plasma and wall has been used. It's worth noticing that this equation is decoupled from the eddy currents equation. Therefore when the normal current is provided, this equation can be solved independently of the eddy currents. Nevertheless the source/sink currents will affect the magnetic field and the eddy currents, which in turn will determine the normal current as shown in figure 3.1.

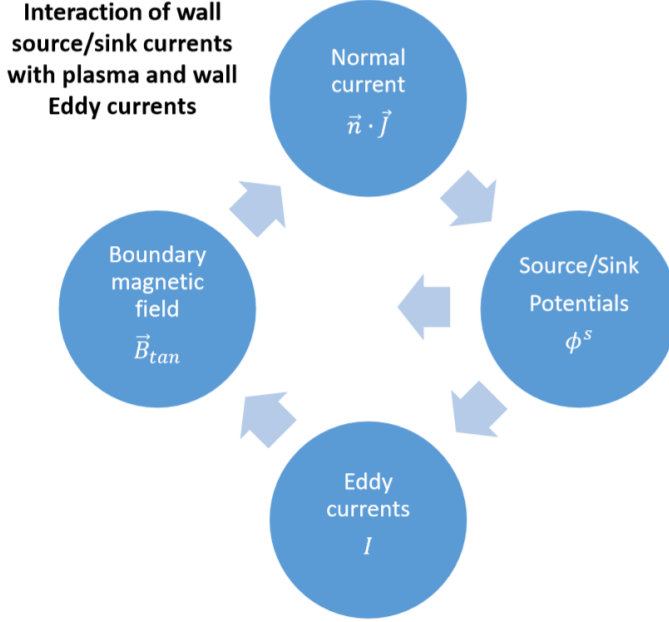


FIGURE 3.1: Scheme showing the interaction of the source/sink wall currents with the wall eddy currents and the plasma.

### 3.1.2 The weak form

For the equation of the source/sink currents, the weak form is obtained by multiplying (3.12) with the test function  $\phi^*$  and integrating it over the wall surface ( $S_w$ )

$$\begin{aligned} \int \phi^* \nabla \cdot (\sigma_w d_w \nabla \phi^s) dS_w &= - \int \sigma_w d_w \nabla \phi^* \cdot \nabla \phi^s dS_w + \oint_{S_w} \sigma_w d_w \phi^* (\mathbf{n} \times \nabla \phi^s) \cdot d\mathbf{l} = \\ &= - \int \phi^* J_\perp dS_w \end{aligned} \quad (3.13)$$

where integration by parts has been used and  $J_\perp \equiv \mathbf{n} \cdot \mathbf{J}|_{\text{plasma}}$ . The contour integral takes into account the external voltage applied to the edges of the wall and vanishes when there is no source/sink of the current through the edges as occurs in most of the cases. For closed tori, the contour integral formally vanishes and the final weak form is

$$\int \sigma_w d_w \nabla \phi^* \cdot \nabla \phi^s dS_w = \int \phi^* J_\perp dS_w \quad (3.14)$$

The weak form of the eddy current equation associated with the virtual currents is obtained by performing the scalar product of equation (3.9) with the test function  $\mathbf{j}_p^* \equiv \nabla I_p^* \times \mathbf{n}_p$  and integrating it over the JOREK-STARWALL boundary surface

$$\int \mathbf{j}_p^* \cdot \mathbf{A}_p dS_p = \frac{\mu_0}{4\pi} \sum_{i=1}^{N_{\text{surf}}} \int \int \frac{\mathbf{j}_p^* \cdot \mathbf{j}_i(\mathbf{r}')}{|\mathbf{r} - \mathbf{r}'|} dS'_i dS_p \quad (3.15)$$

As demonstrated in section 2.3, the LHS term of the latter equation is independent of the chosen electromagnetic gauge and can be written in terms of  $(\mathbf{B} \cdot \mathbf{n})$ . Similarly the equation for

the *wall* Eddy currents (3.9) is projected with the test function  $\mathbf{j}_w^* \equiv \nabla I_w^* \times \mathbf{n}_w$  and integrated over the respective *wall* surface

$$-\int \frac{1}{\sigma_w d_w} \mathbf{j}_w^* \cdot \mathbf{j}_{w,I} dS_w - \oint_{S_w} (\Phi_w - \phi^s) \nabla I_w^* \cdot d\mathbf{l} = \frac{\mu_0}{4\pi} \sum_{i=1}^{N_{\text{surf}}} \iint \frac{\mathbf{j}_w^* \cdot \partial_t \mathbf{j}_i(\mathbf{r}')}{|\mathbf{r} - \mathbf{r}'|} dS'_i dS_w \quad (3.16)$$

where  $\mathbf{j}_{w,I} \equiv \nabla I_w \times \mathbf{n}_w$ . Note that the contour integral appears when applying the Stoke's theorem and the vectorial relation  $(\nabla I^* \times \mathbf{n}_w) \cdot \nabla \Phi = \nabla \times (\Phi \nabla I^*) \cdot \mathbf{n}_w$ . As mentioned for the source/sink currents, the contour integral over the wall edges will usually vanish, however in the case of a coil the contour integral simply becomes an external imposed voltage  $U$ .

### 3.1.3 Matrix form

The weak form of the equations presented in the latter section is valid for any type of discretization used for the thin surfaces. In this section a detailed description of the STARWALL's discretization and the choice of test functions is given. The aim of the following section is to be able to write the equations in a matrix form as the key feature of STARWALL is the computation and manipulation of the resulting matrices.

The torus shaped walls that will represent tokamak vacuum vessels and the JOREK boundary are described in STARWALL with the global coordinates  $(u, v)$ . The coordinate  $u$  is an angular coordinate running over the poloidal direction and  $v$  running over the toroidal direction as shown in figure 3.2. Both coordinates are normalised such that an increase of  $\Delta u = 1$  corresponds to one poloidal turn and  $\Delta v = 1$  corresponds to one toroidal turn.

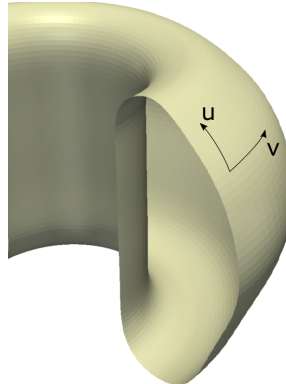


FIGURE 3.2: Scheme showing the angular coordinates describing the torus shaped surfaces.

The global  $(u, v)$  coordinates are mapped into the local coordinates describing the triangular elements (see figure 2.3) where the position and the potentials are linearly interpolated

$$\mathbf{r} = \mathbf{r}_a + \alpha \mathbf{r}_{ba} + \beta \mathbf{r}_{ca} \quad (3.17)$$

$$I = I_a + \alpha I_{ba} + \beta I_{ca} \quad (3.18)$$

$$\phi^s = \phi_a^s + \alpha \phi_{ba}^s + \beta \phi_{ca}^s \quad (3.19)$$

$$\alpha \geq 0, \beta \geq 0, \alpha + \beta \leq 1 \quad (3.20)$$

and  $I_{fg} \equiv I_f - I_g$  where the subscripts denote the values at the nodes  $(a, b, c)$  of the triangle.

For poloidally and toroidally closed surfaces, net current potentials must be added to the single-valued periodic  $I_s(u, v)$  potentials describing the eddy currents. The requirement of these extra potentials comes from the fact that an integral over a closed path of a function of

the form  $\nabla I_s$  vanishes when  $I_s$  is periodic. On a rectangular mesh with  $n_u$  poloidal and  $n_v$  toroidal meshpoints, the total potential  $I$  at the node  $(u_i, v_j)$  can be decomposed as

$$I(u_i, v_j) = I^T u_i + I^P v_j + I_s(u_i, v_j) \quad (3.21)$$

where  $I^T$  and  $I^P$  are the net-toroidal and net-poloidal currents and

$$(u_i, v_j) = \left( \frac{i-1}{n_u}, \frac{j-1}{n_v} \right) \quad (3.22)$$

where  $i = 1, \dots, n_u + 1$  and  $j = 1, \dots, n_v + 1$ . The chosen dependence for the net current potentials is  $I^{\text{net}} = I^T u + I^P v$  such that

$$\mathbf{I}_\phi^{\text{net}} = \oint_0^1 \mathbf{j}_\phi^{\text{net}} dl_u = \oint_0^1 I^T (\mathbf{n} \times \nabla u) \frac{du}{|\nabla u|} = I^T \mathbf{e}_\phi \quad (3.23)$$

$$\mathbf{I}_\theta^{\text{net}} = \oint_0^1 \mathbf{j}_\theta^{\text{net}} dl_v = \oint_0^1 I^P (\mathbf{n} \times \nabla v) \frac{dv}{|\nabla v|} = I^P \mathbf{e}_\theta \quad (3.24)$$

where  $\mathbf{e}_\phi$  and  $\mathbf{e}_\theta$  are respectively the toroidal and poloidal normalized basis vectors.

In the case where the wall is not toroidally (poloidally) closed,  $I^T$  ( $I^P$ ) are given by the difference of the current potential value at the two boundaries of the wall. When applying the spatial discretization presented above to the definition of the STARWALL current (2.46), the total form of the current density on a triangle has the following expression

$$\mathbf{j}_\Delta = \frac{I_a \mathbf{r}_{cb} + I_b \mathbf{r}_{ac} + I_c \mathbf{r}_{ba}}{2S} + \sigma_w d_w \left( \frac{\phi_a^s \mathbf{r}_{cb} + \phi_b^s \mathbf{r}_{ac} + \phi_c^s \mathbf{r}_{ba}}{2S} \right) \times \mathbf{n} \quad (3.25)$$

where  $S \equiv |\mathbf{r}_{ba} \times \mathbf{r}_{ac}|/2$  is the surface of the triangle and  $\mathbf{n} = (\mathbf{r}_{ba} \times \mathbf{r}_{ac})/2S$ . Note that in the case of the JOREK boundary or a coil surface the source/sink potentials are not included ( $\phi^s = 0$ ). It's convenient to write the latter expression in terms of the basis vectors  $\mathbf{e}_i$  associated to the triangle node  $i$

$$\mathbf{j}_\Delta = \sum_{i=1}^3 (I_i \mathbf{e}_i + \sigma_w d_w \phi_i^s \mathbf{e}_i \times \mathbf{n}) \quad (3.26)$$

where the basis vectors have been defined as

$$\mathbf{e}_1 = \frac{\mathbf{r}_{cb}}{2S}, \quad \mathbf{e}_2 = \frac{\mathbf{r}_{ac}}{2S}, \quad \mathbf{e}_3 = \frac{\mathbf{r}_{ba}}{2S} \quad (3.27)$$

With this discretization the current density is constant over each triangle and the total surface integrals can be decomposed as sums of triangle integrals

$$\int \frac{\partial_t \mathbf{j}(\mathbf{r}')}{|\mathbf{r} - \mathbf{r}'|} dS' = \sum_{m=1}^{N_\Delta} \int_{\Delta_m} \frac{\partial_t \mathbf{j}_{\Delta_m}(\mathbf{r}')}{|\mathbf{r} - \mathbf{r}'|} dS' = \sum_{m=1}^{N_\Delta} \partial_t \mathbf{j}_{\Delta_m} \int_{\Delta_m} \frac{1}{|\mathbf{r} - \mathbf{r}'|} dS' \quad (3.28)$$

where  $N_\Delta$  is the the number of triangles. The numerical integration scheme for the surface integrals  $\int_{\Delta_m} dS'/|\mathbf{r} - \mathbf{r}'|$  is shown in detailed in [MS15]. For the eddy currents, the global test function  $\mathbf{j}_q^* \equiv \nabla I_q^* \times \mathbf{n}$  associated with the independent variable at node  $q$  is the ensemble of basis vectors involving the  $q$  node

$$\mathbf{j}_q^* = \bigcup_{k=1}^{N_\Delta} \mathbf{e}_q|_k \quad (3.29)$$

where  $\mathbf{e}_q|_k$  is the basis vector defined in (3.27) belonging to the triangle  $k$  and associated with the node  $q$ . Similarly, the global test function for the source/sink current potentials is

$$\phi_q^* = \bigcup_{k=1}^{N_\Delta} b_q|_k \quad (3.30)$$

where  $b_q|_k$  are the shaping functions  $(1 - \alpha - \beta, \alpha, \beta)$  presented in 3.20.

When applying the presented spatial discretization and using the previous definition for the test functions, equations (3.14), (3.15) and (3.16) can be written in the following matrix form

$$M_{SS}\phi^s = M_{SJ}\mathbf{J}_\perp \quad (3.31)$$

$$M_{pp}\mathbf{I}^p + M_{pw}\mathbf{I}^w + M_{ps}\phi^s = \sum_l^3 M_{pe,l}\mathbf{A}_{p,l}^e/\mu_0 \quad (3.32)$$

$$M_{wp}\dot{\mathbf{I}}^p + M_{ww}\dot{\mathbf{I}}^w + M_{ws}\dot{\phi}^s = -R_{ww}\mathbf{I}^w/\mu_0 \quad (3.33)$$

where the  $M$  symbol denotes the geometrical matrices specified in the appendix B.2,  $\phi^s$  is a vector listing the degrees of freedom of the *wall* source/sink potentials,  $\mathbf{I}^p$  lists the degrees of freedom of the virtual eddy current potentials at the JOREK boundary,  $\mathbf{I}^w$  lists the degrees of freedom of the *wall* eddy currents and  $\mathbf{A}_{p,l}^e$  contains a list of the involved degrees of freedom of the component  $l$  of the vector potential  $\mathbf{A}_p$  at the JOREK boundary. Note that  $M_{pp}\mathbf{I}^p$  is the short form of the following matrix multiplication  $M_{pp}\mathbf{I}^p \equiv \sum_l M_{k,l}^{pp} I_l^p$ .

## Reduction of the equations and similarity transform

The linearity of the equations (3.31) and (3.32) allows to express the source/sink potentials in terms of the normal current  $\mathbf{J}_\perp$  as well as the virtual current potentials in terms of the other variables

$$\phi^s = M_{SS}^{-1}M_{SJ}\mathbf{J}_\perp \quad (3.34)$$

$$\mathbf{I}^p = M_{pp}^{-1} \left( -M_{pw}\mathbf{I}^w - M_{ps}\phi^s + \sum_l M_{pe,l}\mathbf{A}_{p,l}^e/\mu_0 \right) \quad (3.35)$$

When using the latter expressions in the *wall* eddy currents equation (3.33), the *wall* potentials are written in terms of the plasma magnetic field and normal current at the JOREK boundary

$$\tilde{M}_{ww}\dot{\mathbf{I}}^w = -R_{ww}\mathbf{I}^w/\mu_0 - \sum_l^3 \tilde{M}_{we,l}\dot{\mathbf{A}}_{p,l}^e/\mu_0 - \tilde{M}_{wJ}\mathbf{J}_\perp \quad (3.36)$$

where we have defined the following matrices

$$\tilde{M}_{ww} \equiv M_{ww} - M_{wp}M_{pp}^{-1}M_{pw} \quad (3.37)$$

$$\tilde{M}_{we,l} \equiv M_{wp}M_{pp}^{-1}M_{pe,l} \quad (3.38)$$

$$\tilde{M}_{wJ} \equiv \left( M_{ws} - M_{wp}M_{pp}^{-1}M_{ps} \right) M_{SS}^{-1}M_{SJ} \quad (3.39)$$

Finally a similarity transform can be applied to the system (3.36) in order to define the set of normal variables  $\mathbf{Y}$

$$\mathbf{I}^w \equiv \begin{pmatrix} \mathbf{I}^{\text{coils}} \\ \mathbf{I}^{\text{wall}} \end{pmatrix} = S\mathbf{Y} \quad (3.40)$$

such that

$$S^T \tilde{M}_{ww} S = D \quad \text{and} \quad S^T R_{ww} S = I_d \quad (3.41)$$

where  $D$  is a diagonal matrix and  $I_d$  is the identity matrix. The matrix  $S$  can be found by solving the general eigenvalue problem  $\tilde{M}_{ww}\mathbf{x} = \lambda R_{ww}\mathbf{x}$  and it's constructed by writing the found eigenvectors in columns. By applying the similarity transform, the equation for the *wall* currents reads

$$\mu_0 \dot{\mathbf{Y}} = -M_{yy} \mathbf{Y} - \sum_l^3 M_{ye,l} \dot{\mathbf{A}}_{p,l}^e - \mu_0 M_{yJ} \mathbf{J}_\perp \quad (3.42)$$

where the following matrices have been defined

$$M_{yy} \equiv D^{-1} \quad (3.43)$$

$$M_{ye,l} \equiv D^{-1} S^T \tilde{M}_{we,l} \quad (3.44)$$

$$M_{yJ} \equiv D^{-1} S^T \tilde{M}_{wJ} \quad (3.45)$$

Finally when performing the following JOREK normalization

$$\begin{aligned} t_{SI} &= t \sqrt{\mu_0 \rho_0} \\ \mathbf{Y}_{SI} &= \mathbf{Y} / \mu_0 \\ \sigma_{SI} &= \sigma \sqrt{\rho_0 / \mu_0} \\ \mathbf{J}_{\perp,SI} &= \mathbf{J}_\perp / \mu_0 \end{aligned}$$

the final form for the *wall* Eddy currents equation is

$$\dot{\mathbf{Y}} = -M_{yy} \mathbf{Y} - \sum_l^3 M_{ye,l} \dot{\mathbf{A}}_{p,l}^e - M_{yJ} \mathbf{J}_\perp$$

(3.46)

### 3.1.4 $\mathbf{B} \times \mathbf{n}$ at the JOREK boundary

The tangential magnetic field at the JOREK boundary is found by applying the curl operator to equation (3.1) and the vectorial product with the normal vector  $\mathbf{n}$

$$\mathbf{B}_{tan} \equiv \mathbf{B} \times \mathbf{n} = \frac{\mu_0}{4\pi} \mathbf{n} \times \sum_{i=1}^{N_{surf}} \sum_{m=1}^{N_{\Delta_i}} \mathbf{j}_{i,\Delta_m} \times \nabla \int_{\Delta_m} \frac{1}{|\mathbf{r} - \mathbf{r}'|} dS'_i \quad (3.47)$$

When performing the surface integrals at the JOREK boundary and at the *wall* surface,  $\mathbf{B}_{tan}$  is written in terms of the current potentials

$$\mathbf{B}_{tan} / \mu_0 = \mathbf{M}_{\parallel w} \mathbf{I}^w + \mathbf{M}_{\parallel p} \mathbf{I}^p + \mathbf{M}_{\parallel s} \boldsymbol{\phi}^s \quad (3.48)$$

where the following matrices have been defined in appendix B.2 and the bold symbols " $\mathbf{M} = (M_R, M_Z, M_\phi)$ " represent a list matrices for each component of the magnetic field. By replacing the plasma current potentials with expression (3.35), equation (3.48) becomes

$$\mathbf{B}_{tan} / \mu_0 = \tilde{\mathbf{M}}_{\parallel w} \mathbf{I}^w + \sum_l^3 \mathbf{M}_{\parallel e,l} \mathbf{A}_{p,l}^e / \mu_0 + \mathbf{M}_{\parallel J} \mathbf{J}_\perp \quad (3.49)$$

where the new matrices are

$$\tilde{\mathbf{M}}_{\parallel w} \equiv \mathbf{M}_{\parallel w} - \mathbf{M}_{\parallel p} M_{pp}^{-1} M_{pw} \quad (3.50)$$

$$\mathbf{M}_{\parallel e,l} \equiv \mathbf{M}_{\parallel p} M_{pp}^{-1} M_{pe,l} \quad (3.51)$$

$$\mathbf{M}_{\parallel J} \equiv (\mathbf{M}_{\parallel s} - \mathbf{M}_{\parallel p} M_{pp}^{-1} M_{ps}) M_{SS}^{-1} M_{SJ} \quad (3.52)$$

After applying the JOREK normalization and using the similarity transform we finally have

$$\mathbf{B}_{\tan} = \mathbf{M}_{ey} \mathbf{Y} + \sum_l^3 \mathbf{M}_{\parallel e,l} \mathbf{A}_{p,l}^e + \mathbf{M}_{\parallel J} \mathbf{J}_{\perp}$$

(3.53)

where

$$\mathbf{M}_{ey} \equiv \tilde{\mathbf{M}}_{\parallel w} S \quad (3.54)$$

As a last step, the function  $\mathbf{B}_{\tan}$  is projected into the Bézier space for implementing the expression in JOREK. Finally equations (3.46) and (3.53) are sufficient for closing the system of MHD equations and are implemented through natural boundary conditions as explained in section 2.3.

## 3.2 Computation of free-boundary equilibria

The first step required for a simulation that includes free-boundary conditions for the axisymmetric mode is to compute a free-boundary equilibrium that is consistent with equations (3.46) and (3.53). Note that the BCs are imposed independently for each mode in JOREK, and therefore it is still possible to study the free-boundary evolution of asymmetric modes ( $n \neq 0$ ) while using Dirichlet BCs for the axisymmetric mode ( $n=0$ ). Even if the latter case is interesting for the study of resistive wall modes (RWMS), instabilities such as the VDEs and the simulation of vertical vertical kicks require the free-boundary treatment for the  $n=0$  mode and thus a free-boundary equilibrium. The solution of the Grad-Shafranov equation with free-boundary conditions has been extensively studied in the literature as it's an essential part of well known equilibrium reconstruction codes such as EFIT [Lao+85]. In this section the method used during this thesis and its associated difficulties are presented.

### 3.2.1 Picard iterations and FEM

The Grad-Shafranov (GS) equation is typically solved with the Picard iterations method. The Picard iterations avoid the problem of the non-linearities of the GS equation by using the value of the poloidal flux of the previous iteration  $\psi^n$  in the RHS

$$\Delta^* \psi^{n+1} = j(\psi^n) \quad (3.55)$$

where  $j(\psi) \equiv -RJ_\phi = -\mu_0 R^2 p'(\psi) - FF'(\psi)$  is the normalized toroidal current. The initial condition is typically provided with a prescribed set of nested flux surfaces positioned at the center of the computational mesh. The Picard iterations are interrupted when the difference between the old and new solution is smaller than the specified tolerance  $\epsilon_{tol}$

$$\varepsilon_{diff} \equiv \frac{\|\psi^{n+1} - \psi^n\|}{\|\psi^n\|} < \epsilon_{tol} \quad (3.56)$$

where the norm is defined as  $\|\psi\| = \int_S \psi^2 dS$ .

The approach that is used in JOREK for solving the GS equation is similar to the approach used in the HELENA code [HGK91] where the convergence rate of the solution is of fourth

order on the grid size for  $\psi$  and third order for  $\nabla\psi$ . The difference between both codes lies on the different choice of the spatial discretization, where JOREK uses the Bézier elements presented in 2.1.2 and HELENA uses isoparametric bicubic Hermite elements. The Galerkin FEM method is applied to the GS equation as well by multiplying it by the test function  $\psi^*$  and integrating over the computational volume

$$\int_V \frac{\psi^*}{R^2} \Delta^* \psi^{n+1} dV = - \int_V \frac{1}{R^2} \nabla \psi^* \cdot \nabla \psi^{n+1} dV + \int_S \frac{\psi^*}{R^2} \nabla \psi^{n+1} \cdot \mathbf{n} dS = \int_V \frac{\psi^* j(\psi^n)}{R^2} dV \quad (3.57)$$

The latter equation can be directly iterated until a solution is found. Nevertheless the GS equation can be written as well in its perturbative form by using  $\psi^{n+1} \equiv \psi^n + \delta\psi^n$

$$\int_V \frac{1}{R^2} \nabla \psi^* \cdot \nabla \delta\psi^n dV - \int_S \frac{\psi^*}{R^2} \nabla \delta\psi^n \cdot \mathbf{n} dS = - \int_V \frac{\psi^* j(\psi^n)}{R^2} dV - \int_V \frac{1}{R^2} \nabla \psi^* \cdot \nabla \psi^n dV + \int_S \frac{\psi^*}{R^2} \nabla \psi^n \cdot \mathbf{n} dS \quad (3.58)$$

Empirically, solving for  $\delta\psi$  instead of  $\psi$  is found to work better in terms of convergence and robustness, specially for free-boundary equilibria. In addition, the chosen Picard iterations incorporate a *blending* or a *back-averaging* technique that mixes the old solution of  $\psi$  with the new one

$$\psi^{n+1} = \psi^n + (1 - a_{\text{mix}}) \delta\psi^n \quad (3.59)$$

where  $0 < a_{\text{mix}} < 1$  is the *blending* parameter. This parameter can be increased to improve the convergence of complicated equilibria where the initial guess is very far from the final solution. Specially for free-boundary equilibria, this parameter is empirically found to require a high value  $a_{\text{mix}} \sim 0.7 - 0.95$  as the convergence is very challenging.

In order to further improve the convergence and to prevent converging to the trivial solution, the dependence of the source function  $j(\psi)$  is defined in order to keep certain physical quantities constant during the iterations. The main constraints are the pressure profile and the current profile which are defined in terms of the normalized flux  $\psi_N \equiv (\psi - \psi_{\text{axis}})/(\psi_{\text{bnd}} - \psi_{\text{axis}})$ . With the choice of  $\psi_N$  as a coordinate the source  $j(\psi_N)$  is geometrically constrained by the position of the magnetic axis and the definition of the plasma boundary  $\psi_{\text{bnd}}$ . In order to have a smooth convergence, it's important that the position of the magnetic axis and the plasma boundary are properly found and that their evolution is continuous during the iterations so sudden jumps of these quantities are avoided. In subsection 3.2.5 the methods to calculate the magnetic axis and the plasma boundary are exposed.

### 3.2.2 Fixed-boundary equilibria

When applying the Dirichlet BC to the poloidal flux  $\psi$ , the boundary terms that arise in the GS equation (3.58) vanish and the boundary condition is imposed directly in the matrix. The fixed BC is simply forced by implementing the following relation for the boundary nodes

$$z_{\text{big}} \delta\psi_b = 0 \quad (3.60)$$

where  $z_{\text{big}} = 10^{12}$  is a big number in order to force the solution  $\delta\psi_b \approx 0$ . When the boundary of the computational domain corresponds to a flux surface, the flux value is constant over the boundary and the initial condition is chosen to be  $\psi_b = 0$ . For plasmas including X-points, the value of the flux is given as a function of the position over the boundary of the computational domain.

### 3.2.3 Free-boundary equilibria

For calculating the free-boundary equilibria, the boundary terms of equation (3.58) must be included together with the following natural boundary condition given by STARWALL

$$\nabla\psi \cdot \mathbf{n}/R = \mathbf{B}_{\tan} \cdot \mathbf{e}_\phi = M_{ey}\mathbf{Y} + M_{\parallel ee}\boldsymbol{\psi} \quad (3.61)$$

where this equation is a particular case of equation (3.53) with  $\psi \equiv RA_\phi$ . With this Neumann BC, the normal gradient at one particular position on the boundary is coupled to the values the poloidal flux at other positions of the boundary. The passive conductor currents are initialized to zero while the PF coil currents providing the equilibrium are imposed with the following matrix multiplication

$$\mathbf{Y} = S^T \begin{pmatrix} \mathbf{I}_{\text{coils}} \\ \mathbf{0} \end{pmatrix} \quad (3.62)$$

where  $S^T$  is the inverse of the similarity transform matrix and  $\mathbf{I}_{\text{coils}}$  is a vector containing the PF coil currents. Note that the PF coils currents are set to be constant during the iterations ( $\delta\mathbf{Y} = 0$ ) and therefore

$$\nabla\delta\psi^n \cdot \mathbf{n}/R = M_{\parallel ee}\delta\boldsymbol{\psi}^n \quad (3.63)$$

Once expressions (3.61) and (3.63) are implemented into the GS equation (3.58), the system of equations is closed and it can be solved through the Picard iterations.

#### Feedback control on plasma current and vertical position

As the plasma shape and position vary during the iterations, some constraints have to be imposed to ensure convergence to a physical solution. One of the obvious choices is to keep the total toroidal current constant within the plasma ( $I_p$ ). For that purpose, a feedback control system on the total plasma current actuates at each iteration. The toroidal current profile is multiplied by a factor  $\alpha_I$

$$j^{n+1}(\psi_N) = \alpha_I^{n+1} j^n(\psi_N) \quad (3.64)$$

which is calculated at each iteration. The factor  $\alpha_I^{n+1}$  is calculated from the previous iteration with a technique based on a proportional-integral (PI) controller algorithm

$$\alpha_I^{n+1} = \alpha_I^n \left( 1 - \gamma_{I1} \frac{I_p^n - I_{p,\text{ref}}}{I_{p,\text{ref}}} - \gamma_{I2} \frac{\sum_{l=0}^n (I_p^l - I_{p,\text{ref}})}{I_{p,\text{ref}}} \right) \quad (3.65)$$

where  $I_{p,\text{ref}}$  is the target current and the numerical parameters  $\gamma_{I1}$  and  $\gamma_{I2}$  have to be tuned by the user as they will depend on the equilibrium properties. Typically the values of these coefficients are in the range  $\gamma_{I1} \sim 0.1 - 0.4$  and  $\gamma_{I2} \sim 0.00 - 0.02$ .

Vertically elongated plasmas are unstable to axisymmetric instabilities. During the Picard iterations this feature also arises and the plasma moves through the iterations searching the minimum of energy even if the solved equation is an equilibrium equation. Similarly to the total current, a feedback control system has to be implemented for the vertical position of the plasma as it's done in experiments. In this case the feedback control is performed through the PF coils that produce the radial magnetic field  $B_R$ . The feedback control parameter  $\alpha_Z$  is used to increase or to decrease in the currents in those coils

$$I_{B_R}^{n+1} = I_{B_R,0}(1 \pm \alpha_Z) \quad (3.66)$$

where the feedback control scheme has the form

$$\alpha_Z^{n+1} = \alpha_{Z1}(Z_{axis}^n - Z_{ref}) + \alpha_{Z2} \sum_{l=0}^n (Z_{axis}^l - Z_{ref}) + \alpha_{Z3}(Z_{axis}^n - Z_{axis}^{n-1}) \quad (3.67)$$

where  $Z_{ref}$  is the target vertical position and the  $\alpha_{Zi}$  numerical parameters are tuned as well by the user. In this case the feedback parameters will strongly depend on the plasma elongation and on the strength of the radial field produced by the coils. The additional feedback parameter  $\alpha_{Z3}$  acts like a *velocity* controller for the plasma position.

## Common difficulties

In all the tested cases, the convergence rate of the free-boundary equilibria is found to be much lower than for the fixed-boundary cases. The number of required iterations is typically an order of magnitude bigger (see figure 3.4 (c)). In addition, the initial conditions conditions for free-boundary equilibria require to be closer to the final equilibrium state. For that purpose, a fixed-boundary equilibrium is pre-calculated and given as the initial condition for the free-boundary calculation.

The first iterations are the most challenging as the BCs transition from Dirichlet to natural boundary conditions. In addition, if the feedback control parameters are not adapted for the given case, oscillations in the plasma current or in the plasma position can appear and can lead the plasma too far from the final equilibrium to converge. These are the reasons why the *blending* parameter  $a_{mix}$  has to be set to high values compared to the fixed boundary equilibria.

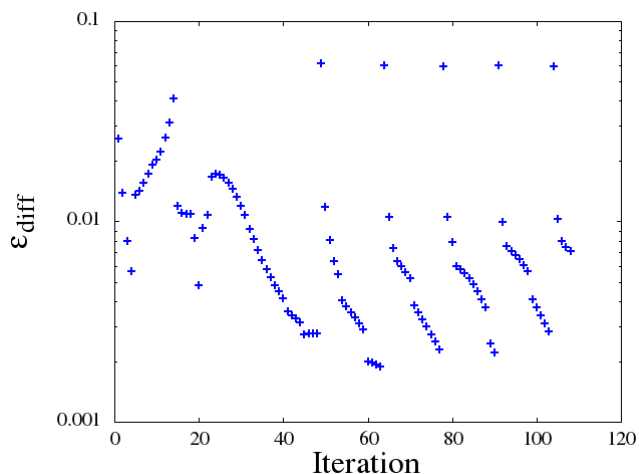


FIGURE 3.3: Failed convergence of a free-boundary equilibrium for an elongated JET plasma showing repetitive cycles in the convergence rate.

The convergence can be particularly cumbersome if the position of the axis abruptly jumps from one iteration to the next one as the feedback position control could react strongly to it. In these cases it has been observed that the convergence parameter  $\varepsilon_{diff}$  oscillates between a minimum and a maximum value and that the iterations fall into repetitive cycles which never converge to the specified tolerance (see figure 3.3). This unfortunate behaviour is related with the proximity of the magnetic to the grid center, which is a special node of the computational mesh as more than 4 Bezier elements join at that point. In the current version of X-point grid in JOREK (see figure 2.2), the proximity of the grid center to the magnetic axis is able to affect strongly the solution of  $\nabla\psi = 0$  and causes distortions around that point. A trivial solution to this problem is simply to choose grids which center is separated from the expected position of the magnetic axis, however this problem should be solved in the future by adapting the FEM method in the grid center.

### 3.2.4 Reconstruction of experimental equilibria

In this section an example of the computation of a free-boundary equilibrium is presented. The chosen plasma parameters are obtained from the ASDEX-Upgrade (AUG) discharge #31128 at time  $t = 2.4$  s. The code CLISTE [MMS99] which is used in AUG for the reconstruction of AUG experimental equilibria, computes the GS equation by constraining the solution to experimental magnetic measurements. The input parameters and profiles used in JOREK were provided by the output of CLISTE for the mentioned discharge.

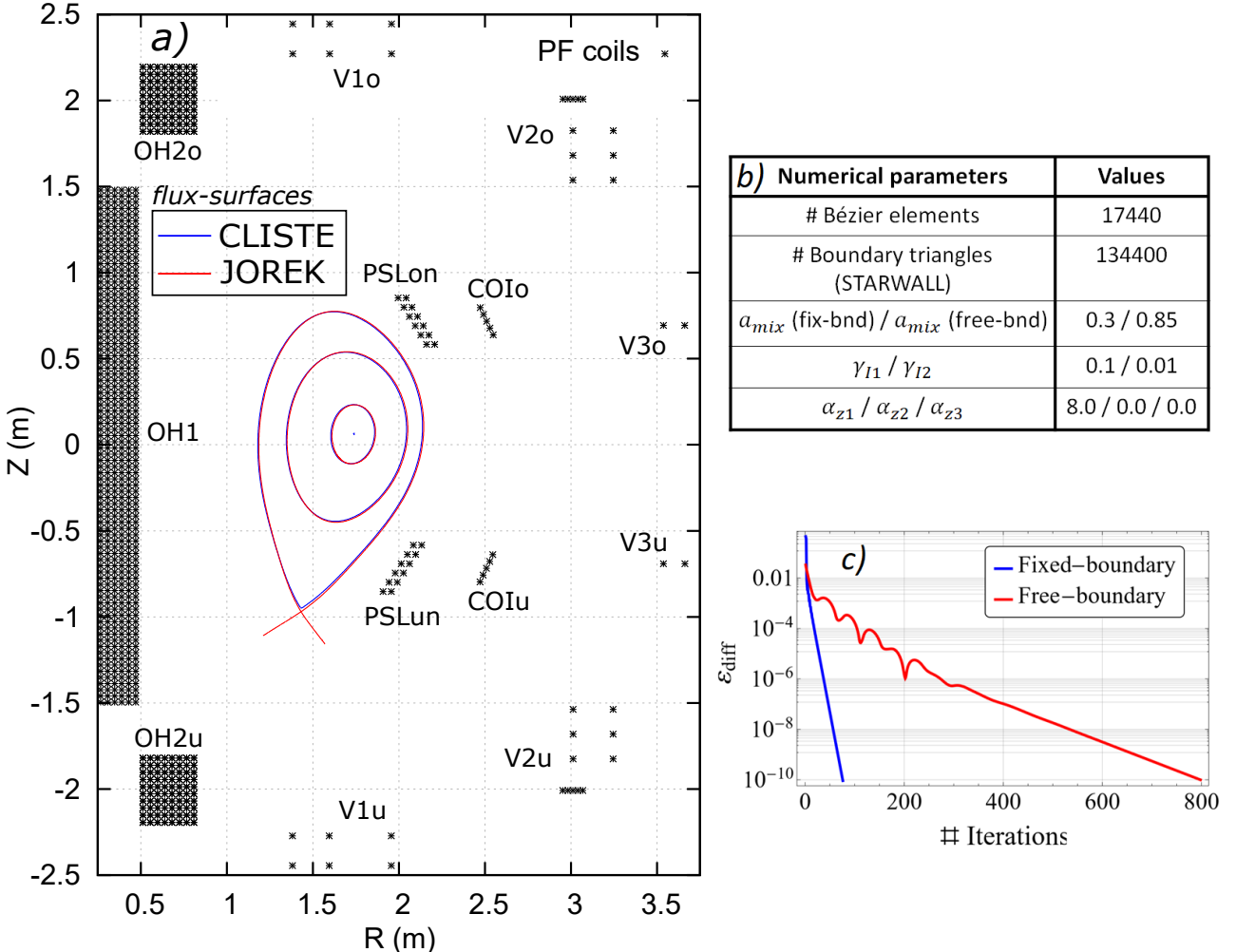


FIGURE 3.4: Equilibrium reconstruction of the AUG discharge # 31128 at time  $t = 2.4$  s. (a) Geometry implemented in JOREK-STARWALL for the PF coils and comparison of the obtained flux-surfaces between JOREK and CLISTE. (b) Numerical parameters used for the free-boundary equilibria in JOREK-STARWALL. (c) Fixed-boundary and free-boundary equilibrium convergence of the AUG case.

The discretization that CLISTE uses for the axisymmetric AUG PF coils has been implemented in JOREK-STARWALL (see figure 3.4 (a)). The passive stabilizing loops (PSL) have been also taking into account for the equilibrium reconstruction. The number of Picard iterations required for obtaining the same level of accuracy in the equilibrium is an order of magnitude bigger for the free-boundary equilibrium than for the fixed-boundary equilibrium (see figure 3.4 (c)). The convergence rate of the free-boundary equilibrium shows oscillations that are related with the stabilization of the feedback on the total toroidal current and on the vertical position. After 200 iterations, the feedback system is stabilized and the convergence rate is constant over the ensuing iterations. The numerical parameters that have been used for this case are shown in figure 3.4 (b).

A comparison between JOREK-STARWALL and CLISTE in the final equilibrium quantities is presented in figure 3.5 (c), where the relative differences are below 1%. The obtained pressure and q-profiles are compared in figure 3.5 and the geometry of the flux-surfaces (including the separatrix) is compared in figure 3.4 (a) showing a good agreement.

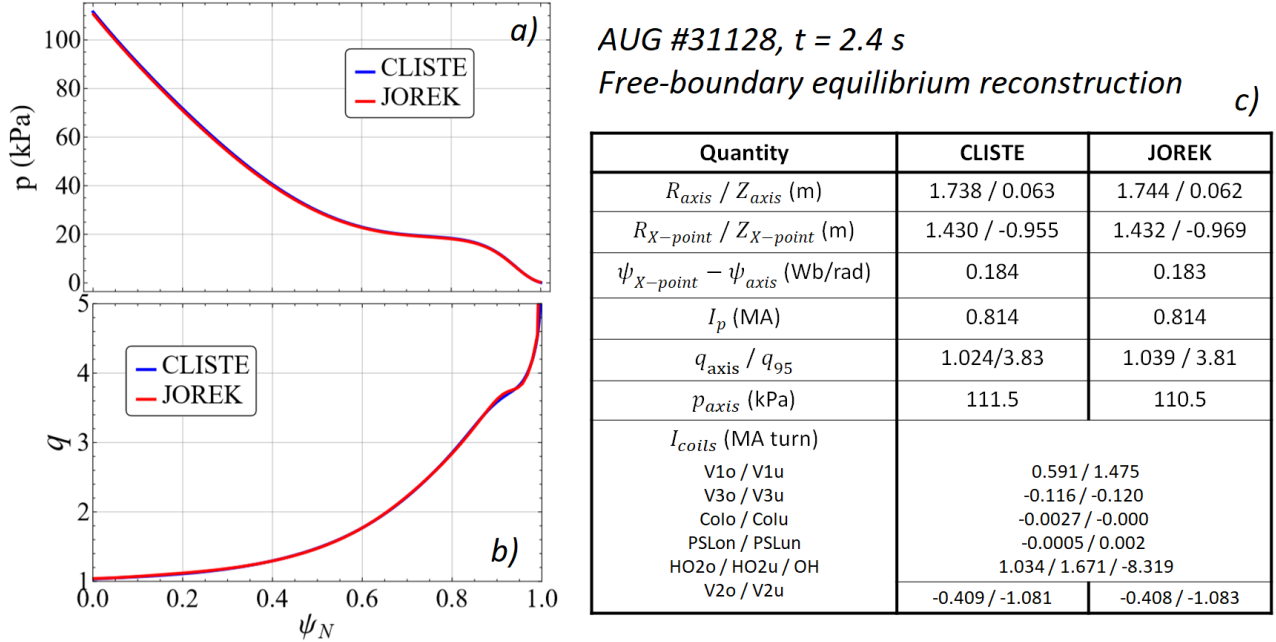


FIGURE 3.5: Comparison of the free-boundary equilibrium between JOREK and CLISTE. (a) The pressure profile. (b) The safety factor profile. (c) Table comparing different obtained equilibrium quantities.

### 3.2.5 Identification of plasma boundary and special points

The proper calculation of the the special points of the plasma, such as the magnetic axis, the limiter and the X-points is essential for the definition of the normalized poloidal flux  $\psi_N$ . As mentioned previously, the normalized flux plays an important role not only for the computation of the GS equilibrium but also for the time evolution runs where the perpendicular diffusion coefficients  $D_\perp(\psi_N)$  and other quantities may be defined in terms of this coordinate. Moreover the normalized flux is a radial coordinate that can be very useful for diagnostic purposes. In the following, the methods to calculate these points and the plasma boundary are presented, which will finally serve to calculate  $\psi_N \equiv (\psi - \psi_{axis}) / (\psi_{bnd} - \psi_{axis})$  and to define the plasma boundary.

#### Calculation of the limiter point

The calculation of the limiter point is performed by finding the extrema<sup>1</sup> of  $\psi$  along the boundary of the JOREK grid. The extremum value ( $\psi_{min}/\psi_{max}$ ) can be found by solving analytically the equation  $\partial_s \psi = 0$  at every boundary element<sup>2</sup>, which becomes a simple second order polynomial equation. Note that the boundary is periodic in the poloidal direction and thus an extremum of  $\psi$  always exists.

In the cases where the computational domain contains an X-point, the extremum of  $\psi$  along the boundary may not correspond to the limiter of the plasma. If a private region exists

<sup>1</sup>The limiter will be a maximum or a minimum of  $\psi$  depending on the sign of the toroidal current.

<sup>2</sup>here  $s$  is the local coordinate along the boundary of an element

between the X-point and the boundary of the mesh, an extremum of  $\psi$  always exists in that region. In figure 3.6 such case is presented<sup>3</sup> where two minima of  $\psi$  can be observed, the limiter point at the top of the plasma and another minimum in the private region below the X-point. For these cases the algorithm that searches the limiter point must always exclude the private regions from the search.

In order to distinguish numerically the private flux regions, the fact that  $\nabla\psi$  changes sign across the X-points can be used (see figure 3.6). The vector pointing from the magnetic axis to the private region points to the opposite(same) direction of  $\nabla\psi$  for positive(negative) plasma currents. Thus the limiter point can be numerically defined as the boundary point that has the following value for the poloidal flux

$$\psi_{\text{lim}} = \begin{cases} \psi_{\min} & \text{if } \nabla\psi \cdot (\mathbf{r}_{\min} - \mathbf{r}_{\text{axis}}) > 0 \text{ and } I_p > 0 \\ \psi_{\max} & \text{if } \nabla\psi \cdot (\mathbf{r}_{\max} - \mathbf{r}_{\text{axis}}) < 0 \text{ and } I_p < 0 \end{cases} \quad (3.68)$$

where  $\mathbf{r}_{\min}/\mathbf{r}_{\max}$  is the position vector of the found extremum  $\psi_{\min}/\psi_{\max}$  and  $\mathbf{r}_{\text{axis}}$  is the position vector of the magnetic axis. Note that this technique is valid as well for the double-null X-point plasmas.

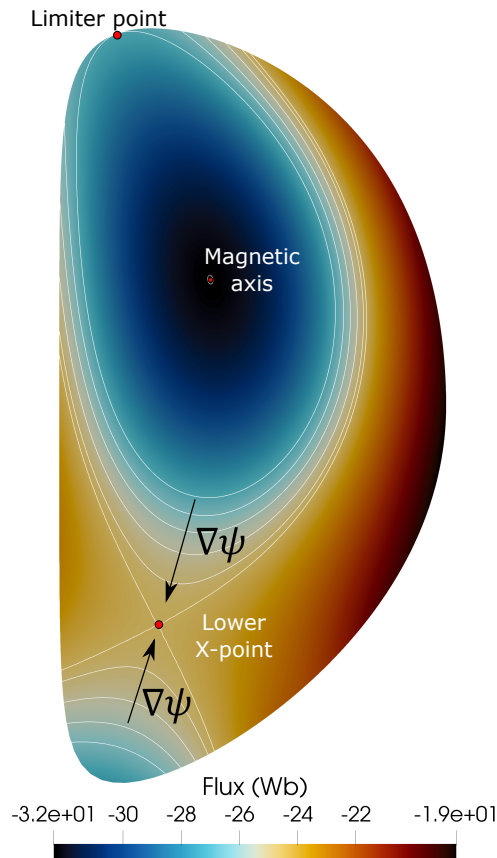


FIGURE 3.6: Contour plot of the poloidal magnetic flux indicating the different special points that are relevant to define the plasma boundary. The plot was generated from an ITER VDE case simulated with JOREK-STARWALL.

### Calculation of the magnetic axis and the X-points

The procedure to find the magnetic axis and the X-points is based on finding the points in the  $(R, Z)$  plane where the the poloidal field  $\mathbf{B}_p = \nabla\psi \times \nabla\phi$  is zero. Thus is sufficient to

---

<sup>3</sup>The plot was obtained from an ITER VDE simulation that will be presented in chapter 5.

find the points in the domain where  $\nabla\psi = 0$ . The algorithm implemented in JOREK has been improved with the algorithm presented in figure 3.7. The procedure calculates  $\nabla\psi$  in 16 Gaussian points at every Bézier element within a given  $(R, Z)$  region and uses Newton's method to find the root of the equation  $|\nabla\psi| = 0$  in the element with minimum  $|\nabla\psi|$ . If the root is not found, the tested element is excluded from the search list and Newton's method is applied to the next element that has the minimum  $|\nabla\psi|$ . The regions in the poloidal plane that are used to find the extrema are chosen such that the magnetic axis and X-points are distinguishable. Once the magnetic axis and the X-points are found in the first time-step of the simulation, the search region may be defined as a disk around the previous magnetic axis/X-point. The choice of the dynamic disk regions that move with the extrema is specially convenient for VDE simulations where large displacements of these special points occur.

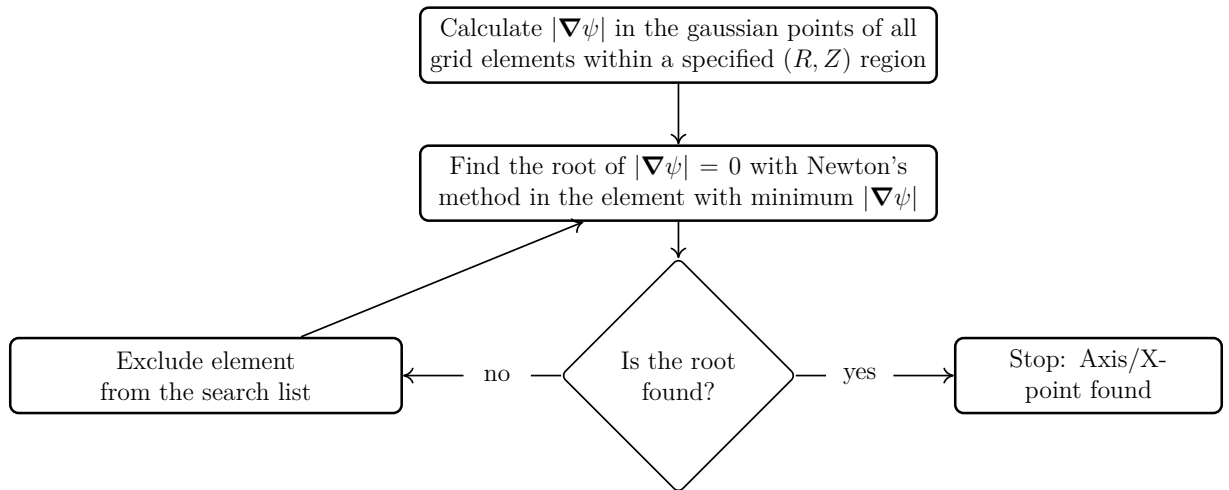


FIGURE 3.7: Implemented algorithm in JOREK to find the magnetic axis and the X-points.

### Definition of the plasma boundary

The plasma boundary is defined as the last closed flux surface (LCFS) or the last flux surface where the magnetic field-lines don't intersect the boundary of the domain. Once the magnetic axis, the limiter and the X-points are found, the boundary of the plasma is defined as the closed flux surface that has the following value

$$\psi_{\text{bnd}} = \begin{cases} \psi_{\text{lim}} & \text{if } |\psi_{\text{lim}} - \psi_{\text{axis}}| < |\psi_{\text{X-point}} - \psi_{\text{axis}}| \\ \psi_{\text{X-point}} & \text{if } |\psi_{\text{X-point}} - \psi_{\text{axis}}| \leq |\psi_{\text{lim}} - \psi_{\text{axis}}| \end{cases} \quad (3.69)$$

where  $\psi_{\text{X-point}}$  is the flux at the dominant<sup>4</sup> X-point and  $\psi_{\text{lim}}$  is the flux at the limiter point defined in (3.68). Note that to exclude the private regions from the search of the limiter point is required to use the definition (3.69). In the example of figure 3.6 it can be observed how the definition of the boundary (3.69) provides the correct LCFS which in this case is defined by the limiter point.

## 3.3 Optimization of coil currents for arbitrary equilibria

There are cases where the equilibrium quantities such as the plasma shape and the plasma profiles may be varied for physics studies. When dealing with fixed boundary equilibria, to

<sup>4</sup>The dominant X-point is defined as the X-point which distance in absolute flux to the magnetic axis  $|\psi - \psi_{\text{axis}}|$  is smaller.

vary these quantities is relatively simple as the plasma shape and position are directly imposed with the Dirichlet BCs for the poloidal flux. In the case of free-boundary equilibria, the coil currents have to be adapted as the plasma position and shape are sensitive to changes in  $l_i$  and  $\beta_p$ . Moreover, in some situations it may be convenient to create a free-boundary equilibrium from an arbitrary fixed-boundary equilibrium where the coil currents are not known. In these cases a numerical tool that finds the optimal currents in a given set coils in order to compute the arbitrary free-boundary equilibrium is required. Otherwise to manually test different currents for the different coils may be very problematic and time consuming. In this section we present a simple method that we have implemented in JOREK in order to compute these currents.

In a steady state equilibrium, the external field  $B^{\text{ext}} \equiv B - B^{\text{plasma}}$  is totally given by the PF coils. The presented method is based on fitting the currents in the given set of PF coils in order to reproduce the boundary  $B^{\text{ext}}$  that is calculated from the fixed-boundary equilibrium. For finding the optimal coil currents, the following error function is minimized

$$E = \sum_{i=1}^{N_{\text{points}}} w_i \left( B_i^{\text{ext}} - \sum_{j=1}^{N_{\text{coils}}} c_{i,j} I_j \right)^2 \quad (3.70)$$

where the index  $i$  runs over a set of points along the boundary,  $w_i$  are weighting coefficients,  $I_j$  are the coil currents and  $c_{i,j}$  are the coefficients that give the magnetic field produced by the coils at the boundary ( $B_i^{\text{coil},j} = c_{i,j} I_j$ ). The fitted field  $B^{\text{ext}}$  can be chosen to be the tangential field  $\mathbf{B}_{\tan} \cdot \mathbf{e}_\phi$  or the normal field  $\mathbf{B} \cdot \mathbf{n}$ . The method relies on the fact that once the magnetic field is defined at the boundary of the computational domain, the equilibrium solution is determined. Therefore the chosen geometry for the PF coils is not relevant if the produced boundary field reproduces the target  $B^{\text{ext}}$ . The set of equations for the coil currents is found by searching a minimum of the error function  $E$  by calculating  $\partial E / \partial I_k = 0$ . The corresponding equation to the  $k^{\text{th}}$  coil current is therefore

$$\sum_{j=1}^{N_{\text{coils}}} \sum_{i=1}^{N_{\text{points}}} w_i c_{i,k} c_{i,j} I_j = \sum_{i=1}^{N_{\text{points}}} w_i c_{i,k} B_i^{\text{ext}} \quad (3.71)$$

The resulting set of  $N_{\text{coils}}$  linear equations can be written in the matrix form  $\mathbf{A} \cdot \mathbf{I} = \mathbf{b}$  and solved with a common algebra library such as LAPACK. The weighting coefficients  $w_i$  can have the following dependence on the external field

$$w_i = \begin{cases} |B_{\max}^{\text{ext}}| / |B_i^{\text{ext}}| & \text{for } |B_i^{\text{ext}}| / |B_{\max}^{\text{ext}}| \geq \lambda_w \\ \lambda_w & \text{for } |B_i^{\text{ext}}| / |B_{\max}^{\text{ext}}| < \lambda_w \end{cases} \quad (3.72)$$

where  $B_{\max}^{\text{ext}}$  is the maximum value of the external field and  $\lambda_w$  is a parameter that avoids the singularities that can appear in the weighting coefficients when  $|B_i^{\text{ext}}| \approx 0$ . The weighting coefficients have the latter dependence so all the boundary points have the same contribution to the error function regardless of the value of the external field. The evaluation of the external field requires to calculate first the magnetic field produced by the plasma  $\mathbf{B}^p$  at the boundary. The plasma field is computed by using the following expression

$$\mathbf{B}^p(R, Z) = \int J_\phi \mathbf{G}(R, R', Z, Z') dR' dZ' \quad (3.73)$$

where the Green's function  $\mathbf{G}(R, R', Z, Z')$  is analytically calculated [Jar10].

The method to calculate the PF coil currents has been tested with the AUG free-boundary equilibrium described in the previous section (see figure 3.4). If the method is perfectly reliable, it should reproduce exactly the coil currents that were used to compute the equilibrium.

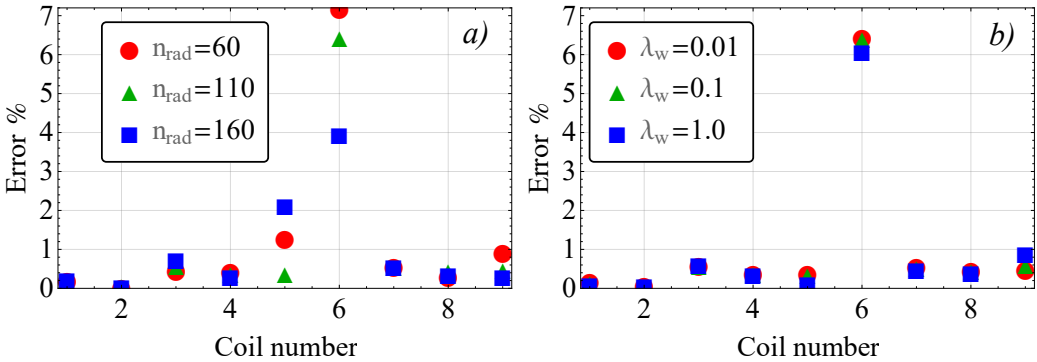


FIGURE 3.8: Test of the method to calculate the optimal coil currents. (a) Scan on the number of radial points in the JOREK grid. (b) Scan on the weighting coefficient parameter  $\lambda_w$ .

However the solution can be influenced by the grid resolution and the choice of the weighting coefficients ( $\lambda_w$ ).

The method is able to reproduce the coil currents with relative errors of  $\sim 1\%$  for most of the coils (see figure 3.8). Coils #5 and #6 have a small current compared with the rest of the coil currents (about a factor 80 smaller than coil #9) and therefore the relative errors can be bigger ( $\sim 4 - 7\%$ ). The relative errors decrease with the number of radial resolution of the JOREK grid (see figure 3.8 (a)) for the coils that carry more current (#4 and #9). A scan on the weighting coefficient  $\lambda_w$  (see figure 3.8 (b)) reveals that the choice of this parameter is not relevant for this case.

### Application to the JET's iron core case

One of the important applications for the presented technique to find optimal coil currents is to reconstruct experimental equilibria that includes ferromagnetic components. Several tokamaks use an inductor with a ferromagnetic iron core in order to induce the plasma current with a reduced amount of energy in the electromagnetic system of the inductor. Due to the presence of a medium with a different magnetic permeability  $\mu_r \equiv \mu_{\text{iron}}/\mu_0 \gg 1$ , the ferromagnetic components such as the iron core are able to deform the magnetic field produced by the PF coils and to substantially change the equilibrium configuration. Typically the iron core structures present large asymmetries in the toroidal direction and to include their ferromagnetic effects in equilibrium codes can be difficult [OBr+92].

In order to reconstruct free-boundary equilibria of tokamaks such as JET, the PF coil currents can be modified in order to mock-up the iron core effects. The use of this technique is justified by the fact that once the boundary magnetic field is given correctly, the equilibrium is uniquely determined. However special care should be taken when varying the coil currents during the time evolution as the absence of the iron core will give different external magnetic fields. Moreover the induction of currents in the passive conductors will be different without the iron core. Finally this technique is generally justified for the time evolution if the boundary external field is fixed over time or if the time scales are such that the vacuum vessel can shield the iron core effects.

An equilibrium reconstruction of the JET discharge #85186 is shown in figure 3.9. The equilibrium was obtained from the EFIT++ code which takes into account the iron core effects. The computation of the free-boundary equilibrium by using directly the EFIT++ coil currents was not possible as the absence of the ferromagnetic effects made the plasma to drift radially outwards during the Picard's iterations. However when the coil currents were adapted by minimizing the error  $E$  (3.70), a good agreement was obtained between the equilibrium properties

between the fixed-boundary equilibrium including the iron core effects and the free-boundary calculation with the mock-up coil currents (see figure 3.9 (a) and (b)). In table 3.9 (c) the currents in the JET’s PF coil circuits obtained in EFIT++ and the JOREK modified currents are compared. The comparison reveals that the iron core effects are quite significant and that in order to obtain the same equilibrium without the iron core effects, the PF coil currents have to be substantially modified. As expected, the coil currents require a larger amplitude in order to reproduce the iron core effects. For this case the currents in the JET’s divertor coils were used directly from the EQDSK calculation as the iron core effects are smaller for these coils due to their proximity to the plasma.

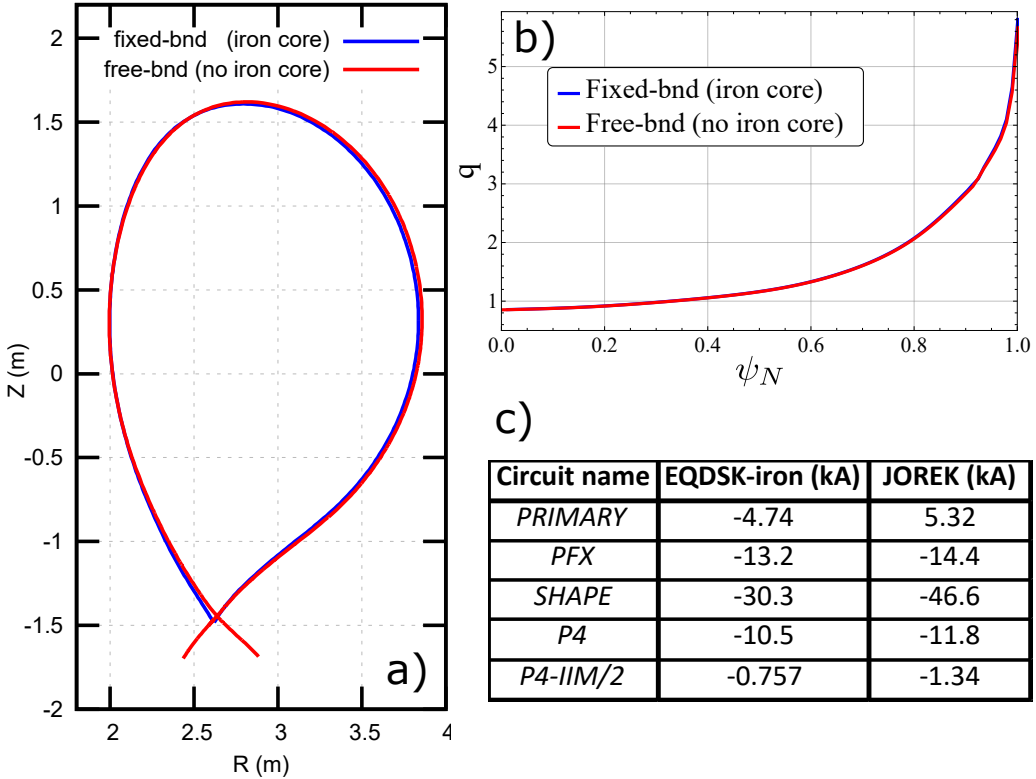


FIGURE 3.9: Equilibrium reconstruction of the JET discharge #85186 including ferromagnetic effects with the use of the presented method to calculate the optimal coil currents for arbitrary equilibria. (a) Separatrix and (b)  $q$ -profile comparison between the fixed-boundary equilibria including iron core effects and the computed free-boundary equilibria using the adapted coil currents in JOREK. (c) Comparison of the current in the JET’s PF coil circuits in the EQDSK equilibrium including the iron core and the JOREK free-boundary equilibrium with the mock-up currents.

### 3.4 Implicit imposition of coil currents over time

The control of the plasma through the variation of currents in different types of coils is an essential feature of every tokamak. Many of the main plasma instabilities such as VDEs, RMWs and ELMs can be controlled with the use of PF and RMP coils. In experiments, the coil currents are imposed through complicated feedback systems actuating on the coils voltage [Gri+15a]. In free-boundary MHD codes such as JOREK-STARWALL, the coil voltages can be easily implemented in equation (3.46) as a source term. For practical purposes, it may be convenient to impose directly the coil currents without the numerical implementation of the complicated feedback systems for the coils voltage. When using an implicit time stepping scheme for the plasma equations, the evolution of the coil currents must respect the implicit scheme as well. Otherwise, the change of field on the plasma side wouldn’t be consistent with

the change of current in the coils and the numerical solution can significantly differ from the real solution.

In order to impose implicitly the coil currents in JOREK-STARWALL, a source term is included in the evolution equation for the coil currents (3.36)

$$\tilde{M}_{cw} \dot{\mathbf{I}}^w = -R_{cw} (\mathbf{I}^w - \mathbf{I}_{\text{coils}}) / \mu_0 - \sum_l^3 \tilde{M}_{ce,l} \dot{\mathbf{A}}_{p,l}^e / \mu_0 \quad (3.74)$$

where the label  $c$  denotes "coil",  $\mathbf{I}_{\text{coils}}$  are the imposed coil currents over time and the source/sink ( $\phi_s$ ) term does not exist for coils. If a very large value is chosen for the resistivity of the coil  $c$ , the coil resistance  $R_{cc}$  becomes dominant and the time evolution equation for the coil  $c$  is

$$\tilde{M}_{cc} \dot{I}^c \approx -R_{cc} (I^c - I_{\text{coils},c}) / \mu_0 \quad (3.75)$$

The resulting expression is equivalent to the equation for a resistor-inductor RL circuit ( $L\dot{I} + RI = V$ ) where the analytical solution for such a system is simply  $I(t) = V/R(1 - e^{-tR/L})$ . If the chosen voltage is  $V = R_{cc}I_{\text{coils},c}$  as it is done in equation (3.75), then the coil current exponentially decays to the specified value  $I_{\text{coils},c}$  in the  $L/R$  time of the coil.

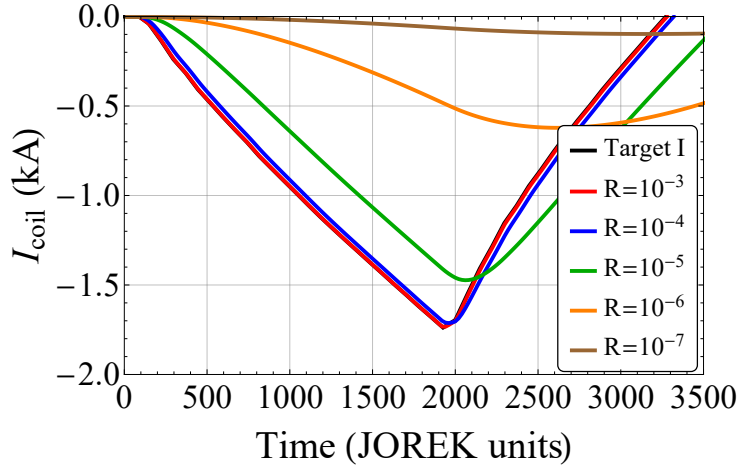


FIGURE 3.10: Imposition of coil currents in JOREK-STARWALL. Value of the test coil current over time for different coil resistances  $R[\Omega]$ .

A simple and robust method to impose implicitly the coil currents over time is to choose a very large coil resistivity and to implement the source term in the evolution equation for the coil currents. In order to have an effective control of the coil currents with this method, the resistive decay time ( $L/R$ ) of the coils has to be much smaller than the time scale of interest. Finally the modified equation for the *wall* currents is

$$\dot{\mathbf{Y}} = -M_{yy} (\mathbf{Y} - \mathbf{Y}_0(t)) - \sum_l^3 M_{ye,l} \dot{\mathbf{A}}_{p,l}^e - M_{yJ} \dot{\mathbf{J}}_\perp \quad (3.76)$$

where

$$\mathbf{Y}_0(t) = S^T \begin{pmatrix} \mathbf{I}_{\text{coils}}(t) \\ \mathbf{0} \end{pmatrix} \quad (3.77)$$

Note that with this formulation all the mutual inductances between the coils and the passive conductors are taken into account. This form of imposing currents includes the fact that a variation of the coil currents immediately induces currents in the other passive conductors. It

should be noted that to impose the currents directly through  $\delta\mathbf{Y}$  wouldn't be possible as this vector contains the change of the currents in the other passive components which is not known.

An example of the imposition of coil currents in JOREK-STARWALL is shown in figure 3.10. For this case an axisymmetric coil was placed near a free-boundary equilibrium plasma and a target waveform for the coil current was prescribed (black curve). A scan on the coil resistivity shows that for sufficiently large values of the coil resistance ( $R = 10^{-3}\Omega$ ) the coil currents exactly follow the target wave form. For smaller resistances, the coil current time trace deviates from the specified values as the  $L/R$  time of the coil becomes bigger than the waveform time scale. In addition, when the resistance is low enough the inductive terms also can play role in the evolution of the coil current.



# Chapter 4

## Simulation of Edge Localised Mode triggering via vertical oscillations

### 4.1 Introduction

In this chapter the physics of the ELM pacing method via vertical position oscillations (see [1.2.3](#)) is explored. The JOREK-STARWALL code presented in the previous chapters is applied with the aim to reveal the physics mechanism underlying the ELM triggering. The results shown here have been published in [\[Art+18\]](#).

Linear stability studies were performed for vertical position oscillation simulations for JET [\[Lun+15\]](#) and ITER [\[Gri+15a\]](#). These studies concluded that the main destabilizing factor was an increase of edge current produced by the oscillations, which is known to destabilize peeling-balloonning modes [\[Huy05\]](#). However the authors of [\[Kim+09\]](#) argued that for the AUG case, ELMs were destabilized when the edge current was decreasing and therefore, ELMs could be triggered by other more subtle factors such as the change in plasma shape or in pressure gradient. The main goal of this work is to clarify which is the determining factor for the ELM destabilization through non-linear simulations and as well, to provide an understanding of the current induction during the plasma motion in ITER plasmas.

In order to simulate correctly the vertical position oscillations of the plasma, the axisymmetric mode ( $n = 0$ ) requires a free-boundary description and the resistive effects of the passive conductors surrounding the plasma must be taken into account. To perform the studies in this work we have included realistic PF and in-vessel coils in JOREK-STARWALL which take into account all the mutual inductances of the system. All these features allow us to simulate for the first time realistic vertical oscillations together with non-linear MHD ELM triggering simulations in a consistent single scheme.

This chapter is organized as follows, in section [4.2](#) we investigate the physics of the edge current induction during the plasma vertical motion, where we show analytical results and then we present simulations of both a simplified plasma and a realistic ITER plasma. In section [4.3](#) we analyse the non-linear stability of an ITER plasma during a vertical oscillation and we investigate the main causes of ELM destabilization. In this work the destabilization of peeling-balloonning modes is shown up to the non-linear saturation phase and therefore the study of the non-linear dynamics related with ELM crashes and transient outbursts is left for future work. Finally we present our conclusions in section [4.4](#).

## 4.2 Understanding the axisymmetric induction of edge currents during vertical oscillations

The authors of [Lun+15] and [Gri+15a] concluded that the mechanism underlying ELM triggering was an increase of the edge toroidal current driving the plasma into the unstable MHD peeling-balloonning regime. The induction of edge toroidal current was mainly attributed to a fast reduction of the plasma volume due to the vertical motion through an inhomogeneous magnetic field. Here we investigate this effect analytically in the frame of an MHD model and we show simulations of both a simple elongated plasma and a realistic ITER 7.5MA/2.65T plasma.

In the following we aim to give some analytical insights into the current induction in a moving plasma. This effect can be understood by analysing the MHD equation for the poloidal flux  $\psi^1$

$$\frac{\partial \psi}{\partial t} + \mathbf{v} \cdot \nabla \psi = \eta J_\phi \quad (4.1)$$

where  $t$ ,  $\mathbf{v}$ ,  $\eta$ ,  $J_\phi$  are respectively time, velocity, resistivity and toroidal current density. By separating the poloidal flux into a contribution of the plasma plus an external contribution ( $\psi = \psi_p + \psi_{ext}$ ) and using the convective time derivative ( $d/dt \equiv \partial_t + \mathbf{v} \cdot \nabla$ ) Eq. (1) becomes

$$\frac{d\psi_p}{dt} = -\frac{\partial \psi_{ext}}{\partial t} - \mathbf{v} \cdot \nabla \psi_{ext} + \eta J_\phi \quad (4.2)$$

In the reference frame of the plasma (i.e. following a flux surface) we find that

$$\delta\psi_p \approx -\delta\psi_{ext} + \eta J_\phi \delta t \quad (4.3)$$

where  $\delta\psi_{ext} \approx \delta\psi_{ext}(\mathbf{r}_0) + \delta\mathbf{r} \cdot \nabla \psi_{ext}$  and  $\delta\mathbf{r}$  is the displacement of the flux surface. For an axisymmetric case, the plasma contribution to the poloidal flux can be written in terms of the plasma current

$$\psi_p(R, Z) = \mu_0 \int J_\phi(R', Z') G(R, Z, R', Z') dR' dZ' \quad (4.4)$$

where  $G(R, Z, R', Z')$  is a Green's function given by [Jar10]. The latter integral can be analytically calculated for a cylindrical plasma with a spatially constant current density  $J_\phi(t)$  going from the radius  $r_0$  to the plasma edge, which is given by  $a(t) \equiv r_0 + w_r(t)$  (see Figure 4.1 a). With these assumptions the plasma poloidal flux is

$$\psi_p(a, t) \approx \psi_p(r_0) - B_\theta(r_0) R_0 w_r(t) - \frac{\mu_0}{4\pi} R_0 I_\phi^{w_r}(t) \quad (4.5)$$

where  $I_\phi^{w_r}(t) = 2\pi r_0 w_r(t) J_\phi(t)$  is the total toroidal current contained in the edge region  $r \in [r_0, a(t)]$  and we have also assumed that  $w_r/r_0 \ll 1$ . If we assume now that during the plasma motion the plasma moves rigidly without any change in the region  $r \leq r_0$ , equation (3) becomes

$$\delta I_\phi^{w_r} = \frac{4\pi}{\mu_0 R_0} [\delta\psi_{ext}(a) - B_\theta(r_0) R_0 \delta w_r - \eta J_\phi \delta t] \quad (4.6)$$

and the change of current density is

$$\delta J_\phi = \frac{1}{2\pi r_0 w_r} \left( \delta I_\phi^{w_r} - I_\phi^{w_r} \frac{\delta w_r}{w_r} \right) \quad (4.7)$$

From equations (6) and (7) we can extract the following conclusions:

---

<sup>1</sup>here  $\psi \equiv R_0 A_\phi$  where  $R_0$  is the major radius and  $A_\phi$  is the toroidal component of the magnetic vector potential

- The total induced current  $\delta I_\phi^{w_r}$  only depends on the speed of the motion ( $\delta t$ ) through the resistive decay term, which can be considered to be small. Therefore there is no velocity dependence for an ideal conductor.
- The total induced current  $\delta I_\phi^{w_r}$  is induced by 3 mechanisms
  1. Due to a local change in external flux  $\delta\psi_{ext}(a_0)$  (i.e. produced by time variation of currents in PF coils or walls).
  2. Due to the motion of the plasma through an inhomogeneous static magnetic field  $\delta\mathbf{r} \cdot \nabla\psi_{ext}$ . For this effect, a gradient of external flux is required and plasma deformation also plays an important role through  $\delta\mathbf{r}$ .
  3. Due to plasma compression or expansion ( $\delta w_r$ ).
- The variation of current density  $\delta J_\phi$  is inversely proportional to the radial width ( $w_r$ ). This width could be approximated as the skin depth  $w_r \sim \sqrt{\eta/(\pi\mu_0 f)}$ , where  $f$  is the oscillation frequency.
- $\delta J_\phi$  can be produced by two effects
  1. An increase in total current in the region of induction ( $\delta I_\phi^{w_r}$ ).
  2. A change in the width of the region of induction  $\delta w_r$  (redistribution of current).

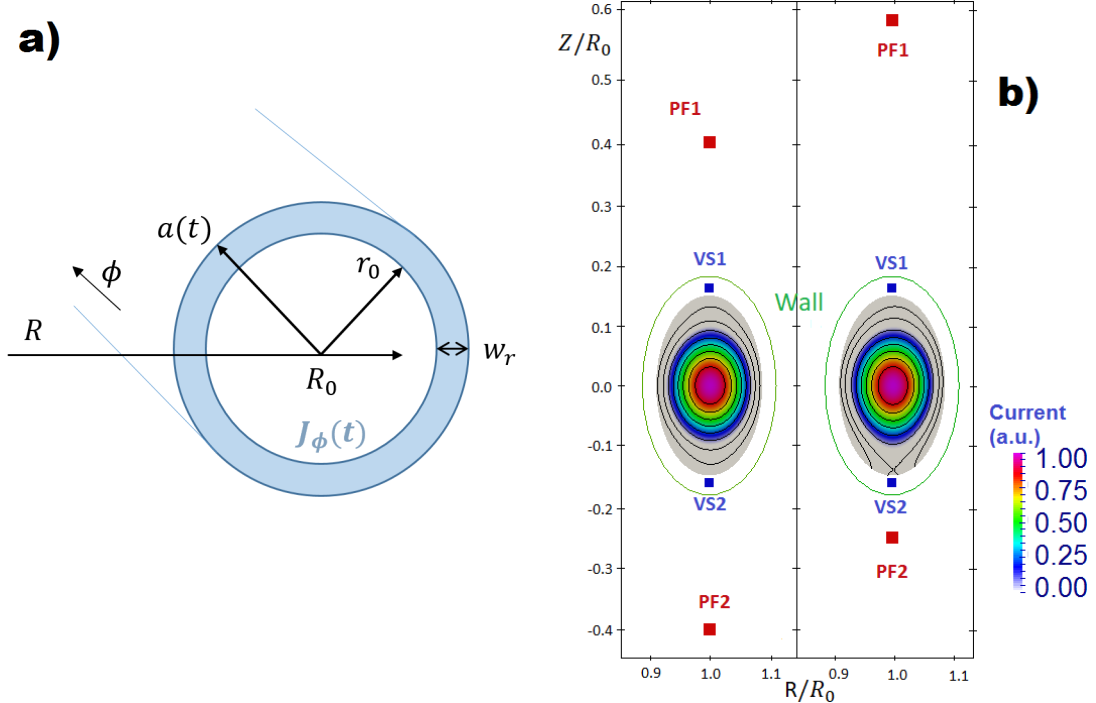


FIGURE 4.1: (a) Graphical representation of the cylindrical model used for the current induction analytical calculation. (b) The two different equilibrium configurations used for the simple plasma simulation cases.

#### 4.2.1 Simple elongated plasma

In the following, we present the case of a simple elongated pressure-less plasma ( $\beta_p \ll 1$ ) that vertically oscillates for 2 different PF coil configurations. For both cases (Figure 4.1 b) the inverse aspect ratio ( $\epsilon = 0.07$ ), the elongation ( $\kappa = 1.4$ ), the ratio between wall and plasma

radius ( $b_w/a = 1.6$ ), the plasma size, position and total toroidal current are the same. Besides the 2 PF coils located moderately far from the plasma (PF1,PF2) that provide its elongation, we have also included 2 coils (VS1,VS2)<sup>2</sup> in which currents oscillate in a sinusoidal form and which are located close to the plasma. The latter are used to vary the plasma position over time. These simulations were performed with JOREK-STARWALL using the reduced MHD model presented on [HC07]. The used grid has a polar structure formed by 2200 bicubic Bezier elements, the maximum Lundquist number is  $\sim 10^7$  and the magnetic Prandtl number is  $\sim 20$ . We use a temperature dependent resistivity ( $\eta \propto T^{-3/2}$ ) for these simulations, where the ratio between the vertical oscillation period and the plasma resistive time varies from  $10^{-3}$  at the plasma core up to 10 at the plasma edge. This means that the plasma behaves as an ideal conductor in the plasma core and it transitions continuously to a very resistive plasma at the edge region. The ratio between wall and plasma core resistivity is taken to be 10. The perpendicular particle diffusivity and thermal conductivity are neglected for this study.

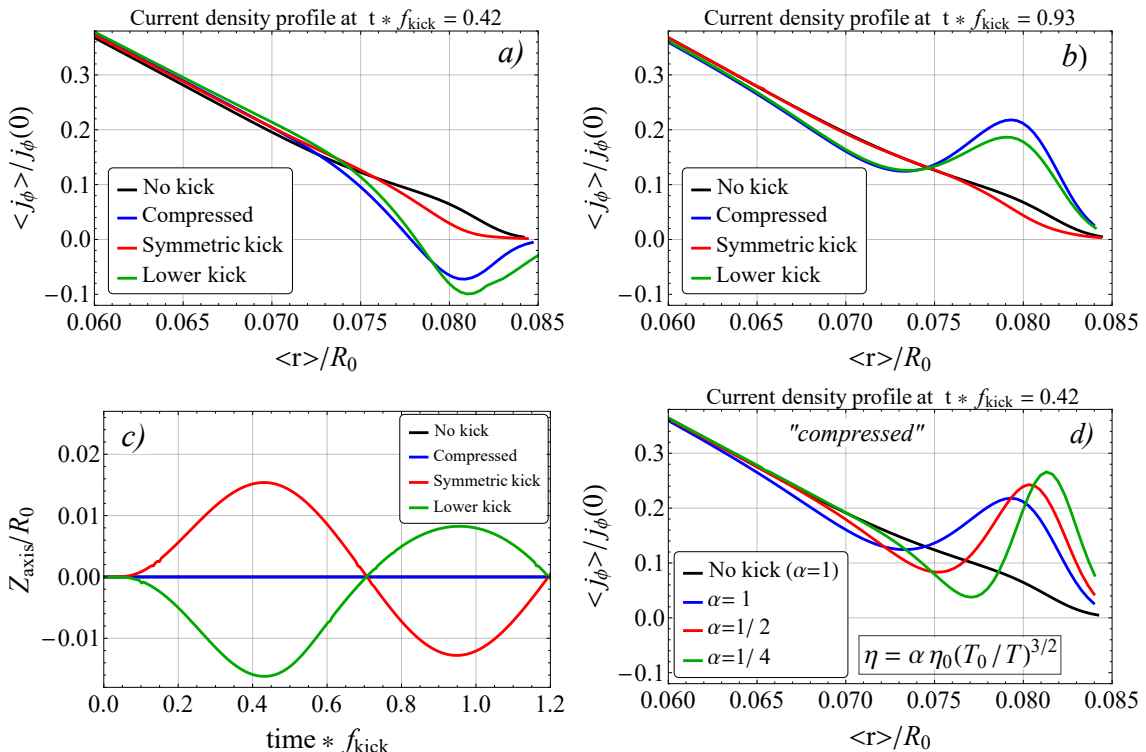


FIGURE 4.2: Current induction during vertical oscillations for the symmetric PF coil configuration. (a) Averaged toroidal current density as a function of the averaged minor radius at time  $\bar{t} = t f_{\text{kick}} = 0.42$ , (b) same for time  $\bar{t} = t f_{\text{kick}} = 0.93$ . (c) Vertical position of the magnetic axis as a function of time. (d) Averaged toroidal current as a function of minor radius at time  $\bar{t} = t f_{\text{kick}} = 0.93$  for different plasma resistivities. Note that  $\alpha$  is a scaling factor for the resistivity profile. The legends are explained in detail in section 2.1.1.

## Symmetric PF coils

The first PF coil configuration respects vertical symmetry with respect to the plasma magnetic axis (Figure 4.1 b) and the coils (PF1/PF2) have currents with equal sign and magnitude. The VS coil currents are sinusoidally varied over time with a frequency  $f$  for 3 different current waveforms

<sup>2</sup>In what follows we'll use the name Vertical Stabilization (VS) coils for the coils in which currents vary over time.

1. "**Compressed**": The coil currents try to compress or expand the plasma as they share equal magnitude and sign.  $I_{VS1} = I_{VS2} = I_0 \sin(2\pi ft)$ . No vertical motion is expected.
2. "**Symmetric kick**": Currents have equal magnitude but different signs.  $I_{VS1} = -I_{VS2} = I_0 \sin(2\pi ft)$ . Vertical motion is expected.
3. "**Lower coil kick**": Only the lower coil is used.  $I_{VS1} = 0$  and  $I_{VS2} = 2 * I_0 \sin(2\pi ft)$ . Vertical motion is expected with enhanced lower displacement.

In figure 4.2, we show the position of the plasma center over time together with the averaged<sup>3</sup> toroidal current profiles at the times when the plasma reaches its extreme positions. From this figure we observe that the impact of a symmetric oscillation on the edge current is not significant. However, only using the lower coil or using both coils with the same current sign induces a significant amount of negative edge current. This is in agreement with our previous analytical model (equation 4.6) when considering the term  $\delta\psi_{ext}(a_0)$  which can drive current without plasma motion. Only the cases that produce net external flux  $\delta\psi_{ext}$  induce currents, the "symmetric kick" case is the only one that doesn't produce net external flux because the fluxes produced by the VS coils with different sign and same magnitude cancel. A scan on the resistivity ( $\eta$ ) is also performed for the "compressed" case, which reveals that the penetration depth of the current increases with resistivity; this agrees quantitatively with the scaling of the skin depth  $\delta_{skin} \propto \sqrt{\eta}$ . As shown in figure 4.2 (d), increasing the resistivity by a factor 4 implies an increase of the penetration depth by a factor 2.

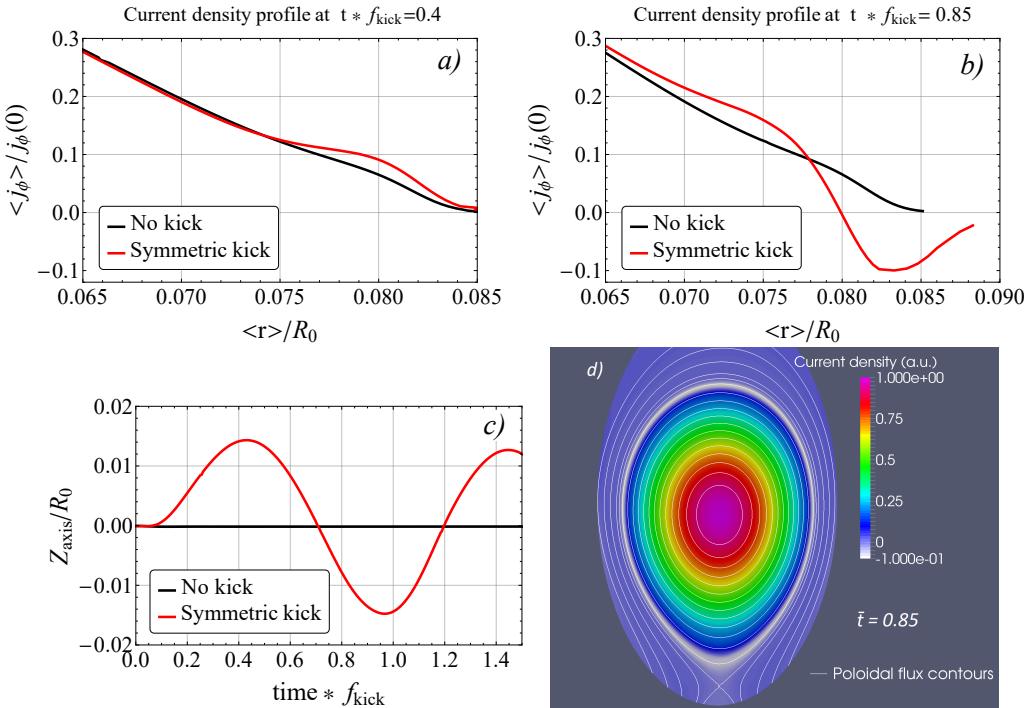


FIGURE 4.3: Current induction during oscillations for the asymmetric PF coil configuration. (a) Averaged toroidal current density as a function of the averaged minor radius for time  $\bar{t} = tf_{kick} = 0.4$  at highest vertical position, (b) same for time  $\bar{t} = tf_{kick} = 0.85$  at lowest position. (c) Vertical position of the magnetic axis as a function of time. (d) 2D contour map of the current density profile showing that the negative induced current is poloidally distributed along the flux surfaces at  $\bar{t} = tf_{kick} = 0.85$ .

<sup>3</sup>Quantities with  $\langle \rangle$  are averaged on the flux surfaces contours.  $\langle A \rangle \equiv \left( \oint_{\psi=cte} Adl \right) / \left( \oint_{\psi=cte} dl \right)$

## Asymmetric PF coils

The second configuration has a vertical asymmetry on the PF coils with respect to the magnetic axis (see Figure 4.1 b), which creates a lower X-point close to the plasma.

In figure 4.3 we show the induced current for the case of an oscillation with symmetry in the VS coils ("symmetric kick"). When moving upwards, a small positive current is induced, but when moving towards the near X-point a significant negative current is induced. Our analytical model can explain these results by considering the terms  $\delta\mathbf{r} \cdot \nabla\psi_{ext}$  and  $-B_\theta(r_0)R_0\delta w_r$  of equation (4.6). The magnetic field gradient is larger in the lower position and therefore when the plasma approaches PF2 it experiences a net increase of external poloidal flux which drives a current by the term  $\delta\mathbf{r} \cdot \nabla\psi_{PF2}$ . The plasma also experiences an expansion as its lower part is more attracted by PF2 than the upper part. This enhances as well an additional decrease of current through the term  $-B_\theta(r_0)R_0\delta w_r$ . A more intuitive explanation for the negative sign is the fact that the plasma approaches a current with the same sign, and therefore a screening current with opposite sign is induced inside the plasma. From this point of view, we would generally expect to induce negative currents when the plasma moves towards the closest X-point. However, positive currents are induced in that situation for JET and ITER geometries. As it will be shown in the next section, ITER plasmas experience a reduction of volume in the latter case, which is the main cause of the increase in positive current.

### 4.2.2 ITER case

Here we perform an analysis of a realistic vertical position oscillation with a 7.5MA/2.65T ITER H-mode plasma. This case was presented in [Gri+15a] for vertical oscillation studies with the code DINA and we have used it to benchmark JOREK-STARWALL. For the benchmark we have included the same 2D axisymmetric model for the ITER wall and passive structures, which STARWALL discretises in thin triangles (see Figure 4.4). The vacuum vessel is modelled as two thin stainless steel layers with a width of 6 cm each, the conducting OTS (Outer Triangular Support) and DIR (Divertor Inboard Rail) are included as well.

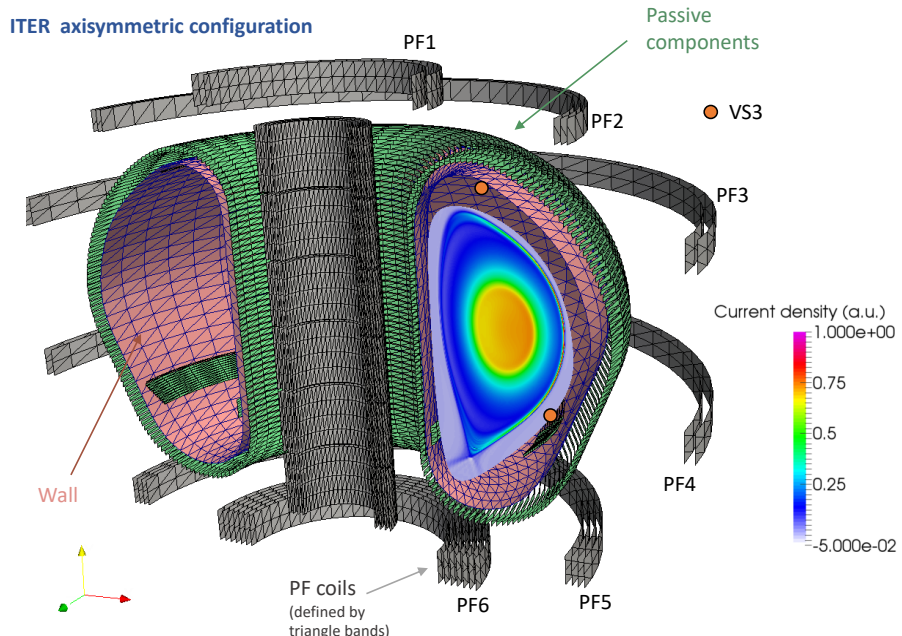


FIGURE 4.4: Geometrical modelling of PF coils, walls and passive structures in JOREK-STARWALL for the ITER case presented in [Gri+15a].

We show the agreement of the plasma vertical position over time between JOREK-STARWALL and DINA in Figure 4.5. It is important to note that in order to get this good agreement between the two codes we had to carefully implement all the mutual inductances of the system, in particular the mutual inductance between passive components and coils was required, otherwise the plasma final displacement obtained for a given set of currents could be overestimated by a factor of 2. This is due to the fact that the coils used to produce the vertical motion (VS3 in Figure 4.4) are very close to the vacuum vessel and the triangular support, which can screen significantly the poloidal field created by the coils.

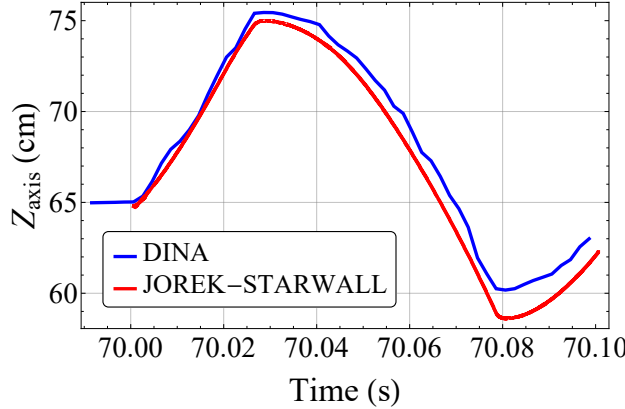


FIGURE 4.5: Benchmark of JOREK-STARWALL with the DINA case. The vertical position of the magnetic axis is shown over time during the vertical oscillation.

The vertical oscillation frequency for the benchmark case was  $f = 10$  Hz and the total current variation in the in-vessel coils (VS3 system) was  $\Delta I_{VS3} = 240$  kA-turns which is the maximum achievable with the VS3 coil design in ITER. In the following simulations, we have added two extra PF coils (AUX-1, AUX-2) in order to study the influence of different coil configurations on the induction of edge current during the vertical oscillation (see figures 4.6 and 4.7). The MHD model used for these simulations [Huy+09] includes parallel flows, Bohm boundary conditions and free outflow of density and temperature at the divertor plates. As an additional boundary condition, there is no current flow into the divertor targets. The plasma grid is aligned with the initial flux surfaces and the number of used Bezier elements is 24464, mesh accumulation is used as well at the pedestal and at the X-point. The pedestal gradients are maintained due to a local reduction of the density and temperature diffusivities ( $D_{\perp ped} = 0.2 \times D_{\perp core} = 4 \text{ m}^2/\text{s}$ ,  $\chi_{\perp ped} = 0.1 \times \chi_{\perp core} = 2 \text{ m}^2/\text{s}$ ). The parallel heat diffusivity and kinematic viscosity at the core are respectively  $\chi_{\parallel core} = 8.4 \times 10^9 \text{ m}^2/\text{s}$  and  $\nu_{\parallel core} = 20 \times \nu_{\perp core} = 40 \text{ m}^2/\text{s}$ . Where the latter quantities have the following temperature dependences  $\chi_{\parallel} \propto T^{5/2}$  and  $\nu_{\parallel} \propto T^{-3/2}$ . Note that the closure for the parallel heat flux assumes that the pedestal plasma is collisional, which is not the case. The investigation of more appropriate integral closures for the calculation of the parallel heat flux [Ji+17] is left for future work, although the chosen closure is not expected to have a major impact on the profiles before the ELM crash phase, which is the subject of our study.

Because of numerical stability related to the non-linear MHD ELM triggering simulations to be discussed in section 3, we have increased the plasma and wall resistivities by a factor of 15 as well as the oscillation frequency ( $f_{new} = 150$  Hz) keeping constant the ratio  $\tau_{kick}/\tau_{\eta}$  so that edge current induction in these simulations is representative of ITER plasmas. Thus the pedestal top resistivity corresponds to the Spitzer value for a temperature of 430 eV, which corresponds to a real plasma temperature of  $\sim 2.5$  keV (when  $f = 10$  Hz) as expected for 7.5MA/2.65T H-modes.

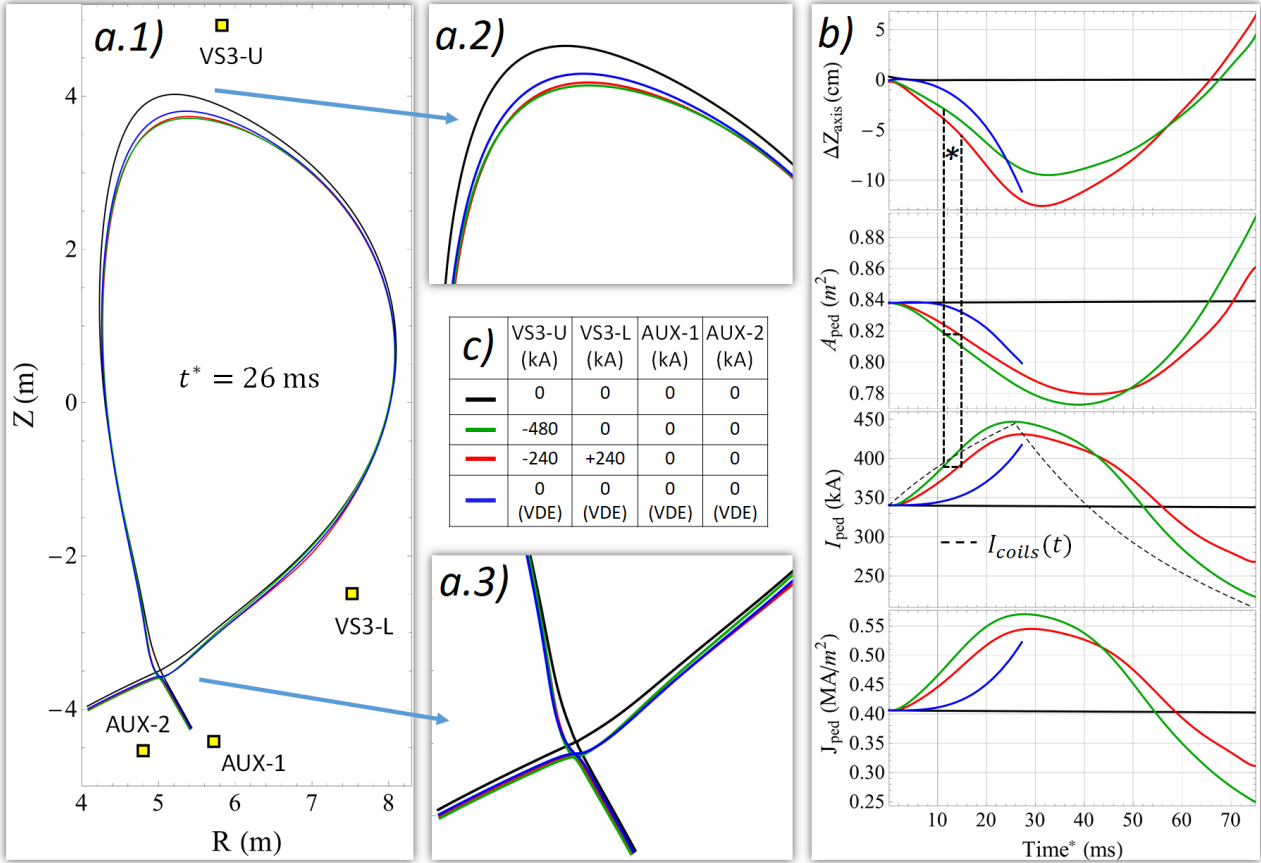


FIGURE 4.6: ITER current induction study for different coil configurations. a) Separatrix at  $t^* = 26$  ms for different coil currents and geometries. b) Time traces of the vertical displacement of the magnetic axis  $\Delta Z_{axis}$ , the pedestal area  $A_{ped}$ , the pedestal toroidal current  $I_{ped}$  and the averaged toroidal current density  $J_{ped} \equiv I_{ped}/A_{ped}$ . c) Maximum current used (in kA-turns) in the time-varying coils for the different cases. Note that currents larger than 240 kA-turns in any of the VS3 coils is beyond the ITER design limits, these values are only used to extract physics results. Note as well that the AUX coils do not exist in the ITER design and are only used for physical understanding.

We have divided the results of the study into two figures (figures 4.6 and 4.7), where we show the different PF coil geometries, the used PF coil currents and the obtained time traces of different plasma quantities. The separatrix at time  $t^* = 26$  ms<sup>4</sup> is also compared for the different configurations. The legend tables indicate the maximum total current used in the VS3 and AUX coils for the different cases. Note that currents larger than 240 kA-turns in any of the VS3 coils is beyond the ITER design limits, these values are only used to explore a wider range of the induced currents with an ITER-like geometry. Similarly the AUX coils do not exist in the ITER design and they are only used for understanding how edge currents are induced. Note that there is a special time trace (dark blue), where we have increased the wall resistivity by a further factor of 10 such that a natural VDE was destabilised. For that case, the chosen wall resistivity was such that the the plasma moved downwards with a similar time scale and displacement as the oscillation cases; this case allows us to study the current induction without the influence of time-varying coil currents.

The cases where more current  $I_{ped}$  is induced are the cases in which the plasma develops a larger reduction of the pedestal cross-sectional area  $A_{ped}$  (see Figures 4.6 b and 4.7 b). It should be noted that some coil configurations are more efficient than others in reducing the plasma cross-section and thus inducing current. For example to use only the upper VS3 coil

<sup>4</sup>for clarity, we define the re-scaled time as  $t^* \equiv 15 \times t_{simulated}$

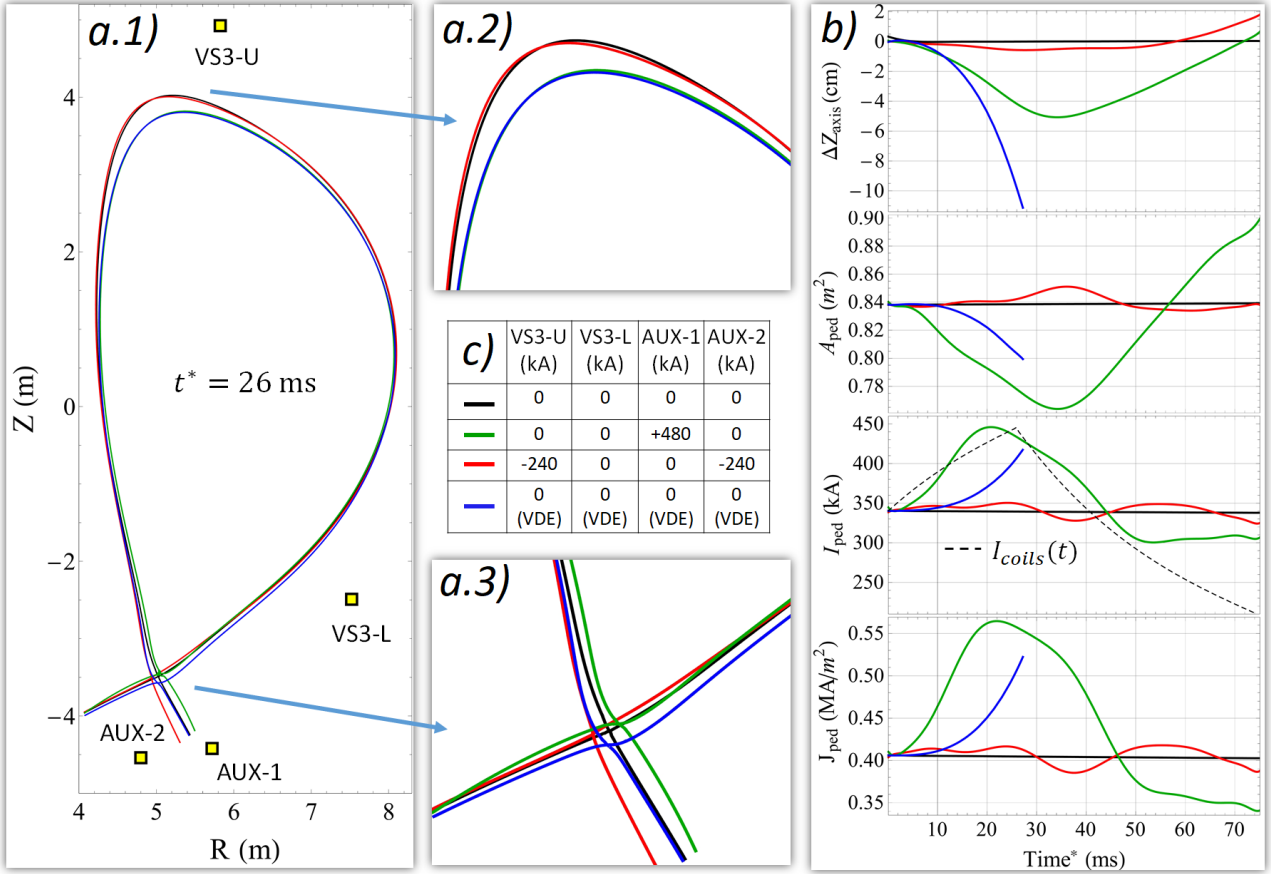


FIGURE 4.7: ITER current induction study for different coil configurations. a) Separatrix at  $t^* = 26$  ms for different coil currents and geometries. b) Time traces of the vertical displacement of the magnetic axis  $\Delta Z_{axis}$ , the pedestal area  $A_{ped}$ , the pedestal toroidal current  $I_{ped}$  and the averaged toroidal current density  $J_{ped} \equiv I_{ped}/A_{ped}$ . c) Maximum current used (in kA-turns) in the time-varying coils for the different cases. Note that currents larger than 240 kA-turns in any of the VS3 coils is beyond the ITER design limits, these values are only used to extract physics results. Note as well that the AUX coils do not exist in the ITER design and are only used for physical understanding.

(green curve in figure 4.6) is more efficient than to use the two ITER VS3 coils in anti-series (red curve in figure 4.6) as required for vertical plasma stabilization. In order to obtain the same  $I_{ped} = 390$  kA, using the VS3 coils in anti-series requires a vertical displacement of  $\Delta Z_{axis} = 5.5$  cm while only using the upper VS3 coil requires  $\Delta Z_{axis} = 3$  cm (see figure 4.6 b\*). The compression can be also enhanced by moving the position of the X-point with the AUX coils (see green curve in figure 4.7).

The VDE case is very similar to the case in which both VS3 coils are used in anti-series in terms of current induction, comparable currents are induced at similar positions and pedestal areas (see figure 4.6 b). From this observation it can be concluded that the time-varying coil currents do not directly influence the pedestal current, but it is rather the resulting plasma motion that causes the compression and induces current. Therefore the term  $\delta\psi_{ext,coils}(a_0)$  of equation (4.6) has little impact in this case. If that term were the dominant one, the case where the plasma position has been kept fixed and the coil currents aim to compress the plasma would have induced a significant current (see red curve of Figure 4.7).

The change in plasma cross section is due to the fact that the top of the plasma (see figure 4.6 a.2) moves faster than the X-point (see figure 4.6 a.3). This effect is due to the vertical asymmetry of the external magnetic field produced by the PF coils. Therefore we expect a weaker induction of current for symmetric double-null plasmas. In Figure 4.8 we show the

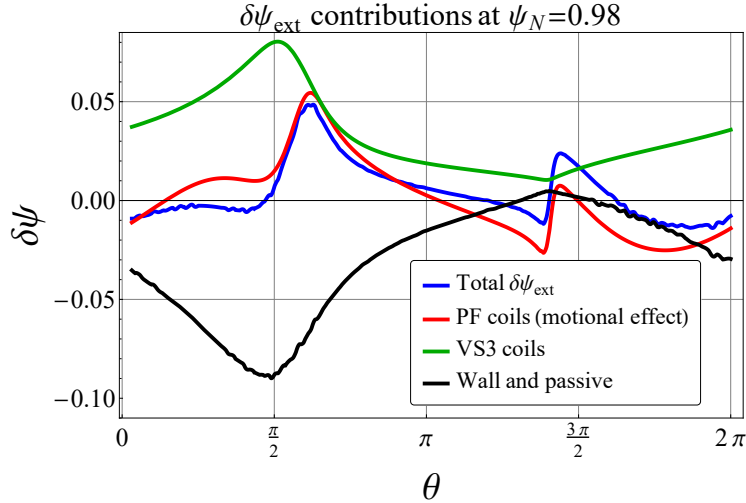


FIGURE 4.8: External flux variation at the  $\psi_N = 0.98$  flux surface after a downward displacement of  $-1.4$  cm.  $\theta$  is the angle along the flux poloidal contour and the curves represent the different contributions to  $\delta\psi_{ext}$ . This case corresponds to the oscillation with  $I_{VS3L} = -I_{VS3U} = 240$  kA. The flux difference is done with a small  $\Delta Z$  in order to keep the plasma deformation small so the angle  $\theta$  still identifies correctly the displaced position.

change in external flux along the poloidal angle  $\theta$  for the flux surface  $\psi_N = 0.98^5$ , the flux difference is taken after a downward displacement of  $\Delta Z_{axis} = -1.4$  cm. The change in total external flux (blue curve) is separated into the contributions due to the currents in the walls and passive structures, the currents in the VS3 coils and the motion through the static field produced by the PF coils (motional effect). The figure reveals that total change in external flux ( $\delta\psi_{ext}$ ) is determined by the motional effect contribution ( $\delta\mathbf{r} \cdot \nabla\psi_{PF}$ ) while the other contributions cancel approximately each other.

As an overall conclusion, the increase in pedestal current arises from the motion of the plasma through the asymmetric magnetic field produced by the PF coils in ITER single-null plasmas. During the vertical motion, the reduction of plasma cross-section and the variation of external flux cause an increase of current through the terms  $-B_\theta(r_0)R_0\delta w_r$  and  $\delta\mathbf{r} \cdot \nabla\psi_{PF}$  of Eq. (4.6). Plasma compression can be enhanced by using different coil configurations to move the plasma as well.

Finally the time traces also show that the change in the averaged current density  $\delta J_{ped}$  is dominated by the change in total current  $\delta I_{ped}/I_{ped} \sim 23\%$  rather than the change in the pedestal area  $\delta A_{ped}/A_{ped} \sim 8\%$ .

### 4.3 ELM triggering for an ITER plasma

In this section we study the non-linear MHD stability of ITER plasmas subjected to vertical position oscillations as described in the previous section. As a reminder, the frequency of the vertical motion was scaled by a factor 15 ( $f = 10 \rightarrow 150$  Hz) as well as the wall and plasma resistivities in order to keep the ratio  $\tau_{kick}/\tau_\eta$  constant. Unless noted otherwise, the vertical oscillation is performed with the ITER baseline coil configuration (VS3 U/L) with maximum current amplitudes of 240 kA-turns per coil. As our main interest is to show the ELM destabilization principle, we only consider the toroidal mode number  $n = 6$  interacting non-linearly with the axisymmetric mode  $n = 0$  for the sake of simplicity. More realistic

---

<sup>5</sup>The radial coordinate  $\psi_N$  is the normalized poloidal flux, being 1 at the separatrix and 0 at the plasma core.

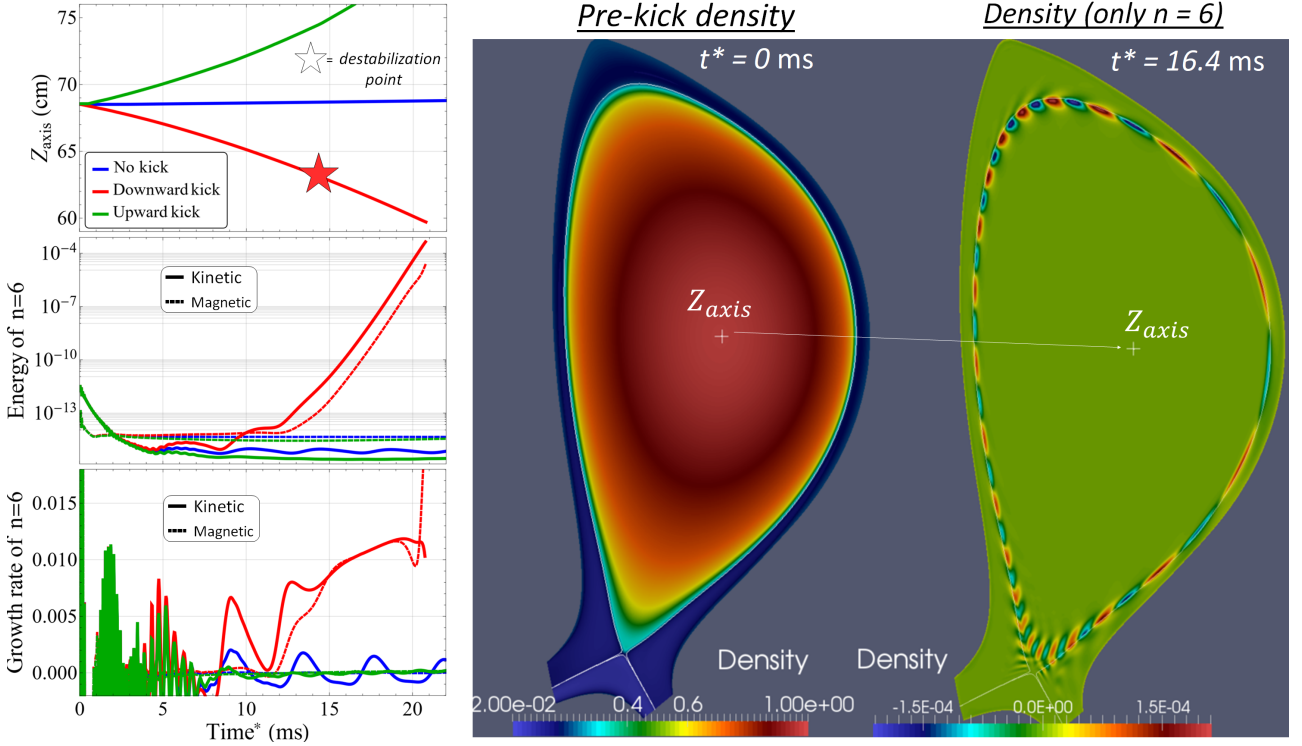


FIGURE 4.9: (Left) Time traces of the position of the magnetic axis, the normalized energies and growth rates of the mode  $n = 6$ . (Right) Pre-kick plasma density and the destabilized  $n = 6$  linear mode structure of the density.

simulations would require to include diamagnetic and neoclassical flows in our model in order to stabilize high- $n$  mode numbers; we leave this task for future work.

In Figure 4.9 we present an example of how an initially stable  $n = 6$  mode can be destabilized by applying a vertical downward motion. The destabilized mode structure presents the characteristics of a peeling-balloonning mode [Huy05] formed close to the plasma separatrix. We define the destabilization point as the time in which the magnetic and kinetic growth rates agree within 10 % and a mode structure is clearly formed. An upward vertical motion was also applied but this does not lead to the increase of the plasma kinetic and magnetic energies nor to the triggering of an ELM. In order to study in more detail the effect of upward and downward motions, we repeat the same study for an initially unstable case and we analyse its influence on the growth rate.

The study shown in Figure 4.10 reveals that a downward motion can further destabilize an initially unstable peeling-balloonning mode by increasing its growth rate. On the other hand, the upward motion can decrease the growth rate down to negative values and stabilize the mode. A comparison of the current and pressure gradient profiles at points with increasing, constant and decreasing growth rate shows that the destabilizing mechanism can be associated with changes in the pedestal current. Indeed increasing the current density at the pedestal and at the separatrix drives the peeling-balloonning modes more unstable. It is also important to note that in these simulations the edge pressure gradient increases during the downward motion and this could be an additional destabilization mechanism for the ELM.

Experiments in JET [Lun+15] demonstrated that the triggering of ELMs by vertical plasma oscillations strongly depends on the plasma displacement  $\Delta Z_{axis}$  but not on the plasma velocity during the oscillation. In Figure 4.11 we show the results of a scan on the plasma vertical velocity for a downward motion. For an initially stable case, an ELM was destabilized at the same vertical displacement ( $\Delta Z_{axis} \approx 5.5$  cm) for the three cases with different velocities of

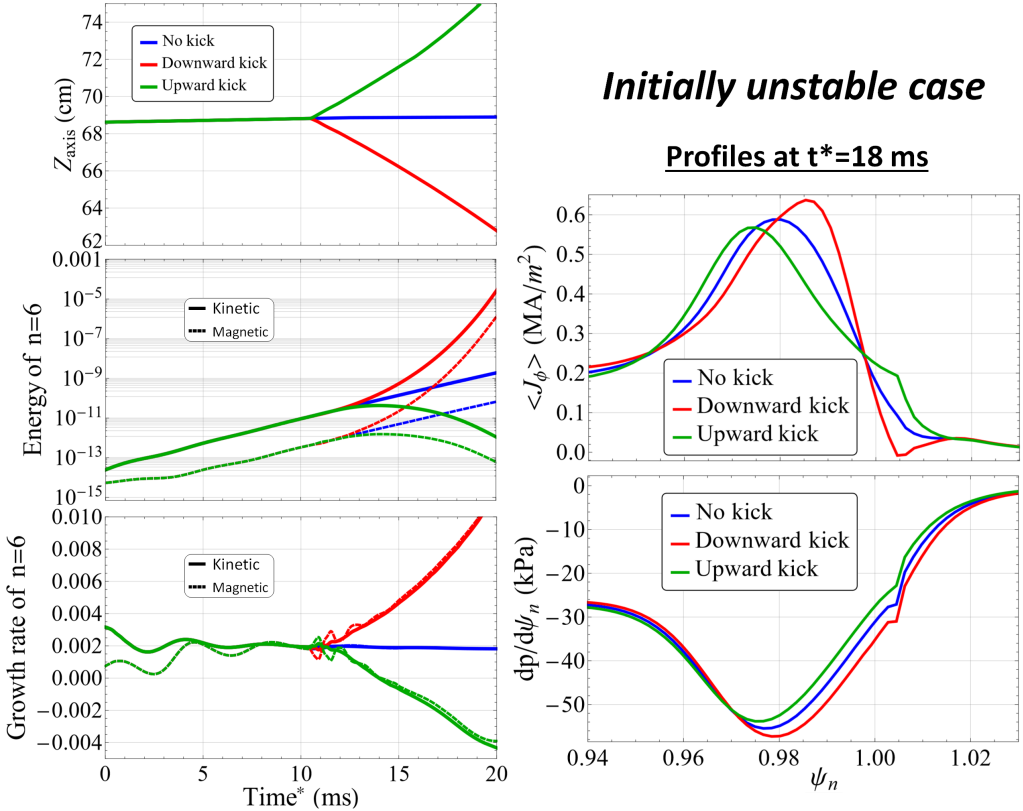


FIGURE 4.10: (Left) Time traces of the position of the magnetic axis, the normalized energies and growth rates of the mode  $n = 6$ . (Right) Averaged toroidal current and pressure gradient profiles at  $t^* = 18$  ms. For this particular case, the time-scale of the motion  $\tau_{kick}$  has been reduced by a factor 2 to better observe the change in the growth rates before reaching the non-linear phase of the downward kick case.

the vertical motion in agreement with experimental observations. If we assume that the induced edge current is the main cause of the ELM destabilization, this could be well explained by the prediction of equation 4.6, where the plasma speed only plays a role through the resistive decay term (which is expected to be very small for the high pedestal plasmas in ITER H-modes). At the destabilization point, the current and pressure gradient profiles were very similar, supporting the idea that the ELM triggering can be described in terms of the stability of equilibrium states, i.e. it does not depend on the kick velocity.

In order to further explore the influence of the induced edge current on the triggering of ELMs, we have performed the same vertical position oscillation on four different starting equilibria. For this vertical oscillation study only the upper VS3 coil has been used as this coil configuration induces more current for smaller displacements and makes these physics target simulations possible<sup>6</sup>. The different starting equilibria have the same pressure profile but different averaged current profiles (Figure 4.12 "pre-kick profiles"). If the instability is triggered by an increase of edge current during the vertical motion, we expect to require bigger displacements for lower initial edge currents. Indeed, the results shown in Figure 4.13 support this hypothesis. Moreover, the destabilization occurs when the current density values become comparable to the initially unstable case, i.e. the black curve. As it can be observed, the pressure profiles also vary during the motion, this is due to the adiabatic compression of the pedestal that follows the law  $PV^\gamma = cte$ . Therefore the evolution of the pressure profile could

<sup>6</sup>for the equilibrium with lowest current, the use of both VS3 coils in anti-series would require a downward displacement of  $\sim 16$  cm which significantly modifies the plasma geometry at the divertor making it very difficult to model.

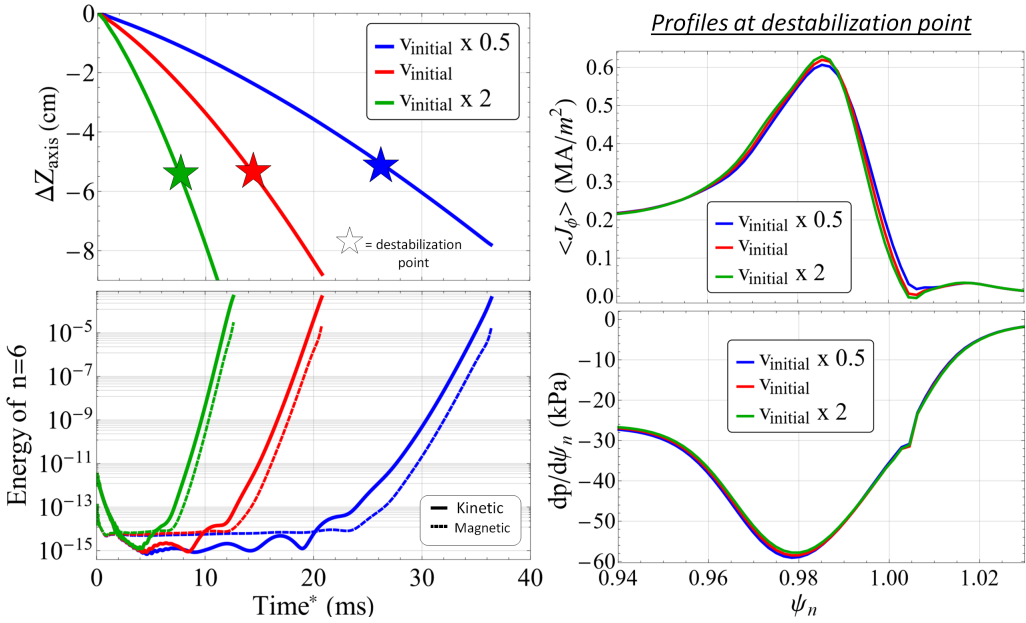


FIGURE 4.11: (Left) Time traces of the position of the magnetic axis and the normalized energies of the mode  $n = 6$ . (Right) Averaged toroidal current and pressure gradient profiles at the destabilization point.

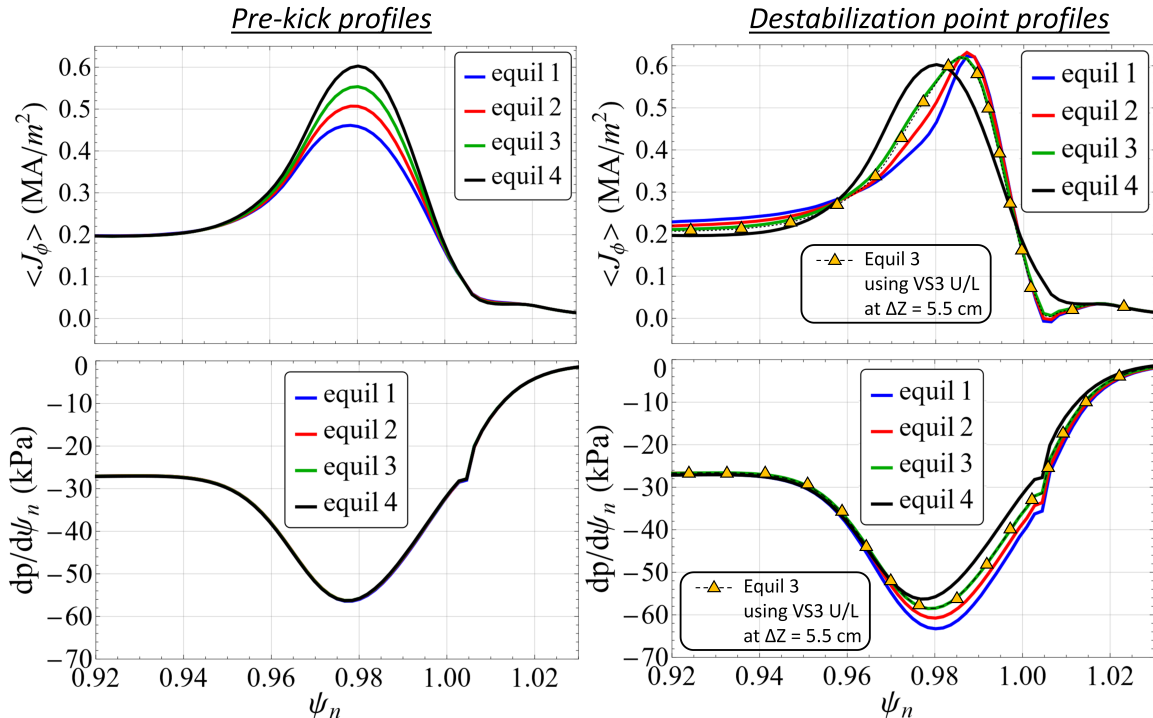


FIGURE 4.12: Profiles for the vertical oscillation shown in (Figure 4.13). (Left) Initial current and pressure profiles. (Right) Profiles at the destabilization points. For reference, the dashed curve indicates the profiles at the destabilization point when using the baseline coil configuration (see Figure 4.9), where the starting equilibrium corresponds to the green curve.

potentially contribute to the triggering of the ELM instability. However this effect cannot be the dominant one, as the starting pressure profiles were identical in all the cases and they present different peak values at the destabilization points which shows that the main destabilizing factor is the edge current. In addition the mode structure has a strong peeling component (Figure 4.9) which reinforces the idea of the current as the main mechanism that destabilizes

the ELM.

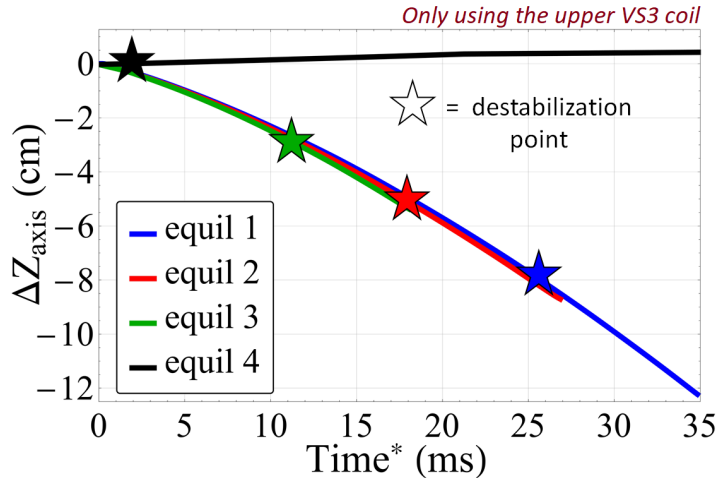


FIGURE 4.13: Plasma vertical displacement with time for the different starting equilibria (Figure 4.12). The destabilization points are marked with a star symbol.

## 4.4 Conclusions

ELM triggering via vertical position oscillations has been experimentally demonstrated in the TCV [Deg+03], AUG [Lan+04] and JET [Lun+15] tokamaks proving to be a reliable technique for the ELM frequency control. In this paper, the physics of the ELM triggering mechanism via vertical oscillations was studied for the first time in non-linear MHD simulations with the free-boundary code JOREK-STARWALL and applied to ITER 7.5MA/2.65T H-mode plasmas.

References [Lun+15; Gri+15a] propose the induction of edge current during the vertical oscillation to trigger ELMs by this scheme. In this chapter, a simple analytical model was derived in order to illustrate the origin of this current (equation 4.6), showing it to be independent on the speed of the vertical motion for ideal plasmas and to result from a change on the boundary external flux and plasma compression. The edge current induction was also studied with JOREK-STARWALL for a simple elongated plasma and for a realistic ITER 7.5MA/2.65T H-mode plasma. For the simple case, the analysis showed that the induced current can be understood as a screening current reaction of the plasma against the change of external magnetic flux, either if the change is produced by a strong asymmetry in the VS coils ( $\delta\psi_{VS}(a_0)$ ) or by the plasma motion through an inhomogeneous magnetic field ( $\delta\mathbf{r} \cdot \nabla\psi_{PF}$ ). The ITER case revealed that the induced edge current can also be strongly related to the plasma compression due to its motion through the top-down asymmetric magnetic field. In addition, the results in figures 4.6 and 4.7 indicate that the compression and the induced current can be enhanced by choosing different geometries and current waveforms for the coils used to displace the plasma as already considered in [Gri+15b].

The phenomenology of the non-linear MHD ELM triggering via vertical position oscillations was simulated in a consistent dynamic scheme for the first time. An initially stable  $n = 6$  mode was found to be destabilized by a downward motion and to remain stable when applying an upward one (see Figure 4.9). The destabilized mode has the structure of a peeling-balloonning mode with a dominant peeling component. Additional simulations with an initially unstable plasma (see in Figure 4.10), revealed that the mode was stabilized by the upward motion and further destabilized by a downward one. JOREK-STARWALL simulations revealed that the pre-oscillation edge current profile determines the minimum plasma displacement required

to destabilize ELMs, with larger displacements being required for lower pre-oscillation edge currents (see Figure 4.13). In agreement with experiments, ELM triggering does not depend on the plasma velocity but on the plasma displacement  $\Delta Z_{axis}$  (figure 4.11). For practical applications at ITER, the minimum vertical displacement that is required for ELM triggering will strongly depend on the edge current, which is expected to be large in ITER due to the low pedestal collisionalities of H-mode plasmas. In the H-mode 7.5MA/2.65T plasma modelled, ELMs were triggered for displacements of 5–6 cm, these displacements can be obtained with the ITER VS3 coil set in anti-series for typical oscillation frequencies of 10 – 15 Hz and maximum currents of  $I_{VS3} = 160 – 200$  kA-turns [Gri+15a].

The simulations confirm the hypothesis of the induced edge current as the essential mechanism for the ELM destabilization. The requirement of larger displacements for lower initial currents and the fact that the edge current increases for downward motions reinforce the idea of the edge current as the main destabilizing factor. The destabilized mode presents a strong peeling structure as well. This mechanism can also explain the weak dependence of the ELM triggering on the vertical speed as indicated by equation (4.6). The role of pressure profile modifications during the vertical plasma oscillation do not seem to be the main driver for ELM triggering. However, an accurate assessment of the effects of the pressure gradient changes on the ELM triggering by vertical position oscillations requires further investigations.



# Chapter 5

## Vertical Displacements Events

### 5.1 Tests and benchmarks for JOREK-STARWALL

In this section several benchmarks and tests are conducted with the aim to validate the axisymmetric VDE evolution of realistic plasmas. A first test is performed to verify the flux-conserving properties of an ideal wall (5.1.1). Secondly a module to solve for the source/sink current equation (3.31) has been implemented in STARWALL. In 5.1.2, this module is benchmarked for a given normal current distribution entering an ITER-like wall including holes. Thirdly a benchmark with the M3D-C1 code [Jar+08] is conducted for the linear VDE growth rates of an experimental NSTX plasma at different wall resistivities (5.1.3). The last benchmark is a comparison with the code DINA [KL93] for an ITER mitigated disruption where the vertical motion is dominated by the current decay of the plasma. In the following simulations "model199" was used, which similar to "model303" (see 2.1.1) but with ( $v_{\parallel} = 0$ ).

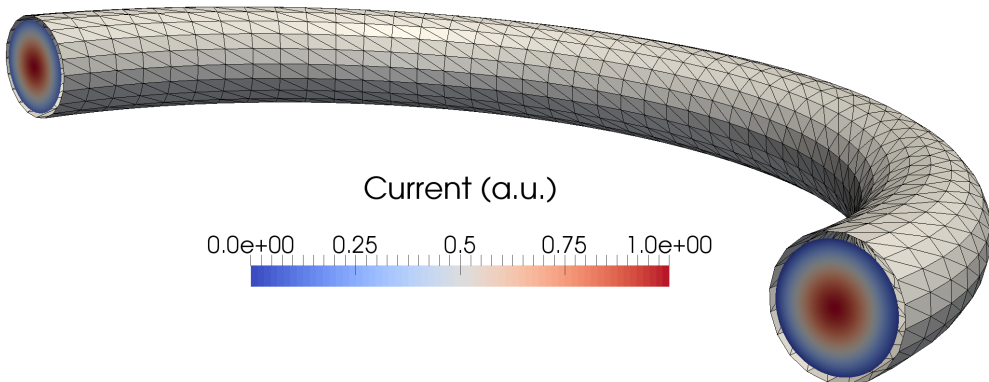


FIGURE 5.1: The circular plasma and wall used for the test for the toroidal net-current potential. The initial current profile of the plasma is shown with a color map.

#### 5.1.1 Test for the toroidal net-current potential

The fast loss of thermal energy ( $\sim 1$  ms) that is produced during a disruption, typically reduces the plasma temperature to a few eV and thus increases the plasma resistivity considerably. During the consequent current quench phase, the toroidal current decays in the time-scale given by the  $L/\mathcal{R}$  time of the plasma. If the current quench is fast enough compared with  $L/\mathcal{R}$  time of the wall (or a nearby conducting component), most of the toroidal current can be transferred to wall. This transfer of net current is captured in JOREK-STARWALL with the net current potential  $I^T$ . It's therefore important to check the behaviour of this current potential in JOREK-STARWALL with a test case.

A simple test case can be constructed by using a circular plasma with a large aspect ratio. If the plasma is surrounded by an ideally and closed conducting wall, the wall will screen every change of the plasma magnetic field, thus keeping the outside magnetic field constant over time. If the aspect ratio ( $A \equiv R_0/a$ ) of wall and plasma is large enough, both can be represented with two wire-loops placed at the same location ( $R_0$ ). The analytical solution of the magnetic field created by the two wire-loops at their geometrical center ( $R = 0, Z = 0$ ) is

$$B_0 = \frac{\mu_0}{2R_0} (I_p + I_w) \quad (5.1)$$

where  $I_p$  is the total plasma toroidal current and  $I_w = I^T$  is the net-current potential containing the total toroidal current of the wall. As mentioned above, the ideal wall implies that  $\partial B_0 / \partial t = 0$  and therefore

$$I_p + I_w = I_0 \quad (5.2)$$

where  $I_0$  is a constant. The constant is the plasma current prior to the current quench when there are not any wall currents. The test consists on checking that equation (5.2) is verified in JOREK-STARWALL. The prepared test case has a plasma minor radius of  $a = 1$  m and a

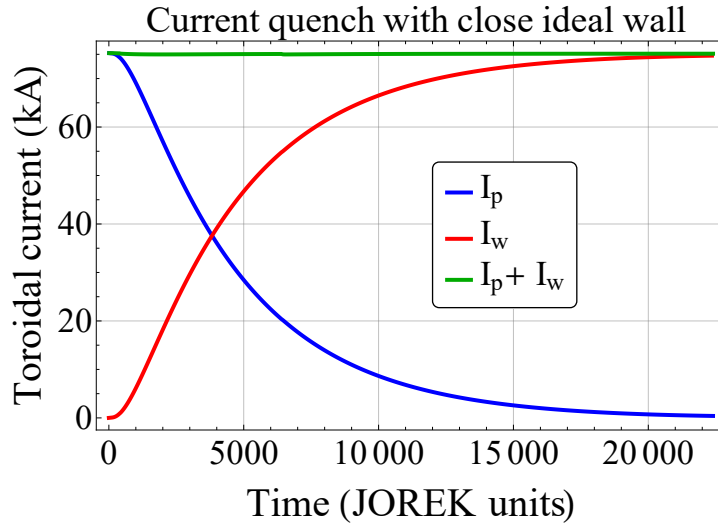


FIGURE 5.2: Plasma ( $I_p$ ) and wall ( $I_w$ ) total toroidal currents and their sum over time.

major radius of  $R_0 = 10$  m, thus its aspect ratio is 10. Similarly the wall has a major radius of  $R_0 = 10$  and a minor radius of  $b = 1.1$  m (see figure 5.1). The initial toroidal current is  $I_0 = 75$  kA and the plasma resistivity is chosen to be spatially constant. The wall time is of the order of 5000 times longer than the resistive decay time of the plasma and thus the wall can be considered as ideal.

The current quench shown in figure 5.2 shows the exponential decay of the current over time. As the plasma current decays, net toroidal current is induced in such a way that the sum of both plasma and wall currents is conserved with deviations of 0.3% with respect to  $I_0$  (see green curve). Thus the conservation law shown in equation (5.2) is well verified in JOREK-STARWALL. Meaning that the STARWALL's ideal wall is able to screen correctly the outside magnetic field.

### 5.1.2 Benchmark for the source/sink current potentials

The equation for the source/sink currents (3.31) can be inverted to obtain the source/sink current potentials ( $\phi^s$ ) as a function of the perpendicular currents ( $\mathbf{J}_\perp$ ) entering the wall

$$\phi^s = M_{SS}^{-1} M_{SJ} \mathbf{J}_\perp \quad (5.3)$$

This allows to calculate the distribution of currents tangential to the wall once the perpendicular currents are provided. During this thesis, a module written in FORTRAN has been implemented in STARWALL in order to calculate the product  $M_{SS}^{-1}M_{SJ}$ . This module has been benchmarked with the SSC code [Ata+16] which solves the same equation. For the benchmark, an ITER-like wall including holes has been considered where the normal current distribution shown in figure 5.3 (a) is specified. The chosen boundary condition is such that the current can not flow across the boundaries. This BC is implemented naturally with the finite element method approach by dropping the contour line integral of equation (3.13).

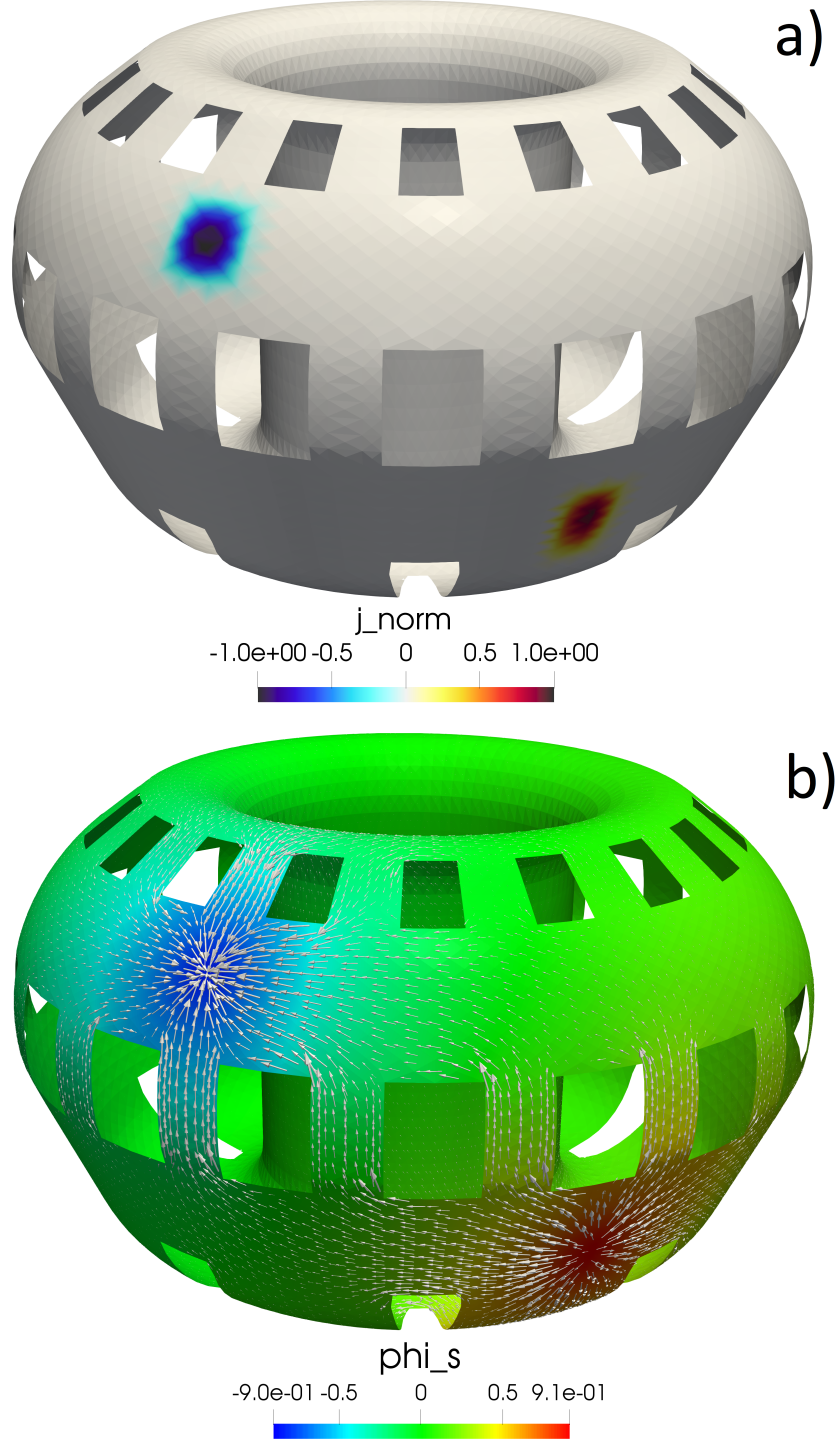


FIGURE 5.3: (a) Distribution of the imposed normal current to the wall. (b) Solved  $\phi_s$  with the resulting current density distribution (white arrows).

In order to be consistent with the boundary condition, the prescribed normal currents must satisfy  $\int J_\perp dS_w = 0$ . Additionally, the potential is free up to a constant and therefore is numerically required to impose a single potential value. The solution to the normal current distribution shown in figure 5.3 (a) is shown in figure 5.3 (b), where it can be observed how the currents flow from the normal current source to the normal current sink by avoiding the wall's holes. For simplicity, the product of wall's conductivity and thickness is chosen as  $\sigma_w d_w = 1$ . The solution found in the STARWALL's new module agrees well with the SSC code as it can be seen in figure 5.4 where the relative differences between the two codes are below  $10^{-7}$ .

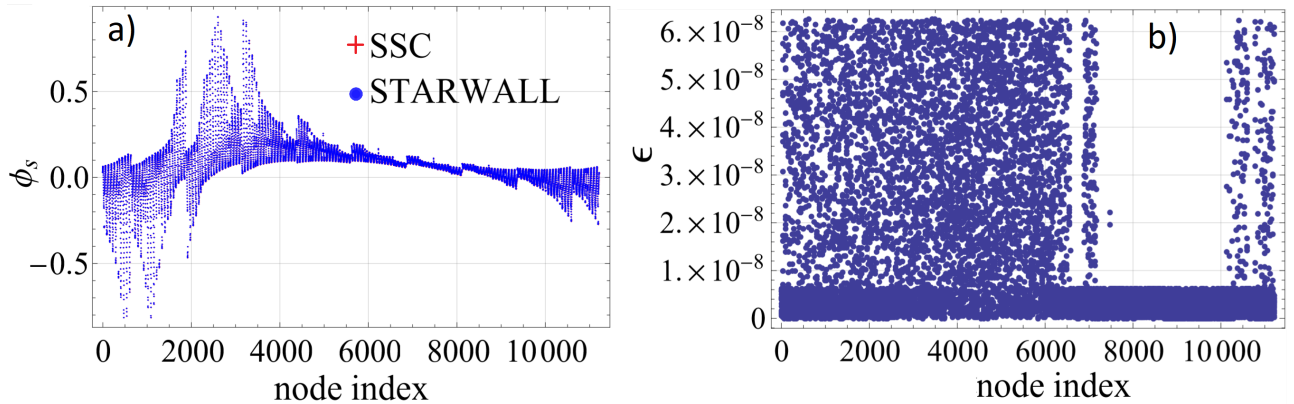


FIGURE 5.4: (a) Node index versus potential value in STARWALL and SSC. (b) Error difference ( $\epsilon = |\phi_s^{\text{STR}} - \phi_s^{\text{SSC}}| / \phi_s^{\text{max}}$ ) between STARWALL and SSC as a function of the node index.

This benchmarked module already allows to calculate the wall forces generated by halo currents once the normal current is provided (i.e. from a VDE simulation). However further work is required to achieve the full coupling between the plasma and the source sink currents which is presented in equations (3.46) and (3.53). In particular the matrices  $M_{ps}$  and  $\mathbf{M}_{\parallel,s}$  need to be computed together with a current conserving mapping between the JOREK Bézier elements and the STARWALL's triangles.

### 5.1.3 Benchmark with M3D-C1

As shown in 1.2.4, the growth rate of VDEs is proportional to the specific resistivity of the wall ( $\gamma_{\text{VDE}} \propto \eta_w$ ). A benchmark between JOREK-STARWALL and the M3D-C1 code [Jar+08] for the linear growth rates of axisymmetric VDEs has been performed at different wall resistivities. It is important to remind the relevance of benchmarking these codes for the fusion community as they are among the leading codes in the field of 3D MHD simulations with free-boundary conditions in toroidal geometry. The starting equilibrium is obtained from the reconstruction of an NSTX experimental discharge where a natural VDE was destabilized. The plasma has a total toroidal current of 0.57 MA and 0.37 T of toroidal field at the magnetic axis. The chosen boundary conditions are Dirichlet for all the plasma variables except for the magnetic field and the current density (which are given by STARWALL). The pressure and safety factor profiles are shown in figure 5.5, where  $p_{\text{axis}} = 11.85$  kPa and  $q_{95} = 7.5$ . The ionic and electronic temperature profiles are assumed to be equal and have the following initial profile

$$T_e = T_i = T/2 = 0.946 \text{ keV} \cdot \left( \frac{p(\psi)}{p(0)} \right)^{0.6} \quad (5.4)$$

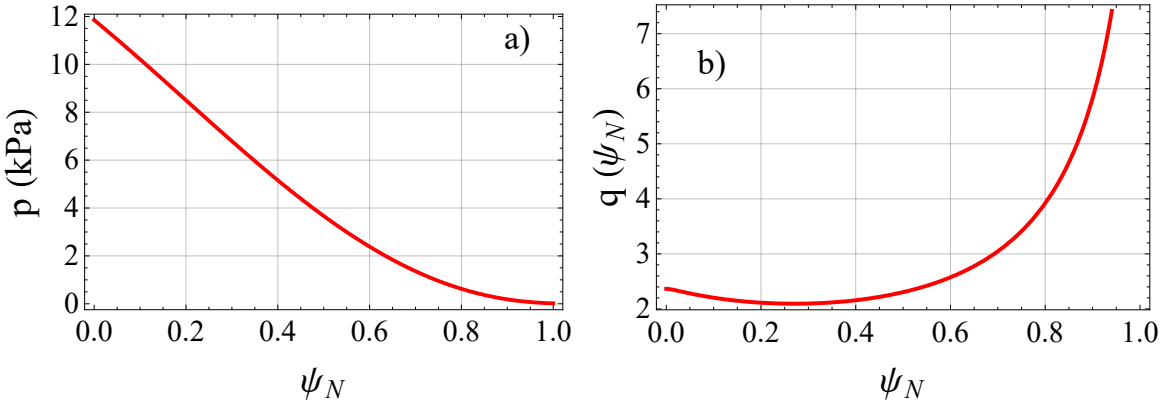


FIGURE 5.5: (a) Pressure profile and (b) safety factor profiles for the benchmark with M3D-C1.

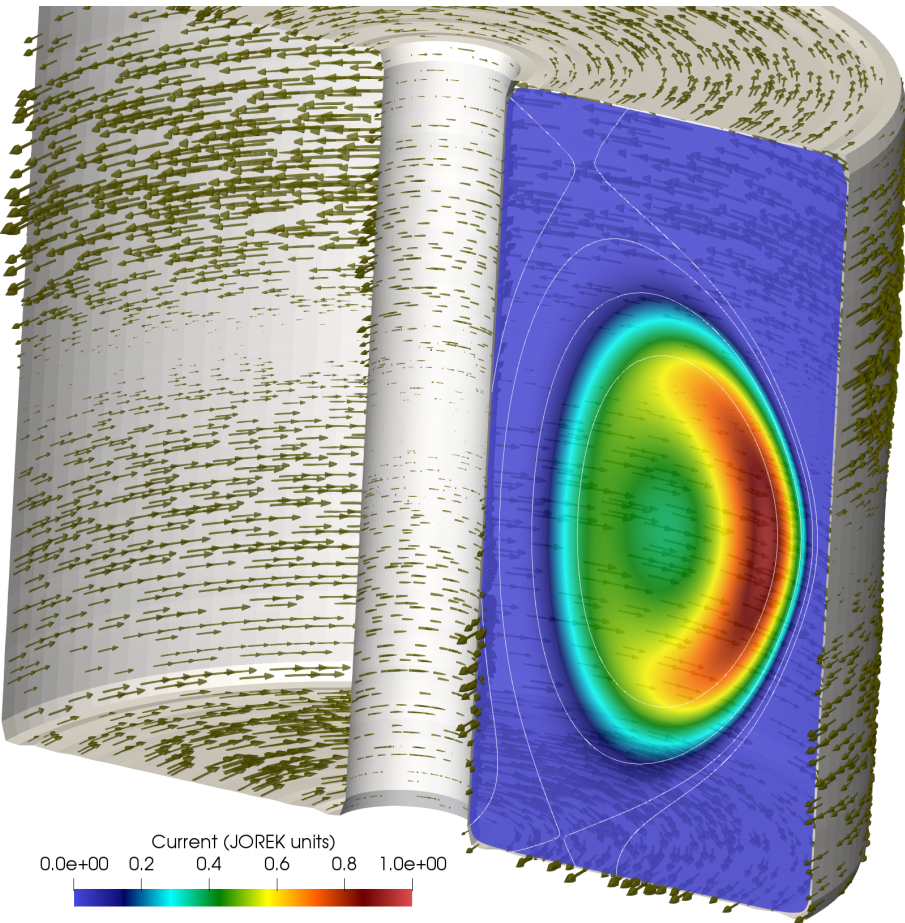


FIGURE 5.6: Contour plot of the toroidal current profile in JOREK together with the rectangular wall for the benchmark with M3D-C1. The arrows represent the induced eddy currents flowing on the wall and the white contours represent the poloidal flux surfaces.

and the profile for the ionic and electronic particle density is

$$n_e = n_i = \frac{p}{T} \quad (5.5)$$

The resistive wall is chosen to be rectangular (see figure 5.6) with the aim to perform a future benchmark with the code NIMROD [Gla+99]. The wall's thickness is  $d_w = 1.5$  cm and its inner boundary has corners at ( $R = 0.24$  m,  $Z = -1.4$  m) and ( $R = 1.6$  m,  $Z = 1.4$  m). When the VDE instability takes place, the vertical position of the magnetic axis ( $Z_{\text{axis}}$ ) follows

an exponential behaviour as it can bee seen in figure 5.7. The growths rates are calculated in JOREK and in M3D-C1 by performing the exponential fit ( $Z_{\text{axis}}(t) = Z_0 + \delta Z e^{\gamma t}$ ). Typically the first points of the  $Z_{\text{axis}}(t)$  curve are removed from the fit as they present numerical noise.

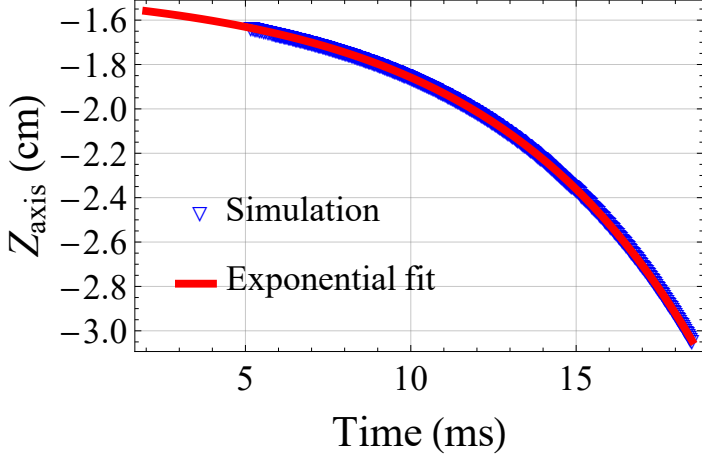


FIGURE 5.7: Exponential behaviour of the vertical position of the magnetic axis with time for the NSTX VDE case. The wall resistivity for this case was set to  $\eta_w = 3\mu\Omega$ .

In the plasma, the resistivity profile has the following Spitzer's dependence

$$\eta = \eta_0 \left( \frac{T_{\text{eff}}}{T_{\text{axis}}} \right)^{-3/2} \quad (5.6)$$

where an effective temperature  $T_{\text{eff}} \equiv T - T_{\text{offset}}$  has been introduced. As the open field-line region is also modelled with the MHD equations, this area can act as a stabilizing wall if the resistivity is not large enough. Note that even if the value of the resistivity can be large for low plasma temperatures ( $\eta(15\text{eV}) \approx 3.10^{-5}\Omega\text{m}$ ), the thickness of the open-field line region can be very large as well ( $d_{\text{SOL}} \sim 30 \text{ cm}$ ) so the relevant ratio for the open-field region's resistance ( $\mathcal{R}_{\text{SOL}} \propto \eta/d \sim 10^{-4}\Omega$ ) can be still comparable with the wall's resistance ( $\mathcal{R}_w \propto \eta/d \sim 0.5 \cdot 10^{-4}\Omega$  for stainless steel). As the wall resistivity is increased, the effect of the open field-line region becomes more relevant as ( $\mathcal{R}_{\text{SOL}} < \mathcal{R}_w$ ) and the vertical motion is regulated by the open-field region.

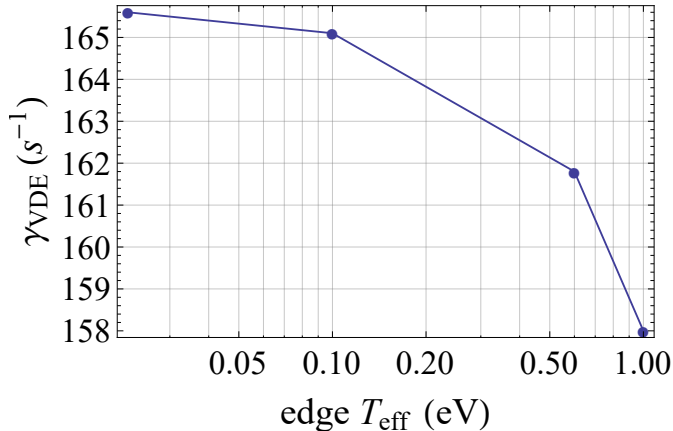


FIGURE 5.8: VDE growth rate as a function of the edge  $T_{\text{eff}}$  for the case with  $\eta_w = 3\mu\Omega$ .

The effective temperature is used in order to avoid the stabilizing effect of the currents induced in the open field-line region. This allows to increase considerably just the domain's

boundary resistivity by tuning  $T_{\text{offset}}$  in order to decrease the boundary's  $T_{\text{eff}}$  without affecting the resistivity of the hot plasma. The influence of  $T_{\text{eff}}$  in the growth rate is shown in figure 5.8. It can be observed that very low values of the temperature are required (below 1 eV) in order to obtain a convergence in the growth rate below 3%. It is important to note that temperatures below 1 eV are rather unrealistic as hydrogenic plasmas start to recombine.

Finally the results for the benchmark are presented in figure 5.9 where for intermediate values of the wall resistivity, the growth rates of both codes agree up to a 2%. For the lowest wall resistivity case, JOREK-STARWALL gives a slightly higher value (9% larger) than the expected from the relation  $\gamma_{VDE} \propto \eta_w$ , which could be related by the fact that at those time-scales the plasma current significantly decays and the current profile changes.

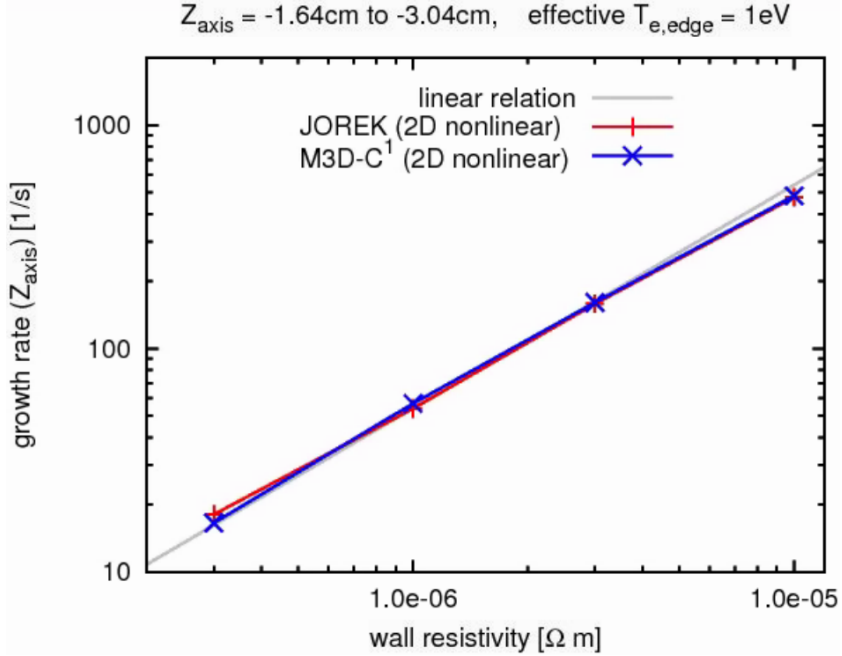


FIGURE 5.9: Axisymmetric VDE growth rate as function of the wall resistivity in JOREK and M3D-C1. The M3D-C1 simulations were prepared and performed by I. Krebs at the PPPL (Princeton Plasma Physics Laboratory) in the U.S.A.

### 5.1.4 Axisymmetric comparison with the DINA code

An additional benchmark has been conducted in order to study the vertical position evolution when the plasma drifts into the first wall. In this case JOREK-STARWALL is compared with the code DINA with an ITER 15MA/5.3T plasma which has disrupted. In DINA, the temperature is reduced to  $\sim 10\text{eV}$  in a time-scale of 1-2 ms and the current profile is flattened in order to mimic a disruption. As the DINA plasmas are toroidally axisymmetric, the disruption phase can't be modelled self-consistently. The current profile is artificially flattened in the region inside the  $q = 2$  flux-surface by assuming conservation of magnetic helicity during this non-ideal process.

The JOREK initial equilibrium is based on an EQDSK file produced by DINA after the flattening of the current profile. The ITER vacuum vessel, poloidal field coils and passive conductors that are used in STARWALL for these simulations are the ones shown in figure 4.4. The JOREK boundary is constructed in order to match the ITER's first wall (limiter) at the upper region where in this case the plasma touches the wall (see figure 5.13). Note that in these simulations a vacuum region between the ITER's first wall (JOREK's computational

boundary) and the ITER's vacuum vessel (STARWALL's wall) is considered. The boundary conditions for the magnetic field are those given by STARWALL and for the electric potential the BC is simply  $u = 0$ . This implies that the tangential electric field ( $\nabla_{\text{tan}} u$ ) along the JOREK's boundary is 0, and thus the first wall is ideally conducting in the poloidal direction but resistive in the toroidal direction. The current quench time for this case is very short

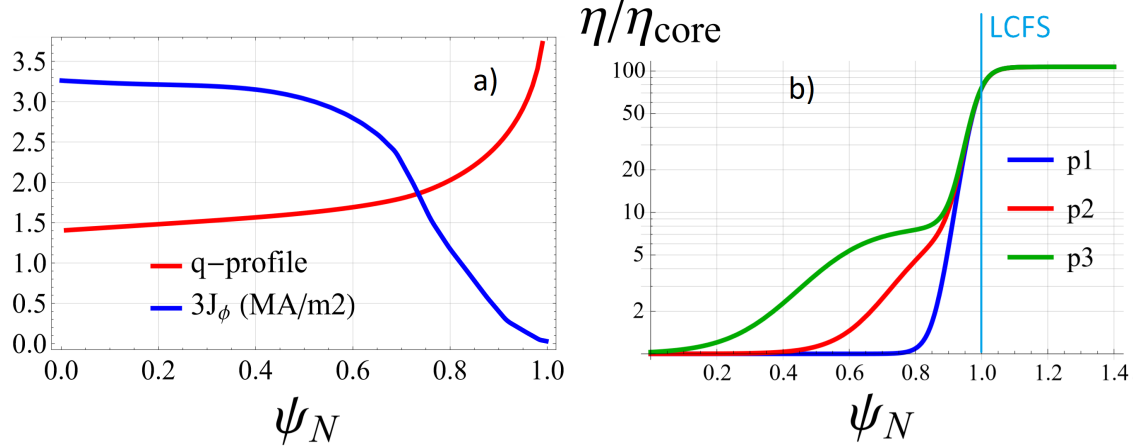


FIGURE 5.10: (a) Initial toroidal current density and safety factor profile for the ITER mitigated disruption case. (b) Different flux-dependent resistivity profiles (normalized to the core resistivity) used for the comparison with DINA.

( $\tau_{\text{CQ}} \sim 20$  ms) compared with the ITER's vacuum vessel wall time ( $\tau_w \sim 0.5$  s), therefore the vertical position is regulated by the decay of the plasma current as it will be shown in next section. In order to define the current quench time, the following definition used in [Eid+15] is taken

$$\tau_{\text{CQ}} = (t_{80\%} - t_{20\%})/0.6 \quad (5.7)$$

where  $t_{80\%}$  and  $t_{20\%}$  are the times where the toroidal current reaches 80% and 20% of its pre-disruptive value.

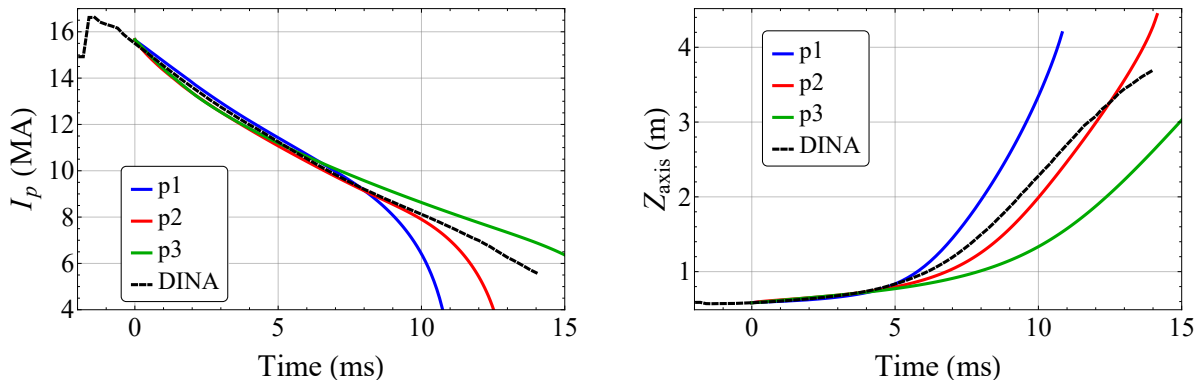


FIGURE 5.11: Toroidal current (left) and vertical position of the magnetic axis (right) over time for the different tested resistivity profiles shown in 5.10 (b).

For these simulations a flux-dependent resistivity profile  $\eta(\psi)$  has been used. This choice is made in order to have a full control of the resistivity profile so its influence on the vertical motion can be studied without the complexity of controlling the temperature profile. For the comparison, three tested resistivity profiles shown in figure 5.10 (b) are scaled by a factor in

order to match the DINA's current time trace  $I_p(t)$  (see figure 5.11 (a)). The resistivity in the open-field region is chosen to be 100 times bigger than in the plasma core and therefore the induced halo currents are not significant in these simulations.

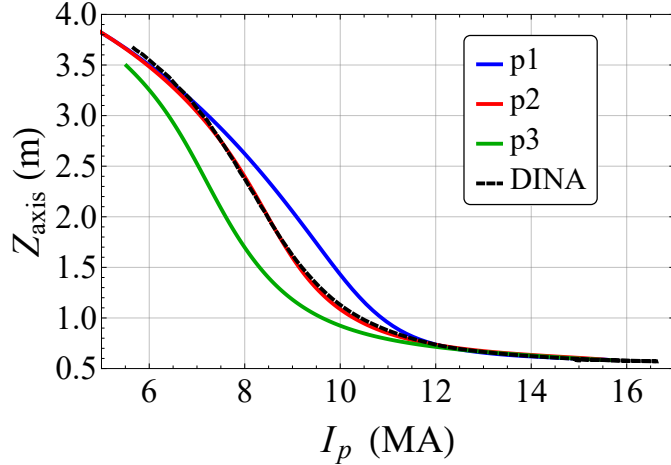


FIGURE 5.12: Vertical position of the magnetic axis as a function of the plasma toroidal current for the different tested resistivity profiles shown in 5.10 (b).

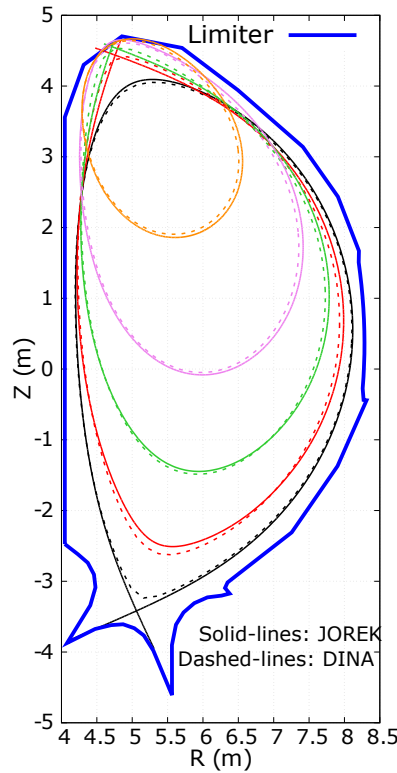


FIGURE 5.13: Comparison of the LCFS during the ITER cold vertical displacement in DINA (dashed) and JOREK (solid) at same positions of the magnetic axis for the profile "p2".

In figure 5.12 it can be observed that the resistivity profile "p2" is the best choice to reproduce the DINA results where the resistivity profile varies with time. Note that even if there are differences in the time traces for  $Z_{axis}$  and  $I_p$ , the curve  $Z_{axis}(I_p)$  is very well reproduced for that resistivity profile. For that resistivity profile, the LCFS found in JOREK at the same  $Z_{axis}$  agrees very well with the DINA simulations (see figure 5.13).

It is noteworthy that the flattest resistivity profile "p1", which causes the plasma internal inductance ( $l_i$ ) to be the smallest over time, reaches higher  $Z_{\text{axis}}$  for the same  $I_p$  than the other profiles involving higher  $l_i$ . Therefore it can be stated that ITER plasmas with smaller inductances are more unstable (in terms of larger vertical displacements for the same current decay) than plasmas with higher inductances. This is a different picture from pure VDEs where ( $\tau_w \ll \tau_{\text{CQ}}$ ) and the growth rate increases with the internal inductance. During the first 5 ms of the simulation, the three resistivity profiles give very similar results which start to differ when plasma reaches the wall at  $Z_{\text{axis}} = 1$  m.

## 5.2 Studies for ITER VDEs

### 5.2.1 Universality of the $Z_{\text{axis}}(I_p)$ curve at low $\tau_{\text{CQ}}/\tau_w$ for ITER

In the simplified analytical model presented in [KB17] it was shown that when a wall surrounding the plasma stabilizes completely the VDEs, the plasma motion only depends on the dissipation of the plasma current. This implies that the vertical position can be calculated from the  $I_p(t)$  curve together with the geometrical properties of the plasma and the wall. In other words, when  $\tau_{\text{CQ}}/\tau_w \ll 1$ , the  $Z_{\text{axis}}(I_p(t))$  curve does not depend on the time-scale at which the plasma current is dissipated. For ITER disruptions this implies that a minimum  $I_p$  will reach the wall regardless of how fast the plasma current is quenched.

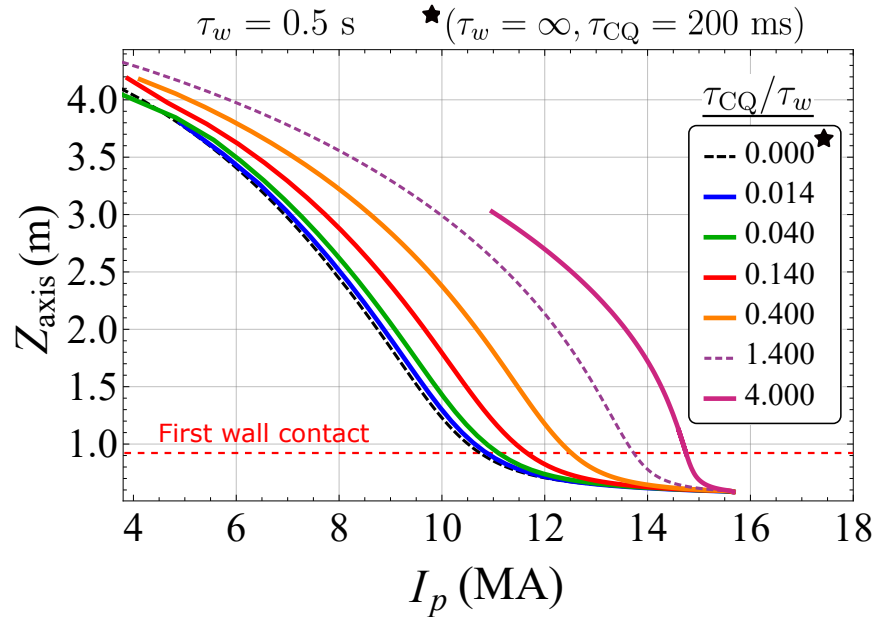


FIGURE 5.14: Vertical position of the magnetic axis as a function of the plasma current for different  $\tau_{\text{CQ}}/\tau_w$  ratios.

In this subsection the  $Z_{\text{axis}}(I_p)$  curve is studied for different  $\tau_{\text{CQ}}/\tau_w$ . The ITER plasma presented in 5.1.4 is used with the expected ITER's wall resistivity ( $\eta_w = 8 \cdot 10^{-7} \Omega \text{m}$ ) and wall thickness ( $d_w = 6 \text{ cm}$ ). The ratio  $\tau_{\text{CQ}}/\tau_w$  is varied by changing  $\tau_{\text{CQ}}$  which is performed by scaling the resistivity profile by a factor. The chosen resistivity profile is the flux-dependent profile "p1" shown in figure 5.10 (b) which does not allow the formation of currents in the open field-line region.

The JOREK simulation results are shown in figure 5.14 where it can be seen how the  $Z_{\text{axis}}(I_p)$  curve is almost identical for the cases with  $\tau_{\text{CQ}}/\tau_w \leq 0.04$  regardless of the different time-scales for the current decay and vertical motion (see figure 5.15). The importance of the

$\tau_{\text{CQ}}/\tau_w$  ratio for the  $Z_{\text{axis}}(I_p)$  curve is clear when comparing the case with  $\tau_{\text{CQ}}/\tau_w = 0.014$  with the special case where the wall resistivity has been set to 0 so  $\tau_w = \infty$  and  $\tau_{\text{CQ}}/\tau_w = 0$ . Even if these two cases have very different time-scales for the current quench time,  $\tau_{\text{CQ}} = 7$  ms and  $\tau_{\text{CQ}} = 200$  ms respectively (see figure 5.15), both cases have exactly the same  $Z_{\text{axis}}(I_p)$  curve. This fact demonstrates the universality of the  $Z_{\text{axis}}(I_p)$  curve which is independent on time-scales when  $\tau_{\text{CQ}}/\tau_w \ll 1$ . However it is important to remember that in these simulations the resistivity profile is fixed geometrically as a flux function and therefore it only depends in the plasma and wall currents. If the resistivity profile had a temperature dependence, the time-scales at which the current is quenched would influence the temperature evolution which would result in different resistivity profiles. The different resistivity profiles imply different plasma current density profiles (or different internal inductances) which give other  $Z_{\text{axis}}(I_p)$  curves as seen in figure 5.12.

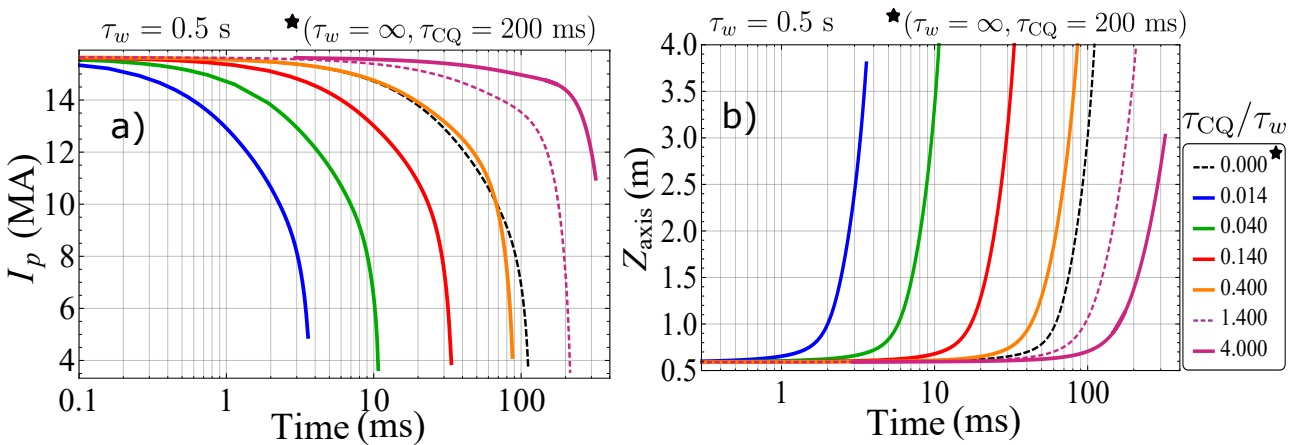


FIGURE 5.15: (a) Toroidal current and (b) vertical position of the magnetic axis over time for the different  $\tau_{\text{CQ}}/\tau_w$  ratios.

As  $\tau_{\text{CQ}}/\tau_w$  is increased, the plasma reaches higher vertical positions at higher plasma currents. If  $\tau_{\text{CQ}}/\tau_w \gg 1$ , pure VDEs are destabilized and the plasma can drift vertically without losing plasma current (see the case with  $\tau_{\text{CQ}}/\tau_w = 4$  in figure 5.14). ITER requirements impose a lower limit in the current quench time of 50 ms in order to avoid electromagnetic forces in the blanket modules due to the induction of eddy currents. For a larger current quench time of 70 ms (see red curve in figure 5.14), these simulations indicate that the  $Z_{\text{axis}}(I_p)$  curve is still close to the ideal wall limit and starts deviating significantly from the ideal wall limit for current quench times of 200 ms (orange curve). This implies that in ITER, the  $Z_{\text{axis}}(I_p)$  curve could approach the ideal wall limit without crossing the engineering limits, which will depend on the post-disruption plasma temperature achieved with the disruption mitigation system. However for unmitigated disruptions or hot VDEs, ITER plasmas will be on the limit with  $\tau_{\text{CQ}}/\tau_w \gg 1$  and the plasma will reach the wall with all its initial current.

### 5.2.2 Influence of the $\tau_{\text{CQ}}/\tau_w$ ratio in the halo current fraction

In this subsection the influence of the  $\tau_{\text{CQ}}/\tau_w$  on the generation of halo currents is studied. The ITER plasma from the previous section is used with a different resistivity profile allowing the induction of currents at the open field-line region. The chosen resistivity profile has a resistivity in the open-field line region which is three times higher than the core resistivity (see figure 5.16 (b)). After some width in poloidal flux, a very high resistivity is chosen in order to

mimic a vacuum. The flux value at which the vacuum is implemented ( $\psi_{\text{vac}}$ ) is defined as

$$\psi_{\text{vac}} = \psi_{\text{LCFS}} + \alpha(\psi_{\text{xpoint}} - \psi_{\text{LCFS}}) \quad (5.8)$$

where  $\psi_{\text{xpoint}}$  is the flux at the lower X-point that is well defined during all the simulation and  $\alpha \in [0, 1]$  is a numerical parameter to vary the halo width. For the following simulations  $\alpha = 0.5$ . An example of a VDE simulation with this type of resistivity profile is shown in figure figure 5.16 (a) where significant toroidal current is induced in the open field-line region.

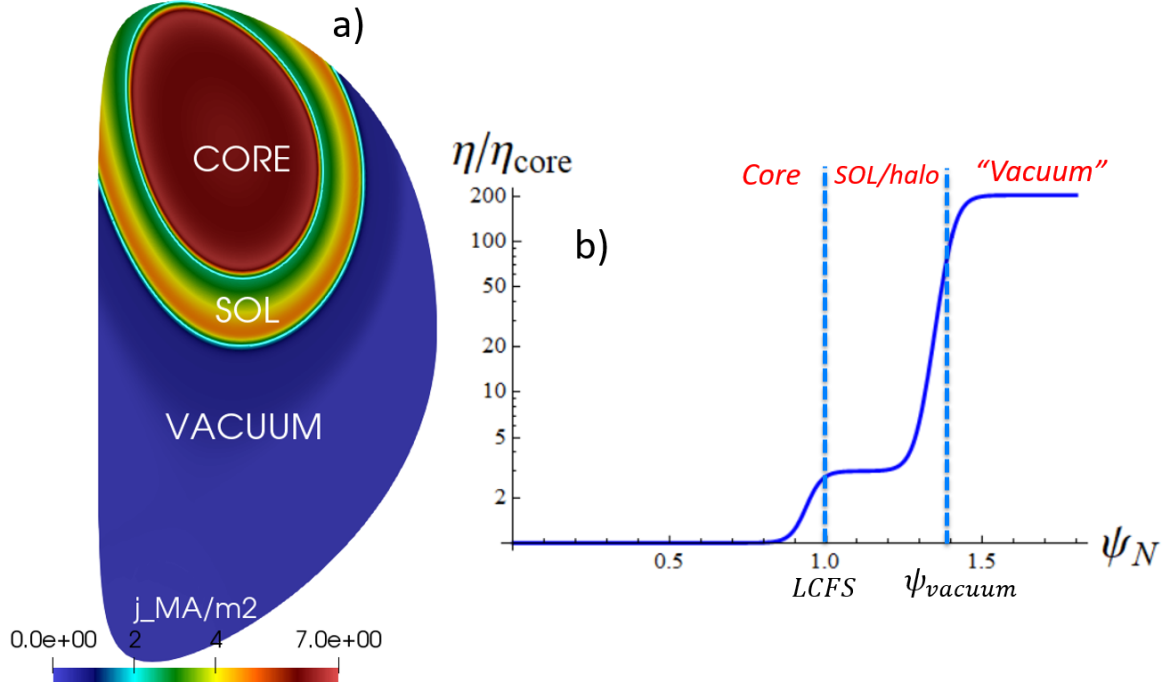


FIGURE 5.16: (a) Toroidal current density with the separate resistivity regions during an ITER VDE. (b) Resistivity profile used for the scan on the  $\tau_{\text{CQ}}/\tau_w$  ratio including halo currents.

When using reduced MHD models, the poloidal currents have to be inferred from the reduced MHD variables as the poloidal currents do not appear in the reduced equations (see section 2.1.1). For time-scales much longer than the Alfvén time, as it is the case for these simulations which take place in the order of milliseconds and seconds, the plasma can be considered in equilibrium. In this case the Grad-Shafranov equilibrium can be used and the poloidal current stream function is a poloidal flux function  $F(\psi)$  which gives the following expression for the poloidal current ( $\mathbf{J}_p$ )

$$\mathbf{J}_p = \nabla \times (F \nabla \phi) = \nabla F \times \nabla \phi = F' \nabla \psi \times \nabla \phi \approx -\frac{j}{F_0} \nabla \psi \times \nabla \phi \quad (5.9)$$

where in the last step the Grad-Shafranov equation  $j = -FF'$  has been used and the thermal energy of the plasma has been neglected. The thermal energy contribution to the equilibrium equation can be neglected in general for disrupted plasmas which present high currents and very low temperatures. However this assumption is not valid for hot VDEs where the temperatures are still high. With expression (5.9) and the definition (1.29) the halo fraction is numerically computed. The evolution of poloidal current in reduced MHD is explored in appendix D.4.

Finally the results for the halo current fraction for different  $\tau_{\text{CQ}}/\tau_w$  ratios are shown in figure 5.17. The HF is plotted as a function of the magnetic axis position as it is a monotonic function of time. For small  $\tau_{\text{CQ}}/\tau_w$  ratios, the halo current fraction follows the same HF( $Z_{\text{axis}}$ ) curve regardless of the current quench time-scales as it was observed in previous subsection for

the  $Z_{\text{axis}}(I_p)$  curve. This demonstrates that for small  $\tau_{\text{CQ}}/\tau_w$  ratios the wall provides total VDE stabilization and the position of the plasma and the halo currents are completely determined by the plasma current. This implies that a minimum halo current fraction will exist regardless of the disruption mitigation technique used in ITER. These simulations indicate that the minimum halo fraction expected is 7.7%. As the ratio  $\tau_{\text{CQ}}/\tau_w$  is increased the HF increases up to 36%, which is almost a factor 5 difference with respect to the minimum HF. The maximum HF observed in these simulations (HF = 36%) is of the same order as the maximum halo current fraction observed with the DINA code [Leh+15] which is between 40% and 50%. Nevertheless the dependence of the HF with the resistivity profile and the halo width needs to be studied and is left for future work.

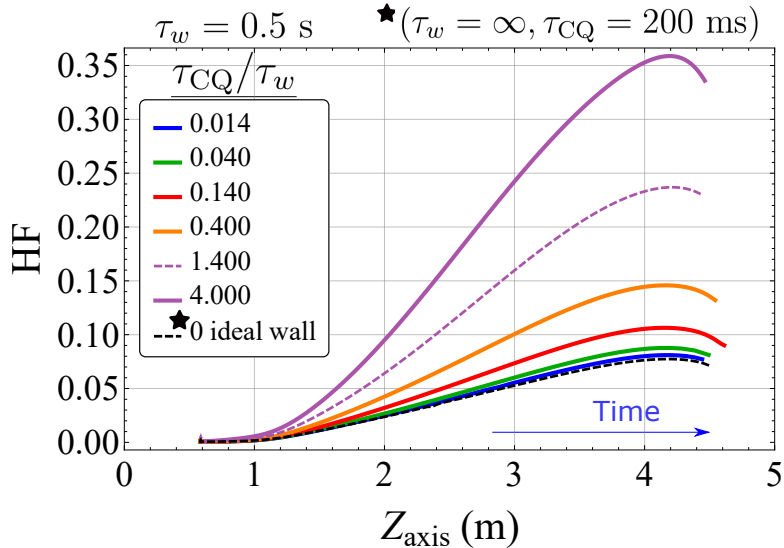


FIGURE 5.17: Halo current fraction versus plasma position for different  $\tau_{\text{CQ}}/\tau_w$  ratios.

### 5.2.3 Simulations of cold AVDEs in ITER

In this section preliminary simulations of asymmetric VDEs are presented. The ITER case shown in the previous section is used where the axisymmetric ( $n = 0$ ) mode interacts with the  $n = 1$  mode non-linearly. This choice is motivated by the fact that in current VDE experiments, the AVDEs have a dominant  $n = 1$  component [Gra+96]. The chosen resistivity profile is the one shown in figure 5.16 (b) and the wall resistivity is  $\eta_w = 8 \cdot 10^{-7} \Omega \text{m}$  such that  $\tau_{\text{CQ}}/\tau_w \ll 1$  for the following simulations. As the resistivity profile only depends on the poloidal flux and the temperature is initially low ( $T \sim 10 \text{ eV}$ ), the temperature does not play an important role either in the induction or in the momentum equation. For the sake of simplicity, the temperature and density equations are dropped as well as the parallel velocity equation. Therefore these simulations have the following setting  $T = 0$ ,  $\rho = 1$  and  $v_{\parallel} = 0$ . As these ad-hoc assumptions are rather restrictive, these simulations do not aim to predict realistic AVDEs but they are rather intended to give first insights in the evolution of ( $n = 1$ ) kink modes during VDEs in a simple manner.

The asymmetric  $n = 1$  mode is added to the axisymmetric simulation when the HF has reached a considerable value (with respect to its final value) of 6% (see figures 5.18 (c) and (d)). The mode is linearly unstable and reaches a saturation phase where the magnetic energy of the mode remains fairly constant while the plasma current decays (see figure 5.18 (c)). The toroidal peaking factor (TPF) reaches its maximum value of 1.2 at the beginning of the saturation phase and decays as the magnetic energy decreases. The product  $\text{HF} \times \text{TPF}$  depends mainly of the HF

as the TPF is rather small ( $\sim 1.1$ ). The maximum value obtained for the product  $\text{HF} \times \text{TPF}$  is 0.11, which implies very low electromagnetic loads compared with the highest case of 0.75 that has been observed in tokamak experiments. When the  $n = 1$  mode reaches its maximum amplitude at  $t = 8$  ms, a jump in the halo fraction can be observed. Note that the halo fraction is calculated with the toroidal average of the poloidal currents and therefore the mode  $n = 1$  does not contribute directly to the HF. Nevertheless the non-linear interaction of  $n = 1$  during its fast growth with  $n = 0$  leads to an indirect induction of axisymmetric halo currents. This phenomenon requires further investigations and is left for future work, however this already indicates the importance of performing 3D MHD simulations in order to calculate the HF.

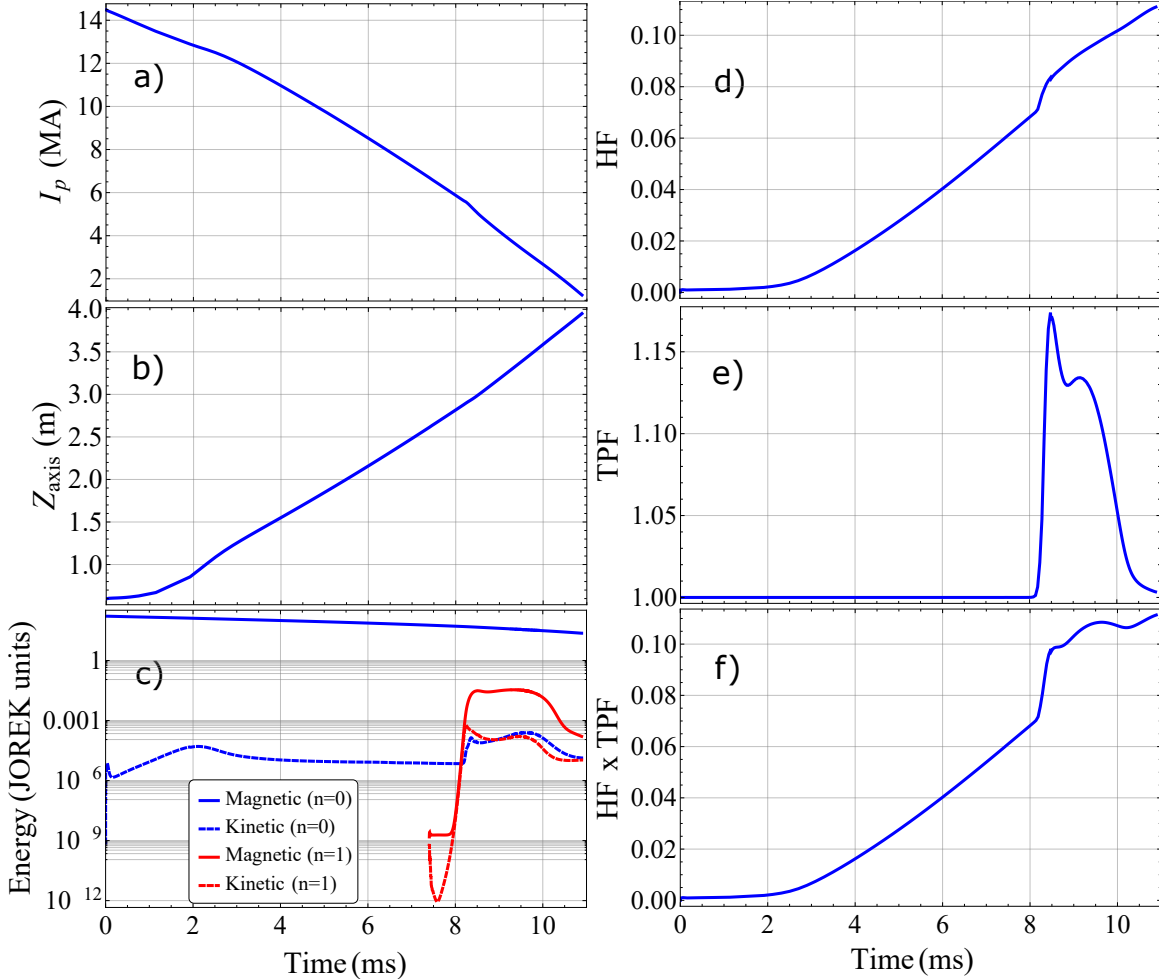


FIGURE 5.18: Time traces of (a) the plasma current, (b) the vertical position of the magnetic axis, (c) the volume integrated magnetic and kinetic energies, (d) the halo fraction factor, (e) the toroidal peaking factor and (f) the product of the toroidal peaking factor with the halo fraction for a simulation with  $\tau_{\text{CQ}} = 11$  ms.

The mode has a poloidal  $m = 2$  structure (see figure 5.19) and it is located at the rational surface  $q = 2$  lying at the plasma edge. As the rational surface lies inside the plasma, it is not appropriate to name this mode as a "external kink mode" in the ideal MHD sense<sup>1</sup>, consequently it will be referred to as an edge resistive kink mode or an edge tearing mode. In the time-scales at which the current decays, the 2/1 mode structure rotates in poloidal rotation (see figure 5.19).

<sup>1</sup>External kink modes in ideal MHD are stable when their associated rational surface lies inside the plasma due to the topological constraints imposed by the frozen theorem. They become unstable when the rational surface exists in the vacuum where the magnetic reconnection can occur.

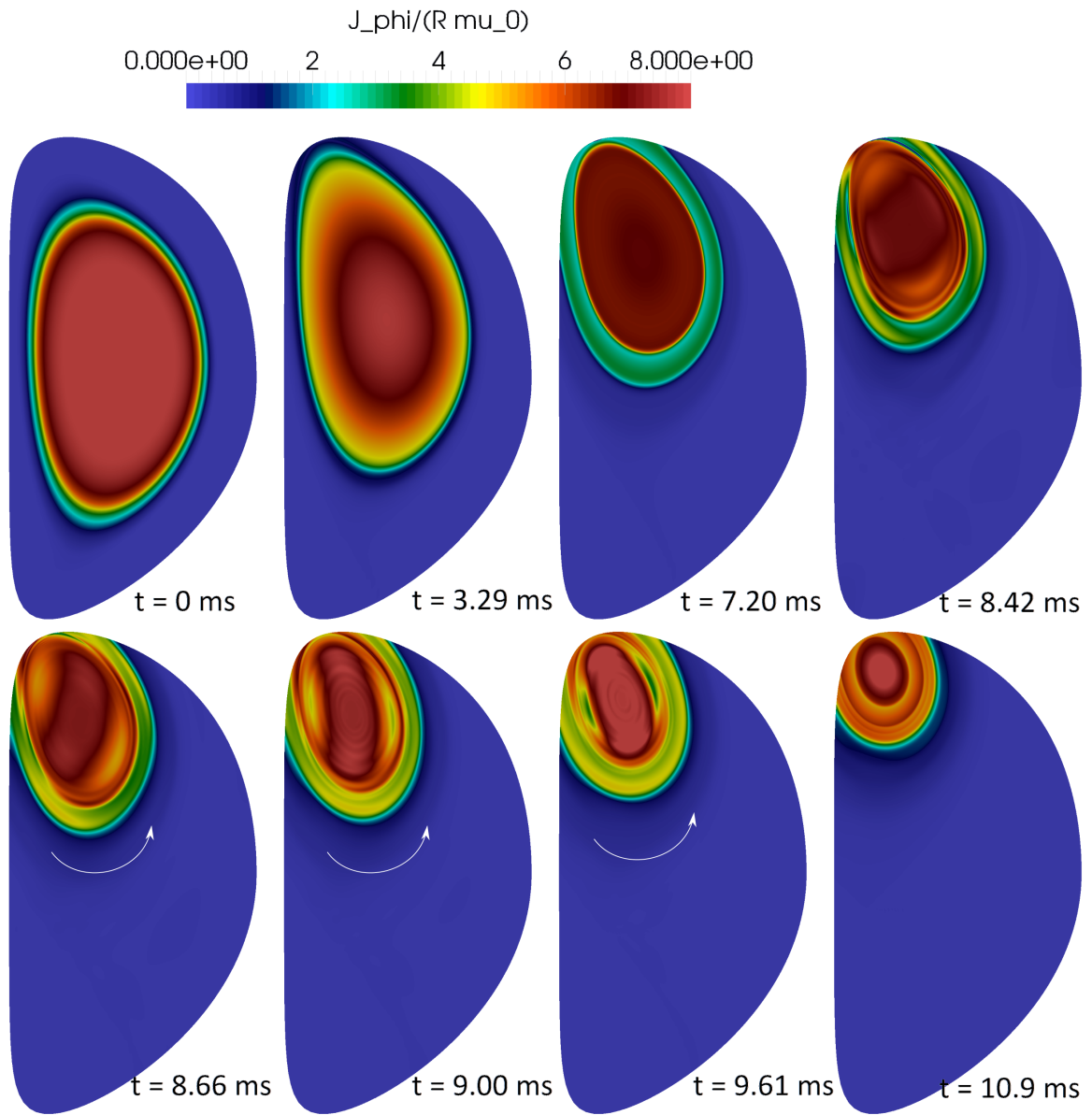


FIGURE 5.19: Contour plot of the toroidal current density profile for different time slices during an ITER cold AVDE. The arrows indicate the sense of the poloidal rotation of the mode structure.

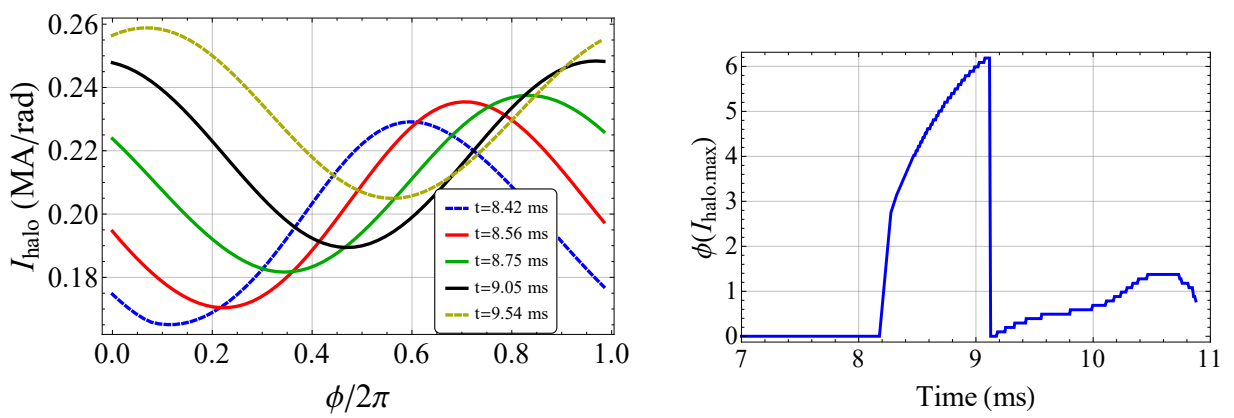


FIGURE 5.20: (Left) Halo current angular density as a function of the toroidal angle. (Right) Toroidal angle with maximum halo current angular density versus time.

This rotation is also observed in the toroidal direction as it is shown in figure 5.20, where the peak of the profile  $I_{\text{halo}}(\phi)$  ( $I_{\text{halo,max}}$ ) moves in the positive toroidal direction. As it can be inferred from the mentioned figures, the halo current peak completes up 0.5 rotations around the torus as the plasma is extinguished. The found rotation frequency of the presented case is of the order of  $\langle f_h \rangle \sim 0.5$  kHz. As the rotation decelerates over time (see figure 5.20 (b)), the definition of the average rotation frequency is somehow arbitrary. The chosen procedure calculates the average rotation frequency as  $\langle f_h \rangle = \Delta\phi/(2\pi\Delta t)$ . Here the chosen angular displacement of the halo current peak is  $\Delta\phi = 2.3$  which starts to be measured when the mode's amplitude begins to saturate and  $\Delta t$  is the time that it takes to achieve that angular displacement.

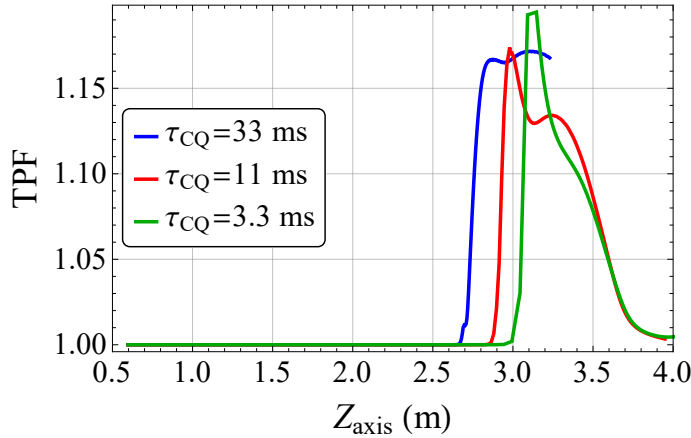


FIGURE 5.21: Toroidal peaking factor as a function of the vertical position of the magnetic axis for different current quench time-scales.

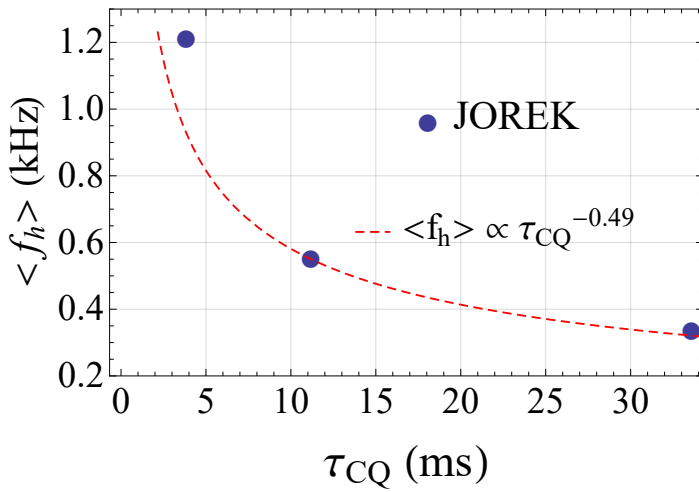


FIGURE 5.22: Rotation frequency of the asymmetry of the halo currents versus current quench time.

With the same parameter set-up the same simulation has been run for three different current quench times by scaling the resistivity profile by a factor. The TPF is plotted versus the magnetic axis position for the three cases in figure 5.21, revealing that the plasma resistivity and the current quench time does not have an important effect in the toroidal peaking factor. Finally the average rotation frequency presents a similar dependence on the current quench time ( $\langle f_h \rangle \sim \tau_{\text{CQ}}^{-0.5}$ ) as found empirically in [Mye+17] (see figure 5.22).

These preliminary simulations show the capabilities to simulate AVDEs with JOREK-STARWALL. Nevertheless many studies still need to be conducted. In particular the origin of

the halo current rotation and its dependence on the current quench time needs to be understood and characterized. Other more relevant regimes with  $\tau_{\text{CQ}}/\tau_w \gg 1$  must be conducted as well. Additionally the dependence of these simulations on different numerical parameters such as the wall and coil resolutions and the chosen viscosity needs to be assessed. Finally more realistic simulations including several toroidal harmonics, appropriate models for the temperature and density and a temperature dependent resistivity must be considered for predicting the asymmetries of the VDEs in ITER.



# Chapter 6

## Conclusions and future work

In this thesis the MHD numerical code JOREK-STARWALL has been adapted and applied to the simulation of ELM triggering via vertical position oscillations (1.2.3) and VDEs (1.2.4) in realistic tokamak geometries. As it was reviewed in chapter 1, these instabilities can severely limit the lifetime of the plasma facing components due to the large heat and electromagnetic loads that they entail. The complexity of these instabilities requires numerical simulations in order to clarify their underlying physical mechanisms and to predict their possible implications for large scale tokamaks such as ITER.

The MHD theory reviewed in chapter 1 gives a good description for the spatial and temporal time-scales of these instabilities and therefore it is used as base model for the numerical simulations. The numerical simulations were performed with the non-linear reduced MHD code JOREK presented in chapter 2, which is used for the plasma equations. As these instabilities require a free-boundary description in order to allow for vertical axisymmetric motions of the plasma, JOREK is coupled to the code STARWALL (see chapter 2), which takes into account the electromagnetic interaction of the plasma with the vacuum and its surrounding conductors.

In chapter 3 a newly developed derivation of the STARWALL's equations is performed based on the weak form of a finite element method. The new derivation is a straightforward procedure to obtain the *wall* system of equations directly from Maxwell's equations and Ohm's law. The procedure is generalized for halo currents and their interaction with eddy currents through the source/sink current potentials ( $\phi_s$ ). In this respect, a module has been implemented in STARWALL to solve the equation for  $\phi_s$  given the perpendicular currents to the wall ( $J_\perp$ ). This module has been benchmarked in (5.1.2) with the SSC code for an ITER-like wall including holes showing an excellent agreement. Nevertheless the interaction of the source/sink potentials with the plasma and with the *wall* eddy currents still needs to be implemented. Additionally the procedure to follow in order to implement free-boundary conditions in the full MHD model has been indicated in section (2.3).

During this thesis the computation of free-boundary equilibria has received special attention as it is the starting point for all the performed simulations. The implementation of poloidal field coils in STARWALL has led to the successful reconstruction of experimental equilibria of AUG and JET tokamak discharges (see chapter 3.2). For the JET case, the equilibrium reconstruction requires to include iron-core effects which is achieved by adapting the PF coil currents. For this task, an automatic procedure has been implemented in JOREK to calculate the optimal coil currents in order to reproduce a given arbitrary fixed-boundary equilibrium (see section 3.3). Although the converged free-boundary equilibria agrees well with the expected solution, the method to solve the Grad-Shafranov equation through Picard iterations is somehow cumbersome. In this respect, several parameters, such as the blending parameter ( $a_{\text{mix}}$ ) and the current and vertical control system parameters require adaptation for each

equilibrium. Consequently several improvements in the GS solver need to be explored.

ELMs triggered via vertical positions have been investigated in chapter 4. The implemented technique to impose coil currents over time in a implicit form (see section 3.4) has lead to successful axisymmetric vertical oscillations that have been benchmarked with the DINA code for an ITER 15MA/5.3T plasma (see figure 4.5). The induction of axisymmetric edge current during the vertical plasma motion has been studied with a simple analytical model and with simulations. The analytical model indicates that induction of edge current originates from a change in the external poloidal flux and from the compression of the plasma cross section during the plasma motion (see equation (4.6)). This effect is found to be independent of the vertical position velocity when the plasma edge behaves as an ideal conductor. In this case, the total amount of induced current only depends on difference between the initial and final plasma state. Being the induced current the cause of the ELM triggering, this could explain the strong empirical dependence of the ELM triggering efficiency on the vertical position amplitude but not on the vertical velocity (see section 1.2.3).

For vertical position oscillations in ITER plasmas, the induced edge current is due to the plasma compression due to its motion through the top-down asymmetric magnetic field. Particularly, positive (negative) edge current (with respect to the plasma current) is induced when the plasma moves towards (away from) the main X-point because the plasma top moves faster than the plasma bottom. In addition, the results in figures 4.6 and 4.7 indicate that the induced current can be enhanced by choosing different geometries and waveforms for the coils used to displace the plasma.

The triggering of ELMs through vertical position oscillations has been simulated in a self-consistent dynamical scheme for the first time. For ITER 7.5MA/2.65T plasmas, the analysis of a single toroidal harmonic ( $n = 6$ ) shows that initially stable plasmas can be destabilized by applying a downward vertical motion (compression of the plasma cross section) and initially unstable plasmas can be stabilized when applying an upward motion (expansion of the plasma cross section). The destabilized mode has strong peeling component. These results directly point towards the edge current as the main ELM driving mechanism. Moreover plasmas with initially larger bootstrap currents require a smaller vertical displacement in order to destabilize ELMs, which can explain the empirical dependence of the triggering with the collisionality (see figure 1.14). Additionally ELMs are triggered at same vertical positions but at different vertical velocities as experimentally observed. Finally all these observations found with the performed simulations confirm the hypothesis of the induced edge current as the essential mechanism for the ELM destabilization. Nevertheless simulations with several toroidal harmonics should be conducted and the influence of the initial pressure profile on the ELM triggering has to be assessed.

In chapter 5 JOREK-STARWALL has been applied to VDE simulations where different benchmarks and tests have been conducted. These benchmarks have shown that STARWALL's ideal wall is able to conserve properly the poloidal magnetic flux (5.1.1), that the calculated VDE linear growth rates for complicated plasmas agree well with other existing free-boundary MHD codes (5.1.3) and that the 2D plasma evolution is well reproduced for an ITER plasma drifting into the first wall (5.1.4). Additionally, VDE simulations have been conducted for an ITER 15MA/5.3T plasma revealing the universality of the  $Z_{\text{axis}}(I_p)$  curve at low  $\tau_{\text{CQ}}/\tau_w$  ratios regardless of the time-scales of the current quench time as predicted by [KB17]. The influence of the  $\tau_{\text{CQ}}/\tau_w$  ratio on the halo current fraction (HF) has been assessed revealing that a minimum halo fraction will exist (which is found to be  $\sim 8\%$ ) regardless of the current quench mitigation schemes used in ITER. For cases with high  $\tau_{\text{CQ}}/\tau_w$  ratios, pure VDEs are destabilized and the plasma arrives to the first wall with all its initial current. These cases

show a maximum halo fraction of (36%) which is a factor 5 bigger than the minimum expected HF and is similar to the values found by the DINA code [Leh+15].

Finally preliminary asymmetric cold VDE simulations have been performed in subsection 5.2.3. In these simulations a dominant  $m = 2/n = 1$  resistive kink mode is destabilized at the plasma edge where the rational  $q = 2$  surface exists. The mode structure causes a toroidal asymmetry characterized by a low toroidal peaking factor (TPF) of the order of 1.15 which is independent on the current quench time. The produced asymmetry of the halo currents is found to complete around 0.5 rotations around the torus. The found averaged frequency of this rotation is of the order of the 0.5 kHz for a current quench time of 11 ms and is found to scale with  $\tau_{\text{CQ}}$  as  $\langle f_h \rangle \sim \tau_{\text{CQ}}^{-0.5}$  as found by experimental scaling laws. When the asymmetric mode is added to the simulation and the non-linear phase takes place, a sudden increase in the halo fraction is observed. Therefore the initial interaction of the 2/1 mode with the  $n = 0$  is able to induce an extra axisymmetric component of the HF that can't be observed with 2D codes. This result reveals the importance of performing 3D simulations in order to predict the halo currents. Nevertheless these simulations must be refined as very strong assumptions haven been made for the resistivity, the temperature, the density and the parallel velocity profiles. Additionally the dependence of these simulations on different numerical parameters such as the wall and coil resolutions and the chosen viscosity needs to be assessed. Finally many studies still need to be conducted. Particularly the halo current rotation and its dependence on the current quench time must be understood and characterized for different  $\tau_{\text{CQ}}/\tau_w$  ratios.

# Appendices

## A.1 Plasma shape and geometry

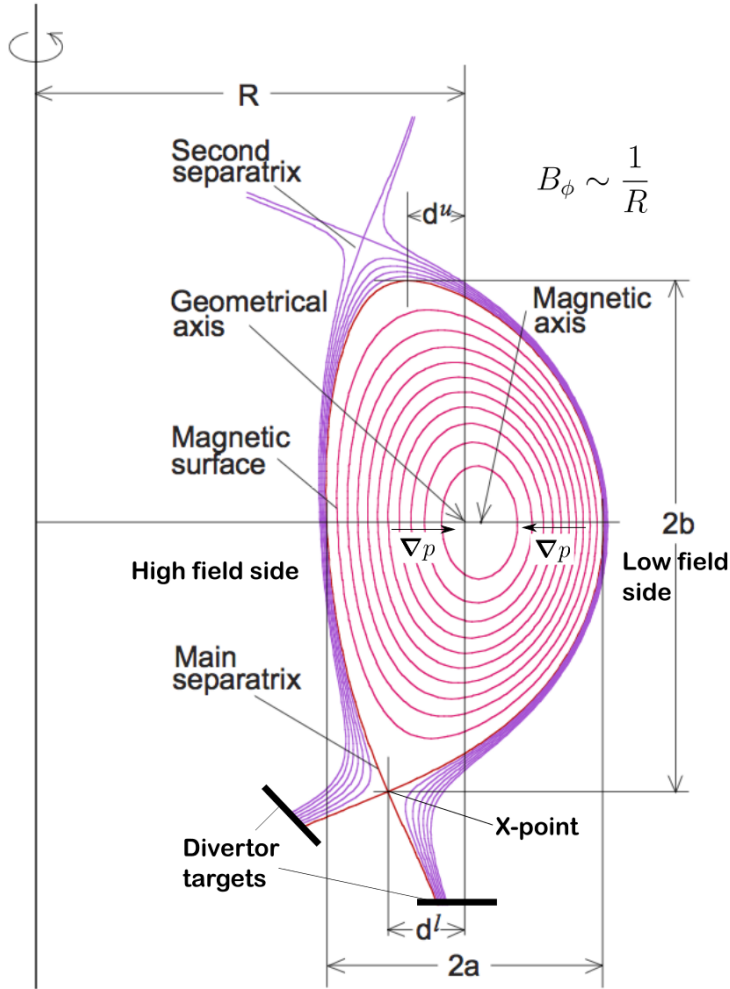


FIGURE 1: Plasma shape definitions. For a limiter case use an horizontal tangent instead of the x-point.

**Minor radius:**

$$a = (R_{max} - R_{min})/2$$

**Geometric axis:**

$$R_0 = (R_{max} + R_{min})/2$$

**Magnetic axis:**

$(R_{axis}, Z_{axis})$  Point inside the plasma where  $B_p = 0$

**Shafranov shift:**

$$\Delta_{sh} = R_{axis} - R_0$$

**Elongation:**

$$\kappa = b/a = (Z_{max} - Z_{min})/2a$$

**Triangularity averaged:**

$$\delta = (d^l + d^u)/2a$$

**Triangularity upper/lower:**

$$\delta = d^{u/l}/a$$

**Aspect ratio:**

$$A = R_0/a$$

**Inverse aspect ratio:**

$$\epsilon = a/R_0$$

**Main separatrix:**

First open flux surface

**X-point:**

Point in the separatrix where  $B_p = 0$

**Scrape off layer (SOL):**

Plasma outside the main separatrix

## B.2 JOREK variables and normalization

TABLE 1: Definition of the JOREK quantities and their normalization. The normalization factor  $\rho_0$  is the mass density at the plasma core and  $\mu_0$  is the vacuum permeability

Variable	Meaning	Normalization (SI units)
$t$	Time	$t_{\text{SI}}[\text{s}] = t\sqrt{\rho_0\mu_0}$
$R$	Major radius	$R_{\text{SI}}[\text{m}] = R$
$Z$	Vertical coordinate	$Z_{\text{SI}}[\text{m}] = Z$
$\rho$	Mass density	$\rho_{\text{SI}}[\text{kg m}^{-3}] = \rho\rho_0$
$n$	Particle density	$n_{\text{SI}}[\text{m}^{-3}] = \rho n_0$
$\mathbf{v}$	Velocity	$\mathbf{v}_{\text{SI}}[\text{m s}^{-1}] = \mathbf{v}/\sqrt{\rho_0\mu_0}$
$v_{\parallel}$	Parallel velocity	$v_{\parallel,\text{SI}}[\text{m s}^{-1}] = v_{\parallel}B_{\text{SI}}/\sqrt{\rho_0\mu_0}$
$T$	Temperature	$T_{\text{SI}}[\text{K}] = T/(n_0k_B\mu_0)$
$\mathbf{B}$	Magnetic field	$\mathbf{B}_{\text{SI}}[\text{T}] = \mathbf{B}$
$\mathbf{J}$	Current density	$\mathbf{J}_{\text{SI}}[\text{A m}^{-2}] = \mathbf{J}/\mu_0$
$\mathbf{A}$	Magnetic vector potential	$\mathbf{A}_{\text{SI}}[\text{T m}] = \mathbf{A}$
$\Phi$	Electric potential	$\Phi_{\text{SI}}[\text{V}] = \Phi/\sqrt{\rho_0\mu_0}$
$\psi$	Poloidal flux	$\psi_{\text{SI}}[\text{Wb/rad}] = \psi$
$u$	Velocity stream function	$u_{\text{SI}}[\text{m s}^{-1}] = u/\sqrt{\rho_0\mu_0}$
$w$	Toroidal vorticity	$w_{\phi,\text{SI}}[\text{m}^{-1}\text{s}^{-1}] = w/\sqrt{\rho_0\mu_0}$
$j$	Toroidal current density	$J_{\phi,\text{SI}}[\text{A m}^{-2}] = -j/(\mu_0R)$
$\eta$	Resistivity	$\eta_{\text{SI}}[\Omega \text{ m}] = \eta\sqrt{\mu_0/\rho_0}$
$D$	Particle diffusivity	$D_{\text{SI}}[\text{m}^2\text{s}^{-1}] = D/\sqrt{\rho_0\mu_0}$
$\kappa$	Heat diffusivity	$\kappa_{\text{SI}}[\text{m}^{-1}\text{s}^{-1}] = \kappa\sqrt{\mu_0/\rho_0}$
$\mu$	Dynamic viscosity	$\mu_{\text{SI}}[\text{kg m}^{-1}\text{s}^{-1}] = \mu\sqrt{\rho_0/\mu_0}$
$S_{\rho}$	Particle source	$S_{\rho,\text{SI}}[\text{kg m}^{-3}\text{s}^{-1}] = S_{\rho}\sqrt{\rho_0/\mu_0}$
$S_T$	Heat source	$S_{T,\text{SI}}[\text{W m}^{-3}] = S_T/\sqrt{\mu_0^3\rho_0}$
$F$	Poloidal current stream function, $F \equiv RB_{\phi}$	$F_{\text{SI}}[\text{T m}] = F$
$\psi_N$	Normalized poloidal flux, $\psi_N \equiv (\psi - \psi_{axis})/(\psi_{bnd} - \psi_{axis})$	adimensional

### C.3 Geometrical matrices in STARWALL

In the following definitions the  $\delta$  symbols correspond to the Kronecker deltas and the integer function  $\text{ind}(n, j)$  provides the global index of the independent degree of freedom of the potential provided the triangle number  $n$  and the local node index  $j$ .

$N_{\Delta p}$  is the number of triangles at the JOREK boundary,  $N_{\Delta w}$  is the number of *wall* triangles,  $\langle \sigma_w \rangle_m = (\sigma_a + \sigma_b + \sigma_c)/3|_m$  is the average resistivity of the triangle  $m$  and the vectorial basis functions  $\hat{\mathbf{b}}_e^l$  are used to decomposed the boundary magnetic vector potential  $\mathbf{A}_{p,l} = \sum_e A_{p,l}^e \hat{\mathbf{b}}_e^l(u, v)$  at the boundary. The following properties of triangular elements (3.20) are used for the calculation of the STARWALL's matrices

$$\nabla \alpha = \frac{\mathbf{n} \times \mathbf{r}_{ac}}{2S_{\Delta}}, \quad \nabla \beta = \frac{\mathbf{n} \times \mathbf{r}_{ba}}{2S_{\Delta}} \quad (1)$$

$$\int_{\Delta} \alpha dS = \int_{\Delta} \beta dS = \frac{S_{\Delta}}{3} \quad (2)$$

$$\int_{\Delta} \alpha^2 dS = \int_{\Delta} \beta^2 dS = \frac{S_{\Delta}}{6} \quad (3)$$

$$\int_{\Delta} \alpha \beta dS = \frac{S_{\Delta}}{12} \quad (4)$$

where  $S_{\Delta}$  is the surface of the triangle.

### Matrices

$$M_{SS} \equiv M_{k,l}^{SS} \equiv \sum_{i,j=1}^3 \sum_{m=1}^{N_{\Delta w}} \delta_{k,\text{ind}(m,i)} \delta_{l,\text{ind}(m,j)} \mathbf{e}_i^w|_m \cdot \mathbf{e}_j^w|_m \langle \sigma_w \rangle_m d_w \int_{\Delta_m} dS_w \quad (5)$$

$$M_{SJ} \equiv M_{k,l}^{SJ} \equiv \sum_{i,j=1}^3 \sum_{m=1}^{N_{\Delta w}} \delta_{k,\text{ind}(m,i)} \delta_{l,\text{ind}(m,j)} \frac{1 + \delta_{k,l}}{12} \int_{\Delta_m} dS_w \quad (6)$$

$$M_{pp} \equiv M_{k,l}^{pp} \equiv \frac{1}{4\pi} \sum_{i,j=1}^3 \sum_{m,n=1}^{N_{\Delta p}} \delta_{k,\text{ind}(n,j)} \delta_{l,\text{ind}(m,i)} \mathbf{e}_i^p|_m \cdot \mathbf{e}_j^p|_n \int_{\Delta_m} \int_{\Delta_n} \frac{dS'_p dS_p}{|\mathbf{r} - \mathbf{r}'|} \quad (7)$$

$$M_{pw} \equiv M_{k,l}^{pw} \equiv \frac{1}{4\pi} \sum_{i,j=1}^3 \sum_{n=1}^{N_{\Delta p}} \sum_{m=1}^{N_{\Delta w}} \delta_{k,\text{ind}(n,j)} \delta_{l,\text{ind}(m,i)} \mathbf{e}_i^w|_m \cdot \mathbf{e}_j^p|_n \int_{\Delta_m} \int_{\Delta_n} \frac{dS'_w dS_p}{|\mathbf{r} - \mathbf{r}'|} \quad (8)$$

$$M_{ps} \equiv M_{k,l}^{ps} \equiv \frac{1}{4\pi} \sum_{i,j=1}^3 \sum_{n=1}^{N_{\Delta p}} \sum_{m=1}^{N_{\Delta w}} \delta_{k,\text{ind}(n,j)} \delta_{l,\text{ind}(m,i)} \mathbf{e}_j^p|_n \cdot (\mathbf{e}_i^w \times \mathbf{n})|_m \int_{\Delta_m} \int_{\Delta_n} \frac{\sigma_w d_w dS'_w dS_p}{|\mathbf{r} - \mathbf{r}'|} \quad (9)$$

$$M_{wp} \equiv M_{k,l}^{wp} \equiv \frac{1}{4\pi} \sum_{i,j=1}^3 \sum_{n=1}^{N_{\Delta w}} \sum_{m=1}^{N_{\Delta p}} \delta_{k,\text{ind}(n,j)} \delta_{l,\text{ind}(m,i)} \mathbf{e}_i^p|_m \cdot \mathbf{e}_j^w|_n \int_{\Delta_m} \int_{\Delta_n} \frac{dS'_p dS_w}{|\mathbf{r} - \mathbf{r}'|} \quad (10)$$

$$M_{ww} \equiv M_{k,l}^{ww} \equiv \frac{1}{4\pi} \sum_{i,j=1}^3 \sum_{m,n=1}^{N_{\Delta w}} \delta_{k,\text{ind}(n,j)} \delta_{l,\text{ind}(m,i)} \mathbf{e}_i^w|_m \cdot \mathbf{e}_j^w|_n \int_{\Delta_m} \int_{\Delta_n} \frac{dS'_w dS_w}{|\mathbf{r} - \mathbf{r}'|} \quad (11)$$

$$M_{ws} \equiv M_{k,l}^{ws} \equiv \frac{1}{4\pi} \sum_{i,j=1}^3 \sum_{m,n=1}^{N_{\Delta w}} \delta_{k,\text{ind}(n,j)} \delta_{l,\text{ind}(m,i)} \mathbf{e}_j^w|_n \cdot (\mathbf{e}_i^w \times \mathbf{n})|_m \int_{\Delta_m} \int_{\Delta_n} \frac{\sigma_w d_w dS'_w dS_p}{|\mathbf{r} - \mathbf{r}'|} \quad (12)$$

$$R_{ww} \equiv R_{k,l}^{ww} \equiv \sum_{i,j=1}^3 \sum_{n=1}^{N_{\Delta w}} \delta_{k,\text{ind}(n,j)} \delta_{l,\text{ind}(n,i)} \mathbf{e}_i^w|_n \cdot \mathbf{e}_j^w|_n \frac{1}{\langle \sigma_w \rangle_n d_w} \int_{\Delta_n} dS_w \quad (13)$$

$$M_{pe,l} \equiv M_{k,f}^{pe,l} \equiv \sum_{i=1}^3 \sum_{n=1}^{N_{\Delta p}} \sum_e \delta_{k,\text{ind}(n,i)} \delta_{f,e} \int_{\Delta_n} \mathbf{e}_i^w|_n \cdot \hat{\mathbf{b}}_e^l dS_p \quad (14)$$

$$\mathbf{M}_{\parallel w} \equiv \mathbf{M}_{i,k}^{\parallel w} \equiv \frac{1}{4\pi} \mathbf{n}_p \times \sum_{j=1}^3 \sum_{m=1}^{N_{\Delta w}} \delta_{k,\text{ind}(m,j)} \mathbf{e}_j^w |_m \times \boldsymbol{\nabla} \int_{\Delta_m} \frac{1}{|\mathbf{r}_i - \mathbf{r}'|} dS'_w \quad (15)$$

$$\mathbf{M}_{\parallel p} \equiv \mathbf{M}_{i,k}^{\parallel p} \equiv \frac{1}{4\pi} \mathbf{n}_p \times \sum_{j=1}^3 \sum_{m=1}^{N_{\Delta p}} \delta_{k,\text{ind}(m,j)} \mathbf{e}_j^p |_m \times \boldsymbol{\nabla} \int_{\Delta_m} \frac{1}{|\mathbf{r}_i - \mathbf{r}'|} dS'_p \quad (16)$$

$$\mathbf{M}_{\parallel s} \equiv \mathbf{M}_{i,k}^{\parallel s} \equiv \frac{1}{4\pi} \mathbf{n}_p \times \sum_{j=1}^3 \sum_{m=1}^{N_{\Delta w}} \delta_{k,\text{ind}(m,j)} (\mathbf{e}_j^w \times \mathbf{n}_w) |_m \times \boldsymbol{\nabla} \int_{\Delta_m} \frac{\sigma_w d_w}{|\mathbf{r}_i - \mathbf{r}'|} dS'_w \quad (17)$$

## Derived matrices

$$\tilde{M}_{ww} \equiv M_{ww} - M_{wp} M_{pp}^{-1} M_{pw} \quad (18)$$

$$\tilde{M}_{we,l} \equiv M_{wp} M_{pp}^{-1} M_{pe,l} \quad (19)$$

$$\tilde{M}_{wJ} \equiv (M_{ws} - M_{wp} M_{pp}^{-1} M_{ps}) M_{SS}^{-1} M_{SJ} \quad (20)$$

$$\tilde{\mathbf{M}}_{\parallel w} \equiv \mathbf{M}_{\parallel w} - \mathbf{M}_{\parallel p} M_{pp}^{-1} M_{pw} \quad (21)$$

$$\mathbf{M}_{\parallel e,l} \equiv \mathbf{M}_{\parallel p} M_{pp}^{-1} M_{pe,l} \quad (22)$$

$$\mathbf{M}_{\parallel J} \equiv (\mathbf{M}_{\parallel s} - \mathbf{M}_{\parallel p} M_{pp}^{-1} M_{ps}) M_{SS}^{-1} M_{SJ} \quad (23)$$

$$S^T \tilde{M}_{ww} S = D \quad \text{and} \quad S^T R_{ww} S = I_d \quad (24)$$

where the similarity transform  $S$  is such that  $D$  is a diagonal matrix and  $I_d$  is the identity matrix.

$$M_{yy} \equiv D^{-1} \quad (25)$$

$$M_{ye,l} \equiv D^{-1} S^T \tilde{M}_{we,l} \quad (26)$$

$$M_{yJ} \equiv D^{-1} S^T \tilde{M}_{wJ} \quad (27)$$

$$\mathbf{M}_{ey} \equiv \tilde{\mathbf{M}}_{\parallel w} S \quad (28)$$

## Time-stepping

$$\hat{S}_{kk} \equiv 1 + \xi + \Delta t \theta M_{kk}^{yy} \quad (29)$$

$$\hat{A}_{kj,l} \equiv -(1 + \xi) M_{kj}^{ye,l} / \hat{S}_{kk} \quad (30)$$

$$\hat{B}_{kk} \equiv -\Delta t M_{kk}^{yy} / \hat{S}_{kk} \quad (31)$$

$$\hat{C}_{kk} \equiv \xi / \hat{S}_{kk} \quad (32)$$

$$\hat{D}_{kj,l} \equiv \xi M_{kj}^{ye,l} / \hat{S}_{kk} \quad (33)$$

$$\hat{\mathbf{E}}_{ij,l} \equiv \mathbf{M}_{ij}^{\parallel e,l} + \sum_k \mathbf{M}_{ik}^{ey} \hat{A}_{ik,l} \quad (34)$$

$$\hat{\mathbf{F}}_{ik} \equiv \mathbf{M}_{ik}^{ey} (1 + \hat{B}_{kk}) \quad (35)$$

$$\hat{\mathbf{G}}_{ik} \equiv \mathbf{M}_{ik}^{ey} \hat{C}_{kk} \quad (36)$$

$$\hat{\mathbf{H}}_{ij,l} \equiv \mathbf{M}_{ij}^{\parallel e,l} \quad (37)$$

## D.4 Poloidal current evolution equation in reduced MHD

Let's consider that the poloidal current stream function ( $F \equiv RB_\phi$ ) is not constant and that  $F = F_0 + \delta F$ . The evolution equation for  $F$  is

$$R^2 \nabla \phi \cdot \frac{\partial \mathbf{B}}{\partial t} = -R^2 \nabla \phi \cdot \nabla \times \mathbf{E} \quad (38)$$

$$\frac{\partial F}{\partial t} = -R^2 \nabla \cdot (\mathbf{E} \times \nabla \phi) \quad (39)$$

$$\frac{\partial F}{\partial t} = -R^2 \nabla \cdot ((-\mathbf{v} \times \mathbf{B} + \eta \mathbf{J}) \times \nabla \phi) \quad (40)$$

with the velocity ansatz of reduced MHD

$$\mathbf{v} = -R^2 \nabla u \times \nabla \phi \quad (41)$$

the term  $\mathbf{v} \times \mathbf{B}$  becomes

$$\mathbf{v} \times \mathbf{B} = [\psi, u] \nabla \phi + F \nabla_{pol} u \quad (42)$$

so (40) becomes

$$\frac{\partial F}{\partial t} = R[F, u] - R^2 \nabla \cdot (\eta \mathbf{J} \times \nabla \phi) \quad (43)$$

and by using the expression for the poloidal currents  $\mathbf{J}_p = \nabla F \times \nabla \phi$

$$\frac{\partial F}{\partial t} = R[F, u] + \eta \Delta^* F + \nabla_{pol} F \cdot \nabla \eta \quad (44)$$

This equation could be independently solved by prescribing  $u$ , which is given by the reduced MHD equations. In order to be consistent with the solved equations,  $\delta F/F_0 \ll 1$ . The question is if the resulting poloidal current equation is consistent with the calculation of the poloidal currents using the equilibrium condition.

### D.4.1 Consistency of the toroidal Faraday's equation with the equilibrium condition

The main goal of this section is to investigate if the equation (44) for the poloidal currents is satisfied when obtaining these currents from the Grad-Shafranov equation

$$\mathbf{J} \times \mathbf{B} = \nabla p \quad (45)$$

The poloidal currents can be expressed as

$$\mathbf{J}_p = \nabla F \times \nabla \phi = F' \nabla \psi \times \nabla \phi \quad (46)$$

because  $F = F(\psi, t)$  due to the equilibrium condition. We write all the terms of equation (44) in terms of the poloidal flux

$$\frac{\partial F}{\partial t} = F' \frac{\partial \psi}{\partial t} + \left. \frac{\partial F}{\partial t} \right|_{\psi=cte} \quad (47)$$

$$R[F, u] = F' R[\psi, u] \quad (48)$$

$$\eta \Delta^* F = F' \eta \Delta^* \psi + \eta F'' |\nabla_{pol} \psi|^2 \quad (49)$$

$$\nabla_{pol} F \cdot \nabla \eta = F' \eta' |\nabla_{pol} \psi|^2 \quad (50)$$

were we have used that the resistivity is a flux function. Plugging all the calculated terms into equation (44) we find

$$\frac{\partial \psi}{\partial t} + \frac{1}{F'} \frac{\partial F}{\partial t} \Big|_{\psi=cte} = R[\psi, u] + \eta j + \left( \eta' + \eta \frac{F''}{F'} \right) |\nabla_{pol} \psi|^2 \quad (51)$$

Using the reduced MHD equation for the poloidal flux ( $\partial_t \psi = R[\psi, u] + \eta j$ ) the equation for the poloidal currents is

$$\frac{\partial F}{\partial t} \Big|_{\psi=cte} = (\eta F')' |\nabla_{pol} \psi|^2 \quad (52)$$

When writing the equation ( $\partial_t \psi = R[\psi, u] + \eta j$ ) in terms of  $F$  we find

$$\frac{\partial F}{\partial t} = R[F, u] + \eta \Delta^* F + \frac{\partial F}{\partial t} \Big|_{\psi=cte} - \eta \frac{F''}{F'} |\nabla_{pol} \psi|^2 \quad (53)$$

which is the same equation as (44) provided (52).

# Bibliography

- [A K] A. Kirk. <http://www.fusion-cdt.ac.uk/field-area/test-field>. [Online; accessed 30-August-2018].
- [A W] A. White. [www.ens-lyon.fr/PHYSIQUE/Equipe2/LesHouches15/Talks\\_files/White\\_ExperimentalTokamaks.pdf](http://www.ens-lyon.fr/PHYSIQUE/Equipe2/LesHouches15/Talks_files/White_ExperimentalTokamaks.pdf). [Online; accessed 20-August-2018].
- [Art+18] Francisco Javier Artola et al. “Non-linear magnetohydrodynamic simulations of Edge Localised Mode triggering via vertical position oscillations in ITER”. In: *Nuclear Fusion* (2018). DOI: [10.1088/1741-4326/aace0e](https://doi.org/10.1088/1741-4326/aace0e).
- [Ata+16] Calin V Atanasiu et al. “Simulation of surface currents excited by plasma wall-touching kink and vertical modes in tokamak”. In: *Fundamentals of Electrical Engineering (IS-FEE), 2016 International Symposium on*. IEEE. 2016, pp. 1–4. DOI: [10.1109/isfee.2016.7803235](https://doi.org/10.1109/isfee.2016.7803235).
- [Bay+13] Larry R Baylor et al. “Reduction of edge-localized mode intensity using high-repetition-rate pellet injection in tokamak H-mode plasmas”. In: *Physical review letters* 110.24 (2013), p. 245001. DOI: [10.1103/physrevlett.110.245001](https://doi.org/10.1103/physrevlett.110.245001).
- [Béz82] Pierre Bézier. “Petite histoire d’une idée bizarre (2)”. In: *Bulletin de la section d’histoire des usines Renault* 4.24 (1982), pp. 256–268.
- [Boo12] Allen H Boozer. “Theory of tokamak disruptions”. In: *Physics of plasmas* 19.5 (2012), p. 058101. DOI: [10.1063/1.3703327](https://doi.org/10.1063/1.3703327).
- [BS02] Cornelis Marius Braams and Peter E Stott. *Nuclear fusion: half a century of magnetic confinement fusion research*. CRC Press, 2002.
- [CCE99] ITER Physics Expert Group on Confin Transport, ITER Physics Expert Group on Confin Database, and ITER Physics Basis Editors. “Chapter 2: Plasma confinement and transport”. In: *Nuclear Fusion* 39.12 (Dec. 1999), pp. 2175–2249. DOI: [10.1088/0029-5515/39/12/302](https://doi.org/10.1088/0029-5515/39/12/302).
- [CH08] Olivier Czarny and Guido Huysmans. “Bézier surfaces and finite elements for MHD simulations”. In: *Journal of computational physics* 227.16 (2008), pp. 7423–7445. DOI: [10.1016/j.jcp.2008.04.001](https://doi.org/10.1016/j.jcp.2008.04.001).
- [Cha+14] IT Chapman et al. “The stabilizing effect of core pressure on the edge pedestal in MAST plasmas”. In: *Nuclear Fusion* 55.1 (2014), p. 013004. DOI: [10.1088/0029-5515/55/1/013004](https://doi.org/10.1088/0029-5515/55/1/013004).
- [CHH16] JW Connor, CJ Ham, and RJ Hastie. “The effect of plasma beta on high-n ballooning stability at low magnetic shear”. In: *Plasma Physics and Controlled Fusion* 58.8 (2016), p. 085002. DOI: [10.1088/0741-3335/58/8/085002](https://doi.org/10.1088/0741-3335/58/8/085002).
- [CHT79] JW Connor, RJ Hastie, and JB Taylor. “On ballooning transformation”. In: *Proc. Royal Soc. A*. Vol. 365. 1979, pp. 1–17.
- [Con+98] JW Connor et al. “Magnetohydrodynamic stability of tokamak edge plasmas”. In: *Physics of Plasmas* 5.7 (1998), pp. 2687–2700. DOI: [10.1063/1.872956](https://doi.org/10.1063/1.872956).
- [COP15] COP21. <http://www.cop21paris.org>. [Online; accessed 19-July-2018]. 2015.

- [Deg+03] AW Degeling et al. “Magnetic triggering of ELMs in TCV”. In: *Plasma physics and controlled fusion* 45.9 (2003), p. 1637. DOI: [10.1088/0741-3335/45/9/306](https://doi.org/10.1088/0741-3335/45/9/306).
- [Dud+09] BD Dudson et al. “BOUT++: A framework for parallel plasma fluid simulations”. In: *Computer Physics Communications* 180.9 (2009), pp. 1467–1480. DOI: [10.1016/j.cpc.2009.03.008](https://doi.org/10.1016/j.cpc.2009.03.008).
- [Eid+15] NW Eidietis et al. “The ITPA disruption database”. In: *Nuclear Fusion* 55.6 (2015), p. 063030. DOI: [10.1088/0029-5515/55/6/063030](https://doi.org/10.1088/0029-5515/55/6/063030).
- [Eva+05] TE Evans et al. “Suppression of large edge localized modes in high confinement DIII-D plasmas with a stochastic magnetic boundary”. In: *Journal of nuclear materials* 337 (2005), pp. 691–696. DOI: [10.1016/j.jnucmat.2004.10.062](https://doi.org/10.1016/j.jnucmat.2004.10.062).
- [Fed+15] N Fedorczak et al. “Tungsten transport and sources control in JET ITER-like wall H-mode plasmas”. In: *Journal of nuclear materials* 463 (2015), pp. 85–90. DOI: [10.1016/j.jnucmat.2014.12.044](https://doi.org/10.1016/j.jnucmat.2014.12.044).
- [Fre14] Jeffrey P Freidberg. *ideal MHD*. Cambridge University Press, 2014. DOI: [10.1017/cbo9780511795046](https://doi.org/10.1017/cbo9780511795046).
- [Fut+14] S Futatani et al. “Non-linear MHD modelling of ELM triggering by pellet injection in DIII-D and implications for ITER”. In: *Nuclear Fusion* 54.7 (2014), p. 073008. DOI: [10.1088/0029-5515/54/7/073008](https://doi.org/10.1088/0029-5515/54/7/073008).
- [GGP04] JP Hans Goedbloed, JP Goedbloed, and Stefaan Poedts. *Principles of magnetohydrodynamics: with applications to laboratory and astrophysical plasmas*. Cambridge university press, 2004. DOI: [10.1017/cbo9780511616945](https://doi.org/10.1017/cbo9780511616945).
- [GKP10] Johan P Goedbloed, Rony Keppens, and Stefaan Poedts. *Advanced magnetohydrodynamics: with applications to laboratory and astrophysical plasmas*. Cambridge University Press, 2010. DOI: [10.1017/cbo9781139195560](https://doi.org/10.1017/cbo9781139195560).
- [Gla+99] AH Glasser et al. “The NIMROD code: a new approach to numerical plasma physics”. In: *Plasma Physics and Controlled Fusion* 41.3A (1999), A747. DOI: [10.1088/0741-3335/41/3a/067](https://doi.org/10.1088/0741-3335/41/3a/067).
- [Goh+88] P Gohil et al. “Study of giant edge-localized modes in DIII-D and comparison with ballooning theory”. In: *Physical review letters* 61.14 (1988), p. 1603. DOI: [10.1103/physrevlett.61.1603](https://doi.org/10.1103/physrevlett.61.1603).
- [Gra+96] RS Granetz et al. “Disruptions and halo currents in Alcator C-Mod”. In: *Nuclear fusion* 36.5 (1996), p. 545. DOI: [10.1088/0029-5515/36/5/i02](https://doi.org/10.1088/0029-5515/36/5/i02).
- [Gri+15a] Y Gribov et al. “Plasma vertical stabilisation in ITER”. In: *Nuclear Fusion* 55.7 (2015), p. 073021. DOI: [10.1088/0029-5515/55/7/073021](https://doi.org/10.1088/0029-5515/55/7/073021).
- [Gri+15b] Y Gribov et al. “Study of ELM triggering by axisymmetric in-vessel coils”. In: *42th EPS Conf. Plasma Physics*. Vol. 39E. 4. 2015, p. 125.
- [Gui15] Hervé Guillard. “The mathematical theory of reduced MHD models for fusion plasmas”. In: *arXiv preprint arXiv:1506.01843* (2015).
- [Hav+16] JW Haverkort et al. “Implementation of the full viscoresistive magnetohydrodynamic equations in a nonlinear finite element code”. In: *Journal of Computational Physics* 316 (2016), pp. 281–302. DOI: [10.1016/j.jcp.2016.04.007](https://doi.org/10.1016/j.jcp.2016.04.007).
- [HC07] GTA Huysmans and O Czarny. “MHD stability in X-point geometry: simulation of ELMs”. In: *Nuclear fusion* 47.7 (2007), p. 659. DOI: [10.1088/0029-5515/47/7/016](https://doi.org/10.1088/0029-5515/47/7/016).
- [HF89] SW Haney and JP Freidberg. “Variational methods for studying tokamak stability in the presence of a thin resistive wall”. In: *Physics of Fluids B: Plasma Physics* 1.8 (1989), pp. 1637–1645. DOI: [10.1063/1.858941](https://doi.org/10.1063/1.858941).

- [HGK91] GTA Huysmans, JP Goedbloed, and W Kerner. “Isoparametric bicubic Hermite elements for solution of the Grad-Shafranov equation”. In: *International Journal of Modern Physics C* 2.01 (1991), pp. 371–376. DOI: [10.1142/s0129183191000512](https://doi.org/10.1142/s0129183191000512).
- [Hir07] Charles Hirsch. *Numerical computation of internal and external flows: The fundamentals of computational fluid dynamics*. Butterworth-Heinemann, 2007.
- [Hoe+14] M Hoelzl et al. “Non-linear simulations of MHD instabilities in Tokamaks including Eddy current effects and perspectives for the extension to Halo currents”. In: *Journal of Physics: Conference Series*. Vol. 561. 1. IOP Publishing. 2014, p. 012011. DOI: [10.1088/1742-6596/561/1/012011](https://doi.org/10.1088/1742-6596/561/1/012011).
- [Höl+12] M Hözl et al. “Coupling JOREK and STARWALL codes for non-linear resistive-wall simulations”. In: *Journal of Physics: Conference Series*. Vol. 401. 1. IOP Publishing. 2012, p. 012010. DOI: [10.1088/1742-6596/401/1/012010](https://doi.org/10.1088/1742-6596/401/1/012010).
- [Höl+18] M Hözl et al. “Simulating tokamak edge instabilities: advances and challenges”. In: *45th EPS Conference on Plasma Physics*. 2018.
- [HRR02] Pascal Hénon, Pierre Ramet, and Jean Roman. “PASTIX: a high-performance parallel direct solver for sparse symmetric positive definite systems”. In: *Parallel Computing* 28.2 (2002), pp. 301–321. DOI: [10.1016/s0167-8191\(01\)00141-7](https://doi.org/10.1016/s0167-8191(01)00141-7).
- [Hub04] Joseph D Huba. *NRL: Plasma formulary*. Tech. rep. NAVAL RESEARCH LAB WASHINGTON DC BEAM PHYSICS BRANCH, 2004. DOI: [10.21236/ada429448](https://doi.org/10.21236/ada429448).
- [Huy+02] GTA Huysmans et al. “MHD stability of current hole plasmas”. In: *Joint Varenna-Laussane Workshop on the Theory of Fusion Plasmas*. 2002.
- [Huy+09] GTA Huysmans et al. “Non-linear MHD simulations of edge localized modes (ELMs)”. In: *Plasma Physics and Controlled Fusion* 51.12 (2009), p. 124012. DOI: [10.1088/0741-3335/51/12/124012](https://doi.org/10.1088/0741-3335/51/12/124012).
- [Huy05] GTA Huysmans. “ELMs: MHD instabilities at the transport barrier”. In: *Plasma Physics and Controlled Fusion* 47.12B (2005), B165. DOI: [10.1088/0741-3335/47/12b/s13](https://doi.org/10.1088/0741-3335/47/12b/s13).
- [Jac99] John David Jackson. *Classical electrodynamics*. Wiley, 1999.
- [Jar+08] SC Jardin et al. “The M3D-C1 approach to simulating 3D 2-fluid magnetohydrodynamics in magnetic fusion experiments”. In: *Journal of Physics: Conference Series*. Vol. 125. 1. IOP Publishing. 2008, p. 012044. DOI: [10.2172/959333](https://doi.org/10.2172/959333).
- [Jar10] Stephen Jardin. *Computational methods in plasma physics*. CRC Press, 2010. DOI: [10.1201/ebk1439810958](https://doi.org/10.1201/ebk1439810958).
- [Ji+17] Jeong-Young Ji et al. “Electron parallel transport for arbitrary collisionality”. In: *Physics of Plasmas* 24.11 (2017), p. 112121.
- [K+99] M Keilhacker, JET Team, et al. “Fusion physics progress on JET”. In: *Fusion engineering and design* 46.2-4 (1999), pp. 273–290. DOI: [10.1016/s0920-3796\(99\)00020-4](https://doi.org/10.1016/s0920-3796(99)00020-4).
- [KB17] DI Kiramov and BN Breizman. “Model of vertical plasma motion during the current quench”. In: *Physics of Plasmas* 24.10 (2017), p. 100702. DOI: [10.1063/1.4993071](https://doi.org/10.1063/1.4993071).
- [Kei+84] M Keilhacker et al. “Confinement studies in L and H-type Asdex discharges”. In: *Plasma Physics and Controlled Fusion* 26.1A (1984), p. 49. DOI: [10.1088/0741-3335/26/1a/305](https://doi.org/10.1088/0741-3335/26/1a/305).
- [Ker+98] W Kerner et al. “CASTOR: Normal-mode analysis of resistive MHD plasmas”. In: *Journal of computational physics* 142.2 (1998), pp. 271–303. DOI: [10.1006/jcph.1998.5910](https://doi.org/10.1006/jcph.1998.5910).
- [Kim+09] SH Kim et al. “Comparing magnetic triggering of ELMs in TCV and ASDEX Upgrade”. In: *Plasma Physics and Controlled Fusion* 51.5 (2009), p. 055021. DOI: [10.1088/0741-3335/51/5/055021](https://doi.org/10.1088/0741-3335/51/5/055021).

- [KL93] RR Khayrulinov and VE Lukash. “Studies of plasma equilibrium and transport in a tokamak fusion device with the inverse-variable technique”. In: *Journal of Computational Physics* 109.2 (1993), pp. 193–201. DOI: [10.1006/jcph.1993.1211](https://doi.org/10.1006/jcph.1993.1211).
- [Kre+13] I. Krebs et al. “Nonlinear excitation of low-n harmonics in reduced magnetohydrodynamic simulations of edge-localized modes”. In: *Physics of Plasmas* 20.8 (Aug. 2013), p. 082506. DOI: <https://doi.org/10.1063/1.4817953>.
- [Lan+04] PT Lang et al. “Frequency control of type-I ELMs by magnetic triggering in ASDEX Upgrade”. In: *Plasma physics and controlled fusion* 46.11 (2004), p. L31. DOI: [10.1088/0741-3335/46/11/102](https://doi.org/10.1088/0741-3335/46/11/102).
- [Lan+08] PT Lang et al. “Investigation of pellet-triggered MHD events in ASDEX Upgrade and JET”. In: *Nuclear Fusion* 48.9 (2008), p. 095007. DOI: [10.1088/0029-5515/48/9/095007](https://doi.org/10.1088/0029-5515/48/9/095007).
- [Lao+85] LL Lao et al. “Reconstruction of current profile parameters and plasma shapes in tokamaks”. In: *Nuclear fusion* 25.11 (1985), p. 1611. DOI: [10.1088/0029-5515/25/11/007](https://doi.org/10.1088/0029-5515/25/11/007).
- [Leh+15] Michael Lehnert et al. “Disruptions in ITER and strategies for their control and mitigation”. In: *Journal of Nuclear Materials* 463 (2015), pp. 39–48. DOI: [10.1016/j.jnucmat.2014.10.075](https://doi.org/10.1016/j.jnucmat.2014.10.075).
- [Leh18] M. Lehnert. “ITER Disruptions Issues”. In: *31st ITPA MHD Disruption and Control Topical Group*. 2018.
- [Liu+15] F Liu et al. “Nonlinear MHD simulations of Quiescent H-mode plasmas in DIII-D”. In: *Nuclear Fusion* 55.11 (2015), p. 113002. DOI: [10.1088/0029-5515/55/11/113002](https://doi.org/10.1088/0029-5515/55/11/113002).
- [LL08] Hinrich Lütjens and Jean-François Luciani. “The XTOR code for nonlinear 3D simulations of MHD instabilities in tokamak plasmas”. In: *Journal of Computational Physics* 227.14 (2008), pp. 6944–6966. DOI: [10.1016/j.jcp.2008.04.003](https://doi.org/10.1016/j.jcp.2008.04.003).
- [Loa+02] A Loarte et al. “Characteristics and scaling of energy and particle losses during Type I ELMs in JET H-modes”. In: *Plasma Physics and Controlled Fusion* 44.9 (2002), p. 1815. DOI: [10.1088/0741-3335/44/9/303](https://doi.org/10.1088/0741-3335/44/9/303).
- [Loa+03] A Loarte et al. “Characteristics of type I ELM energy and particle losses in existing devices and their extrapolation to ITER”. In: *Plasma Physics and Controlled Fusion* 45.9 (2003), p. 1549. DOI: [10.1088/0741-3335/45/9/302](https://doi.org/10.1088/0741-3335/45/9/302).
- [Loa+04] A Loarte et al. “Characterization of pedestal parameters and edge localized mode energy losses in the Joint European Torus and predictions for the International Thermonuclear Experimental Reactor”. In: *Physics of plasmas* 11.5 (2004), pp. 2668–2678. DOI: [10.1063/1.1707025](https://doi.org/10.1063/1.1707025).
- [Loa+14] A Loarte et al. “Progress on the application of ELM control schemes to ITER scenarios from the non-active phase to DT operation”. In: *Nuclear Fusion* 54.3 (2014), p. 033007. DOI: [10.1088/0029-5515/54/3/033007](https://doi.org/10.1088/0029-5515/54/3/033007).
- [Lun+15] Elena de la Luna et al. “Understanding the physics of ELM pacing via vertical kicks in JET in view of ITER”. In: *Nuclear Fusion* 56.2 (2015), p. 026001. DOI: [10.1088/0029-5515/56/2/026001](https://doi.org/10.1088/0029-5515/56/2/026001).
- [Mag+13] P Maget et al. “MHD stability of the pedestal in ITER scenarios”. In: *Nuclear Fusion* 53.9 (2013), p. 093011. DOI: [10.1088/0029-5515/53/9/093011](https://doi.org/10.1088/0029-5515/53/9/093011).
- [McA14] Rachel McAdams. “Non-linear magnetohydrodynamic instabilities in advanced tokamak plasmas”. PhD thesis. University of York, 2014.
- [Mei+09] Malte Meinhagen et al. “Greenhouse-gas emission targets for limiting global warming to 2 C”. In: *Nature* 458.7242 (2009), p. 1158. DOI: [10.1038/nature08017](https://doi.org/10.1038/nature08017).
- [Mik+97] AB Mikhailovskii et al. “Optimization of computational MHD normal-mode analysis for tokamaks”. In: *Plasma Physics Reports* 23.10 (1997), pp. 844–857.

- [Mil08] Glenn Milne. “How the climate drives sea-level changes”. In: *Astronomy & Geophysics* 49.2 (2008), pp. 2–24. DOI: [10.1111/j.1468-4004.2008.49224.x](https://doi.org/10.1111/j.1468-4004.2008.49224.x).
- [Min+17] AF Mink et al. “Nonlinear coupling induced toroidal structure of edge localized modes”. In: *Nuclear Fusion* 58.2 (2017), p. 026011. DOI: [10.1088/1741-4326/aa98f7](https://doi.org/10.1088/1741-4326/aa98f7).
- [MMS99] Patrick J McCarthy, Peter Martin, and Wolfgang Schneider. “The CLISTE interpretive equilibrium code”. In: (1999).
- [MS15] P Merkel and E Strumberger. “Linear MHD stability studies with the STARWALL code”. In: *arXiv preprint arXiv:1508.04911* (2015).
- [Mye+17] CE Myers et al. “A multi-machine scaling of halo current rotation”. In: *Nuclear Fusion* 58.1 (2017), p. 016050. DOI: [10.1088/1741-4326/aa958b](https://doi.org/10.1088/1741-4326/aa958b).
- [OBr+92] DP O’Brien et al. “Equilibrium analysis of iron core tokamaks using a full domain method”. In: *Nuclear Fusion* 32.8 (1992), p. 1351. DOI: [10.1088/0029-5515/32/8/i05](https://doi.org/10.1088/0029-5515/32/8/i05).
- [Oos+18] W Oosterbeek et al. “Evaluation of core beta effects on pedestal MHD stability in ITER and consequences for energy confinement”. In: *45th EPS Conference on Plasma Physics*. Vol. 42A. 2018. Chap. P2, p. 1055. ISBN: 979-10-96389-08-7.
- [Ora+13] F Orain et al. “Non-linear magnetohydrodynamic modeling of plasma response to resonant magnetic perturbations”. In: *Physics of Plasmas* 20.10 (2013), p. 102510. DOI: [10.1063/1.4824820](https://doi.org/10.1063/1.4824820).
- [Pam+16] S Pamela et al. “Multi-machine modelling of ELMs and pedestal confinement: From validation to prediction”. In: *26th IAEA Fusion Energy Conference, 17-22 October 2016*. 2016.
- [Pam+17] SJP Pamela et al. “Recent progress in the quantitative validation of JOREK simulations of ELMs in JET”. In: *Nuclear Fusion* 57.7 (2017), p. 076006. DOI: [10.1088/1741-4326/aa6e2a](https://doi.org/10.1088/1741-4326/aa6e2a).
- [Par+99] W. Park et al. “Plasma simulation studies using multilevel physics models”. In: *Physics of Plasmas* 6.5 (May 1999), pp. 1796–1803. DOI: <https://doi.org/10.1063/1.873437>.
- [PBP06] Richard Pitts, Richard Buttery, and Simon Pinches. “Fusion: the way ahead”. In: *Physics World* 19.3 (2006), p. 20. DOI: [10.1088/2058-7058/19/3/35](https://doi.org/10.1088/2058-7058/19/3/35).
- [Rie91] K-U Riemann. “The Bohm criterion and sheath formation”. In: *Journal of Physics D: Applied Physics* 24.4 (1991), p. 493. DOI: [10.1088/0022-3727/24/4/001](https://doi.org/10.1088/0022-3727/24/4/001).
- [SAL99] Olivier Sauter, Clemente Angioni, and YR Lin-Liu. “Neoclassical conductivity and bootstrap current formulas for general axisymmetric equilibria and arbitrary collisionality regime”. In: *Physics of Plasmas* 6.7 (1999), pp. 2834–2839. DOI: [10.1063/1.873240](https://doi.org/10.1063/1.873240).
- [Sch+11] Tyge Schioler et al. “Dynamic response of the ITER tokamak during asymmetric VDEs”. In: *Fusion Engineering and Design* 86.9-11 (2011), pp. 1963–1966. DOI: [10.1016/j.fusengdes.2010.11.016](https://doi.org/10.1016/j.fusengdes.2010.11.016).
- [Sny+11] PB Snyder et al. “A first-principles predictive model of the pedestal height and width: development, testing and ITER optimization with the EPED model”. In: *Nuclear Fusion* 51.10 (2011), p. 103016. DOI: [10.1088/0029-5515/51/10/103016](https://doi.org/10.1088/0029-5515/51/10/103016).
- [Sny+15] Philip B Snyder et al. “Super H-mode: theoretical prediction and initial observations of a new high performance regime for tokamak operation”. In: *Nuclear Fusion* 55.8 (2015), p. 083026. DOI: [10.1088/0029-5515/55/8/083026](https://doi.org/10.1088/0029-5515/55/8/083026).
- [SS86] Youcef Saad and Martin H Schultz. “GMRES: A generalized minimal residual algorithm for solving nonsymmetric linear systems”. In: *SIAM Journal on scientific and statistical computing* 7.3 (1986), pp. 856–869. DOI: [10.1137/0907058](https://doi.org/10.1137/0907058).
- [Sta+00] Peter C Stangeby et al. *The plasma boundary of magnetic fusion devices*. Vol. 224. Institute of Physics Publishing Bristol, 2000.

- [Str76] Hank R Strauss. “Nonlinear, three-dimensional magnetohydrodynamics of noncircular tokamaks”. In: *The Physics of Fluids* 19.1 (1976), pp. 134–140. DOI: [10.1063/1.861310](https://doi.org/10.1063/1.861310).
- [SZ72] VD Shafranov and LE Zakharov. “Use of the virtual-casing principle in calculating the containing magnetic field in toroidal plasma systems”. In: *Nuclear Fusion* 12.5 (1972), p. 599. DOI: [10.1088/0029-5515/12/5/009](https://doi.org/10.1088/0029-5515/12/5/009).
- [TS98] Y. Todo and T. Sato. “Linear and nonlinear particle-magnetohydrodynamic simulations of the toroidal Alfvén eigenmode”. In: *Physics of Plasmas* 5.5 (May 1998), pp. 1321–1327. DOI: <https://doi.org/10.1063/1.872791>.
- [Wag+82] Fritz Wagner et al. “Regime of improved confinement and high beta in neutral-beam-heated divertor discharges of the ASDEX tokamak”. In: *Physical Review Letters* 49.19 (1982), p. 1408. DOI: [10.1103/physrevlett.49.1408](https://doi.org/10.1103/physrevlett.49.1408).
- [WC11] John Wesson and David J Campbell. *Tokamaks*. Vol. 149. Oxford University Press, 2011.
- [Wes78] JA Wesson. “Hydromagnetic stability of tokamaks”. In: *Nuclear Fusion* 18.1 (1978), p. 87. DOI: [10.1088/0029-5515/18/1/010](https://doi.org/10.1088/0029-5515/18/1/010).
- [Zak+15] Leonid E Zakharov et al. “Electromagnetic thin-wall model for simulations of plasma wall-touching kink and vertical modes”. In: *Journal of Plasma Physics* 81.6 (2015).
- [Zak08] Leonid E Zakharov. “The theory of the kink mode during the vertical plasma disruption events in tokamaks”. In: *Physics of Plasmas* 15.6 (2008), p. 062507.
- [Zoh96] Hartmut Zohm. “Edge localized modes (ELMs)”. In: *Plasma Physics and Controlled Fusion* 38.2 (1996), p. 105. DOI: [10.1088/0741-3335/38/2/001](https://doi.org/10.1088/0741-3335/38/2/001).



## Abstract

One of the most promising concepts for future fusion reactors is the tokamak. In these devices, a hot ionized plasma is confined with the use of large magnetic fields. As these systems are typically out of thermodynamic equilibrium, they are prone to instabilities that deteriorate the plasma confinement and can also damage the plasma facing components. The subject of this thesis is the study of a particular type of tokamak instabilities with numerical MagnetoHydroDynamic (MHD) simulations. The numerical code JOREK-STARWALL is adapted and applied to the simulation of the so-called free-boundary instabilities. The investigation of this type of instabilities requires a special treatment for the plasma boundary conditions for the magnetic field, where the interaction of the plasma with the vacuum and the surrounding conducting structures needs to be taken into account. In this work, the modelling of the electromagnetic plasma-wall-vacuum interaction is reviewed and generalized for time-varying coil currents and for the so-called halo currents, which are electric currents flowing from the plasma to the wall and vice versa. The adapted JOREK-STARWALL code is applied to realistic plasma geometries in order to study the physics of two particular free-boundary instabilities: Edge Localized Modes (ELMs) triggered by vertical position oscillations and Vertical Displacement Events (VDEs). Two major results are obtained: 1. The triggering of ELMs during vertical position oscillations is for the first time reproduced with self-consistent simulations. These allow for the investigation of the physical mechanism underlying this phenomenon. The simulations reveal that for the international ITER project, a large-scale tokamak, these triggered ELMs are mainly due to an increase in the plasma edge current due to the vertical plasma motion. 2. For VDEs, several benchmarks are performed with other existing MHD codes showing a good agreement and therefore allowing the performance of ITER simulations to estimate the expected amount of halo currents in ITER. Additionally, preliminary toroidally asymmetric VDE simulations are presented.

## Résumé

Un des dispositifs les plus prometteurs pour réaliser la fusion contrôlée est le réacteur de type tokamak. Dans ces réacteurs, un plasma chaud ionisé est confiné à l'aide d'un champ magnétique intense. Puisqu'un tel plasma est généralement hors équilibre thermodynamique, il est le siège d'instabilités qui détériorent son confinement et peuvent également endommager les composants qui l'entourent. Ce travail de thèse porte sur l'étude d'une classe particulière d'instabilités au sein d'un tokamak. Cette étude est menée par des simulations numériques basées sur des modèles magnétohydro-dynamiques (MHD). Le code numérique JOREK-STARWALL est adapté et appliqué pour étudier les instabilités dites à frontière libre. Ce type d'instabilités nécessitent un traitement spécial concernant les conditions de bord du plasma pour le champ magnétique, où l'interaction du plasma avec le vide et les structures conductrices environnantes doit être prise en compte. La modélisation de l'interaction électromagnétique plasma-paroi-vide est généralisée pour les courants de bobine variables dans le temps et pour les courants dits de halo, qui sont des courants électriques circulant du plasma vers la paroi et vice versa. JOREK-STARWALL permet d'utiliser des géométries réalistes afin d'étudier la physique de deux instabilités particulières à frontière libre: les modes localisés au bord ("Edge Localized Modes", ELMs) déclenchés par des oscillations de la position verticale du plasma et les evenements de déplacement vertical (Vertical Displacement Events, VDEs). Deux résultats majeurs sont obtenus: 1. Le déclenchement des ELMs par des oscillations de la position verticale est pour la première fois reproduit avec des simulations auto-cohérentes. Celles-ci permettent d'étudier le mécanisme physique sous-jacent à ce phénomène. Les simulations révèlent que pour le projet international ITER, un tokamak à grande échelle, ces ELMs déclenchés sont principalement dus à une augmentation du courant au bord du plasma due au mouvement vertical. 2. Pour les VDEs, plusieurs comparaisons effectuées avec d'autres codes MHD existants montrent un bon accord avec JOREK-STARWALL et permettant ainsi de réaliser des simulations pour estimer la quantité attendue de courants de halo dans ITER. Finalement, des simulations préliminaires des VDEs avec des asymétries toroïdales sont présentées.